Experimental parameter estimation in incoherent images via spatial-mode demultiplexing

Clémentine Rouvière

Thèse de doctorat de
Sorbone Université

présentée par

Clémentine Rouvière

pour obtenir le grade de Docteur de Sorbonne Université
sur le sujet:

Experimental parameter estimation in incoherent images via spatial-mode demultiplexing

Laboratoire Kastler Brossel
Physique quantique et applications

Membres du jury :

Pr. Daniele FACCIO	Rapporteur
Pr. Konrad BANASZEK	Rapporteur
Pr. Sophie BRASSELET	Examinatrice
Pr. Catherine SCHWOB	Présidente du jury
Dr. Olivier PINEL	Membre invité
Dr. Mattia WALSCHAERS	Membre invité
Pr. Nicolas TREPS	Directeur de thèse

Abstract

Historically, the resolution of optical imaging systems was dictated by diffraction, and the Rayleigh criterion was long considered an unsurpassable limit. Superresolution techniques have been developed to overcome this limit, however, they are often domain-specific, and reaching sub-Rayleigh resolution remains a challenge. Examining imaging problems through the lens of parameter estimation elucidates the constraints inherent in traditional super-resolution approaches and provides a quantum-optimal measurement based on photodetection in the Hermite-Gaussian mode basis. In this thesis, we implemented this metrology-inspired approach for estimating the separation between two incoherent sources, achieving a sensitivity of five orders of magnitude beyond the Rayleigh limit thanks to a multimodal approach. In our setup, based on a spatial mode demultiplexer, we investigated scenes with bright and faint sources. Analyzing sensitivity and accuracy over an extensive range of separations, we demonstrate the remarkable effectiveness of demultiplexing for sub-Rayleigh separation estimation. This work paves the way for reaching high sensitivity in more intricate optical scenes, closer to realistic imaging situations.

Acknowledgements

This manuscript concludes the four incredible years I spent in the Multimode Quantum Optics group. During my time here, I had the privilege to interact with so many kind and talented people. I'm going to try to express how grateful I am to have had the opportunity to work with you all.
First, I would like to thank the members of the jury, Konrad Banaszek, Daniele Faccio, Sophie Brasselet, Olivier Pinel and Catherine Schwob, for reviewing my work and for the interesting discussion that followed the defence. In particular, many thanks to Konrad Banaszek and Daniele Faccio for reading my PhD thesis in great detail and for your insightful comments.
Thanks to all the members of LKB, especially to the members of the Jussieu site, I'm keeping so many great memories of coffee breaks, LKBars and game nights. In particular, I want to thank the admin and technical teams of the lab, without whom this thesis couldn't be what it is: Bintou, Adil, Tan Trung and Rémy, Elie, Loïc, David et Bérengère, Carou and Gaël. And huge thanks to Stéphanie, Laetitia, David, Céline et Thierry for having always patiently answered my questions about contracts, orders and other ordres de mission.
Of course, many thanks to all the members of the MQO team with whom we crossed paths throughout these four years, for the lunches at the canteen (at 11:45 sharp thanks to Ilya), the pauses crêpe, the beers at La Bulle à Bière, the climbing sessions at Arkose, and for making life in the lab seriously fun or funly serious depending on the time. Huge thanks to the ones who collaborated to the PEsto project. Manuel for supervising me and introducing me to the world of parameter estimation during the lockdown, Giacomo for explaining the theoretical concepts with infinite pedagogy, Ilya for always answering my questions but also increasing my confusion about thermal states, David for accepting to divide your time between SPOPO and PEsto and for your help on the experiment when life made it difficult for me to work on it, Antonin for joining us on the experiment, for always improving it but also for your creepy questions about grocery shopping, and Alexander for keeping an eye on Antonin and spending days on reading this manuscript in details. I learned so much with you all and this thesis is the result of the many extremely interesting discussions we had.
Thanks to the video gang, the escape game crew, and most of all, thanks to my girl squad, Beate and Francesca for all the moments we shared together drinking beers and coffees, dancing, escaping rooms and roller disco skating. Having met you and getting the chance to know you is highly precious to me. Thanks to Ganaël for your support and for introducing me to folk dances. Thanks to Niels for your joy and your playfulness, your infinite energy, your jokes, our discussions about fantasy books and life, I was always sure to find light in the cave thanks to you.
Last but not least, many thanks to Valentina, Mattia and Nicolas, for giving me the

opportunity of being part of the whimsical family that is the MQO group. Working with you was an amazing experience, you are extremely inspiring people and you always take the time to discuss scientific (or not) subjects even though your calendars are completely full all the time. In particular, thanks to Mattia and Nicolas for supervising my thesis and for balancing my pessimism with your optimism. Mattia, I would have liked to do more theory during these last three years but life decided otherwise. Thank you for teaching me to write an article and for taking the time to explain to me the subtleties of the P function. I'll make sure to never challenge you in a duel now that I know that you are an expert in medieval sword arts. Nicolas, I'm not sure I have the words to thank you. Thanks a lot for trusting me for the PEsto project and for your brilliant supervision throughout the last four years. They were true turning points for me, which you understood, transmitting much more than your knowledge about physics.
Finally, I want to thank my family and friends, whose support was crucial to me. Eugénia, Clément, Alice, Corentin, Guillaume, Aline and Louis, you probably don't realize it but you contributed a great deal to the success of this thesis. Benoît, thank you so much for always supporting me, for your encouragement and for taking care of me. I can't say how lucky I feel to have you by my side. This thesis wouldn't be what it is without you.

Contents

Introduction

The *Bureau International des Poids et Mesures* (BIPM) defines metrology as "the science of measurement, embracing both experimental and theoretical determinations at any level of uncertainty in any field of science and technology" [collectif 2012]. The impact of metrology spans numerous fields beyond purely scientific domains and this characteristic is imprinted in the roots of modern metrology. Indeed, one of its most famous tasks is to establish common definitions of units, and this was initiated in France, right after the Revolution, for political motivations of unifying the nation [Jedrzejewski 2002]. This led to the last revised definition of the International Unit System based on fixed values of seven physical constants in 2019 [BIPM 2019]. It also plays a critical role in health as it ensures reliable measurements for diagnosis, as well as in economics since trade is ensured by precisely manufactured and tested products, or in communications where atomic clocks ensure a common and precise time reference for satellites. Finally, metrology is also of paramount importance for the advancement of science. Indeed, scientific theories are confirmed or refuted by performing measurements. One of the most striking examples of the last few years was the detection of gravitational waves by the LIGO-Virgo collaboration, a phenomenon that was predicted by the theory of general relativity [Virgo Collaboration 2019].
Many measurements, however, do not give direct access to the quantities of interest. For example, optical measurements are always based on intensity measurements, and the determination of relevant quantities are achieved through more or less sophisticated data processing. Most of the quantities of interest are said to be parameters that are encoded in a probe by a physical interaction and estimated from the outcomes of measurements performed on the probe. Formally, parameter estimation theory is the branch of statistics that establishes the mathematical framework of metrology [Kay 1993].
Another task of metrology is to reach high accuracy and high precision in the measurements by studying the sources of noise and how to limit their impact on the measurements. This analysis can be performed with the tools provided by the parameter estimation theory. The noises can be technical, such as mechanical or thermal fluctuations, but also intrinsic, i.e. arising from the quantum nature of some systems, which poses the most fundamental limit in the measurement precision and accuracy. This last noise source is taken into account in a quantum version of estimation theory, adapted by Helstrom [Helstrom 1967; Helstrom 1969] at the end of the 20th century. For a quantum parameter estimation task, the unknown parameter is encoded into a quantum probe and this could provide an experimental quantum advantage, outperforming classical strategies and getting closer to the fundamental precision limit [Caves 1981; Braunstein 1994; Giovannetti 2011; Barbieri 2022].

Light plays a crucial role in the task of parameter estimation. It carries information that we can extract either to learn more about our environment or to communicate with each other, and it allows us to perform precise non-invasive measurements. The Revised International System of Units ties the meter to the speed of light in vacuum, showcasing the centrality of light in precision measurements. Optical range-finding measurements can measure extremely long distances with high accuracy, for instance, the Lunar Laser Ranging experiment determined the distance between Earth and the Moon with an accuracy of a few millimeters [Murphy 2008].
For a long time, light was studied and used through its classical part, or its different degrees of freedom (amplitude, phase, polarization, spectral and temporal properties) called modes. On the other hand, light has a unique status among quantum objects, its quantum nature can emerge relatively easily in the lab. This is why light is a probe of choice while studying quantum metrology problems. Tailoring specific quantum states of light can provide a quantum advantage in measurements. Notably, the so-called NOON states can enhance the sensitivity in phase estimation tasks [Slussarenko 2017], while squeezed states were shown to improve the sensitivity in the context of gravitational wave detection [Virgo Collaboration 2019] and beam displacement estimations [Treps 2003].

Imaging is a domain that would profit from precision enhancement. The resolution of imaging systems is historically known to be diffraction-limited and the minimal resolvable distance is given by Rayleigh's limit, i.e. of the order of the beam size [Abbe 1873; Rayleigh 1879]. Despite the development of superresolution techniques both in microscopy [Hell 1994; Betzig 2006; Hell 2007; Dickson 1997] and in astronomy, the gain was still limited to an order of magnitude at best. Moreover, these techniques are domain-specific, some of them requiring intricate control over the light source [Hell 1994; Hell 2007], manipulations of the illuminated sample [Betzig 2006; Dickson 1997], or very sophisticated apparatus.
However, a quantum parameter estimation analysis revealed that Rayleigh's limit is not a fundamental limit and that it could be overcome by several orders of magnitude, even with classical resources. This conclusion emerged by reducing imaging tasks to their essence which is the estimation of separation between two point-like sources imaged by a diffraction-limited optical system [Tsang 2016]. Through a quantum metrology analysis, they determined that the diffraction limit can be overcome by changing the detection apparatus, from a camera, typically used in imaging contexts, to a spatial-mode demultiplexer (SPADE), which decomposes the light over a given spatial mode basis, in our case, the Hermite-Gaussian mode basis [Morizur 2010].
SPADE was proven to provide a scaling advantage for the minimal resolvable distance compared with DI in an ideal scenario. This advantage is preserved in the presence of experimental noise even if the scaling is degraded [Gessner 2020a; Len 2020; Lupo 2020; Sorelli 2021b] Since then, the advantages provided by this metrology-inspired approach have been theoretically extended to other related problems such as discrimination tasks [Lu 2018; Grace 2022] and multiparameter estimation [Řehaček 2017; Napoli 2019; Tsang 2017], also including more general photon statistics [Nair 2016; Lupo 2016]. Early experiments used interferometric schemes to implement a simplified version of the demultiplexing approach [Yang 2016; Paúr 2016;

Tang 2016; Tham 2017; Zhou 2019a; Zanforlin 2022; Parniak 2018; Wadood 2021; Santamaria 2023]. A comprehensive literature review of these articles is provided in chapter 3.

During the last two decades, our group has developed expertise in the study of spatial modes in quantum optics [Schwob 1997; Treps 2001; Gigan 2004; Delaubert 2007; Chalopin 2009; Morizur 2011; Boucher 2018]. In particular, the thesis of Jean-François Morizur resulted in the creation of the company Cailabs in 2013 which specialized in the development of spatial-mode demultiplexers via multi-plane light conversion (MPLC).
Using an MPLC, Boucher *et al.* demonstrated that SPADE is potentially efficient, but did not achieve an ultra-sensitive separation estimation [Boucher 2020]. In the footsteps of these advancements, this thesis aims to contribute to the experimental realization of ultra-sensitive separation estimation between incoherent equally bright sources using spatial-mode demultiplexing.

This thesis is organized as follows.
Chapter 1 introduces the main concepts of quantum optics, in particular, the spatial modes that are central to this work.
Chapter 2 presents the tools for parameter estimation that we use, in particular the quantum Fisher information for separation estimation of two incoherent equally bright sources and the Fisher information for SPADE.
Chapter 3 exposes the limitations of the traditional approaches for superresolution and provides a literature review of the various experiments that were performed in the scope of separation estimation. This chapter also describes the experimental setup we used to conduct an ultra-sensitive separation estimation.
Chapter 4 examines the different noise sources arising from the setup and provides a prediction of the sensitivity that the experimental setup could reach.
Finally, chapter 5 presents the experimental results that we obtained, as well as some prospects for this project. In particular, we discuss the sensitivity for separation estimation we measured either for a low photon flux (3500 detected photons in total per integration time) where the performances of any camera are outperformed or for a high photon flux (10^{13} detected photons in total per integration time) where we achieved a five order of magnitude gain compared to Rayleigh's limit.

Chapter 1

Modes and states and measurements in quantum optics

Contents

This chapter introduces the concepts and notations necessary to describe the electromagnetic field, see [Grynberg 2010] and paper "Modes and states in quantum optics" by [Fabre 2020] for a more thorough development. We first explore the two sides of quantum optics, the optical modes in the first section and the quantum states in the second section. Finally, in the third section, we mention the measurements that will be discussed in this thesis.

1.1 Modes

Let us begin with the description of the classical electromagnetic field, based on the concept of modes. We will then focus on the so-called Hermite-Gaussian modes, which are one of the building blocks of this work.

1.1.1 Modes of the electromagnetic field

The time-frequency Fourier decomposition of the electric field is written as follows:

$$\mathbf{E}(\mathbf{r},t) = \frac{1}{\sqrt{2\pi}} \int_{-\infty}^{+\infty} d\omega \, e^{-i\omega t} \tilde{\mathbf{E}}(\mathbf{r},\omega), \tag{1.1}$$

where $\tilde{\mathbf{E}}(\mathbf{r},\omega)$ is the Fourier transform of the complex electric field $\mathbf{E}(\mathbf{r},t)$. The electric field can be separated into a positive frequency component $\mathbf{E}^{(+)}(\mathbf{r},t)$ and a negative frequency component $\mathbf{E}^{(-)}(\mathbf{r},t)$:

$$\mathbf{E}(\mathbf{r},t) = \mathbf{E}^{(+)}(\mathbf{r},t) + \mathbf{E}^{(-)}(\mathbf{r},t), \tag{1.2}$$

where

$$\mathbf{E}^{(+)}(\mathbf{r},t) = \frac{1}{\sqrt{2\pi}} \int_{0}^{+\infty} d\omega \, e^{-i\omega t} \tilde{\mathbf{E}}(\mathbf{r},\omega) \tag{1.3}$$

and

$$\mathbf{E}^{(-)}(\mathbf{r},t) = [\mathbf{E}^{(+)}(\mathbf{r},t)]^*. \tag{1.4}$$

From eq. (1.4), we see that $\mathbf{E}^{(+)}(\mathbf{r},t)$ and $\mathbf{E}^{(-)}(\mathbf{r},t)$ carry redundant information. This is why in the following, we will only consider $\mathbf{E}^{(+)}(\mathbf{r},t)$.

We restrict ourselves to the case where the field is enclosed in a finite volume V, much larger than the physical system. A mode of the electromagnetic field is a vector field $\mathbf{u}_1(\mathbf{r},t)$ which is a solution of Maxwell's equations and that satisfies at any time t the normalization condition

$$\frac{1}{V} \int_V d^3\mathbf{r} \, |\mathbf{u}_1(\mathbf{r},t)|^2 = 1. \tag{1.5}$$

Due to the linearity of Maxwell's equations, one can construct an orthonormal mode basis $\mathbf{u}_\ell(\mathbf{r},t)$. Since the field is enclosed in a finite volume V[1], the mode basis is discrete and the electric field can be expanded as follows:

$$\mathbf{E}^{(+)}(\mathbf{r},t) = \sum_\ell \mathcal{E}_\ell \mathbf{u}_\ell(\mathbf{r},t), \tag{1.6}$$

where $\mathcal{E}_\ell$ is the complex amplitude of the different modes. The modes satisfy the orthonormality condition, i.e. at any time t

$$\frac{1}{V} \int_V d^3\mathbf{r} \, \mathbf{u}_\ell^*(\mathbf{r},t) \mathbf{u}_{\ell'}(\mathbf{r},t) = \delta_{\ell\ell'} \tag{1.7}$$

and the completeness relation, i.e at any time t

$$\sum_\ell \mathbf{u}_\ell^*(\mathbf{r},t) \mathbf{u}_\ell(\mathbf{r}',t) = 2V\delta^{(3)}(\mathbf{r}-\mathbf{r}'). \tag{1.8}$$

[1]This is true for plane waves, with periodical boundary conditions. Throughout this manuscript, we will only exclusively refer to the Hermite-Gaussian modes (see section 1.1.2). These modes have an infinite spatial extension, but they can be decomposed over the plane wave basis, at least approximately.

Mode basis change In principle, the electromagnetic field can be decomposed over any orthonormal complete basis. The choice of the mode basis is not unique and will depend, in practice, on the symmetry of the problem under consideration. It is thus useful to be able to perform mode basis changes. Let $\{v_m(\mathbf{r},t)\}$ be another orthonormal basis. We can define the modal unitary transformation U of complex components

$$\mathrm{U}_{m\ell} = \frac{1}{V}\int_V d^3\mathbf{r}\ \mathbf{u}_\ell^*(\mathbf{r},t)\mathbf{v}_m(\mathbf{r},t). \tag{1.9}$$

The elements of the bases $\{u_\ell(\mathbf{r},t)\}$ and $\{v_m(\mathbf{r},t)\}$ can now be decomposed onto one another with the unitary matrix U:

$$\mathbf{v}_m(\mathbf{r},t) = \sum_\ell \mathrm{U}_{m\ell}\mathbf{u}_\ell(\mathbf{r},t), \tag{1.10}$$

$$\mathbf{u}_\ell(\mathbf{r},t) = \sum_m \mathrm{U}^*_{m\ell}\mathbf{v}_m(\mathbf{r},t). \tag{1.11}$$

In the following, we will give concrete examples of mode bases.

Spatial modes The fields that we are interested in in this work are in the form of laser beams. In other words, we restrict our analysis to beams that are confined close to the propagation axis. We place ourselves, from now on, in the paraxial approximation, i.e. the field is composed of plane waves with wave vectors close to a mean value $\mathbf{k}_0$ ($||\mathbf{k}_0 - \mathbf{k}|| \ll ||\mathbf{k}_0||$), and in the narrow-band approximation, for which the frequencies of the plane waves are close to the central one $\omega_0 = c||\mathbf{k}_0||$ ($\Delta\omega \ll \omega_0$). To simplify the notations, we assume that the propagation axis is the Oz axis and that the electromagnetic field is linearly polarized.
The wave equation of the electric field is

$$\Delta\mathbf{E}(\mathbf{r},t) - \frac{1}{c^2}\frac{\partial^2}{\partial t^2}\mathbf{E}(\mathbf{r},t) = 0, \tag{1.12}$$

whose solutions are of the form:

$$\mathbf{E}(\mathbf{r},t) = \boldsymbol{\varepsilon}\mathcal{E}_0 u'(x,y,z,t)e^{-i(k_0 z-\omega_0 t)}, \tag{1.13}$$

where $\boldsymbol{\varepsilon}$ is the polarization in the xy plane, and we assume that the mode of the field $u'(x,y,z,t)$ is separable in time and space, i.e. can be written $u'(x,y,z,t) = u(x,y,z)g(t-z/c)$, assuming $g(t-z/c)$ is a single temporal mode. By inserting this expression in eq. (1.12), we can rewrite the wave equation:

$$\frac{\partial^2 u}{\partial x^2} + \frac{\partial^2 u}{\partial y^2} + \frac{\partial^2 u}{\partial z^2} - 2ik_0\frac{\partial u}{\partial z} = 0. \tag{1.14}$$

Using the paraxial approximation, where the spatial transverse profile of the beam evolves slowly along Oz compared to the wavelength and to the variations due to the finite transverse size of the beam:

$$\left|\frac{\partial^2 u}{\partial z^2}\right| \ll \left|2k_0\frac{\partial u}{\partial z}\right|, \quad \left|\frac{\partial^2 u}{\partial z^2}\right| \ll \left|\frac{\partial^2 u}{\partial x^2}\right| \quad \text{and} \quad \left|\frac{\partial^2 u}{\partial z^2}\right| \ll \left|\frac{\partial^2 u}{\partial y^2}\right|, \tag{1.15}$$

we obtain the paraxial wave equation:

$$\frac{\partial^2 u}{\partial x^2} + \frac{\partial^2 u}{\partial y^2} - 2ik_0 \frac{\partial u}{\partial z} = 0. \tag{1.16}$$

1.1.2 Hermite-Gaussian modes

The Hermite-Gaussian modes are the real stars of this work. We exhibit the main results that concern them. Note that they are extracted from standard derivations that can be found in many textbooks, for example, [Yariv 1977].

Gaussian beam in homogeneous media

A solution to eq. (1.16) with exponential decrease and cylindrical symmetry around the propagation axis Oz is of the form:

$$u(x,y,z) = f(z) e^{\frac{-ik(x^2+y^2)}{2q(z)}}, \tag{1.17}$$

where $q(z)$ is a complex function. These solutions with a Gaussian transverse envelope are eigenmodes for propagation in free space and in cavities. Injecting eq. (1.17) into eq. (1.16), we find

$$(x^2+y^2)(1-q'(z)) = 0 \qquad \text{and} \qquad f'(z) + \frac{f(z)}{q(z)} = 0. \tag{1.18}$$

Hence, we get

$$q(z) = z - z_0 + iz_R \qquad \text{and} \qquad f(z) = \frac{C}{q(z)}, \tag{1.19}$$

where z_0, C and z_R are real numbers. We can thus rewrite $u(x,y,z)$ as

$$\begin{aligned} u(x,y,z) &= \frac{C}{z - z_0 + iz_R} \exp\left(\frac{-ik(x^2+y^2)}{2(z-z_0+iz_R)}\right) \\ &= C\frac{z-z_0-iz_R}{(z-z_0)^2+z_R^2} \exp\left(-ik\frac{x^2+y^2}{2\left(z-z_0+\frac{z_R^2}{z-z_0}\right)}\right) \\ &\times \exp\left(-k\frac{x^2+y^2}{2z_R(1+(z-z_0)^2/z_R^2)}\right). \end{aligned} \tag{1.20}$$

We can define another constant w_0 called the waist, linked to the Rayleigh range z_R:

$$w_0^2 = \frac{2z_R}{k} = \frac{\lambda z_R}{\pi}. \tag{1.21}$$

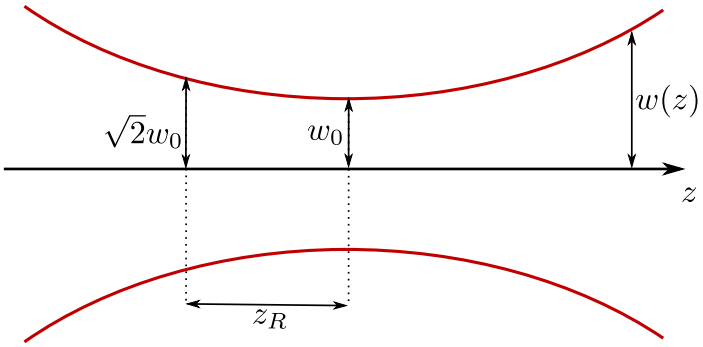

FIGURE 1.1: Gaussian beam.

We also define the functions $w(z)$, $R(z)$ and $\varphi(z)$, respectively the radius, the radius of curvature and the Gouy phase, as

$$\begin{aligned} w(z) &= w_0\sqrt{1+\frac{(z-z_0)^2}{z_R^2}} \\ R(z) &= \frac{z_R^2}{z-z_0}+z-z_0 \\ \tan\varphi(z) &= -\frac{z-z_0}{z_R}. \end{aligned} \tag{1.22}$$

Using the normalisation condition eq. (1.5), we find $C = \sqrt{\frac{2}{\pi}}\frac{z_R}{w_0}$. Finally, we write the solution to eq. (1.16) as the Gaussian beam

$$u_{00}(x,y,z) = \sqrt{\frac{2}{\pi}}\frac{1}{w(z)}\exp\left(-\frac{x^2+y^2}{w^2(z)}\right)\exp\left(-ik\frac{x^2+y^2}{2R(z)}+i\varphi(z)\right). \tag{1.23}$$

Beam parameters

The Gaussian beam is completely characterized by z_0 and z_R or equivalently by only knowing $q(z)$ called the confocal parameter. It can be shown that

$$\frac{1}{q(z)} = \frac{1}{R(z)} - \frac{i\lambda}{\pi w^2(z)}. \tag{1.24}$$

The quantity $w(z)$ gives the evolution of the size of the beam along the propagation. At any given z, 86% of the energy is contained in the disk of radius $w(z)$.
For $z = z_0$, $w(z)$ is minimal and is equal to the waist w_0. For $z = z_0 \pm z_R$, $w(z) = \sqrt{2}w_0$: the variations of the radius are slow within the Rayleigh range, as illustrated in fig. 1.1. Within this range, the beam looks like a plane wave since $R(z) \to \infty$ for $z \ll z_R$. While, for $z \gg z_R$, $w(z) = w_0\frac{z-z_0}{z_R}$ and $R(z) = z - z_0$: the beam diverges as a spherical wave.

Higher-order Gaussian beam modes in homogeneous media

Although the Gaussian beam is a very important solution to Maxwell's equations, it is not the only one. More complex solutions can be found: some with cylindrical symmetry and others with axial symmetries in x and y. The formers will be described later. We will now examine the latters, called the Hermite-Gaussian modes. They are solutions of eq. (1.16) that are separable in the cartesian coordinate system $u_{nm(x,y,z)} = u_n(x,z) \times u_m(y,z)$. A Hermite-Gaussian transverse profile of indices $n \in \mathbb{N}$ along the Ox axis and $m \in \mathbb{N}$ in the y direction, also denoted HG$_{nm}$ mode, is written as

$$\begin{aligned} u_{nm}(x,y,z) = \sqrt{\frac{2}{\pi}} \frac{1}{\sqrt{2^{n+m} n! m! w^2(z)}} H_n\left(\frac{\sqrt{2}x}{w(z)}\right) H_m\left(\frac{\sqrt{2}y}{w(z)}\right) \\ \times \exp\left(-\frac{x^2+y^2}{w^2(z)}\right) \exp\left(-ik\frac{x^2+y^2}{2R(z)} + i\varphi_{nm}(z)\right), \end{aligned} \tag{1.25}$$

where $\varphi_{nm}(z) = -(n+m+1)\arctan\frac{z-z_0}{z_R}$ is the Gouy phase, and $H_n(x)$ and $H_m(y)$ are Hermite polynomials respectively along x and y [Yariv 1977]. These polynomials are orthogonal with respect to the weight function e^{-x^2}:

$$\int_{-\infty}^{\infty} H_n(x) H_m(x) e^{-x^2}\, dx = \sqrt{\pi} 2^n n! \delta_{nm}, \tag{1.26}$$

and the first Hermite polynomials are:

$$\begin{aligned} H_0(x) &= 1 \\ H_1(x) &= 2x \\ H_2(x) &= 4x^2 - 2 \\ H_3(x) &= 8x^3 - 12x \\ H_4(x) &= 16x^4 - 48x + 12. \end{aligned} \tag{1.27}$$

The amplitudes of the first four Hermite-Gaussian modes are represented in fig. 1.2. The Hermite-Gaussian modes $\{u_{nm}(x,y,z)\}$ form an orthonormal mode basis which is very useful for describing fields propagating inside cavities.

The beam solutions presented in eq. (1.25) correspond to circular Hermite-Gaussian beams. A more general solution of Maxwell's equations is elliptic Hermite-Gaussian beams written as [Yariv 1977]

$$\begin{aligned} u_{nm}(x,y,z) = \sqrt{\frac{2}{\pi}} \frac{1}{\sqrt{2^{n+m} n! m! w_x(z) w_y(z)}} H_n\left(\frac{\sqrt{2}x}{w_x(z)}\right) H_m\left(\frac{\sqrt{2}y}{w_y(z)}\right) \\ \times \exp\left(-\frac{x^2}{w_x^2(z)}\right) \exp\left(-\frac{y^2}{w_y^2(z)}\right) \\ \times \exp\left(-ik\frac{x^2}{2R_x(z)} - ik\frac{y^2}{2R_y(z)} + i\varphi_{nx}(z) + i\varphi_{my}(z)\right), \end{aligned} \tag{1.28}$$

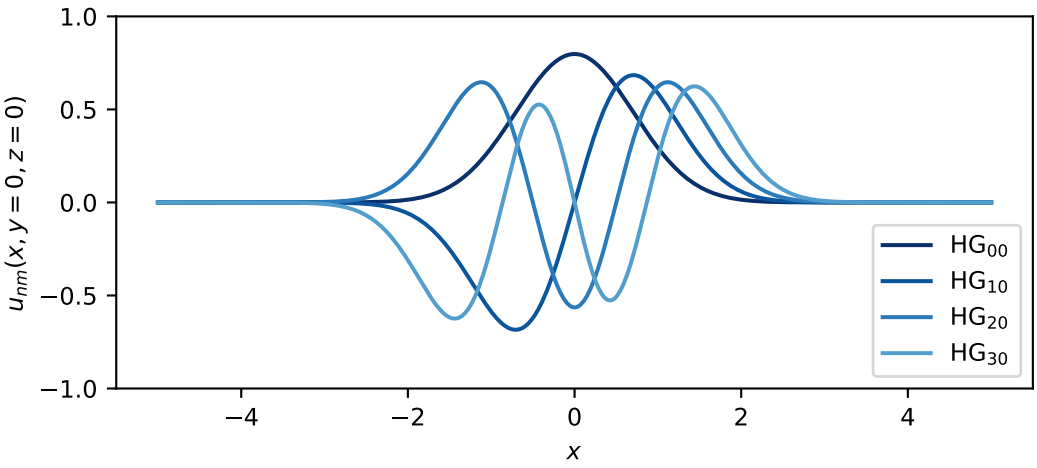

FIGURE 1.2: Amplitudes of the first four Hermite-Gaussian modes with $w_0 = 1$.

where

$$\begin{aligned} w_x(z) &= w_{0x}\sqrt{1 + \frac{(z - z_{0x})^2}{z_{Rx}^2}} \\ R_x(z) &= \frac{z_{Rx}^2}{z - z_{0x}} + z - z_{0x} \\ \tan\varphi_{nx}(z) &= -\left(n + \frac{1}{2}\right)\frac{z - z_{0x}}{z_{Rx}} \\ z_{Rx} &= \frac{w_{0x}^2\pi}{\lambda} \end{aligned} \tag{1.29}$$

All the results derived for the case of circular Hermite-Gaussian beams apply separately to the x and y behavior of the elliptic beams. These beams correspond for example to the output of an astigmatic resonator, as is the case of the triangular cavity presented in section 1.1.3.

ABCD matrix

As stated earlier, Gaussian beams are completely characterized by the confocal parameter $q(z)$ and this is also true for higher-order Hermite-Gaussian modes. Their evolution along the propagation in free space and through optical elements can thus be described in terms of transformations of $q(z)$. Each optical element is represented by a matrix $M = \begin{pmatrix} A & B \\ C & D \end{pmatrix}$, called an ABCD matrix, such that the confocal parameter in the plane z_2 after the element is linked to the confocal parameter in the plane z_1

before the element by the relation [Yariv 1977]

$$q(z_2) = \frac{Aq(z_1) + B}{Cq(z_1) + D}. \tag{1.30}$$

It can easily be shown that if M_1 transforms $q(z_1)$ into $q(z_2)$ and M_2 transforms $q(z_2)$ into $q(z_3)$, then the transformation of $q(z_1)$ into $q(z_3)$ is realized with $M_3 = M_2 M_1$.

We summarize the most common ABCD matrices in table 1.1 [Siegman 1986].

TABLE 1.1: Useful ABCD matrices.

Propagation in free space along a distance d	$\begin{pmatrix} 1 & d \\ 0 & 1 \end{pmatrix}$
Propagation through a thin lens of focal length f	$\begin{pmatrix} 1 & 0 \\ -1/f & 1 \end{pmatrix}$
Reflection on a spherical mirror with a radius of curvature R_c, normal incidence	$\begin{pmatrix} 1 & 0 \\ -2/R_c & 1 \end{pmatrix}$
Reflection on a spherical mirror, incidence θ, $R = R_c \cos\theta$ in the plane of incidence, $R = R_c / \cos\theta$ orthogonal to the plane of incidence	$\begin{pmatrix} 1 & 0 \\ -2/R & 1 \end{pmatrix}$

1.1.3 Hermite-Gaussian modes in optical resonators

Hermite-Gaussian modes are eigenmodes of free-space propagation but also of optical resonators, or cavities. Cavities are one of the building blocks of a laser, where they are used to amplify a beam. They can also be used to clean spatial modes as is the case in this work (see section 4.6.3). Again, the description of optical resonators can be found in many textbooks e.g. [Yariv 1977].

Hermite-Gaussian modes in a linear and a triangular cavity

We will focus on two types of cavities: a triangular cavity composed of two plane mirrors and a spherical concave mirror, with a radius of curvature R_c, which was used in the experiment, and a linear cavity with two spherical mirrors, with the same radius of curvature R_c, for comparison (see fig. 1.3).

We assume that the input and output mirrors, namely the two plane mirrors for the triangular cavity and the two spherical mirrors for the linear cavity, are identical

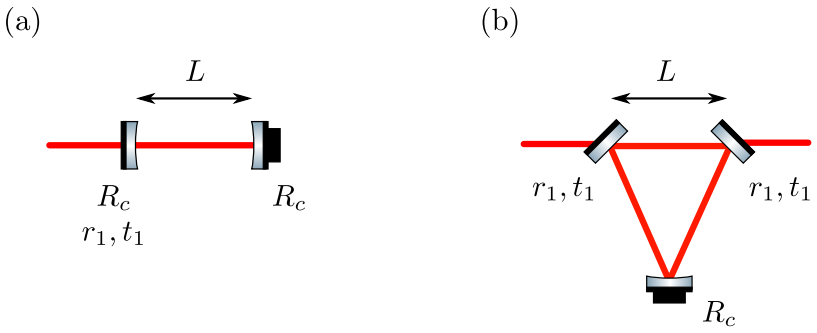

FIGURE 1.3: (a) Linear cavity. (b) Triangular cavity

and have the same reflection and transmission coefficients r_1 and t_1. We note L the distance between the input and output mirrors and D_0 the length of a round trip in the cavity, in particular, for the linear cavity, we have $D_0 = 2L$.
We consider HG modes $u_{nm}(x, y, z)$, as defined by eq. (1.25), propagating inside these cavities, and we want to show that they are eigenmodes of these cavities and to determine their resonance frequencies. By symmetry, the reference plane z_0, i.e. the position of the waist is in the middle of the input and output mirrors. We choose $z_0 = 0$ and the position of the input and output mirrors are respectively $z_1 = -L/2$ and $z_2 = L/2$, and the position of the spherical mirror of the triangular cavity is $z_s = D_0/2$.

Cavity stability condition

We assume that Hermite-Gaussian modes are eigenmodes of these cavities. It means that they should be able to overlap themselves after a round trip in the cavity. We show in this section that this self-reproducing requirement leads to a consistent stability condition. We consider the ABCD matrix of the unwrapped cavity and the reference plane z_0 in which we write the relation for the confocal parameter

$$q = \frac{Aq + B}{Cq + D}, \tag{1.31}$$

leading to the equation $Cq^2 + (D - A)q - B = 0$. Since q is has an imaginary part, we have $\Delta = (D - A)^2 + 4BC < 0$, and using the fact that the ABCD matrix is unitary, i.e. $AD - BC = 1$, we obtain the condition

$$-1 < \frac{A + D}{2} < 1. \tag{1.32}$$

For both cavities, this stability condition translates into a condition on the radius of curvature of the spherical mirror.
For the linear cavity, the ABCD matrix is

$$\begin{pmatrix} A & B \\ C & D \end{pmatrix} = \begin{pmatrix} 1 & D_0/4 \\ 0 & 1 \end{pmatrix} \begin{pmatrix} 1 & 0 \\ -2/R_c & 1 \end{pmatrix} \begin{pmatrix} 1 & D_0/2 \\ 0 & 1 \end{pmatrix} \begin{pmatrix} 1 & 0 \\ -2/R_c & 1 \end{pmatrix} \begin{pmatrix} 1 & D_0/4 \\ 0 & 1 \end{pmatrix} \tag{1.33}$$

and, using eq. (1.32), we obtain the condition:

$$R_c > \frac{D_0}{4}. \tag{1.34}$$

For a triangular cavity, the ABCD matrix reads

$$\begin{aligned}\begin{pmatrix} A & B \\ C & D \end{pmatrix} &= \begin{pmatrix} 1 & D_0/2 \\ 0 & 1 \end{pmatrix} \begin{pmatrix} 1 & 0 \\ -2/R_c & 1 \end{pmatrix} \begin{pmatrix} 1 & D_0/2 \\ 0 & 1 \end{pmatrix} \\ &= \begin{pmatrix} 1 - D_0/R_c & D_0/2(1 - D_0/R_c) + D_0/2 \\ -2/R_c & 1 - D_0/R_c \end{pmatrix},\end{aligned} \tag{1.35}$$

hence, from eq. (1.32), we obtain

$$R_c > \frac{D_0}{2}. \tag{1.36}$$

Under this condition, HG modes can propagate inside a linear and a triangular cavity. In practice, the length of the triangular cavity we used was fixed, so we had to take this condition into account when choosing the radius of curvature of the spherical mirror.

Waist of the beam in the cavity

For symmetry reasons, the radius of curvature of the mirrors and the length of the cavity impose a specific waist to the beams propagating in the cavity. Indeed, the waist position has to be in between the input and output mirrors and the radius of curvature of the mirrors has to correspond to the radius of curvature of the beam at the position of the mirrors. For the linear cavity, we have the relation

$$R(z_2) = R_c \tag{1.37}$$

which, using eqs. (1.21) and (1.22), leads to

$$z_R^{\text{linear}} = \sqrt{\frac{D_0}{4}\left(R_c - \frac{D_0}{4}\right)}, \tag{1.38}$$

$$w_0^2 = \frac{\lambda}{\pi}\sqrt{\frac{D_0}{4}\left(R_c - \frac{D_0}{4}\right)}. \tag{1.39}$$

For the triangular cavity, we have

$$R(z_s) = R_c \tag{1.40}$$

and thus

$$z_R^{\text{triangular}} = \sqrt{\frac{D_0}{2}\left(R_c - \frac{D_0}{2}\right)}, \tag{1.41}$$

$$w_0^2 = \frac{\lambda}{\pi}\sqrt{\frac{D_0}{2}\left(R_c - \frac{D_0}{2}\right)}. \tag{1.42}$$

This waist has to be matched for the HG modes to be eigenmodes of the cavity[2].

Resonance of Hermite-Gaussian modes

The resonances are observed for constructive interferences in the cavity, which are encountered when varying the length of the cavity $D_0 + \epsilon$ with $\epsilon \ll D_0$. We denote $\Delta\varphi$, the phase shift acquired during one round trip in the cavity.
In a linear cavity, the phase shift acquired between the two spherical mirrors by Hermite-Gaussian modes is

$$\frac{\Delta\varphi_{\text{linear}}}{2} = k(z_2 - z_1) + \varphi_{nm}(z = z_2) - \varphi_{nm}(z = z_1), \tag{1.43}$$

where $\varphi_{nm}(z)$ is the Gouy phase of the HG_{nm} mode. Hence, using eq. (1.22), the phase shift acquired during one round trip in a linear cavity is

$$\Delta\varphi_{\text{linear}} = k(D_0 + \varepsilon) - 4(n + m + 1)\arctan\frac{D_0}{4z_R^{\text{linear}}}. \tag{1.44}$$

In a triangular cavity, this phase shift is

$$\Delta\varphi_{\text{triangular}} = k(z_2 - z_1) + \varphi_{nm}(z = z_2) - \varphi_{nm}(z = z_1) - n\pi, \tag{1.45}$$

where z_1 and z_2 are the positions of the spherical mirror in an unwrapped configuration. Since we consider a symmetric cavity, we have $z_2 = -z_1 = D_0/2$, the origin being in the center between the two plane mirrors. The additional $n\pi$ phase delay comes from the fact that, for an odd number of mirrors, the field is flipped in the x-direction and, therefore, the x-antisymmetric modes get an extra $n\pi$ phase, which breaks the degeneracy as it will be shown in fig. 1.4. The phase shift for one round trip is then given by

$$\Delta\varphi_{\text{triangular}} = k(D_0 + \varepsilon) - 2(n + m + 1)\arctan\frac{D_0}{2z_R^{\text{triangular}}} - n\pi. \tag{1.46}$$

The resonance condition is $\Delta\varphi = 2p\pi$ with $p \in \mathbb{Z}$. This shows that the different Hermite-Gaussian modes resonate for different cavity lengths, which is why cavities can be used to clean modes. We also observe a degeneracy for modes with identical $(n + m)$ in the case of a linear cavity, which is no longer the case for a triangular cavity.

Transmitted intensity

We consider monochromatic linearly polarized fields, namely E_i the field injected into the cavity, E_c in the cavity, and E_t transmitted by the cavity. All the fields have the same polarization, frequency ω_0, temporal and spatial modes, hence the scalar

[2] In principle, since the incidence is not normal on the spherical mirror of the triangular cavity, we should take the astigmatism of the cavity into account, which results in $w_{0x} \approx 195\,\mu\text{m}$ and $w_{0y} \approx 202\,\mu\text{m}$. The astigmatism is therefore negligible.

fields are written as follows

$$\begin{aligned} E_i(x,y,z,t) &= \mathcal{E}_i u_{nm}(x,y,z) g(t) e^{-i(k_0 z - \omega_0 t)}, \\ E_c(x,y,z,t) &= \mathcal{E}_c u_{nm}(x,y,z) g(t) e^{-i(k_0 z - \omega_0 t)}, \\ E_t(x,y,z,t) &= \mathcal{E}_t u_{nm}(x,y,z) g(t) e^{-i(k_0 z - \omega_0 t)}, \end{aligned} \tag{1.47}$$

where $\mathcal{E}_i$, $\mathcal{E}_c$ and $\mathcal{E}_t$ are the complex amplitudes of the fields.

We can write the relations between the fields at the two plane mirrors, i.e. for $z = 0$ and $z = L$:

$$\begin{aligned} E_c(x,y,z=0,t) &= t_1 E_i(x,y,z=0,t) + r_1^2 E_c(x,y,z=D,t), \\ E_t(x,y,z=L,t) &= t_1 E_c(x,y,z=L,t), \\ E_r(x,y,z=0,t) &= r_1 E_i(x,y,z=0,t) - t_1 E_c(x,y,z=D,t). \end{aligned} \tag{1.48}$$

From eq. (1.47), we obtain

$$\begin{aligned} \mathcal{E}_c &= t_1 \mathcal{E}_i + r_1^2 \mathcal{E}_c e^{i\Delta\varphi}, \\ \mathcal{E}_t &= t_1 \mathcal{E}_c, \end{aligned} \tag{1.49}$$

where $\Delta\varphi$ is the phase shift acquired during one round trip. Using $R_1 + T_1 = 1$ (where $r_1^2 = R_1$ and $t_1^2 = T_1$), we can write the transmitted intensity

$$I_t = \frac{I_i}{1 + \frac{4R_1^2}{T_1^2} \sin^2 \frac{\Delta\varphi}{2}}, \tag{1.50}$$

where $\Delta\varphi$ has the expression given by eq. (1.44) or eq. (1.46) depending on the cavity. The transmissivity for several Hermite-Gaussian modes propagating inside linear and triangular cavities are represented in fig. 1.4. The modes HG_{01} and HG_{10} are no longer degenerated in the triangular cavity compared to the linear cavity.

Finesse of the cavity

An optical resonator is characterized by its finesse $\mathcal{F}$. This is a measure of how narrow the resonances are and whether they can be distinguished from one another. The finesse is defined as the ratio of the distance between two resonances to the full width at half maximum of one peak. It is linked to the reflectivity of the output mirror R with the relation

$$\mathcal{F} = \frac{\pi\sqrt{R}}{1 - R}. \tag{1.51}$$

1.1.4 Some other mode bases

The aim of this section is not to give an exhaustive list of the existing mode bases, it would be impossible anyway, the list being infinite, depending on the symmetry of the medium of propagation as well as on the detection apparatus. We only wish to give a description of the modes that will be discussed in this work and to give a brief overview of some bases for a better understanding of the concept of mode.

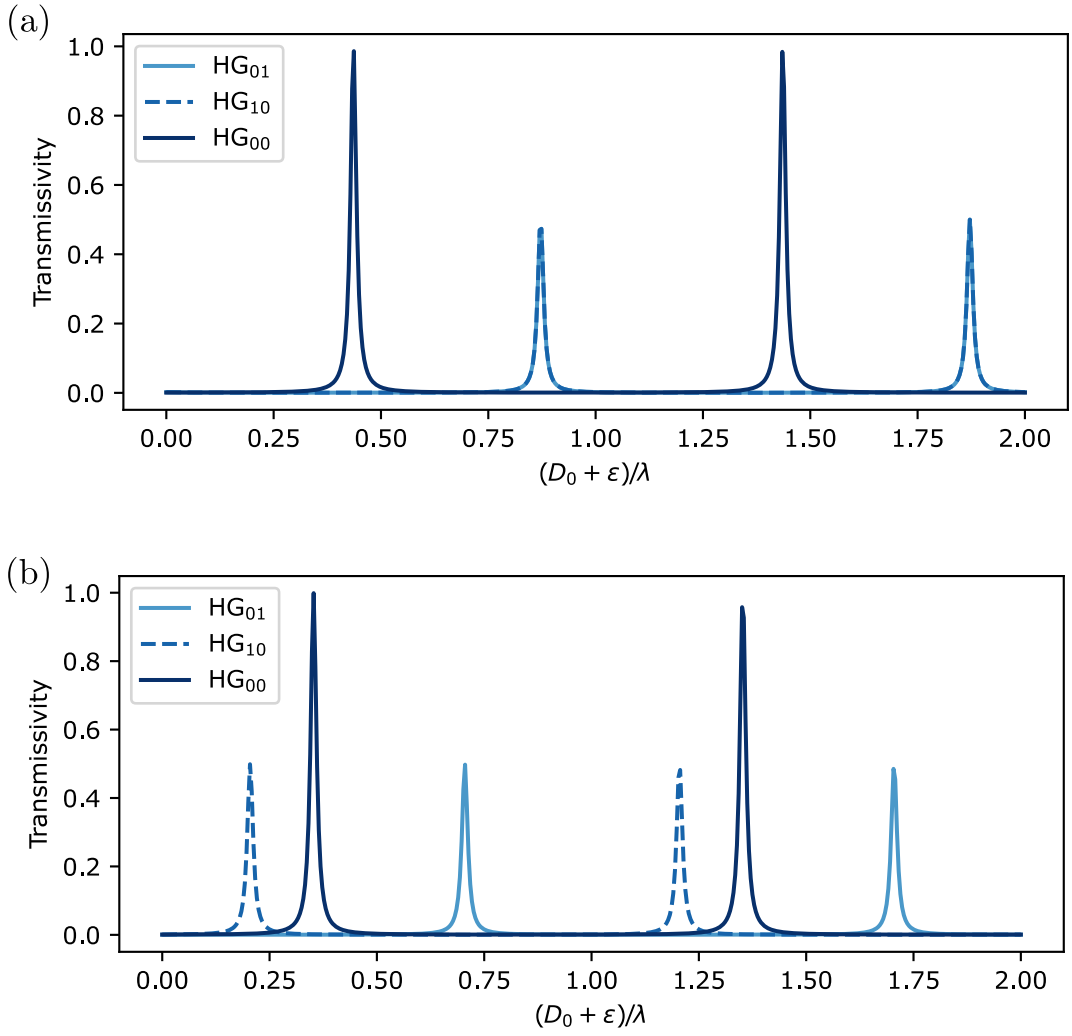

FIGURE 1.4: Transmissivity for (a) a linear cavity and (b) a triangular cavity, for a superposition of the modes HG_{00}, HG_{01} and HG_{10} in proportion 1:0.5:0.5, for $T = 0.05$, $D_0 = 32\,\text{cm}$ and $R_c = 200\,\text{mm}$.

Laguerre-Gaussian modes

When a cylindrical symmetry is considered, we can extract the Laguerre-Gaussian modes from the paraxial wave equation. A Laguerre-Gaussian transverse profile of radial index $p \in \mathbb{N}$ and azimuthal index $\ell \in \mathbb{Z}$, also denoted LG_p^ℓ mode, is written as

$$\begin{aligned} u_{p\ell}(r,\theta,z) = &\sqrt{\frac{2p!}{\pi(|\ell|+p)!}}\frac{1}{w(z)}\left(\frac{\sqrt{2}r}{w(z)}\right)^{|\ell|} L_p^{|\ell|}\left(\frac{2r^2}{w^2(z)}\right) \\ &\times \exp\left(-\frac{r^2}{w^2(z)}\right)\exp\left(-ik\frac{r^2}{2R(z)} + i(2p+\ell+1)\varphi(z) + i\ell\theta\right), \end{aligned} \tag{1.52}$$

where $L_p^\ell(x)$ is a Laguerre polynomial, such as

$$L_0^\ell(x) = 1, \tag{1.53}$$

$$L_1^\ell(x) = -x + \ell + 1, \tag{1.54}$$

$$L_2^\ell(x) = \frac{x^2}{2} - (\ell+2)x + \frac{(\ell+2)(\ell+1)}{2}, \tag{1.55}$$

$$L_3^\ell(x) = \frac{-x^3}{6} + \frac{(\ell+3)x^2}{2} - \frac{(\ell+2)(\ell+3)x}{2} + \frac{(\ell+1)(\ell+2)(\ell+3)}{6}, \tag{1.56}$$

$$L_{p+1}^\ell(x) = \frac{(2p+1+\ell-x)L_p^\ell(x) - (p+\ell)L_{p-1}^\ell(x)}{p+1}. \tag{1.57}$$

The amplitudes of the first four Laguerre-Gaussian modes are represented in fig. 1.5. As for the Hermite-Gaussian modes, it is possible to build an orthonormal and complete mode basis $\{u_{p\ell}(r,\theta,z)\}$ of Laguerre-Gaussian modes from the first element, the Gaussian beam. These modes are extensively used in free-space quantum communication protocols [Sit 2017; Zhou 2019b].

Pixel modes

Another set of spatial modes of interest is the one that fits the symmetry of a CCD camera or, in general, an array of photodetectors. These are known as the pixel modes and can be written as follows for pixels of size $\ell_x \times \ell_y$:

$$u_{nm}(x,y) = \frac{1}{\sqrt{\ell_x \ell_y}}\mathrm{rect}(x, x_n, x_n+\ell_x)\mathrm{rect}(y, y_m, y_m+\ell_y), \tag{1.58}$$

where $\mathrm{rect}(x,a,b)$ is the rectangular function equal to 1 in $[a,b]$ and to 0 elsewhere. The basis $\{u_{nm}(x,y)\}$ is orthonormal but not complete. It is therefore useful to write the modes in the limit of infinitely small pixels. When ℓ_x goes to 0, we have $\frac{1}{\ell_x}\mathrm{rect}(x, x_n, x_n+\ell_x) \to \delta(x-x_n)$, and pixel modes can be written as

$$u'_{nm}(x,y) = \sqrt{\ell_x \ell_y}\,\delta(x-x_n)\delta(y-y_m). \tag{1.59}$$

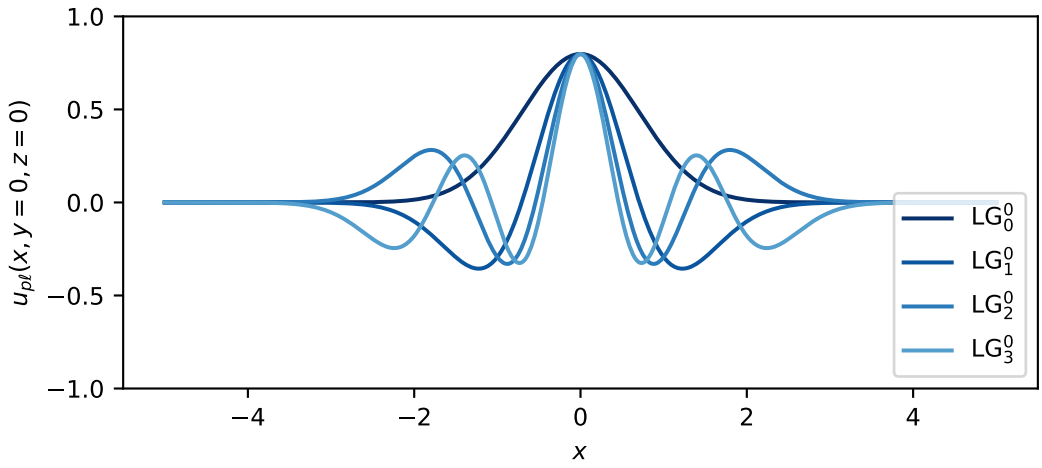

FIGURE 1.5: Amplitudes of the first four Laguerre-Gaussian modes, with $w_0 = 1$.

The continuous basis $\{u'_{nm}(x, y)\}$ is orthonormal and complete. We can find analogs of the pixel mode basis in the time and spectral domains respectively known as the time bin basis and the frequency band basis. They are useful to analyze temporal sequences and broadband sources.

Temporal or frequency Hermite-Gaussian modes

Similarly to pixel modes, there exists a temporal and a spectral equivalent to the Hermite-Gaussian spatial modes. They constitute well-suited orthonormal mode bases to describe light pulses of any temporal and spectral shape. They will not be discussed in this thesis but descriptions and applications can be found in [Brecht 2015; Ansquer 2022; Renault 2022].

Traveling plane-wave modes

Plane waves are the most well-known modes. They are defined as

$$u_\ell(\mathbf{r}, t) = e^{i\varphi(\mathbf{r},t)} = e^{i(\mathbf{k}_\ell \cdot \mathbf{r} - \omega_\ell t)} \tag{1.60}$$

where $\mathbf{k}_\ell$ and ω_ℓ are the wave vector and the frequency of the mode $u_\ell(\mathbf{r}, t)$. Even though these modes are not physical since they carry infinite energy, they provide good approximations in many situations.

Polarized modes

Finally, even though we will consider only linearly polarized beams throughout this manuscript, it is helpful to remember that mode bases can also be composed of a vectorial part. In particular, for a monochromatic Gaussian beam, we can write modes

of the form:

$$\mathbf{u}_\ell(\mathbf{r},t) = \boldsymbol{\varepsilon}_\ell u_{00}(\mathbf{r},t), \tag{1.61}$$

where $\{\boldsymbol{\varepsilon}_\ell\}$ is a set of orthogonal polarization modes, for example, horizontal and vertical linear polarizations, or circular right and circular left polarizations.

1.2 States

We now introduce quantum fields. We will briefly expose the quantization of the electric field, more details can be found in [Mandel 1995; Cohen-Tannoudji 1997; Grynberg 2010]. Then we will describe some quantum states and representations in the continuous variables framework.

1.2.1 Quantization of the electromagnetic field

We establish the electric field operator $\hat{\mathbf{E}}^{(+)}(\mathbf{r},t)$ in the Heisenberg picture as the quantum counterpart of the classical complex field $\mathbf{E}^{(+)}(\mathbf{r},t)$ defined by eq. (1.6). This means that we associate an operator $\hat{a}_\ell$ to the mode $\mathbf{u}_\ell(\mathbf{r},t)$, considering the orthonormal mode basis $\{\mathbf{u}_\ell(\mathbf{r},t)\}$:

$$\hat{\mathbf{E}}^{(+)}(\mathbf{r},t) = i\sum_\ell \mathcal{E}_\ell^{(1)}\hat{a}_\ell \mathbf{u}_\ell(\mathbf{r},t) = \sum_\ell \hat{E}_\ell^{(+)}\mathbf{u}_\ell(\mathbf{r},t), \tag{1.62}$$

where $\mathcal{E}_\ell^{(1)} = \sqrt{\frac{\hbar\omega_\ell}{2\varepsilon_0 V}}$ (see derivation in appendix A) and $\hat{E}_\ell^{(+)} = i\mathcal{E}_\ell^{(1)}\hat{a}_\ell$. The annihilation and creation operators $\hat{a}_\ell$ and $\hat{a}_\ell^\dagger$ associated to the mode ℓ, satisfy the commutation relations

$$[\hat{a}_\ell, \hat{a}_{\ell'}^\dagger] = \delta_{\ell\ell'}, \tag{1.63}$$

$$[\hat{a}_\ell, \hat{a}_{\ell'}] = 0. \tag{1.64}$$

In the following, we will only consider linearly polarized beams, so the electric field can be written as a scalar quantity:

$$\hat{E}^{(+)}(\mathbf{r},t) = i\sum_\ell \mathcal{E}_\ell^{(1)}\hat{a}_\ell u_\ell(\mathbf{r},t). \tag{1.65}$$

The energy of the field is

$$\hat{H} = \sum_\ell \hbar\omega_\ell \left(\hat{a}_\ell^\dagger\hat{a}_\ell + \frac{1}{2}\right) = \sum_\ell \hbar\omega_\ell \left(\hat{N}_\ell + \frac{1}{2}\right), \tag{1.66}$$

where $\hat{N}_\ell = \hat{a}_\ell^\dagger\hat{a}_\ell$ is the photon number operator in the mode $\mathbf{u}_\ell(\mathbf{r},t)$. This expression is formally identical to the Hamiltonian of an assembly of decoupled quantum harmonic oscillators.

1.2.2 Continuous variables

Quadrature operators

Since $\hat{a}_\ell$ and $\hat{a}_\ell^\dagger$ are not Hermitian, they are not observables. It is however possible to define Hermitian operators, named the quadrature operators, $\hat{q}_\ell$ and $\hat{p}_\ell$ such that:

$$\hat{E}^{(+)} = i\sum_\ell \mathcal{E}_\ell^{(1)}\hat{a}_\ell u_\ell = \frac{i}{2}\sum_\ell \mathcal{E}_\ell^{(1)}(\hat{q}_\ell + i\hat{p}_\ell)u_\ell, \tag{1.67}$$

where $\hat{q}_\ell$ and $\hat{p}_\ell$ correspond to the real and imaginary parts of the field amplitude. It can be noted that $\hat{q}_\ell$ and $\hat{p}_\ell$ are equivalent to the position and momentum operators of the quantum harmonic oscillator. Similarly to the position and momentum operators, they have a continuous spectrum, and the eigenstates $\{|q\rangle_\ell\}$ (resp. $\{|p\rangle_\ell\}$) of $\hat{q}_\ell$ (resp. $\hat{p}_\ell$) form an orthonormal and complete basis

$$\hat{q}_\ell |q\rangle_\ell = q\,|q\rangle_\ell\,, \tag{1.68}$$

$${}_\ell\langle q|q'\rangle_\ell = \delta(q-q'), \tag{1.69}$$

$$\int |q\rangle_\ell \langle q|_\ell \; dq = \mathbb{1}, \tag{1.70}$$

with similar relations for $\hat{p}_\ell$,where q and p are real numbers.

Convention

Many conventions for the quadrature operators can be chosen. The one that we use is the following:

$$\hat{q}_\ell = \hat{a}_\ell + \hat{a}_\ell^\dagger, \tag{1.71}$$

$$\hat{p}_\ell = i(\hat{a}_\ell^\dagger - \hat{a}_\ell), \tag{1.72}$$

with

$$[\hat{q}_\ell, \hat{p}_{\ell'}] = 2i\delta_{\ell\ell'} \qquad \text{and} \qquad [\hat{q}_\ell, \hat{q}_{\ell'}] = [\hat{p}_\ell, \hat{p}_{\ell'}] = 0. \tag{1.73}$$

This allows writing the Heisenberg relation[3] as:

$$\Delta\hat{q}_\ell \Delta\hat{p}_\ell \geq 1, \tag{1.74}$$

where $\Delta\hat{q} = \sqrt{\langle(\delta\hat{q})^2\rangle}$, using the fluctuations operator $\delta\hat{O} = \hat{O} - \langle\hat{O}\rangle$. $\Delta\hat{q}$ is the standard deviation of the operator $\hat{q}$ and corresponds to its fluctuations. This relation reflects the intrinsic quantum fluctuations of the field.

Generalized quadrature operator

We introduce the generalized quadrature operator

$$\hat{q}_\ell^\theta = \hat{q}_\ell \cos\theta + \hat{p}_\ell \sin\theta = \hat{a}_\ell e^{-i\theta} + \hat{a}_\ell^\dagger e^{i\theta}. \tag{1.75}$$

[3]Other conventions can be chosen, see appendix A for an alternative one. We use this one because it is convenient to have the quantum noise equal to 1.

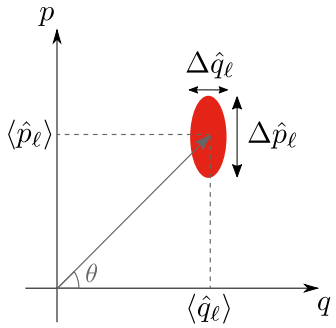

FIGURE 1.6: Phase-space representation

These quadrature operators satisfy the commutation relation

$$[\hat{q}_\ell^\theta, \hat{q}_\ell^{\theta+\frac{\pi}{2}}] = 2i, \tag{1.76}$$

as well as the Heisenberg relation

$$\Delta\hat{q}_\ell^\theta \Delta\hat{q}_\ell^{\theta+\frac{\pi}{2}} \geq 1. \tag{1.77}$$

Phase space representation

The operators $\hat{q}_\ell^\theta$ are observables and can be measured using homodyne detection, which will be described in section 1.3.2. Let us see how the quantum field (Eq eq. (1.67)) is represented from the knowledge of $\hat{q}_\ell^\theta$. For simplicity, we consider the plane wave mode basis, the quantum electric field in mode u_ℓ is written:

$$\begin{aligned}\hat{E}_\ell = \hat{E}_\ell^{(+)} + \hat{E}_\ell^{(-)} &= \frac{1}{2}\mathcal{E}_\ell^{(1)}\left[(\hat{q}_\ell + i\hat{p}_\ell)e^{-i\varphi_\ell} + (\hat{q}_\ell - i\hat{p}_\ell)e^{i\varphi_\ell}\right] \\ &= \mathcal{E}_\ell^{(1)}(\hat{q}_\ell\cos\varphi_\ell + \hat{p}_\ell\sin\varphi_\ell).\end{aligned} \tag{1.78}$$

We can thus represent each mode of the field in a phase diagram (see fig. 1.6). Contrary to a classical field that is represented as a point on this phase diagram, because of the Heisenberg relation, for the quantum field, a disk is displayed to represent the standard deviations of the quadratures.

For a real field, $\langle\hat{p}_\ell\rangle = 0$, which is why $\hat{q}_\ell$ is called the amplitude quadrature and $\hat{p}_\ell$ the phase quadrature. As mentioned earlier, the operators $\hat{q}_\ell$ and $\hat{p}_\ell$ have continuous spectra, hence the denomination continuous variables when the focus is on these observables, as opposed to the discrete variables community whose focus is on the photon-number observable, using photon-counting detection schemes.

1.2.3 Back to the mode basis change

We see from eq. (1.67) that the annihilation operators $\{\hat{a}_\ell^\dagger\}$ are associated to the mode basis $\{\mathbf{u}_\ell(\mathbf{r},t)\}$. We now describe how a modal unitary transformation U, from the basis $\{\mathbf{u}_\ell(\mathbf{r},t)\}$ to the basis $\{\mathbf{v}_m(\mathbf{r},t)\}$, affects the annihilation operators. We inject

eq. (1.11) into eq. (1.65):

$$\hat{E}^{(+)}(\mathbf{r},t) = i\sum_{\ell}\mathcal{E}_{\ell}^{(1)}\hat{a}_{\ell}\sum_{m}\mathrm{U}_{m\ell}^{*}v_{m}(\mathbf{r},t). \tag{1.79}$$

Assuming the transformation only mixes modes of the same frequency, i.e. $\mathcal{E}_{m}^{(1)} = \mathcal{E}_{\ell}^{(1)}$ for any (m,ℓ), we obtain

$$\hat{E}^{(+)}(\mathbf{r},t) = i\sum_{m}\mathcal{E}_{m}^{(1)}v_{m}(\mathbf{r},t)\sum_{\ell}\mathrm{U}_{m\ell}^{*}\hat{a}_{\ell}. \tag{1.80}$$

We can thus write the quantum field in terms of the set of annilation operators $\hat{b}_m$, associated to the basis $\{\mathbf{v}_m(\mathbf{r},t)\}$:

$$\hat{E}^{(+)}(\mathbf{r},t) = i\sum_{m}\mathcal{E}_{m}^{(1)}\hat{b}_{m}v_{m}(\mathbf{r},t), \tag{1.81}$$

with

$$\hat{b}_{m}^{\dagger} = \sum_{\ell}\mathrm{U}_{m\ell}\hat{a}_{\ell}^{\dagger} \tag{1.82}$$

and

$$\hat{a}_{\ell} = \sum_{m}\mathrm{U}_{m\ell}\hat{b}_{m}. \tag{1.83}$$

Since U is unitary, the commutation relations are conserved

$$[\hat{b}_{m},\hat{b}_{m'}^{\dagger}] = \delta_{mm'}, \tag{1.84}$$

$$[\hat{b}_{m},\hat{b}_{m'}] = 0. \tag{1.85}$$

These relations show how intertwined the quantum and optical natures of the electromagnetic field are. Note that the total number of photons in a given state is invariant under any mode basis change

$$\hat{N}_{\mathrm{tot}} = \sum_{\ell}\hat{a}_{\ell}^{\dagger}\hat{a}_{\ell} = \sum_{m}\hat{b}_{m}^{\dagger}\hat{b}_{m}. \tag{1.86}$$

1.2.4 Quantum states

In this section, we introduce several important states of the electromagnetic field. Further descriptions can be found in [Grynberg 2010; Leonhardt 2005].

Fock states

Fock states, denoted $|n\rangle$, are the manifestations of the granular aspect of light. They are eigenstates of the Hamiltonian $\hat{H}$ and of the photon number operator $\hat{N}_{\mathrm{tot}}$, and thus carry a fixed number of photons. For the mode u_ℓ, we have:

$$\hat{N}_{\ell}\,|n\rangle_{\ell} = n\,|n\rangle_{\ell}\,, \tag{1.87}$$

$$\hat{H}_\ell \left|n\right\rangle_\ell = \hbar\omega_\ell(n+\frac{1}{2})\left|n\right\rangle_\ell . \tag{1.88}$$

The $\left|n\right\rangle_\ell$ form a basis of the single-mode state space, i.e. any pure state in mode u_ℓ can be written as $\left|\psi\right\rangle_\ell = \sum_n c_n \left|n\right\rangle_\ell$ with $\sum_n |c_n|^2 = 1$.
For the total state space, a basis is the tensor product of single mode bases: $\left|n_1, ..., n_\ell, ...\right\rangle \equiv \left|n_1\right\rangle_1 \otimes ... \otimes \left|n_\ell\right\rangle_\ell \otimes ...$, and we have:

$$\hat{a}_\ell \left|n_1, ..., n_\ell, ...\right\rangle = \sqrt{n_\ell}\left|n_1, ..., n_\ell - 1, ...\right\rangle , \tag{1.89}$$

$$\hat{a}_\ell^\dagger \left|n_1, ..., n_\ell, ...\right\rangle = \sqrt{n_\ell + 1}\left|n_1, ..., n_\ell + 1, ...\right\rangle , \tag{1.90}$$

$$\left\langle n_1, ..., n_\ell, ...\right| \hat{H} \left|n_1, ..., n_\ell, ...\right\rangle = \sum_\ell \hbar\omega_\ell\Big(n_\ell + \frac{1}{2}\Big). \tag{1.91}$$

The vacuum state

We examine the particular case for which $n_\ell = 0$ for any mode ℓ. This state $\left|0\right\rangle = \left|n_1 = 0, ..., n_\ell = 0, ...\right\rangle$ is called the vacuum state and corresponds to the state with the minimum energy.
Its mean field is zero

$$\left\langle 0\right| \hat{E}^{(+)} \left|0\right\rangle = 0, \tag{1.92}$$

but it has non-zero fluctuations

$$\left\langle 0\right| \hat{E}^2 \left|0\right\rangle = \left\langle 0\right| \hat{E}^{(+)}\hat{E}^{(-)} \left|0\right\rangle = \sum_{\ell\ell'} \mathcal{E}_\ell^{(1)}\mathcal{E}_{\ell'}^{(1)} u_\ell u_{\ell'} \left\langle 0\right| \hat{a}_\ell \hat{a}_{\ell'}^\dagger \left|0\right\rangle = \sum_\ell [\mathcal{E}_\ell^{(1)}]^2 |u_\ell|^2. \tag{1.93}$$

As for the quadratures of the field, eqs. (1.71) and (1.72) result in their fluctuations being

$$\Delta^2\hat{q}_\ell = \left\langle 0\right| \hat{q}_\ell^2 \left|0\right\rangle - \left\langle 0\right| \hat{q}_\ell \left|0\right\rangle^2 = \left\langle 0\right| \hat{a}_\ell \hat{a}_\ell^\dagger \left|0\right\rangle = 1, \tag{1.94}$$

$$\Delta^2\hat{p}_\ell = \left\langle 0\right| \hat{p}_\ell^2 \left|0\right\rangle - \left\langle 0\right| \hat{p}_\ell \left|0\right\rangle^2 = \left\langle 0\right| \hat{a}_\ell \hat{a}_\ell^\dagger \left|0\right\rangle = 1. \tag{1.95}$$

These fluctuations, saturating the Heisenberg relation, are called the vacuum noise.

Coherent states

Coherent states are generated by an ideal laser. They are eigenstates of the annihilation operator:

$$\hat{a}_\ell \left|\alpha\right\rangle_\ell = \alpha \left|\alpha\right\rangle_\ell , \tag{1.96}$$

where α is a complex number and corresponds to the complex wave amplitude in classical optics. These states are often called the quasi-classical states. The intensity of these fields is given by

$$\left\langle \alpha\right| \hat{N}_\ell \left|\alpha\right\rangle = |\alpha|^2 \tag{1.97}$$

and the variance of the intensity is

$$\Delta^2\hat{N}_\ell = |\alpha|^2 = \langle\hat{N}_\ell\rangle. \tag{1.98}$$

This is a standard property of the Poissonian distribution, and these fluctuations are called the shot noise. Indeed, the photon number distribution of coherent states is Poissonian as it is shown by their decomposition over the Fock state basis

$$|\alpha\rangle = e^{-|\alpha|^2/2} \sum_{n=0}^{+\infty} \frac{\alpha^n}{\sqrt{n!}} |n\rangle . \tag{1.99}$$

Contrary to a classical field, the mean energy is not only $\hbar\omega|\alpha|^2$, but is

$$\langle\alpha| \hat{H} |\alpha\rangle = \hbar\omega(|\alpha|^2 + \frac{1}{2}), \tag{1.100}$$

with an extra term $1/2$ which is the vacuum energy and amount for the quantum aspect of light.
Since the mean field of a coherent state in mode u_ℓ is

$$\langle\alpha| \hat{E}_\ell^{(+)} |\alpha\rangle = i\mathcal{E}_\ell^{(1)} \alpha u_\ell, \tag{1.101}$$

with the same fluctuations as the vacuum

$$\Delta^2\hat{q}_\ell = \Delta^2\hat{p}_\ell = 1, \tag{1.102}$$

the quantum vacuum can be seen as a coherent state with $\alpha = 0$ and any coherent state can be interpreted as a displaced vacuum in phase space. We introduce the displacement operator as

$$\hat{D}(\alpha) \equiv \exp\left(\alpha\hat{a}^\dagger - \alpha^*\hat{a}\right) = e^{-i|\alpha|\hat{q}^{\theta-\pi/2}} \tag{1.103}$$

and coherent states can be written

$$|\alpha\rangle = \hat{D}(\alpha) |0\rangle . \tag{1.104}$$

Furthermore, the coherent states form a non-orthogonal overcomplete basis:

$$\langle\beta|\alpha\rangle = \exp\left(-\frac{1}{2}(|\beta|^2 + |\alpha|^2 - 2\beta^*\alpha)\right) \neq \delta(\beta - \alpha), \tag{1.105}$$

$$\frac{1}{\pi}\int |\alpha\rangle \langle\alpha| \ d^2\alpha = \mathbb{1}. \tag{1.106}$$

We can also define a multimode coherent state as $|\psi\rangle = |\alpha_1, ..., \alpha_\ell, ...\rangle$ for which we have: $\hat{a}_\ell |\psi\rangle = \alpha_\ell |\psi\rangle$.

Squeezed states

We saw that coherent states are a family of states that saturate the Heisenberg relation. However, having $\Delta\hat{q}_\ell = \Delta\hat{p}_\ell = 1$ is not the only possibility to minimize this relation. It is indeed possible to have a variance smaller than one for $\hat{q}_\ell$, but this means that it is greater than one for $\hat{p}_\ell$, and vice versa. These states are called

squeezed states and are very useful in quantum metrology and quantum information protocols, or in general in situations where lower fluctuations are needed.
We define the squeezing operator as

$$\hat{S}(\xi) = \exp\left(\frac{\xi}{2}(\hat{a}_\ell^2 - \hat{a}_\ell^{\dagger 2})\right) \tag{1.107}$$

and the squeezed-vacuum state is written

$$|\psi\rangle = \hat{S}(\xi)\,|0\rangle\,, \tag{1.108}$$

where $\xi \in \mathbb{R}$ is the squeezing parameter. Similarly to coherent states being seen as displaced vacuum, squeezed states can be interpreted as displaced squeezed vacuum states.

$$|\psi_\xi\rangle = \hat{D}(\alpha)\hat{S}(\xi)\,|0\rangle\,. \tag{1.109}$$

Details on how these states are generated can be found in [Bachor 2019; Renault 2022].

1.2.5 The density operator

The states cited earlier are pure states as they can be represented by a state vector. However, this is not the most general description of a quantum state. To include states that are not pure, called mixed states, we need to introduce the concept of the density operator, which becomes the density matrix when represented on a given basis.

Density matrix

Mixed states are statistical mixtures of pure states $|\psi_i\rangle$ and their density operator is

$$\hat{\rho} = \sum_i p_i\,|\psi_i\rangle\,\langle\psi_i|\,, \tag{1.110}$$

with $\sum_i p_i = 1$ since p_i is the probability associated to the state $|\psi_i\rangle$. From this definition, we see that $\hat{\rho}$ is Hermitian and is normalized to

$$\mathrm{Tr}\,\hat{\rho} = 1. \tag{1.111}$$

A more comprehensive description of the density operator can be found in many textbooks, for example [Mandel 1995].

Thermal states

Let us introduce mixed states which will be extensively studied in this work: the thermal states. They model the light produced by black body radiation, for example, stars. Thermal states are an incoherent mixture of Fock states (see appendix A for

details) and their density matrix can be written as

$$\hat{\rho}_{th} = \sum_{n=0}^{\infty} P(n) \left|n\right\rangle \left\langle n\right| \tag{1.112}$$

where

$$P(n) = \frac{\langle \hat{n} \rangle^n}{(1 + \langle \hat{n} \rangle)^{n+1}}. \tag{1.113}$$

Thermal states can also be viewed as incoherent mixtures of coherent states, this can be seen with eq. (1.123).

1.2.6 Quasiprobability distributions

We want a representation that corresponds to what is measured experimentally. Indeed, the phase space representation as presented in section 1.2.2 is incomplete as it hides the distribution associated with each quadrature. We thus need to introduce the quasiprobability distributions to finalize the description. We will only give here the definitions, some useful properties and relevant expressions for the quantum states cited earlier. For more details, see [Leonhardt 2005].

The Wigner function

The most extensively used quasiprobability distribution is the Wigner function, it is also the simplest one to interpret. There exists a bijection between the density matrix and the Wigner function. We consider (q, p), real-number coordinates of the phase space that correspond to eigenvalues of $\hat{q}$ and $\hat{p}$, the Wigner function $W(p, q)$ is defined as:

$$W(q,p) = \frac{1}{2\pi} \int_{-\infty}^{+\infty} e^{ivp} \left\langle q - v\right| \hat{\rho} \left|q + v\right\rangle \mathrm{d}v = \frac{1}{2\pi} \int_{-\infty}^{+\infty} e^{-ivq} \left\langle p - v\right| \hat{\rho} \left|p + v\right\rangle \mathrm{d}v. \tag{1.114}$$

Since $\hat{\rho}$ is Hermitian, $W(p, q)$ is real and normalized to:

$$\int \mathrm{d}q\, \mathrm{d}p\, W(q,p) = \frac{1}{2\pi} \int \mathrm{d}q\, \mathrm{d}v\ \left\langle q - v\right| \hat{\rho} \left|q + v\right\rangle \int \mathrm{d}p\, e^{ivp} = \int \mathrm{d}q\ \left\langle q\right| \hat{\rho} \left|q\right\rangle = \mathrm{Tr}\, \hat{\rho} = 1. \tag{1.115}$$

Its marginal distributions are the q and p probability distributions:

$$\int \mathrm{d}p\, W(p,q) = \left\langle q\right| \hat{\rho} \left|q\right\rangle = P(q), \tag{1.116}$$

$$\int \mathrm{d}q\, W(p,q) = \left\langle p\right| \hat{\rho} \left|p\right\rangle = P(p). \tag{1.117}$$

These marginal distributions are obtained by homodyne detection, a measurement that will be described later in this chapter, and mathematical procedures provide access to the reconstruction of the Wigner function from these measurements. Thus, $W(q, p)$ is similar to a joint probability, however, it should be noted that it can have negative values, hence the quasi-probability denomination.

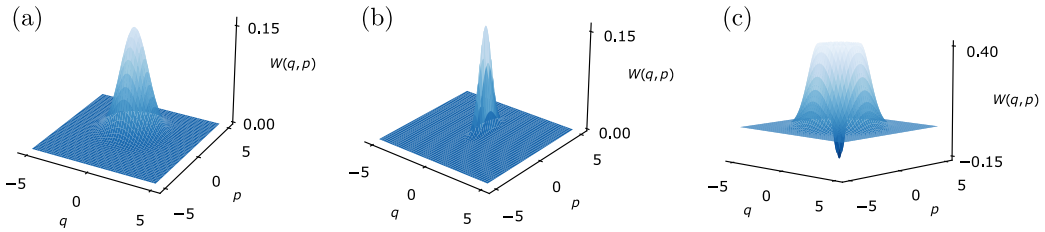

FIGURE 1.7: Wigner functions of (a) a coherent state, (b) a squeezed state and (c) a one-photon Fock state.

The Wigner function of a coherent state with amplitude α is

$$W_{|\alpha\rangle}(q,p) = \frac{1}{2\pi} e^{-((q-q_0)^2+(p-p_0)^2)/2}, \tag{1.118}$$

where $\alpha = \frac{1}{2}(q_0 + ip_0)$. Coherent states are described by Gaussian Wigner functions, which is why they are classified as Gaussian states.
The Wigner functions of a coherent state, a squeezed state, and a one-photon state are represented in fig. 1.7.

We can generalize for a multimode state, if $(\mathbf{q},\mathbf{p}) = (q_1,...,q_M,p_1,...,p_M)$ are eigenvalues of $\hat{\mathbf{q}} = (\hat{q}_1,...,\hat{q}_M)$ and $\hat{\mathbf{p}} = (\hat{p}_1,...,\hat{p}_M)$ in the mode basis $\{u_\ell\}$:

$$\begin{aligned} W(\mathbf{q},\mathbf{p}) &= \frac{1}{(2\pi)^M} \int e^{i\boldsymbol{\nu}\cdot\mathbf{p}} \langle \mathbf{q}-\boldsymbol{\nu}| \hat{\rho} |\mathbf{q}+\boldsymbol{\nu}\rangle \, \mathrm{d}^M\boldsymbol{\nu} \\ &= \frac{1}{(2\pi)^M} \int e^{-i\boldsymbol{\nu}\cdot\mathbf{q}} \langle \mathbf{p}-\boldsymbol{\nu}| \hat{\rho} |\mathbf{p}+\boldsymbol{\nu}\rangle \, \mathrm{d}^M\boldsymbol{\nu}. \end{aligned} \tag{1.119}$$

The Glauber-Sudarshan P function

The Glauber-Sudarshan P function is defined as the coefficients of the decomposition of the density operator over the basis of the coherent states $\{|\alpha\rangle\}_{\alpha\in\mathbb{C}}$

$$\hat{\rho} = \int \mathrm{d}^2\alpha P(\alpha) |\alpha\rangle \langle\alpha| , \tag{1.120}$$

where $\mathrm{d}^2\alpha = \mathrm{d}(\mathrm{Im}\,\alpha)\,\mathrm{d}(\mathrm{Re}\,\alpha)$ is a phase space element, and $|\alpha\rangle$ is a single-mode coherent state. eq. (1.120) is then an integral over all phase space. Like the Wigner function, the P function is real-valued and

$$\int \mathrm{d}^2\alpha P(\alpha) = 1, \tag{1.121}$$

but can also have negative values and is less smooth than the Wigner function, meaning that it can be mathematically irregular.
The interpretation of the P function is not straightforward in general. However, it has a straight physical interpretation [Glauber 1963; Sudarshan 1963; Mandel 1995]. If there exists a classical analog to the system, then its P function is non-negative

everywhere, and, therefore, the state can be regarded as a mixture of coherent states with the relative weights $P(\alpha)$.

It is possible to obtain the Wigner function from the P function by using the following convolution with the Wigner function of a coherent state, as written in eq. (1.118) [Walschaers 2021]:

$$\begin{aligned} W(q,p) &= \int P(\alpha) W_{|\alpha\rangle}(q,p) \mathrm{d}^2\alpha \\ &= \frac{1}{2\pi} \int P(\alpha) e^{-\frac{1}{2}(q-2\,\mathrm{Re}(\alpha))^2 - \frac{1}{2}(p-2Im(\alpha))^2} \mathrm{d}\,\mathrm{Re}(\alpha) \mathrm{d}\,\mathrm{Im}(\alpha). \end{aligned} \tag{1.122}$$

For a thermal state with mean photon number N_{th}, the P function is written:

$$P_{th}(\alpha) = \frac{1}{\pi N_{th}} e^{-|\alpha|^2/N_{th}}. \tag{1.123}$$

This expression is convenient as it shows that thermal states are incoherent mixtures of coherent states weighted by Gaussian functions, the P function corresponds to the probability distribution of measuring a coherent state. Using eq. (1.122), we can extract the Wigner function of a thermal state from eq. (1.123):

$$W_{th}(q,p) = \frac{1}{2\pi(2N_{th}+1)} e^{-\frac{(q^2+p^2)}{2(2N_{th}+1)}}. \tag{1.124}$$

The Husimi Q function

The Husimi Q function is another quasi-probability distribution. Its expression is

$$Q(\alpha) = \frac{1}{4\pi} \langle\alpha|\, \hat{\rho}\, |\alpha\rangle \tag{1.125}$$

where $|\alpha\rangle$ is a coherent state. This function is real but, contrary to the Wigner and P functions, is always positive, and normalized to unity

$$\int Q(\alpha) \mathrm{d}^2\alpha = 1. \tag{1.126}$$

The Q function can also be expressed in terms of the Wigner function

$$Q(\alpha) = \int \mathrm{d}p\mathrm{d}q\; W(q,p) W_0(q_0 - q, p_0 - p), \tag{1.127}$$

where $W_0(q,p)$ is the Wigner function of the vacuum and with $\alpha = \frac{1}{2}(q_0 + ip_0)$. Finally, the Q function is directly measurable with a double homodyne detector.

1.2.7 Quantum covariance matrix

Quantum metrology studies noise sources and their impact on the sensitivity of measurements. It is therefore necessary to have a tool to describe the fluctuations and correlations of the field, which is why we introduce the covariance matrix.

Definition

We consider the quadrature vector in a given mode basis $\{u_\ell(\mathbf{r},t)\}$ with M modes

$$\hat{\mathbf{x}} = (\hat{q}_1, ..., \hat{q}_M, \hat{p}_1, ..., \hat{p}_M)^T. \tag{1.128}$$

From the commutation relation eq. (1.73), we have

$$[\hat{x}_a, \hat{x}_b] = 2i\beta_{ab} \qquad \text{with} \quad \beta = \begin{pmatrix} 0_M & 1_M \\ -1_M & 0_M \end{pmatrix}. \tag{1.129}$$

The associated quantum covariance matrix V is the $2M \times 2M$ matrix:

$$V = \frac{1}{2}\langle \hat{\mathbf{x}}\hat{\mathbf{x}}^T + (\hat{\mathbf{x}}\hat{\mathbf{x}}^T)^T \rangle - \langle \hat{\mathbf{x}} \rangle \langle \hat{\mathbf{x}}^T \rangle, \tag{1.130}$$

i.e.

$$V_{ab} = \frac{1}{2}\langle \hat{x}_a\hat{x}_b + \hat{x}_b\hat{x}_a \rangle - \langle \hat{x}_a \rangle \langle \hat{x}_b \rangle. \tag{1.131}$$

It contains the second moments $\langle \hat{q}_a\hat{q}_b \rangle$, $\langle \hat{q}_a\hat{p}_b \rangle$, $\langle \hat{p}_a\hat{q}_b \rangle$ and $\langle \hat{p}_a\hat{p}_b \rangle$.

Basis change

We now examine the transformation of the covariance matrix under a unitary transformation $\mathrm{U} = X + iY$, where X and Y are real matrices. We have $\hat{\mathbf{b}} = \mathrm{U}\hat{\mathbf{a}}$ where $\hat{\mathbf{b}} = (\hat{b}_1, ..., \hat{b}_M)^T$ and $\hat{\mathbf{a}} = (\hat{a}_1, ..., \hat{a}_M)^T$ are the vectors of field operators respectively in bases $\{v_m(\mathbf{r},t)\}$ and $\{u_\ell(\mathbf{r},t)\}$. We can write the basis change between the quadrature vectors $\hat{\mathbf{y}}$ and $\hat{\mathbf{x}}$ associated respectively to $\hat{\mathbf{b}}$ and $\hat{\mathbf{a}}$ as

$$\hat{\mathbf{y}} = O\hat{\mathbf{x}} \qquad \text{with} \quad O = \begin{pmatrix} X & -Y \\ Y & X \end{pmatrix}. \tag{1.132}$$

Then the covariance matrix V' associated to $\hat{\mathbf{y}}$ is

$$V' = \frac{1}{2}\langle \hat{\mathbf{y}}\hat{\mathbf{y}}^T + (\hat{\mathbf{y}}\hat{\mathbf{y}}^T)^T \rangle - \langle \hat{\mathbf{y}} \rangle \langle \hat{\mathbf{y}}^T \rangle = OVO^T. \tag{1.133}$$

Gaussian states

Gaussian states play an important role in quantum optics, and, in particular, we will only manipulate this kind of state in this work. By definition, Gaussian states are states that have a Gaussian Wigner function

$$W_G(\mathbf{x}) = \frac{1}{(2\pi)^M \sqrt{\det V}} e^{-\frac{1}{2}(\mathbf{x}-\langle \hat{\mathbf{x}} \rangle)^T V^{-1} (\mathbf{x}-\langle \hat{\mathbf{x}} \rangle)}. \tag{1.134}$$

They are completely characterized by their mean field and covariance matrix. The quantum vacuum, coherent states, squeezed states and thermal states are examples of Gaussian states.

Williamson decomposition

It can be shown that the covariance matrix can be expressed in a diagonal form, according to the Williamson theorem [Williamson 1936; Arvind 1995]:

$$V = S\nu_M S^T \qquad \text{with} \qquad \nu_M = \oplus_{k=1}^{M} \nu_k \mathbb{1}_2, \tag{1.135}$$

where S is a symplectic matrix, i.e.

$$S^T \Omega S = \Omega \qquad \text{where} \qquad \Omega = \begin{pmatrix} 0 & \mathbb{1}_M \\ -\mathbb{1}_M & 0 \end{pmatrix}, \tag{1.136}$$

and ν_M is a diagonal matrix whose elements ν_k are known as the symplectic eigenvalues.
This decomposition will be useful to derive useful quantities in section 2.1.4.

Covariance matrix for any set of observables

The concept of covariance matrix is not unique to the quadratures of the field. For any set of observables $\hat{\mathbf{X}} = (\hat{X}_1, ..., \hat{X}_M)^T$, we can define the associated covariance matrix Γ as the $2M \times 2M$ matrix with elements

$$\Gamma_{k\ell}[\hat{\mathbf{X}}] = \langle \hat{X}_k \hat{X}_\ell \rangle - \langle \hat{X}_k \rangle \langle \hat{X}_\ell \rangle. \tag{1.137}$$

1.3 Measurements

This section deals with some types of measurements, which are interesting for this work. We begin with photodetection and homodyne detection which are typically performed in optics and then we present spatial-mode demultiplexing techniques, in particular the multi-plane light conversion, which is at the heart of this thesis.

1.3.1 Photodetection

A building block of any optical measurement is photodetectors like photodiodes, photomultipliers, CCD cameras, or the eyes. They convert the optical signal into a proportional electronic current. At the present time, none of these detectors are fast enough to measure the field directly, they only give access to the light intensity, i.e. the time average of the square of the electric field over the detector surface S and the integration time T. We introduce the intensity operator as being equal to the number of detected photons:

$$\hat{i} = \hat{N} = \sum_\ell \hat{a}_\ell^\dagger \hat{a}_\ell. \tag{1.138}$$

We assume $\langle \hat{i} \rangle \gg 1$ per integration time and $\langle (\delta\hat{a})^2 \rangle \ll \langle \hat{a} \rangle^2$, with $\delta\hat{a} = \hat{a} - \langle \hat{a} - \rangle$. We place ourselves in a single-mode scenario, and we can expand the total photodetection operator:

$$\begin{aligned} \hat{i} &= \hat{a}^\dagger \hat{a} \\ &\simeq \langle \hat{a}^\dagger \rangle \langle \hat{a} \rangle + \delta\hat{a}^\dagger \langle \hat{a} \rangle + \delta\hat{a} \langle \hat{a}^\dagger \rangle. \end{aligned} \tag{1.139}$$

Hence its fluctuations are written

$$\delta\hat{i} = \hat{i} - \langle\hat{i}\rangle = \delta\hat{a}^\dagger\langle\hat{a}\rangle + \delta\hat{a}\langle\hat{a}^\dagger\rangle. \tag{1.140}$$

For a coherent state, we have $\langle\hat{a}\rangle = |\alpha|e^{i\varphi}$, and then

$$\delta\hat{i} = |\alpha|\delta\hat{q}^\varphi, \tag{1.141}$$

where $\hat{q}^\varphi$ is the amplitude quadrature. In realistic situations, we need to add the electronic noise of the detector δN_{EN}, which is a random variable, and the intensity fluctuations become

$$\delta\hat{i} = |\alpha|\delta\hat{q}^\varphi + \delta N_{EN}. \tag{1.142}$$

Here, for simplicity, the quantum efficiency has been chosen as equal to 1. Eq. (1.142) depends only on the measured field and on the noise of the detector. This means that photodetection can only give access to the amplitude quadrature, and for this, we need to overcome the electronic noise of the detector, which is not easily done when the state is close to the vacuum.

1.3.2 Balanced homodyne detection

In order to have access to the field itself and not only to its intensity, an interferometric measurement must be performed. Before presenting this measurement called homodyne detection, we will describe the beamsplitter transformation in the quantum optics formalism.

A small detour: the beamsplitter

We study monochromatic Gaussian beams, all beams having the same frequency and the same waist. The input-output relations of a lossless semi-reflecting mirror, with transmissivity κ are

$$\hat{a}_{\text{out},1} = \sqrt{\kappa}\hat{a}_{\text{in},1} + \sqrt{1-\kappa}\hat{a}_{\text{in},2}, \tag{1.143}$$

$$\hat{a}_{\text{out},2} = \sqrt{\kappa}\hat{a}_{\text{in},1} - \sqrt{1-\kappa}\hat{a}_{\text{in},2}. \tag{1.144}$$

The negative sign is needed for energy conservation. Note that the commutator relations of the outgoing fields follow the ones of quantized fields:

$$[\hat{a}_{\text{out},1}, \hat{a}^\dagger_{\text{out},1}] = [\hat{a}_{\text{out},2}, \hat{a}^\dagger_{\text{out},2}] = 1, \tag{1.145}$$

$$[\hat{a}_{\text{out},1}, \hat{a}_{\text{out},1}] = [\hat{a}_{\text{out},2}, \hat{a}_{\text{out},2}] = 0. \tag{1.146}$$

Measuring the field

Homodyne detection is a standard measurement technique used in quantum optics, initially developed in radio-wave contexts. It gives access to all quadratures of the field of interest, referred to as the signal, by mixing it with a reference beam called the local oscillator on a 50-50 beamsplitter and measuring the intensity at each output with two photodetectors (see fig. 1.8). For the sake of simplicity, we consider

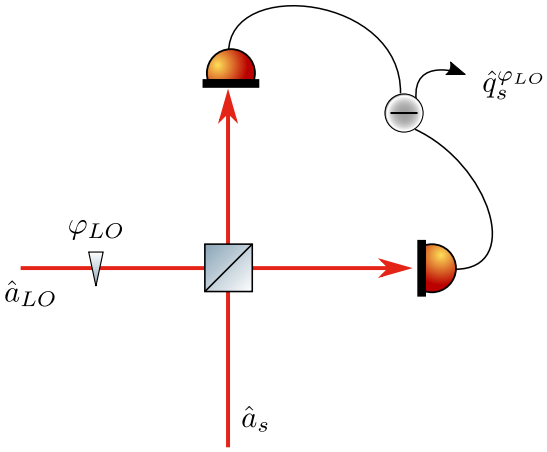

FIGURE 1.8: Homodyne detection.

that both the signal and the local oscillator are single-mode. When their modes are matched, as presented before for the beamsplitter relations, the intensity difference between the two photodetectors is written as follows:

$$\begin{aligned}\hat{N}_- &= \hat{N}_1 - \hat{N}_2 \\ &= \frac{1}{2}(\hat{a}_s^\dagger + \hat{a}_{LO}^\dagger)(\hat{a}_s + \hat{a}_{LO}) - \frac{1}{2}(\hat{a}_s^\dagger - \hat{a}_{LO}^\dagger)(\hat{a}_s - \hat{a}_{LO}) \\ &= \hat{a}_s^\dagger \hat{a}_{LO} + \hat{a}_{LO}^\dagger \hat{a}_s.\end{aligned} \tag{1.147}$$

The local oscillator is chosen to be an intense field, i.e. we assume that its fluctuations and the mean field of the signal beam are negligible compared to its mean field: $\langle \hat{a}_s \rangle$, $\sqrt{\langle (\delta \hat{a}_{LO})^2 \rangle} \ll \langle \hat{a}_{LO} \rangle$ with $\langle \hat{a}_{LO} \rangle = |\alpha_{LO}| e^{i\phi_{LO}}$. Hence, eq. (1.147) becomes

$$\begin{aligned}\hat{N}_- &\simeq |\alpha_{LO}|(\hat{a}_s^\dagger e^{i\varphi_{LO}} + \hat{a}_s e^{-i\varphi_{LO}}) \\ &= |\alpha_{LO}| \hat{q}_s^{\varphi_{LO}}\end{aligned} \tag{1.148}$$

where $\hat{q}_s^{\varphi_{LO}} = \hat{a}_s^\dagger e^{i\varphi_{LO}} + \hat{a}_s e^{-i\varphi_{LO}}$ is the quadrature operator aligned along the local oscillator phase. The fluctuations of the measured signal are thus

$$\delta \hat{N}_- = |\alpha_{LO}| \delta \hat{q}_s^{\varphi_{LO}}, \tag{1.149}$$

and, in a realistic scenario, similarly to the photodetection scheme, we add the detector noise:

$$\delta \hat{N}_- = |\alpha_{LO}| \delta \hat{q}_s^{\varphi_{LO}} + \delta \hat{N}_{EN}. \tag{1.150}$$

We see here that the homodyne detection apparatus allows the amplification of the fluctuations of the field of interest by an external field, the local oscillator. Therefore, it is possible to overcome the electronic noise of the detectors more easily than for photodetection. The measured quadrature is also set by the phase of the local oscillator, giving complete access to the field.
Note that the homodyne detection acts as a modal projective measurement. If the modes of the signal and the local oscillator are unmatched, the measured quadrature

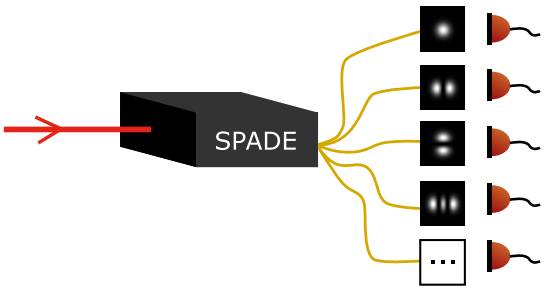

FIGURE 1.9: Spatial-mode demultiplexing consists in decomposing multimode light over single-modes of a basis, in this work, of th transverse Hermite-Gaussian mode basis. We will designate as SPADE the association of a mode-sorting technique with photodetectors.

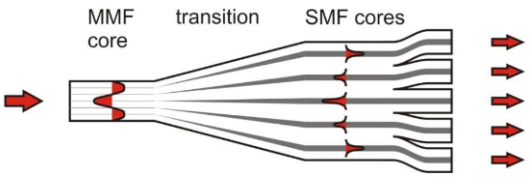

FIGURE 1.10: Photonic lantern [Birks 2015].

corresponds to the one in the local oscillator mode [Bachor 2019].

1.3.3 Spatial-mode demultiplexing

Principle

The measurement at the heart of this work is based on spatial-mode demultiplexing (SPADE). SPADE designates the ability to decompose multimode light over single modes of a basis using a mode-sorting technique. By default, we consider in this manuscript that the considered basis is the transverse Hermite-Gaussian one. At the output of the mode-sorter, it is then possible to perform any measurement. When nothing else is specified, SPADE refers to photodetectors at the single-mode outputs of the mode-sorter (see fig. 1.9).

Mode-sorting techniques

Photonic lantern Photonic lanterns are based on a gradual transition between uncoupled single-mode waveguides to a multimode waveguide. Reviews on this technology can be found in [Birks 2015; Leon-Saval 2015]. Photonic lanterns consist of single-mode cores being gradually reduced until they cannot confine the light anymore. The light is then coupled into the multimode waveguide, as illustrated in fig. 1.10. The transition has to be adiabatic in order to guarantee reversibility.
There are several possible implementations of the photonic lantern, either from a bundle of tapered single-mode fibers or from an array of single-mode waveguides formed via inscription processes with ultrafast lasers. This system allows taking advantage of single-mode-based photonic technologies in a multimode scenario leading to numerous applications in astronomy, spectroscopy and telecommunications.

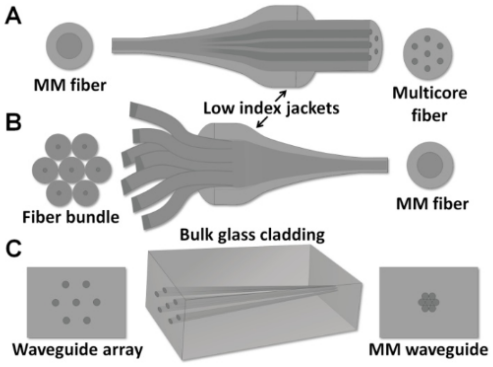

FIGURE 1.11: Photonic lantern implementations [Leon-Saval 2015].

Note, however, that there is no direct correspondence between the single modes and the modes of the multimode core. In other words, light coming from one single-mode core excites several modes of the multimode core. Therefore, it makes it difficult to have access to a specific decomposition like on the Laguerre-Gaussian or Hermite-Gaussian mode bases for example.

Fractional Fourier Transform This approach allows to sort Laguerre-Gaussian modes as it is based on one of their key properties: their effective phase velocity depends on the radial index p (as presented in eq. (1.52)) [Zhou 2017]. LG modes are eigenmodes of fractional Fourier transforms (FRFT), a generalization of the Fourier transform. Under a FRFT, their shape remains unchanged but they gain a mode-dependent phase, as shown in eq. (1.151). The family of FRFT operations $\mathcal{F}^a$, where a is the order of the FRFT, transforms the LG modes from the mode in the initial plane $u_{p\ell}(r_0, \theta_0)$ to the mode in the final plane $u_{p\ell}(r, \theta)$ as follows

$$\mathcal{F}^a[u_{p\ell}(r_0, \theta_0)] = \exp(-i(2p + |\ell|)a) u_{p\ell}(r, \theta). \tag{1.151}$$

The standard Fourier transform corresponds to $a = \pi/2$. This mode-dependent additional phase is referred to as the fractional Gouy phase. The ℓ dependence can be removed with the use of a Dove prism [Leach 2002], leaving only the p-dependent extra phase.
The FRFT $\mathcal{F}^a$ can be realized experimentally with a single lens of focal length f in a z-z configuration, as illustrated in fig. 1.12, where

$$\begin{aligned} z &= \frac{\pi w_0^2}{\lambda} \tan\frac{a}{2}, \\ f &= \frac{\pi w_0^2}{\lambda \sin a}. \end{aligned} \tag{1.152}$$

Therefore, FRFT combined with an interferometer discriminates the modes based on the fractional Gouy phase and sorts the LG modes by routing them to different interferometer outputs. Zhou *et al.* implemented this demultiplexing operation experimentally by coupling lenses, to perform the FRFT, with beamsplitters and phase plates, that form the interferometer and obtained a total crosstalk (the sum of the

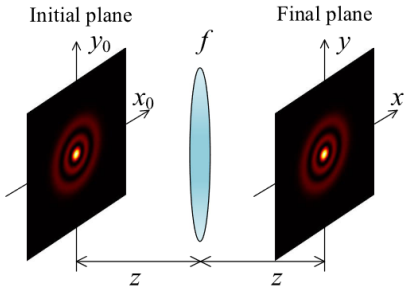

FIGURE 1.12: Realization of the FRFT with a single lens [Zhou 2017].

optical powers at the wrong outputs divided by the total power) of 15% [Zhou 2017] for sorting 3 modes.

Hermite-Gaussian modes can be bijectively converted into Laguerre-Gaussian modes using an astigmatic mode-converter (AMC) [Beijersbergen 1993], composed of two cylindrical lenses. Therefore, combining an AMC with an FRFT-based mode-sorter results in a Hermite-Gaussian mode demultiplexer[4] [Zhou 2018].

The previous sorting approaches[5] are unitary and give access to a high number of modes. However, they are specific to some bases either given by the positions of the single-mode waveguides of the photonic lantern or by exploiting some properties of the Laguerre-Gaussian and Hermite-Gaussian modes with the FRFT-based sorter.

Multi-plane light conversion The multi-plane light conversion [Labroille 2014; Zhang 2023] technology was conceived in Laboratoire Kastler Brossel [Morizur 2011] and is now developed and commercialized by the company Cailabs. This sorting technique can be adapted to any mode basis decomposition. It was shown that any spatial unitary transform can be performed by cascading a finite number of phase masks and Fourier transforms [Morizur 2010]. For practical applications, the input and output are finite subsets of orthonormal modes.

There is no theory on how to analytically optimize the patterns and the number of phase masks, these parameters are not intuitive to determine. Several numerical methods can be used to establish the phase masks, most of them in the inverse design category. It is generally accepted that N phase masks are required to transform N modes. However, a "magic mapping" was recently developed by Fontaine *et al.* and enables a demultiplexing of 1035 modes using 14 phase masks [Fontaine 2021]. Multi-plane light conversion exhibits low losses and low crosstalk - which are imperfections in the mode-basis decomposition - and can be achieved for any spatial-mode transformation. Thanks to these remarkable features, it is an ally of choice for various applications, and in particular, fibered and free-space communications. Let us now examine implementations of the multi-plane light conversion. A spatial

[4] To be precise, there is also an OAM sorter added to the setup to distinguish modes with different ℓ.

[5] One method that was not mentioned is to use a sequence of cavities for sorting modes, for example, by injecting the reflection at the input of a triangular cavity into a second triangular cavity and so on [Santos 2021].

Fourier transform can be realized with a lens of focal length f in a f-f configuration. In practical applications, the multi-plane light conversion is often realized with a reflective design, with the lens replaced by a spherical mirror. A common implementation of the multi-plane light conversion is carried out with several reflections on a spatial light modulator (SLM) [Paúr 2016], on a deformable mirror [Labroille 2014] or a reflective phase plate for Cailabs as the successive phase masks. The unitary transformation is programmable in these situations. In practice, multi-plane light conversion requires local phase shifts and diffraction, making the use of a lens non-mandatory. The multi-plane light converter (MPLC) that we use in this work is the Proteus-C from Cailabs, which is commercialized mostly for telecommunication purposes. It implements phase shifts and diffraction through several reflections on an engraved gold-plated phase plate, serving as successive phase planes. The engraving is chosen such that diffraction occurs between the phase planes. Proteus-C performs the mode basis change between ten spatially separated Gaussian beams to the basis defined by the eigenmodes of a multimode fiber, in our case the spatial Hermite-Gaussian mode basis, as illustrated in fig. 1.13. The basis change is fixed, ensuring low losses and crosstalk. To adapt the MPLC for the study of optical scenes, we removed the multimode fiber, resulting in a free-space input. The transformation can be performed in both directions: from the single-mode fibers to the multimode beam, and vice-versa.

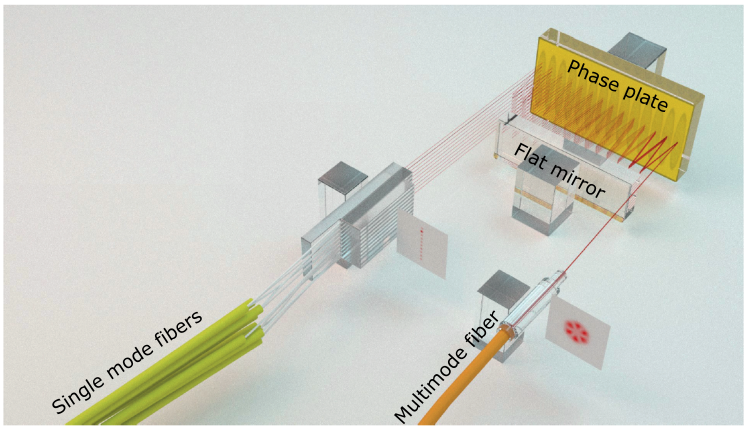

FIGURE 1.13: The Multi-Plane Light Converter (MPLC - Proteus-C) of Cailabs performs the basis change between spatially separated Gaussian beams from single-mode fibers into the eigenmodes of a multimode fiber thanks to multiple reflections on a spherical mirror and a phase plate. Source: [Cailabs].

Dispersion serves as the temporal counterpart to diffraction but its controlled implementation requires non-linear optical processes. Consequently, this mode-demultiplexing technique can be extended to both the temporal and spectral domains at the cost, however, of necessitating more sophisticated setups [Brecht 2015; Ashby 2020; Joshi 2022].

1.3.4 Direct imaging

Direct imaging (DI) corresponds to what is commonly identified as conventional imaging, i.e. the association of a lens, or more generally of an imaging system, with a CCD camera, as illustrated in fig. 1.14.

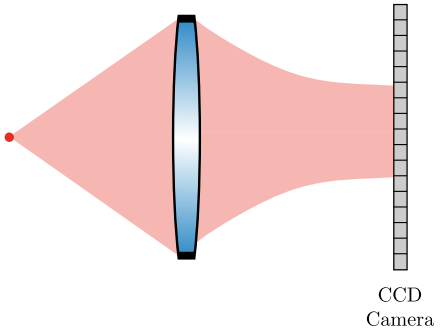

FIGURE 1.14: Direct imaging.

The photons are detected on each pixel of the camera to reconstruct the optical scene. Therefore, direct imaging is a particular type of spatial-mode demultiplexing where the measurement basis is the pixel mode basis. Since it is the conventional way to perform passive imaging, we will often compare the performances of HG SPADE to those of typical direct imaging.

Chapter 2

Estimation theory for separation estimation

Contents

Parameter estimation is a fundamental task in metrology. This is a branch of statistics with applications ranging from physics to politics, as well as telecommunications, speech recognition, medicine, or economics [Schuster 1898; Kay 1993; Taylor 2007; Box 2015; Barbieri 2022].
In the context of experimental physics, due to the unavoidable presence of noises and their intrinsic randomness, measurements exhibit statistical errors that limit their sensitivity. Classical estimation theory which deals with experimental noises like thermal fluctuations, mechanical instabilities, or electronic noises, was extended to a quantum version that includes the intrinsic noises, in particular of the quantum electromagnetic field, as presented in the previous chapter. In some situations, it is possible to improve technologies to reduce the influence of certain noise sources, as well as to engineer the state of the light to access a smaller intrinsic noise. An interesting question is therefore: what is the ultimate sensitivity limit for a given parameter and what measurement reaches it?

Parameter estimation theory and quantum metrology aim to provide a formalism to answer these questions, and their general framework is introduced in the first section. The second section describes the tools extracted from the parameter estimation theory to reach the ultimate sensitivity in various contexts. The third section presents some models and assumptions that will be used in the manuscript to study the particular cases of the estimations of beam displacement and source separation. We will then apply the formalism of parameter estimation to these situations in the last two sections.
For more details about classical estimation theory, see [Kay 1993], and for more comprehensive reviews on quantum metrology, see [Giovannetti 2011; Pezzè 2014; Barbieri 2022].

2.1 Tools for parameter estimation

Within the framework of quantum metrology, variables can be categorized into two distinct types: parameters and observables. Observables (e.g. number of photons, spin) inherently carry noise due to their quantum nature. Their measurement provides access to parameters (e.g. phase, separation between two optical sources), that have a well-defined value, their true value, without any noise. Noise in the parameters arises during the encoding of parameters into the probe — in this work, the electromagnetic field — and during the subsequent measurement of observables.
The parameter estimation theory is concerned with the extent to which collected data - from the measurement of observables - can be used to estimate the unknown parameters, and how the information from the observables can be extracted efficiently to have the best estimation possible of the parameters [1].
The process of parameter estimation can be decomposed into distinct building blocks presented in fig. 2.1: the preparation of the probe, in our case of the light

[1] This formalism can be used in various contexts: estimation of the proportion of the population who will vote for a particular candidate, the position of an object with radar or sonar, the heart rate of a fetus [Widrow 1985], the underground distance of an oil deposit [Justice 1985], the carrier frequency of a signal for telecommunications [Proakis 2007], orbit determination...

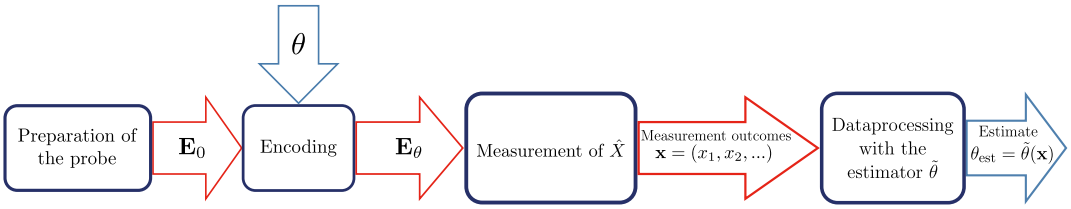

FIGURE 2.1: The building blocks of parameter estimation theory. The probe, i.e. the electromagnetic field $\mathbf{E}_0$, is prepared and goes through the sample where the parameter θ is encoded. Then the θ-dependent electromagnetic field is measured resulting in a set of data points $\mathbf{x} = (x_1, x_2, ...)$ which are data-processed to extract an estimate θ_{est} of the parameter θ using the estimator $\tilde{\theta}$.

beam, the encoding of the parameter θ onto the probe, the measurement of the observables $\hat{X}$ and the data processing, providing an estimate $\theta_{\text{est}} = \tilde{\theta}(\mathbf{x})$ using the estimator $\tilde{\theta}$.
In this section, we introduce the formalism needed to describe estimators and we introduce fundamental bounds used to benchmark estimation procedures.

2.1.1 Estimators

We consider a set of measurement outcomes $\mathbf{x} = (x_1, ..., x_\mu)$ whose distribution depends on an unknown parameter θ. They are formally treated as a realization of μ independent and identically distributed random variables X, obtained with the measurement of the observable $\hat{X}$. The goal is to determine the parameter θ based on the measurement results by building an estimator $\tilde{\theta}(\mathbf{x})$.

An estimator is a function of random variables, hence it is also a random variable and its statistical moments are well-defined. We note $p(\mathbf{x}|\theta)$ the probability distribution function of the measurement results for a given parameter value. The expectation value of the estimator is

$$\langle \tilde{\theta} \rangle = \int p(\mathbf{x}|\theta)\tilde{\theta}(\mathbf{x})\mathrm{d}\mathbf{x}. \tag{2.1}$$

We define the bias of the estimator as

$$b_{\tilde{\theta}} = \langle \tilde{\theta} \rangle - \theta_0, \tag{2.2}$$

where θ_0 is the true value of the parameter. An estimation with low bias is said to have high accuracy. If $b_{\tilde{\theta}} = 0$, the estimator is said to be unbiased. In the following of this manuscript, we will only consider unbiased estimators. Using this assumption, we will quantify the performance of an estimator with its variance:

$$\Delta^2\tilde{\theta} = \langle \tilde{\theta}^2 \rangle - \langle \tilde{\theta} \rangle^2 = \int p(\mathbf{x}|\theta) \left(\tilde{\theta}(\mathbf{x}) - \langle \tilde{\theta} \rangle\right)^2 \mathrm{d}\mathbf{x}. \tag{2.3}$$

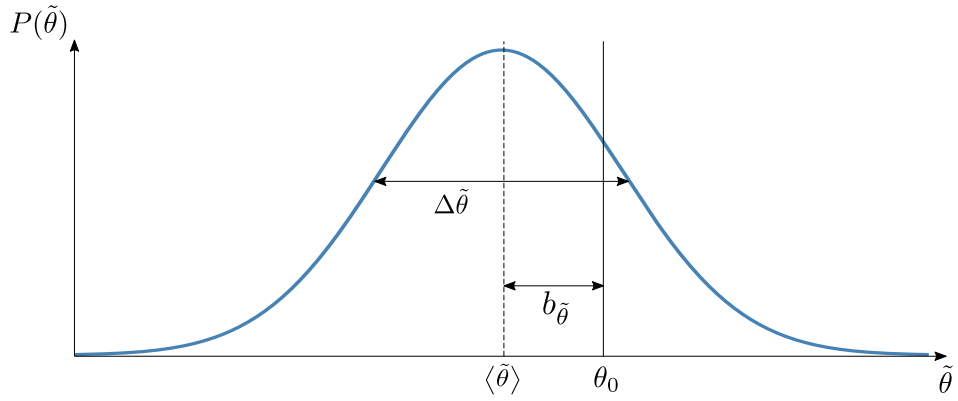

FIGURE 2.2: Properties of an estimator. The bias $b_{\tilde{\theta}}$ and the standard deviation $\Delta\tilde{\theta}$ of the estimator $\tilde{\theta}$ of the parameter θ are represented.

This quantity corresponds to the sensitivity of the estimation. The aim when looking for an optimal estimator is to find an estimator with the minimum variance, i.e. with the highest sensitivity possible.

Frequentist versus Bayesian approach

The parameter estimation framework presents two approaches which are based on two interpretations of the probabilities. In the Bayesian approach, the probability of an event is viewed as the degree of belief in this event, while in the frequentist approach, the probability of an event corresponds to the relative frequency of this event after many realizations.

The Bayesian approach assumes prior information on the parameter θ, which is written as the probability distribution $p(\theta)$. The parameter θ is, therefore, seen as a random variable, and the prior information on the parameter is taken into account using Bayes' theorem to access an estimation through the following probability distribution

$$p(\theta|\mathbf{x}) = \frac{p(\mathbf{x}|\theta)p(\theta)}{p(\mathbf{x})}. \tag{2.4}$$

The estimator continually computes a new probability distribution function $p(\theta|\mathbf{x})$ based on the previous density function and the collected data and converges toward the true value of the parameter as the number of measurements increases.

In this work, we use the frequentist approach, where the parameter θ is treated as a deterministic and unknown constant, without any prior information. As $M \longrightarrow \infty$, the frequency of the collected data tends to reflect the probability density function, hence the denomination. A criticism that is usually addressed to the frequentist approach is that an optimal estimator potentially depends on θ. This could seem counter-intuitive as it appears to conflict with the purpose of parameter estimation. It is however reasonable to assume that it is always possible to have access to prior knowledge on the parameter thanks to theory, previous estimates, or from a fraction of the data set.

2.1.2 Fisher information

To answer the question of what is the sensitivity limit of a given parameter when performing a specific measurement, the parameter estimation theory provides a lower bound for the variance of the estimator, the Cramér-Rao bound (CRB) [Fisher 1925; Kay 1993; Rao 1994; Cramér 1999]:

$$\Delta^2\tilde{\theta} \geq \frac{1}{\mu I_F[\theta, \hat{X}]}, \tag{2.5}$$

where μ is the number of independent measurements and $I_F[\theta, \hat{X}]$ is the Fisher information defined by

$$I_F[\theta, \hat{X}] = -\int p(\mathbf{x}|\theta)\frac{\partial^2 \ln p(\mathbf{x}|\theta)}{\partial\theta^2} = \int \frac{1}{p(\mathbf{x}|\theta)}\left(\frac{\partial p(\mathbf{x}|\theta)}{\partial\theta}\right)^2 \mathrm{d}\mathbf{x}. \tag{2.6}$$

The Fisher information is a non-negative and additive quantity [Kay 1993]. It is often interpreted as the maximal amount of information about the unknown parameter θ that can be extracted with a given measurement. The more the probability distribution depends on the parameter, the better the sensitivity is. The estimation will present a high variance if the probability distribution does not depend or depends only weakly on the parameter θ[2].
The Cramér-Rao bound allows for the benchmarking of the performance of unbiased estimators. An estimator that saturates the Cramér-Rao bound is said to be efficient.

Derivation of the Cramér-Rao bound

Let us derive the Cramér-Rao bound. From the definition of the expectation value of an estimator, since we assume $\tilde{\theta}$ to be unbiased, we have

$$\int \left(\tilde{\theta} - \langle\tilde{\theta}\rangle\right) p(\mathbf{x}|\theta)\mathrm{d}\mathbf{x} = 0. \tag{2.7}$$

We apply ∂_θ to both sides

$$\int \left(\tilde{\theta} - \langle\tilde{\theta}\rangle\right) \frac{\partial p(\mathbf{x}|\theta)}{\partial\theta}\mathrm{d}\mathbf{x} - \frac{\partial\langle\tilde{\theta}\rangle}{\partial\theta}\int p(\mathbf{x}|\theta)\mathrm{d}\mathbf{x} = 0. \tag{2.8}$$

Using the normalization of $p(\mathbf{x}|\theta)$:

$$\int p(\mathbf{x}|\theta)\mathrm{d}\mathbf{x} = 1, \tag{2.9}$$

we obtain

$$\int (\tilde{\theta} - \langle\tilde{\theta}\rangle) p(\mathbf{x}|\theta)\frac{\partial \ln p(\mathbf{x}|\theta)}{\partial\theta}\mathrm{d}\mathbf{x} = \frac{\partial\langle\tilde{\theta}\rangle}{\partial\theta}, \tag{2.10}$$

[2] "Depending on the parameter" here means that we want to maximize $\partial_\theta p(\mathbf{x}|\theta)$ around the true value θ, hence to maximize the second derivative of $p(\mathbf{x}|\theta)$, the curvature around the true value–the derivative $\partial_\theta p(\mathbf{x}|\theta)$ is typically 0 at the true value. This is best shown by the logarithmic formulation of the Fisher information.

and the Cauchy-Schwarz inequality[3] gives

$$\int (\tilde{\theta} - \langle\tilde{\theta}\rangle)^2 p(\mathbf{x}|\theta) \mathrm{d}\mathbf{x} \times \int p(\mathbf{x}|\theta) \left(\frac{\partial \ln p(\mathbf{x}|\theta)}{\partial \theta} \right)^2 \mathrm{d}\mathbf{x} \geq \left(\frac{\partial \langle\tilde{\theta}\rangle}{\partial \theta} \right)^2. \tag{2.11}$$

For an unbiased estimator, $\langle\tilde{\theta}\rangle = \theta$, hence

$$\int (\tilde{\theta} - \langle\tilde{\theta}\rangle)^2 p(\mathbf{x}|\theta) \mathrm{d}\mathbf{x} \times \int p(\mathbf{x}|\theta) \left(\frac{\partial \ln p(\mathbf{x}|\theta)}{\partial \theta} \right)^2 \mathrm{d}\mathbf{x} \geq 1 \tag{2.12}$$

and, since the μ measurement results are independent and identically distributed, we have

$$\int (\tilde{\theta} - \langle\tilde{\theta}\rangle)^2 p(\mathbf{x}|\theta) \mathrm{d}\mathbf{x} \times \mu \int p(x|\theta) \left(\frac{\partial \ln p(x|\theta)}{\partial \theta} \right)^2 \mathrm{d}x \geq 1. \tag{2.13}$$

Finally, we obtain the Cramér-Rao bound as given in eq. (2.5):

$$\Delta^2\tilde{\theta} \geq \frac{1}{\mu I_F[\theta, \hat{X}]} \qquad \text{with} \qquad I_F[\theta, \hat{X}] = \int \frac{1}{p(\mathbf{x}|\theta)} \left(\frac{\partial p(\mathbf{x}|\theta)}{\partial \theta} \right)^2 \mathrm{d}\mathbf{x}. \tag{2.14}$$

2.1.3 Quantum Fisher information

In the previous section, we tackled the task of estimating a parameter θ from the results of a given measurement with the best sensitivity possible. It is however possible to determine the ultimate sensitivity limit for the estimation of θ, i.e. a limit that depends only on the state of the probe after encoding the parameter and not on the measurement apparatus.
The most general description of a measurement is given by positive operator-valued measures (POVM). A POVM is a set of Hermitian operators $\{\hat{F}(\mathbf{x})\}$ which are non-negative and satisfy the normalization condition

$$\int \mathrm{d}\mathbf{x} \hat{F}(\mathbf{x}) = \mathbb{1}. \tag{2.15}$$

The conditional probability to observe the result $\mathbf{x}$ for a given value of the parameter θ is

$$p(\mathbf{x}|\theta) = \mathrm{Tr}\left[\hat{F}(\mathbf{x})\hat{\rho}(\theta)\right]. \tag{2.16}$$

The ultimate limit on the sensitivity of the estimation of θ is obtained by maximizing the Fisher information over all possible POVMs $\{\hat{F}(\mathbf{x})\}$ - which replace the observable $\hat{X}$ - and is given by the quantum Cramér-Rao bound (QCRB) [Helstrom 1967; Braunstein 1994]:

$$\Delta^2\tilde{\theta} \geq \frac{1}{\mu I_F[\hat{\rho}(\theta), \{\hat{F}(\mathbf{x})\}]} \geq \frac{1}{\mu I_Q[\hat{\rho}(\theta)]}, \tag{2.17}$$

[3] The Cauchy-Schwarz inequality states that $\left(\int |uv|\right)^2 \leq \int |u|^2 \int |v|^2$ with equality if and only if $u = \lambda v$. Here, we apply it with $u = (\tilde{\theta} - \langle\tilde{\theta}\rangle)\sqrt{p(\mathbf{x}|\theta)}$ and $v = \sqrt{p(\mathbf{x}|\theta)}\frac{\partial \ln p(\mathbf{x}|\theta)}{\partial \theta}$.

where μ is the number of independent measurements, and $I_Q[\hat{\rho}(\theta)]$ is the quantum Fisher information (QFI) defined as

$$I_Q[\hat{\rho}(\theta)] = \max_{\{\hat{F}(\mathbf{x})\}} I_F[\hat{\rho}(\theta), \{\hat{F}(\mathbf{x})\}] = \mathrm{Tr}\left[\hat{\rho}(\theta)\hat{L}_\theta^2\right]. \tag{2.18}$$

The operator $\hat{L}_\theta$ is the symmetric logarithmic derivative (SLD) defined as a solution of the following equation [Helstrom 1967]

$$\frac{\partial\hat{\rho}(\theta)}{\partial\theta} = \frac{1}{2}(\hat{\rho}(\theta)\hat{L}_\theta + \hat{L}_\theta\hat{\rho}(\theta)). \tag{2.19}$$

As written in eq. (2.18), the QFI is a maximization of the Fisher information over all possible measurements and is therefore an upper bound for this quantity. The QFI provides the ultimate sensitivity for the estimation of the parameter θ whatever the measurement apparatus.

Derivation of the quantum Cramér-Rao bound
For the derivation of the QCRB, we follow [Pezzè 2014].
From eqs. (2.6) and (2.16), we write

$$I_F[\hat{\rho}(\theta), \{\hat{F}(\mathbf{x})\}] = \int \frac{1}{p(\mathbf{x},\theta)}\left(\frac{\partial p(\mathbf{x},\theta)}{\partial\theta}\right)^2 \mathrm{d}\mathbf{x} = \int \mathrm{d}\mathbf{x}\frac{\mathrm{Tr}\left[\hat{F}(\mathbf{x})\partial_\theta\hat{\rho}(\theta)\right]^2}{\mathrm{Tr}\left[\hat{F}(\mathbf{x})\hat{\rho}(\theta)\right]}. \tag{2.20}$$

Using eq. (2.19), we obtain

$$\mathrm{Tr}\left[\hat{F}(\mathbf{x})\partial_\theta\hat{\rho}(\theta)\right] = \frac{1}{2}\left(\mathrm{Tr}\left[\hat{F}(\mathbf{x})\hat{\rho}(\theta)\hat{L}_\theta\right] + \mathrm{Tr}\left[\hat{F}(\mathbf{x})\hat{L}_\theta\hat{\rho}(\theta))\right]\right). \tag{2.21}$$

Since the operators are Hermitian, we have

$$\hat{F}(\mathbf{x})\hat{L}_\theta\hat{\rho}(\theta) = \hat{F}(\mathbf{x})^\dagger\hat{L}_\theta^\dagger\hat{\rho}(\theta)^\dagger = \left(\hat{\rho}\hat{L}_\theta(\theta)\hat{F}(\mathbf{x})\right)^\dagger. \tag{2.22}$$

Then, using

$$\mathrm{Tr}\left[\left(\hat{\rho}\hat{L}_\theta(\theta)\hat{F}(\mathbf{x})\right)^\dagger\right] = \mathrm{Tr}\left[\hat{\rho}\hat{L}_\theta(\theta)\hat{F}(\mathbf{x})\right]^*, \tag{2.23}$$

from eq. (2.21),we obtain

$$\mathrm{Tr}\left[\hat{F}(\mathbf{x})\partial_\theta\hat{\rho}(\theta)\right] = \mathrm{Re}\left\{\mathrm{Tr}\left[\hat{F}(\mathbf{x})\hat{\rho}(\theta)\hat{L}_\theta\right]\right\}, \tag{2.24}$$

and we have

$$\mathrm{Re}\left\{\mathrm{Tr}\left[\hat{F}(\mathbf{x})\hat{\rho}(\theta)\hat{L}_\theta\right]\right\}^2 \leq |\,\mathrm{Tr}\left[\hat{F}(\mathbf{x})\hat{\rho}(\theta)\hat{L}_\theta\right]|^2. \tag{2.25}$$

Moreover, since $\hat{\rho}(\theta)$ and $\hat{F}(\mathbf{x})$ are positive semi-definite operators, the Cauchy-Schwarz inequality[4] gives

$$|\,\mathrm{Tr}\left[\hat{F}(\mathbf{x})\hat{\rho}(\theta)\hat{L}_\theta\right]|^2 \leq \mathrm{Tr}\left[\hat{F}(\mathbf{x})\hat{\rho}(\theta)\right]\mathrm{Tr}\left[\hat{F}(\mathbf{x})\hat{\rho}(\theta)\hat{L}_\theta^2\right]. \tag{2.26}$$

[4]The Cauchy-Schwarz inequality states that $|\,\mathrm{Tr}\left[\hat{A}^\dagger\hat{B}\right]|^2 \leq \mathrm{Tr}\left[\hat{A}^\dagger\hat{A}\right]\mathrm{Tr}\left[\hat{B}^\dagger\hat{B}\right]$ with equality if and only if $\hat{A} = \lambda\hat{B}$.

Consequently, combining eqs. (2.24) to (2.26), we obtain the inequality

$$\mathrm{Tr}\left[\hat{F}(\mathbf{x})\partial_\theta\hat{\rho}(\theta)\right]^2 \leq \mathrm{Tr}\left[\hat{F}(\mathbf{x})\hat{\rho}(\theta)\right]\mathrm{Tr}\left[\hat{F}(\mathbf{x})\hat{\rho}(\theta)\hat{L}_\theta^2\right], \tag{2.27}$$

Hence, using eq. (2.20) and the normalization of the POVM (see eq. (2.15)), the Fisher information satisfies the inequality

$$I_F[\hat{\rho}(\theta), \{\hat{F}(\mathbf{x})\}] \leq \mathrm{Tr}\left[\hat{\rho}(\theta)\hat{L}_\theta^2\right]. \tag{2.28}$$

We note that the right side of the inequality does not depend on the POVM. Moreover, it can be shown that there exists at least one measurement that saturates eq. (2.28), which is the POVM built on the eigenstates of $\hat{L}_\theta$ (see [Pezzè 2014]). We can thus interpret this quantity to be the maximization of $I_F[\hat{\rho}(\theta), \{\hat{F}(\mathbf{x})\}]$ over all possible POVMs, and we define this higher bound to be the QFI $I_Q[\hat{\rho}(\theta)]$ defined in eq. (2.18).

2.1.4 Quantum Fisher information for Gaussian states and mode-encoded parameters

In this work, we are particularly interested in the estimation of two parameters, the displacement of a beam and the separation between two sources. In sections 2.4 and 2.5, we derive the QFI for these two parameters, in order to determine which measurements are optimal.
We consider the case where the probe electromagnetic field is in a thermal state, which is a Gaussian state (as described in section 1.2.7).
In this section, we provide a simplified expression of the QFI derived in [Sorelli 2023], that we apply to beam displacement and source separation estimations in sections 2.4 and 2.5.

These parameters are encoded in the modes of the probe, more specifically the spatial modes. This means that the parameter of interest θ modifies the n initially - before the encoding of the parameter - populated modes of the probe $\{u_k(\mathbf{r})\}$ but not the state of the field $\hat{\rho}$, or, in other words, that the way the state $\hat{\rho}$ is written in the initial mode basis is not affected by changes of the parameter. In order to determine the QFI for mode-encoded parameters and small variations of the parameters, we define the n parameter-dependent modes $\{u_k[\theta](\mathbf{r})\}$ from the modes $\{u_k(\mathbf{r})\}$, and their derivatives $\{\partial_\theta u_k[\theta](\mathbf{r})\}$. For example, when the parameter of interest is the displacement of the beam x_0, the initially populated mode is the centered Gaussian beam $u_{00}(x)$, and we define the parameter-dependent mode such that $u_{00}[x_0](x) = u_{00}(x - x_0)$.

It can be shown that for modes $\{u_k(\mathbf{r})\}$ initially populated with Gaussian states, the QFI can be decomposed into the covariance matrix V and the mean field $\bar{\mathbf{x}} = \langle\hat{\mathbf{x}}\rangle$ contributions [Pinel 2012; Serafini 2017]

$$I_Q[\theta] = I_{Q,V}[\theta] + I_{Q,\bar{\mathbf{x}}}[\theta] \tag{2.29}$$

where $I_{Q,V}[\theta]$ and $I_{Q,\bar{\mathbf{x}}}[\theta]$, the covariance matrix and the displacement vector contributions to the QFI, are written in terms of the symplectic matrix and the symplectic eigenvalues obtained from the Williamson decomposition of V. Their expressions can be found in [Sorelli 2023].

In order to derive an analytical expression for the QFI for mode-encoded parameters, we now introduce two Hilbert spaces: $\mathcal{H}_n$ formed by the n modes $\{u_k[\theta](\mathbf{r})\}$ and $\mathcal{H}_\partial$ formed by their m derivatives $\{\partial_\theta u_k[\theta](\mathbf{r})\}$ that are linearly independent from the modes $\{u_k[\theta](\mathbf{r})\}$. We assume that the n modes $\{u_k[\theta](\mathbf{r})\}$ form an orthonormal basis, and we have dim $\mathcal{H}_n = n$ and dim $\mathcal{H}_\partial = m \leq n$. We can always construct a m-dimensional orthonormal basis $\{u'_k[\theta](\mathbf{r})\}$ of $\mathcal{H}_\partial$ from the derivative modes, so that each derivative mode can be expressed as[5]

$$\partial_\theta u_k[\theta](\mathbf{r}) = \sum_{\ell=1}^{n} c_{k\ell}[\theta] u_\ell[\theta](\mathbf{r}) + \sum_{\ell=1}^{m} d_{k\ell}[\theta] u'_\ell[\theta](\mathbf{r}). \tag{2.30}$$

The covariance matrix and the displacement vector contributions to the QFI can be expressed in terms of the $c_{k\ell}[\theta]$ and $d_{k\ell}[\theta]$[6] , i.e. in terms of the initially populated modes and their derivatives. Both expressions and their derivations are quite heavy and can be found in [Sorelli 2023].

Since we are interested in thermal states, which have a zero mean field, we give their only contribution to the QFI which is the covariance matrix contribution. The covariance matrix V_n of thermal states, expressed in the basis $\{u_k[\theta](\mathbf{r})\}$, is diagonal, and therefore, its Williamson decomposition (eq. (1.135)) is straightforward

$$V_n = S\nu_n S^T \qquad \text{with} \qquad \nu_n = \oplus_{k=1}^{n} \nu_k \mathbb{1}_2 \quad \text{and} \quad S = \mathbb{1}_{2n}. \tag{2.31}$$

The covariance contribution to the QFI is given by [Sorelli 2023]:

$$I_{Q,V}[\theta] = \frac{1}{2} \sum_{\ell=0}^{3} \sum_{j,k=1}^{n} \frac{(a_{j,k}^{(\ell)})^2}{\nu_j \nu_k - (-1)^\ell} + \frac{1}{2} \sum_{\ell=0}^{3} \sum_{j=1}^{n} \sum_{k=1}^{m} \frac{(a_{j,k+n}^{(\ell)})^2 + (a_{k+n,j}^{(\ell)})^2}{\nu_j - (-1)^\ell}, \tag{2.32}$$

where the ν_k are the symplectic values of the covariance matrix expressed in the n initially populated modes and the $a_{j,k}^{(\ell)}$ coefficients are given by

$$a_{j,k}^{(\ell)} = \begin{cases} \mathrm{Tr}\left[A_{j,k}^{(\ell)} B_n\right] & 1 \leq j,k \leq n, \\ \mathrm{Tr}\left[A_{j,(k-n)}^{(\ell)} B_\partial\right] & 1 \leq j \leq n, n < k \leq n+m, \\ \mathrm{Tr}\left[A_{(j-n),k}^{(\ell)} B_\partial\right] & n < j \leq n+m, 1 \leq k \leq n. \end{cases} \tag{2.33}$$

[5] This decomposition is not unique as the bases choice is not unique. If the initially populated modes $u_\ell[\theta](\mathbf{r})$ are more than one, it is possible to apply a unitary transformation to obtain a different mode basis of the same space and the orthonormalization of the derivative modes $u'_\ell[\theta](\mathbf{r})$ is not unique. For example, with the Gram-Schmidt orthogonalization process, the final mode basis depends on which mode is started with.

[6] These are the coefficients of interest as they contain information about consequences of variations of the parameter on the modes on the smallest subspace as shown in eq. (2.30).

Here, the $A_{jk}^{(\ell)}$ matrices are a set of $2n \times 2n$ matrices that are zero everywhere except in the jk block where they are given by $A_\ell = i\sigma_y/\sqrt{2}$, $\sigma_z/\sqrt{2}$, $\mathbb{1}_2/\sqrt{2}$ and $\sigma_x/\sqrt{2}$ for $\ell = 0, 1, 2$ and 3, respectively, with $\sigma_{x,y,z}$ the Pauli matrices[7], and

$$B_n = D_n^T(V_n - \mathbb{1}_{2n}) + (V_n - \mathbb{1}_{2n})D_n + \partial_\theta V_n, \tag{2.35}$$

$$B_\partial = D_\partial^T(V_n - \mathbb{1}_{2n}), \tag{2.36}$$

where D_n and D_∂ are respectively $2n \times 2n$ and $2n \times 2m$ matrices with $k\ell$ blocks given by

$$(D_n)_{k\ell} = \begin{pmatrix} \mathrm{Re}(c_{k\ell}) & -\mathrm{Im}(c_{k\ell}) \\ \mathrm{Im}(c_{k\ell}) & \mathrm{Re}(c_{k\ell}) \end{pmatrix}, \tag{2.37}$$

$$(D_\partial)_{k\ell} = \begin{pmatrix} \mathrm{Re}(d_{k\ell}) & -\mathrm{Im}(d_{k\ell}) \\ \mathrm{Im}(d_{k\ell}) & \mathrm{Re}(d_{k\ell}) \end{pmatrix}, \tag{2.38}$$

using the coefficients $c_{k\ell}$ and $d_{k\ell}$ from eq. (2.30).

In the following, we will consider only real modes $\{u_k[\theta](\mathbf{r})\}$, which is the case for HG modes. This is why we can simplify eqs. (2.37) and (2.38) to

$$(D_n)_{k\ell} = c_{k\ell}\mathbb{1}_2, \tag{2.39}$$

$$(D_\partial)_{k\ell} = d_{k\ell}\mathbb{1}_2. \tag{2.40}$$

We also assume that the modes $\{u_k[\theta](\mathbf{r})\}$ are orthogonal to all the derivative modes $\{\partial_\theta u_k[\theta](\mathbf{r})\}$, again this is the case for HG modes. This leads to $n = m$ and

$$D_n = 0 \qquad \text{and} \qquad (D_\partial)_{k\ell} = \delta_{k\ell}\eta_k\mathbb{1}_2, \tag{2.41}$$

where $\eta_k^2 = ||\partial_\theta u_k[\theta](\mathbf{r})||^2 = \int \mathrm{d}^2\mathbf{r}\ (\partial_\theta u_k[\theta](\mathbf{r}))^2$. As a consequence, the matrices B_n and B_∂ are diagonal and only the terms with $\ell = 2$ survive in eq. (2.32), and the QFI reads

$$I_{Q,V}[\theta] = \frac{1}{2}\sum_{j,k=1}^{n} \frac{\left(a_{j,k}^{(2)}\right)^2}{\nu_j\nu_k - 1} + \sum_{j=1}^{n} \frac{\left(a_{j,j+n}^{(2)}\right)^2}{\nu_j - 1}, \tag{2.42}$$

with

$$a_{j,k}^{(\ell)} = \begin{cases} \frac{1}{\sqrt{2}}\mathrm{Tr}[\partial_\theta V_n] & 1 \le j,k \le n, \\ \frac{1}{\sqrt{2}}\mathrm{Tr}\left[D_\partial^T(V_n - \mathbb{1}_{2n})\right] & 1 \le j \le n, n < k \le 2n. \end{cases} \tag{2.43}$$

The first term in eq. (2.42) contains the sum over only the n modes $\{u_k[\theta](\mathbf{r})\}$, it describes the contribution to the QFI of variations of the state within these n modes due to a parameter change. On the other hand, the second term is composed of a sum

[7] For a better understanding of the structure of the $A_{jk}^{(\ell)}$ matrices, we write the $A_{24}^{(2)}$ matrix with $n = 2$:

$$A_{24}^{(2)} = \frac{1}{\sqrt{2}}\begin{pmatrix} 0 & 0 & 0 & 0 \\ 0 & 1 & 0 & 1 \\ 0 & 0 & 0 & 0 \\ 0 & 1 & 0 & 1 \end{pmatrix} \tag{2.34}$$

over the modes $\{u_k[\theta](\mathbf{r})\}$ but also of a sum over their m orthonormalized derivatives $\{u'_k[\theta](\mathbf{r})\}$. This second term accounts for the coupling between the modes $\{u_k[\theta](\mathbf{r})\}$ and their derivatives induced by parameter variations.

2.2 Reaching the ultimate sensitivity limit in parameter estimation

As stated in the previous section, the ultimate sensitivity for the estimation of a given parameter is given by the QFI. An estimation protocol can be decomposed into four steps: the preparation of the probe and its interaction with the system to be measured which encodes the parameter in the probe, the probe readout, and the data processing which results in an estimate, as illustrated in fig. 2.1.

It is possible to act on three of these points, which we will develop in the following, to optimize the process and hope to saturate the quantum Cramér-Rao bound [Kay 1993; Giovannetti 2011; Barbieri 2022].

2.2.1 Optimal states as the probe

As noticeable in eq. (2.18), the QFI is derived for a given quantum state, and different states provide different scalings of the QFI with the number of photons. An optimal probe state is a state that maximizes the QFI.
The most well-known successes of quantum metrology emerged in phase estimation problems. The textbook examples of optimal states for estimation of phase φ are the so-called NOON states. They are entangled states of the form $|\psi\rangle = \frac{1}{\sqrt{2}}(|N\rangle|0\rangle + |0\rangle|N\rangle)$, which represents a superposition of N particles in one mode with zero particles in the other mode, and vice versa. These states are theoretically known to provide a Heisenberg scaling, i.e. $\Delta\tilde{\varphi} \propto 1/N$ instead of the standard quantum limit where $\Delta\tilde{\varphi} \propto 1/\sqrt{N}$ [Demkowicz-Dobrzański 2015]. An experimental demonstration was realized with $N = 2$ [Slussarenko 2017]. However, NOON states are difficult to generate for $N > 2$ and there is no recipe to prepare them deterministically. They are also extremely sensitive to losses [Giovannetti 2011]. Squeezed states are another kind of quantum state that can be useful to overcome the standard quantum limit for phase estimation [Giovannetti 2011]. One of their famous application is the detection of gravitational waves with the VIRGO interferometer where they allow for a 3dB gain on the sensitivity compared to using coherent states [Virgo Collaboration 2019].

2.2.2 Optimal measurements

As shown in the definition of the QFI eq. (2.18), which is a maximization of the Fisher information over all the POVM, another strategy to improve the sensitivity of the estimation is to perform an optimal readout of the probe. The measurements for which the Fisher information saturates the QFI are said to be quantum optimal. We will illustrate this point with the case of estimating the transverse separation of two incoherent sources in the image plane, which is the core of this thesis.

Measuring the intensities in the pixel mode basis with a CCD camera, i.e. performing direct imaging, as it is commonly implemented in passive imaging contexts, is known to have a low sensitivity when estimating short separations, but high sensitivities for large separations. This is what is conveyed by Rayleigh's criterion (see section 3.1).
However, in the parameter estimation framework, when deriving the QFI for separation estimation (see section 2.5), we find that the QFI is independent of the source separation. The derivation of the Fisher information for direct imaging confirms what is observed experimentally, that direct imaging is a sub-optimal measurement for estimating short separations, and therefore optimal measurements need to be developed in this range.
To saturate the QFI for short separations, Tsang *et al.* suggested performing SPADE with HG modes [Tsang 2016]. Indeed, the Fisher information for SPADE - determined in section 2.5 - saturates the QFI for all separations. Consequently, SPADE is an optimal measurement for separation estimations.

2.2.3 Optimal estimators

Several estimation approaches are available, an overview can be found in [Kay 1993]. Some will perform better than others depending on the parameter of interest and the complexity of the data model.
The Cramér-Rao bound (see eq. (2.5)) provides a lower bound for the sensitivity of the estimation. An estimator is said to be efficient when saturating the Cramér-Rao bound. Such an estimator, however, may not exist, especially when dealing with small data sets.
We present two estimators that are commonly used: the maximum likelihood estimator and the method of moments.

Maximum likelihood estimator

The maximum likelihood estimator is very popular as it is always asymptotically efficient. This is based on the assumption that the probability distribution function is known $p(\mathbf{x}|\theta)$, and provides efficient estimators for large data sets. The procedure is the following: for a fixed data set $\mathbf{x}$, the maximum likelihood estimator $\tilde{\theta}$ is the value of the parameter θ that maximizes the likelihood function $\mathcal{L}(\theta|\mathbf{x}) = \prod_i p(x_i|\theta)$. Unfortunately, this method often requires large data sets and becomes laborious to implement in a multiparameter scenario.

Method of moments

In the method of moments approach, the probability distribution function does not need to be completely known. Instead, from the measured observable $\hat{X}$, a calibration curve $\langle \hat{X} \rangle = h(\theta)$ has to be built, theoretically or experimentally, beforehand. We then perform μ measurements which give the results $\{x_i\}$ and the mean value $\overline{x_\mu}$. The estimator $\tilde{\theta}$ is given by the value of the parameter θ for which $\overline{x_\mu} = \langle \hat{X} \rangle$. In other words, the calibration curve is inverted, we have $\tilde{\theta} = h^{-1}(\overline{x_\mu})$ and the variance

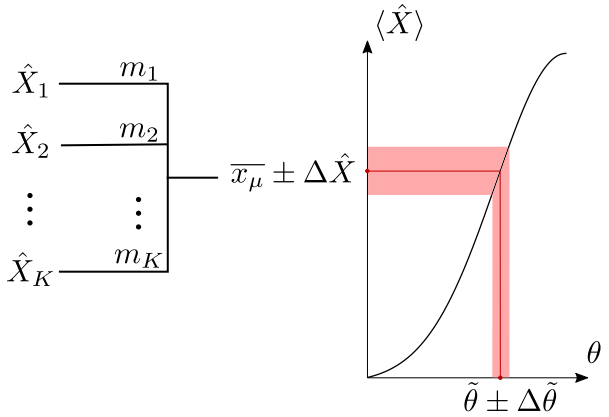

FIGURE 2.3: Illustration of the method of moments. The measured mean values of the available observables are linearly combined, with the optimal coefficient given by eq. (2.47). This allows the building of a calibration curve that is inverted to estimate the parameter.

is given, from the error propagation formula, by

$$\Delta^2\tilde{\theta} = \frac{\chi^2[\theta, \hat{X}]}{\mu} \qquad \text{with} \qquad \chi^2[\theta, \hat{X}] = \frac{\Delta^2\hat{X}}{(\partial_\theta\langle\hat{X}\rangle)^2}. \tag{2.44}$$

The quantity $\chi^2[\theta, \hat{X}]$ obeys the chain of inequalities

$$\chi^{-2}[\theta, \hat{X}] \leq I_F[\theta, \hat{X}] \leq I_Q[\theta]. \tag{2.45}$$

This approach, based on the central limit theorem is simple to implement but, as shown in eq. (2.45), it is not optimal in general. It could, however, be used as a starting point for an efficient estimator.

The method of moments can be extended to a more general situation where K observables $\hat{\mathbf{X}} = (\hat{X}_1, ..., \hat{X}_K)^T$ are accessible [Gessner 2019; Sorelli 2021b; Sorelli 2021a]. Their linear combination is given by $\hat{X}_\mathbf{m} = \mathbf{m}^T\,\hat{\mathbf{X}}$, where $\mathbf{m} = (m_1, ..., m_K)^T$ is the coefficient vector, as illustrated in fig. 2.3. An analytical optimization over all possible linear combinations can be performed and it results in the optimized sensitivity:

$$M[\theta, \hat{\mathbf{X}}] = \max_\mathbf{m} \chi^{-2}[\theta, \mathbf{X}_\mathbf{m}] = \mathbf{D}[\theta, \hat{\mathbf{X}}]^T\Gamma[\theta, \hat{\mathbf{X}}]^{-1}\mathbf{D}[\theta, \hat{\mathbf{X}}], \tag{2.46}$$

where $\mathbf{D}[\theta, \hat{\mathbf{X}}] = \frac{\partial\langle\hat{\mathbf{X}}\rangle}{\partial\theta}$ is the derivative vector. Moreover, this sensitivity is obtained for $\mathbf{m} = \tilde{\mathbf{m}}$ with

$$\tilde{\mathbf{m}} = \eta\Gamma[\theta, \hat{\mathbf{X}}]^{-1}\mathbf{D}[\theta, \hat{\mathbf{X}}], \tag{2.47}$$

where η is a normalization constant. The derivation of eqs. (2.46) and (2.47) is given in appendix B. For our problem of source separation estimation, the method-of-moment sensitivity saturates the first inequality of eq. (2.45).

2.3 Modeling point-like objects imaged by diffraction-limited optical systems

2.3.1 Point-spread function

Along this work, we examine the situation where point-like objects like stars or fluorescent molecules are imaged by a diffraction-limited linear optical system. The imaging system is characterized by its point-spread function (PSF), which gives the image function of perfect point sources.
We consider shift-invariant imaging systems, i.e. the point spread function is independent of the position in the object plane. We also assume there is no distortion, so that the image plane coordinates (u, v) are linearly related to the object plane coordinates (x, y) with the magnification factor $\mathcal{M}$: $(u, v) = (\mathcal{M}x, \mathcal{M}y)$. The PSF $h(u, v, x, y, t)$ links the field in the object plane $E_o(x, y, z_o, t)$ to the field in the image plane $E_i(u, v, z_i, t)$ [Goodman 2000]:

$$E_i(u, v, z_i, t) = \iint \mathrm{d}x\mathrm{d}y \; h(u, v, x, y) E_o(x, y, z_o). \tag{2.48}$$

For point-like objects, it is generally admitted that the spatial modes of the field in the image plane are directly given by the PSF.
Typical point-spread functions for diffraction-limited optical systems involve Bessel functions or Zernike polynomials [Racine 1996; Thompson 2002; Braat 2008]. The 2D Gaussian function is a good approximation of the PSF of diffraction-limited imaging systems and is usually chosen for modeling diffraction-limited optical systems [Cheezum 2001; Zhang 2007; Stallinga 2010; Chao 2016; Aniano 2011; Jarvis 2020]. This is also our choice for this work.

2.3.2 Beamsplitter model for the propagation through a diffraction-limited optical system

The previous subsection describes the evolution of the modes of the electromagnetic field through a diffraction-limited imaging system. We are now interested in the evolution of the associated field operators.
The finite aperture of the optical system and the diffraction introduce some losses and we note κ the transmissivity of the imaging system. The optical system can thus be treated as a beamsplitter with the field of interest $\hat{a}_{\text{in}}$ at one input and vacuum $\hat{v}$ at the other [Lupo 2016; Sorelli 2021a]. Using eq. (1.143), the field operator of the output field is

$$\hat{a}_{\text{out}} = \sqrt{\kappa}\hat{a}_{\text{in}} + \sqrt{1-\kappa}\hat{v}. \tag{2.49}$$

This equation will used in the model for two-source separation estimation in section 2.5.

2.3.3 Poissonian photodetection model

In sections 2.4 and 2.5, we derive the Fisher information for several measurements for beam displacement and source separation estimations. As described in section 2.1.2, the computation of the Fisher information requires the probability distribution of the measurement results conditioned on the value of the parameter.
In this work, we assume that there are no correlations or bunching[8] effects between the detected photons, i.e. that all the detected photons are independent. Therefore, the detection events follow Poissonian statistics. This describes coherent states but also faint sources for which the number of detected photons during the coherence time is smaller than one. This is motivated by the high losses of the imaging systems which results in Poissonian photodetection processes in the image plane [Chao 2016; Zmuidzinas 2003].
Due to the Poissonian distribution, there is no multiphoton coincidence in the image plane, and only the single-photon detection events have to be taken into account for the probability distribution of the measurement results. It is, therefore, possible to equate the probability distribution to the intensity profile, which simplifies the calculation of the Fisher information.

2.4 Beam displacement estimation

This section illustrates the previous concepts in the particular case of beam displacement estimation. It is, however, not only a pretext to have fun with some metrological quantities. In order to assess our source separation estimation during the experimental procedure, we estimate the position of each source individually with a quadrant detector. Therefore, this section gives us the opportunity to show that this measurement is almost optimal for beam displacement estimation.

2.4.1 Modeling beam displacement

We want to estimate the transverse displacement x_0 of a Gaussian beam, with a waist w_0, in the image plane, assumed to be at the position of the waist $z = z_0$. The spatial profile of the beam is defined by $u_{00}(\mathbf{r} - \mathbf{r}_0)$ given by eq. (1.23), where the displacement is along the x-axis without loss of generality, i.e. $\mathbf{r_0} = (x_0, 0)$, as illustrated in fig. 2.4(a).
This mode is populated with a thermal state with mean photon number N.

2.4.2 Quantum Fisher information

We present the results from [Sorelli 2023] for beam displacement estimation. This is a single-mode situation for which the initially populated mode is Gaussian, i.e. $u_0[x_0](\mathbf{r}) = u_{00}(\mathbf{r} - \mathbf{r}_0)$. Since the mode $u_0[x_0](\mathbf{r})$ is initially populated with a thermal state, the QFI is only given by the single-mode covariance matrix contribution of

[8] No bunching means that the intensity fluctuations are the shot noise.

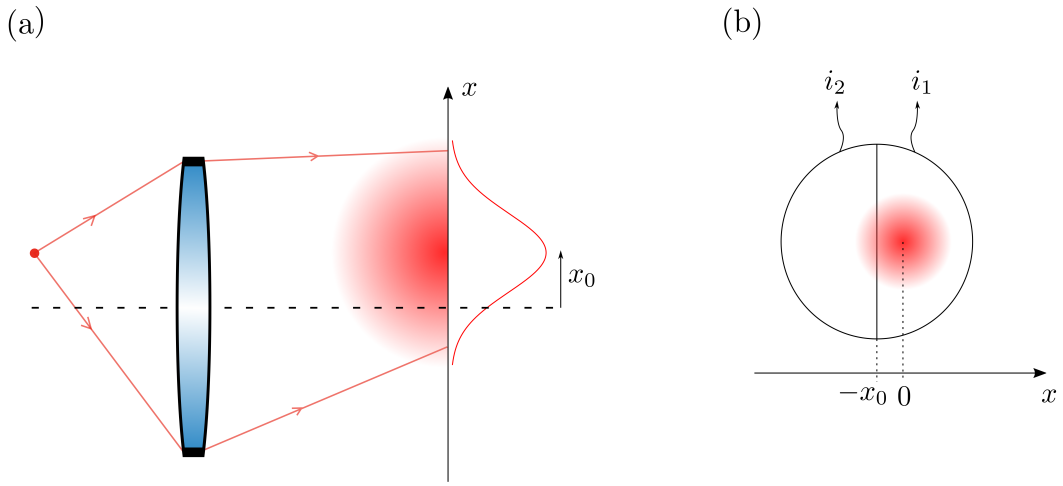

FIGURE 2.4: (a) Gaussian beam displaced along the x-axis with a transverse displacement x_0 in the image plane. (b) A quadrant detector, used in a split configuration, is composed of two pixels, measuring the intensities i_1 and i_2.

eq. (2.42), with $V_1 = (2N+1)\mathbb{1}_2$ and $\nu = 2N+1$ its symplectic eigenvalues:

$$I_Q[x_0] = \frac{1}{2}\frac{(a^{(2)}_{1,1})^2}{\nu^2-1} + \frac{1}{2}\frac{(a^{(2)}_{1,2})^2 + (a^{(2)}_{2,1})^2}{\nu-1}. \tag{2.50}$$

The normalized derivative mode is $u'_0[x_0](\mathbf{r}) = w_0\partial_{x_0}u_0[x_0](\mathbf{r})$. Hence, using eq. (2.41), we have

$$\begin{aligned} I_Q[x_0] &= \frac{1}{2}\frac{\mathrm{Tr}[A_2\,\partial_{x_0}V_1]^2}{\nu^2-1} + \frac{1}{w_0^2}\frac{\mathrm{Tr}[A_2(V_1-\mathbb{1}_2)]^2}{\nu-1} \\ &= \frac{(\partial_{x_0}N)^2}{N(N+1)} + \frac{4N}{w_0^2}. \end{aligned} \tag{2.51}$$

When the mean photon number does not depend explicitly on the displacement, as it is the case here since we consider small displacements, the normalized QFI for displacement estimation is the same as for coherent states [Sorelli 2023]

$$\frac{w_0^2}{N} I_Q[x_0] = 4. \tag{2.52}$$

2.4.3 Fisher information for quadrant detection

A relevant measurement for estimating the displacement of a beam is quadrant detection, used in a split configuration. The quadrant detector we consider is composed of two pixels that give access to two measured intensities i_1 and i_2, as illustrated in fig. 2.4(b). We assume that the pixel size of the detector is much larger than the waist of the beam.

We apply the method of moments to determine the sensitivity of the measurement. We assume the border between the two pixels to be at $x = -x_0$, as presented in fig. 2.4(b). The intensity profile on the quadrant detector is

$$\begin{aligned} I(\mathbf{r}) &= \langle \hat{E}^{(+)\dagger}(\mathbf{r}) \hat{E}^{(+)}(\mathbf{r}) \rangle \\ &\approx N |u_{00}(\mathbf{r})|^2 \\ &= N \frac{2}{\pi w_0^2} \exp\left(-\frac{x^2 + y^2}{2w_0^2} \right), \end{aligned} \tag{2.53}$$

where we used the expansion of the electric field over the Hermite-Gaussian mode basis $\{u_{nm}(\mathbf{r})\}$ and that higher-order modes $u_{nm\geq 1,1}(\mathbf{r})$ are in the vacuum state. Therefore, the normalized intensities on each pixel are

$$i_1 = \frac{1}{N} \int_{-\infty}^{+\infty} \mathrm{d}y \int_{-x_0}^{+\infty} \mathrm{d}x \; I(x,y) = \frac{1}{2} \left(1 + \operatorname{erf}\left(\frac{\sqrt{2} x_0}{w_0} \right) \right), \tag{2.54}$$

$$i_2 = \frac{1}{N} \int_{-\infty}^{+\infty} \mathrm{d}y \int_{-\infty}^{-x_0} \mathrm{d}x \; I(x,y) = \frac{1}{2} \left(1 - \operatorname{erf}\left(\frac{\sqrt{2} x_0}{w_0} \right) \right), \tag{2.55}$$

where the error function, denoted erf, is defined by

$$\operatorname{erf} z = \frac{2}{\sqrt{\pi}} \int_0^z e^{-t^2} \mathrm{d}t. \tag{2.56}$$

As we have a faint source, the two intensities are uncorrelated, leading to a diagonal covariance matrix

$$\Gamma_{mn} = \langle i_m i_n \rangle - \langle i_m \rangle \langle i_n \rangle = \frac{1}{N} i_m \delta_{mn}. \tag{2.57}$$

The sensitivity given by the method of moments (see eq. (2.46)) is then

$$M[x_0, \mathbf{i}] = \sum_{k=1}^{2} N \frac{1}{i_k} \left(\frac{\partial i_k}{\partial x_0} \right)^2. \tag{2.58}$$

Since we consider Poissonian statistics, the probabilities $p(x|x_0)$ associated with the measurement outcomes x are the measurement outcomes, conditioned on the parameter x_0, coincide with the normalized intensities i_k. Hence the normalized Fisher information eq. (2.6) for quadrant detection coincides with this sensitivity. Therefore, for small displacements, we have

$$\frac{w_0^2}{N} I_F^{QD}[x_0] = \sum_{k=1}^{2} \frac{w_0^2}{i_k} \left(\frac{\partial i_k}{\partial x_0} \right)^2 = \frac{8}{\pi}. \tag{2.59}$$

The optimal coefficients are given by eq. (2.47) and, for small displacements, we find

$$m_1 = \frac{1}{i_1} \frac{\partial i_1}{\partial x_0} = -m_2, \tag{2.60}$$

which demonstrates that the estimator $i_- = i_1 - i_2$ of quadrant detection is optimal.

Moreover, we observe that

$$I_F^{QD}[x_0] = \frac{2}{\pi} I_Q[x_0], \tag{2.61}$$

hence, quadrant detection is $2/\pi \approx 64\%$ efficient compared to the quantum limit. It is not a quantum optimal measurement for displacement estimation, contrary to homodyne detection in the HG_{01} mode [Delaubert 2006] or direct imaging [Chao 2016], but an efficient estimator for quadrant detection is easier to implement, which is why we use this measurement to certify our separation estimation measurements.

2.5 Source separation estimation

This thesis aimed to implement experimentally what has been shown theoretically a few years ago: SPADE associated with photodetection is a quantum optimal measurement for source separation estimation and shows higher sensitivity than direct imaging approaches [Tsang 2016]. This section recalls these theoretical results and the derivations for the QFI for source separation estimation, as well as the Fisher information for direct imaging and SPADE with photodetection.

2.5.1 Modeling source separation estimation

We consider two equally bright incoherent point sources separated by a transverse distance d, as illustrated in fig. 2.5. They are located at positions $\pm\mathbf{r}_0$, with $\mathbf{r}_0 = (\frac{d}{2}\cos\theta, \frac{d}{2}\sin\theta)$ and emit a total mean photon number equal to $2N$ in the spatial modes corresponding to the operators $\hat{s}_1$ and $\hat{s}_2$. They are described by the quantum state

$$\hat{\rho}_0 = \hat{\rho}_{s_1}(N) \otimes \hat{\rho}_{s_2}(N) \tag{2.62}$$

where $\hat{\rho}_a(N)$ is the density operator associated with a thermal state with mean photon number N in the mode associated with the operator $\hat{a}$. We consider the point spread function (PSF) of the imaging system to be a Gaussian mode $u_{00}(\mathbf{r})$ as defined in eq. (1.23). Therefore, the images of the sources through the diffraction-limited imaging system with transmissivity κ, are $u_{00}(\mathbf{r} \pm \mathbf{r}_0)$, associated with the operators $\hat{c}_{1,2}$

$$\hat{c}_{1,2} = \sqrt{\kappa}\hat{s}_{1,2} + \sqrt{1-\kappa}\hat{v}_{1,2}. \tag{2.63}$$

This expression is obtained from the beamsplitter model for the propagation [Lupo 2016] where the operators $\hat{v}_{1,2}$ are associated with auxiliary modes, which are in the vacuum state, given eq. (2.49). The modes $u_{00}(\mathbf{r} \pm \mathbf{r}_0)$ are not orthogonal for small separations, leading to resolution difficulties. To construct an orthonormal basis to represent the quantum electric field in the image plane, we introduce the orthonormal image modes:

$$u_\pm(\mathbf{r}, \mathbf{r}_0) = \frac{u_{00}(\mathbf{r}+\mathbf{r}_0) \pm u_{00}(\mathbf{r}-\mathbf{r}_0)}{\sqrt{2(1\pm\delta)}} \tag{2.64}$$

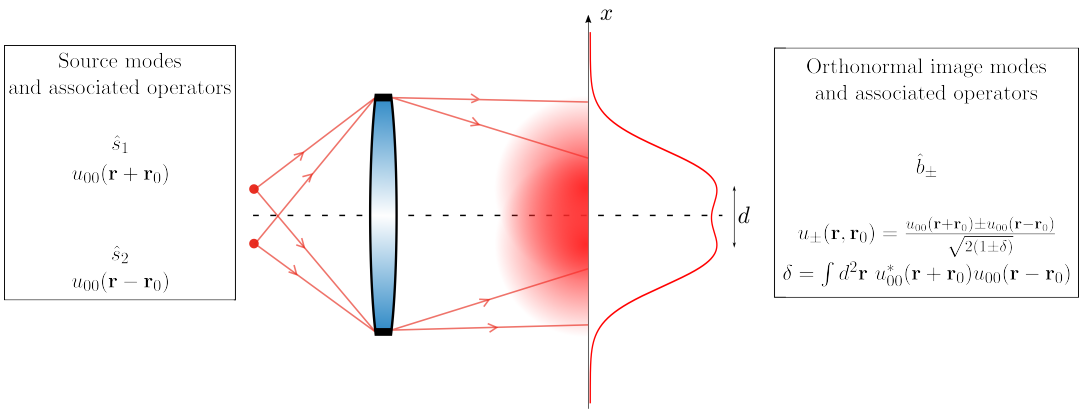

FIGURE 2.5: Two equally bright incoherent sources are separated by a distance d in the image plane.

where δ is the overlap between the source images

$$\delta = \int d^2\mathbf{r}\, u^*_{00}(\mathbf{r}+\mathbf{r}_0)u_{00}(\mathbf{r}-\mathbf{r}_0). \tag{2.65}$$

The symmetric and anti-symmetric modes $u_\pm(\mathbf{r})$ are associated to the operators $\hat{b}_\pm$

$$\hat{b}_\pm = \sqrt{\kappa_\pm}\hat{s}_\pm + \sqrt{1-\kappa_\pm}\hat{v}_\pm \tag{2.66}$$

with $\hat{s}_\pm = (\hat{s}_1 \pm \hat{s}_2)/\sqrt{2}$, $\hat{v}_\pm$ the operators associated to auxiliary modes which are in the vacuum and $\kappa_\pm = \kappa(1\pm\delta)$.

It is convenient to define an auxiliary mode basis $\{w_i(\mathbf{r})\}$ obtained by extending $w_0(\mathbf{r}) = u_+(\mathbf{r})$ and $w_1(\mathbf{r}) = u_-(\mathbf{r})$ to a complete orthonormal basis. Accordingly, for the field operators $\{\hat{b}_i\}$ associated with this basis, we have $\hat{b}_0 = \hat{b}_+$ and $\hat{b}_1 = \hat{b}_-$. The two modes $u_\pm(\mathbf{r})$ are populated with thermal states with mean photon numbers $N_\pm = N\kappa(1\pm\delta)$.

2.5.2 Quantum Fisher information

Several derivations of the QFI for source separation with thermal states can be found here [Tsang 2016; Lupo 2016; Nair 2016]. We choose to present one adapted from [Sorelli 2022; Sorelli 2023]. We assume without loss of generality that the separation is along the x-axis, so $\mathbf{r}_0 = (\frac{d}{2}, 0)$. The quadrature covariance matrix is

$$V_2 = \begin{pmatrix} (2N_+ + 1)\mathbb{1}_2 & 0 \\ 0 & (2N_- + 1)\mathbb{1}_2 \end{pmatrix}, \tag{2.67}$$

and the symplectic eigenvalues are

$$\nu_j = \begin{cases} 2N_+ + 1 & \text{for } j = 1, \\ 2N_- + 1 & \text{for } j = 2. \end{cases} \tag{2.68}$$

We note the initially populated modes

$$u_0[d](\mathbf{r}) = u_+(\mathbf{r}), \tag{2.69}$$

$$v_0[d](\mathbf{r}) = u_-(\mathbf{r}) \tag{2.70}$$

and their orthonormalized derivative modes are

$$u_0'[d](x) = \partial_d u_0[d](\mathbf{r})/\eta_u, \tag{2.71}$$

$$v_0'[d](x) = \partial_d v_0[d](\mathbf{r})/\eta_v, \tag{2.72}$$

for which the expressions of $\eta_u^2 = ||\partial_d u_0[d](\mathbf{r})||^2$ and $\eta_v^2 = ||\partial_d v_0[d](\mathbf{r})||^2$ are given in Appendix. Using eqs. (2.41) and (2.42), we obtain

$$I_Q[d] = \frac{1}{2}\frac{(a_{1,1}^{(2)})^2}{\nu_1^2-1} + \frac{1}{2}\frac{(a_{2,2}^{(2)})^2}{\nu_2^2-1} + \frac{(a_{1,3}^{(2)})^2}{\nu_1-1} + \frac{(a_{2,4}^{(2)})^2}{\nu_2-1}, \tag{2.73}$$

with

$$\begin{aligned}
a_{1,1}^{(2)} &= \mathrm{Tr}\left[A_{1,1}^{(2)}(\partial_d V_2)\right] = 2\sqrt{2}N\kappa(\partial_d\delta),\\
a_{2,2}^{(2)} &= \mathrm{Tr}\left[A_{2,2}^{(2)}(\partial_d V_2)\right] = 2\sqrt{2}N\kappa(\partial_d\delta),\\
a_{1,3}^{(2)} &= \mathrm{Tr}\left[A_{1,1}^{(2)}(V_2-\mathbb{1}_4)\eta_u\right] = \frac{N\kappa}{\sqrt{2}}(1+\delta)\eta_u,\\
a_{2,4}^{(2)} &= \mathrm{Tr}\left[A_{2,2}^{(2)}(V_2-\mathbb{1}_4)\eta_v\right] = \frac{N\kappa}{\sqrt{2}}(1-\delta)\eta_v.
\end{aligned} \tag{2.74}$$

Finally, the normalized QFI is

$$\frac{w_0^2}{2N\kappa}I_Q\left[\frac{d}{w_0}\right] = 1 - \left(\frac{d}{w_0}\right)^2 \frac{N\kappa(1+N\kappa)}{e^{\left(\frac{d}{w_0}\right)^2}(1+N\kappa)^2 - (N\kappa)^2}. \tag{2.75}$$

The QFI is represented in fig. 2.6 for different numbers of detected photons. For faint sources, i.e. $N\kappa \ll 1$, and, in general, for states with Poissonian statistics, the QFI is constant and equal to $\frac{2N\kappa}{w_0^2}$.

2.5.3 Fisher information for direct imaging

Direct imaging is the most standard measurement for source separation estimation, and imaging in general, in particular in microscopy or astronomy contexts [Roggemann 1997; Wizinowich 2000; Chao 2016]. It is, however, well-known that this measurement is not quantum optimal and provides poor sensitivities for small separations, i.e. smaller than the PSF width, due to the non-orthogonality of the two modes $u_{00}(\mathbf{r} \pm \mathbf{r_0})$. This effect is known as the Rayleigh curse [Tsang 2016]. We present here a derivation of the Fisher information for direct imaging to compare it to the QFI for source separation estimation and to the Fisher information for SPADE with photodetection. We consider faint sources, it is, therefore, possible to equate the probability

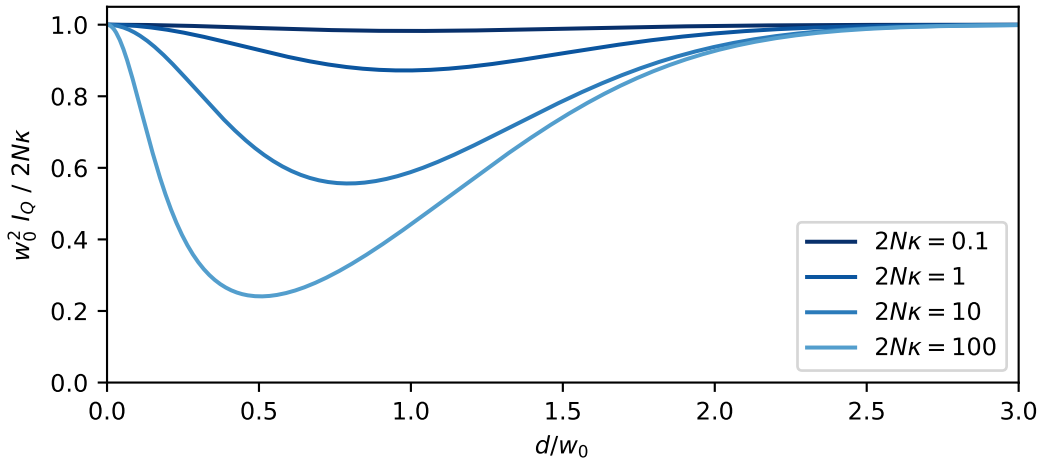

FIGURE 2.6: Normalized quantum Fisher information for source separation estimation for different mean number of detected photons $2N\kappa$. The dip for intermediary separations comes from the fact that, for this range, the only relevant information is in the HG_{10} mode but the intensity is high enough for the noise of the thermal state to reduce the sensitivity.

distribution function with the intensity profile. We assume the CCD detector is ideal, i.e. without any noise, no saturation, perfectly linear and with perfect quantum efficiency. In the limit of continuous direct imaging, where the pixels are infinitely small, the normalized Fisher information is given by [Tsang 2016; Sorelli 2021a]

$$\frac{w_0^2}{2N\kappa} I_F^{\mathrm{DI}}[d] = \frac{w_0^2}{2N\kappa} \int \frac{1}{I(\mathbf{r})} \left(\frac{\partial I(\mathbf{r})}{\partial d} \right)^2 d^2\mathbf{r}. \tag{2.76}$$

We can expand the electric field in the basis $\{w_k(\mathbf{r})\}$ defined in section 2.5.1, and use that all the higher-order modes $w_{k\geq 2}(\mathbf{r})$ are in the vacuum state. The intensity distribution in the image plane is

$$I(\mathbf{r}) = \langle \hat{E}^{(+)\dagger}(\mathbf{r}) \hat{E}^{(+)}(\mathbf{r}) \rangle = \sum_{i,j=\pm} u_i^*(\mathbf{r}) u_j(\mathbf{r}) \langle \hat{b}_i^\dagger \hat{b}_j \rangle, \tag{2.77}$$

where the field operators $\hat{b}_\pm$ are defined in eq. (2.66).
It can be shown that (see appendix C)

$$\begin{aligned} \langle \hat{b}_\pm^\dagger \hat{b}_\pm \rangle &= N\kappa(1 \pm \delta), \\ \langle \hat{b}_\pm^\dagger \hat{b}_\mp \rangle &= 0. \end{aligned} \tag{2.78}$$

Hence, the intensity distribution becomes

$$I(\mathbf{r}) = N\kappa(|u_{00}(\mathbf{r} + \mathbf{r}_0)|^2 + |u_{00}(\mathbf{r} - \mathbf{r}_0)|^2), \tag{2.79}$$

which is expected for incoherent sources. The Fisher information is plotted in fig. 2.8, along with the Fisher information for SPADE that will be derived in the next section and with the QFI. For small separations, i.e. $d/w_0 \ll 1$, the Fisher information can be analytically approximated as

$$\frac{w_0^2}{2N\kappa} I_F^{\mathrm{DI}}\left[\frac{d}{w_0}\right] = 2\left(\frac{d}{w_0}\right)^2 + \mathcal{O}\left(\left(\frac{d}{w_0}\right)^4\right). \tag{2.80}$$

We see in fig. 2.8 that the Fisher information for direct imaging saturates the QFI for large separations but goes to zero for small separations. This is what is known as Rayleigh's curse. This means that direct imaging is fundamentally not efficient when the sources are very close to each other and we need to perform another measurement to achieve higher sensitivities in this regime.

2.5.4 Fisher information for SPADE with photodetection

SPADE associated with photodetection has been proven to be a quantum optimal measurement for source separation estimation [Tsang 2016] when the sources have equal brightness and the centroid is aligned with the demultiplexing apparatus. We present the derivation of the Fisher information for an ideal SPADE scheme, i.e. with ideal photodetectors and ideal mode-decomposition, adapted from the Supplementary material of [Gessner 2020a].

We consider M photodetectors at the outputs of a SPADE detection scheme. For deriving the Fisher information eq. (2.6), we need to determine the conditional probabilities $p(x|d)$, where x are the measurement outcomes when detecting photons at the SPADE outputs. Since we consider a Poissonian photodetection process, as described in section 2.3.3, we can equate the normalized intensities $N_k/2N\kappa$ with the probabilities $p(x|d)$, so that the normalized Fisher information reads

$$\frac{w_0^2}{2N\kappa} I_F^{\mathrm{SPADE}}[d] = \frac{w_0^2}{2N\kappa} \sum_{k=1}^{M} \frac{1}{N_k}\left(\frac{\partial N_k}{\partial d}\right)^2, \tag{2.81}$$

where N_k is the mean photon number detected at the detector k.

In the image plane, we consider the measurement in the ideal Hermite-Gaussian mode basis $\{u_k(\mathbf{r})\}$, with $k = (n, m)$, defined in eq. (1.25), associated to the operators $\{\hat{a}_k\}$. The basis change eqs. (1.9) and (1.82) gives the relation

$$\hat{a}_k = \sum_{k,\ell=\pm} g_{k\ell}\hat{b}_\ell \qquad \text{with} \qquad g_{k\ell} = \int \mathrm{d}^2\mathbf{r}\, u_k^*(\mathbf{r}) w_\ell(\mathbf{r}). \tag{2.82}$$

Using eq. (2.64), we obtain

$$g_{k\pm} = \frac{\beta_{nm}(\mathbf{r}_0) \pm \beta_{nm}(-\mathbf{r}_0)}{\sqrt{2(1\pm\delta)}}, \tag{2.83}$$

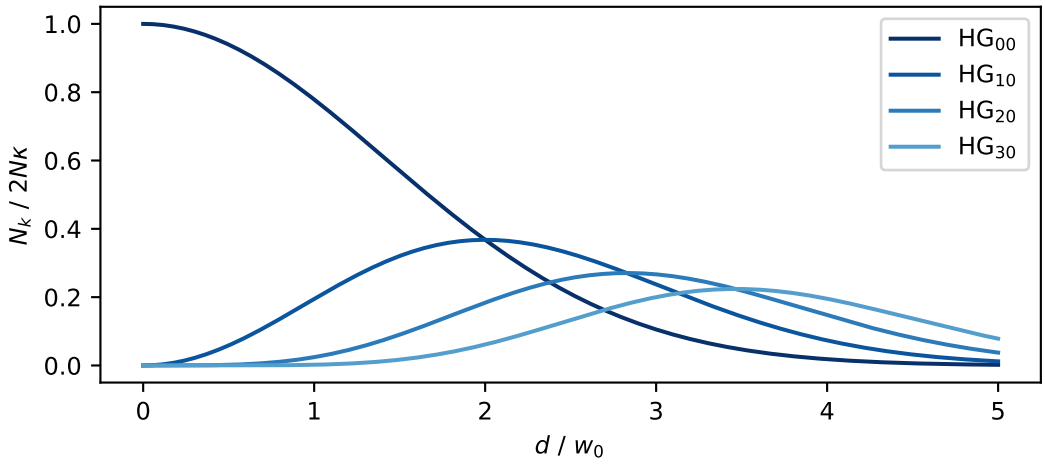

FIGURE 2.7: Normalized intensity in each mode, for $\theta = 0$.

with

$$\beta_{nm}(\pm\mathbf{r}_0) = \int \mathrm{d}^2\mathbf{r}\; u^*_{nm}(\mathbf{r}) u_{00}(\mathbf{r} \pm \mathbf{r}_0). \tag{2.84}$$

With eq. (2.78), the mean photon number in each measured mode is then

$$N_k = \langle \hat{a}^\dagger_k \hat{a}_k \rangle = \sum_{i,j=\pm} g^*_{ki} g_{kj} \langle \hat{b}^\dagger_i \hat{b}_j \rangle = N\kappa(|\beta_{nm}(\mathbf{r}_0)|^2 + |\beta_{nm}(-\mathbf{r}_0)|^2). \tag{2.85}$$

From eqs. (1.25) and (2.84), we obtain

$$\beta_{nm}(\pm\mathbf{r}_0) = \frac{1}{\sqrt{n!m!}} \left(\frac{\pm d}{2w_0}\right)^{n+m} (\cos\theta)^n (\sin\theta)^m e^{-\frac{1}{2}\left(\frac{\pm d}{2w_0}\right)^2}. \tag{2.86}$$

Hence,

$$N_k = 2N\kappa\beta_{nm}(\mathbf{r}_0)^2, \tag{2.87}$$

which is presented in fig. 2.7 for 4 modes. Assuming that all HG modes $u_{n,m}$ with $0 \leq n, m \leq Q$ are measured, and substituting in eq. (2.81), we have

$$\begin{aligned} \frac{w_0^2}{2N\kappa} I_F[d] &= \sum_{n,m=0}^{Q} \frac{w_0^2}{\beta_{nm}(\mathbf{r}_0)^2} \left(\frac{\partial \beta_{nm}(\mathbf{r}_0)^2}{\partial d}\right)^2 \\ &= \sum_{n,m=0}^{Q} \frac{4w_0^2}{d^2} \left(n + m - \left(\frac{d}{2w_0}\right)^2\right)^2 \beta_{nm}(\mathbf{r}_0)^2. \end{aligned} \tag{2.88}$$

Finally, the normalized Fisher information for SPADE reads

$$\frac{w_0^2}{2N\kappa} I_F^{\mathrm{SPADE}}\left[\frac{d}{w_0}\right] = \sum_{n,m=0}^{M} \frac{\left(\frac{d}{w_0}\right)^{2(n+m-1)}}{n!m!} \left(n + m - \left(\frac{d}{w_0}\right)^2\right)^2 (\cos\theta)^{2n} (\sin\theta)^{2m} e^{-\left(\frac{d}{w_0}\right)^2}. \tag{2.89}$$

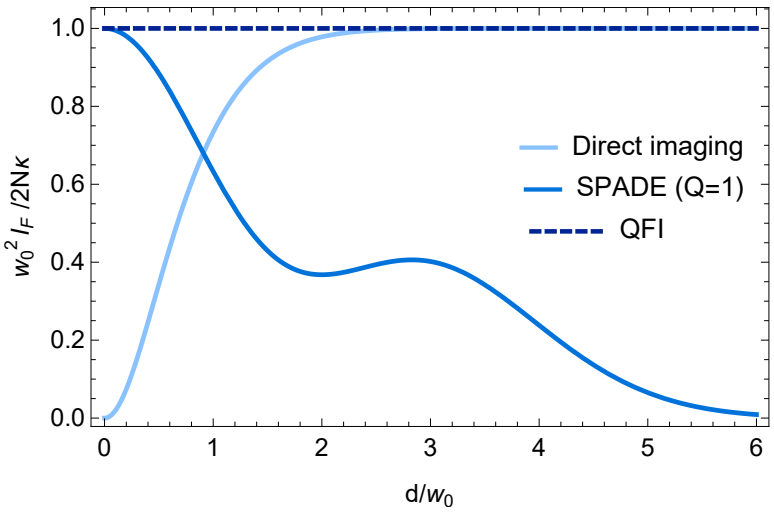

FIGURE 2.8: Normalized Fisher information for SPADE performed with the modes HG_{00}, HG_{01} and HG_{10}, normalized Fisher information with direct imaging and QFI of the separation of Poissonian sources, for $\theta = \pi/6$.

The Fisher information for SPADE performed with only three modes (HG_{00}, HG_{01} and HG_{10}) is represented in fig. 2.8, along with the QFI and the Fisher information for direct imaging. We note that contrary to direct imaging, in the limit of very small separations ($d/w_0 \to 0$) or an infinite number of measured modes ($Q \to \infty$), the Fisher information of ideal SPADE saturates the QFI:

$$\begin{aligned} \lim_{d/w_0 \to 0} \frac{w_0^2}{2N\kappa} I_F^{\text{SPADE}}\left[\frac{d}{w_0}\right] &= 1, \\ \lim_{Q \to \infty} \frac{w_0^2}{2N\kappa} I_F^{\text{SPADE}}[d] &= 1. \end{aligned} \tag{2.90}$$

This means that, in an ideal scenario, SPADE is a quantum optimal measurement and gives access to a much higher sensitivity than direct imaging, enabling it to beat Rayleigh's curse.
The behavior of the Fisher information of SPADE for different values of Q (where $0 \leq n, m \leq Q$) is compared in fig. 2.9. The Fisher information saturates the QFI for a longer range of separations when Q increases (with $0 \leq n, m \leq Q$). This comes from the fact that higher-order HG modes have a larger spatial extension and are, therefore, more sensitive to larger separations. Consequently, in order to have the best sensitivity over a large range of separations, many modes have to be measured and this has to be taken into account for the estimation using the method of moments adapted to several observables.

Finally, we plot in fig. 2.10 the QFI, Fisher information for SPADE with mode HG_{10} and Fisher information for direct imaging when sources are aligned with one of the axes of the demultiplexing apparatus, i.e. for $\theta = 0$, as it is the case in our experimental configuration (see section 3.4.5). This graph shows that for small separations,

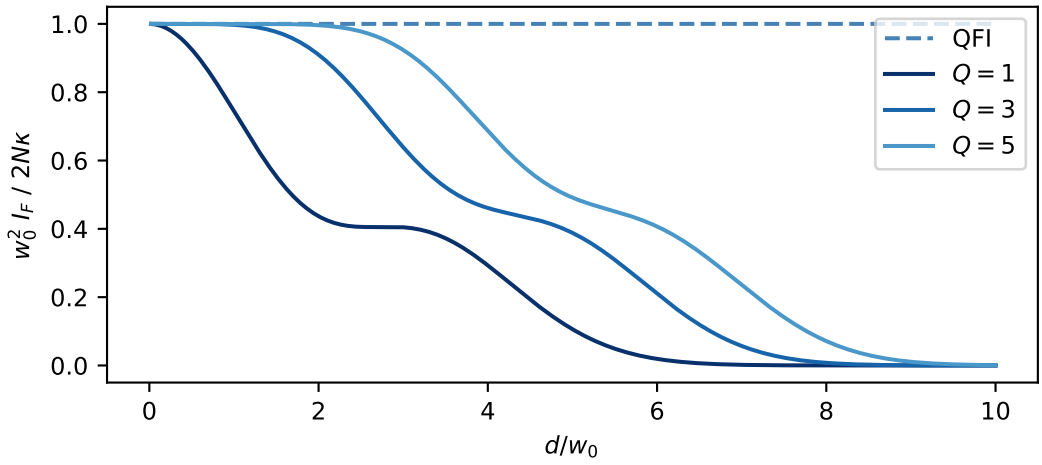

FIGURE 2.9: Normalized Fisher information for SPADE, for $\theta = \pi/6$.

measuring the intensity only in the mode HG_{10} saturates the QFI.

2.5.5 From the Fisher information to the standard deviation of the estimation

From the quantum Cramér-Rao bound (eq. (2.17)), the inverse of the QFI can be seen as the theoretical minimum variance of the estimator, and the inverse of the Fisher information as the theoretical minimum variance for a given measurement. Since metrology is concerned with the noise sources of the measurement and their influence on the noise of the estimation, it is sometimes more convenient to visualize the standard deviation of the estimation as a function of the separation, and this is what is represented in fig. 2.11, using eqs. (2.75), (2.80) and (2.89) for $2N\kappa = 10^6$ detected photons.

2.5.6 Minimal resolvable distance

Signal-to-noise ratio

The signal-to-noise ratio (SNR) is a measure used in signal processing to compare the level of signal with the level of noise. It is often expressed in dB. In this work, we define the SNR as being the ratio between the mean value of the estimator $\langle \tilde{d} \rangle$, which corresponds to the true value of the parameter since we consider unbiased estimators, to the standard deviation of the estimator $\Delta\tilde{d}$:

$$SNR = \frac{\langle \tilde{d} \rangle}{\Delta \tilde{d}}. \tag{2.91}$$

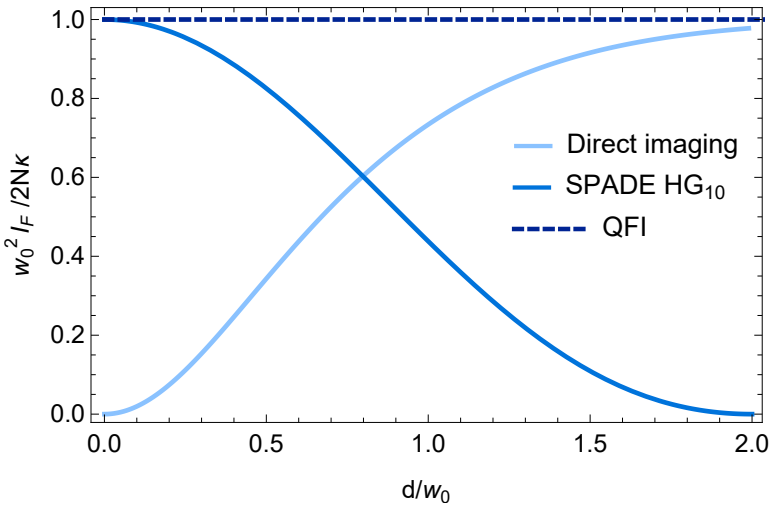

FIGURE 2.10: Normalized Fisher information for SPADE performed with the HG_{10} mode, normalized Fisher information with direct imaging and QFI of the separation of Poissonian sources, for $\theta = 0$.

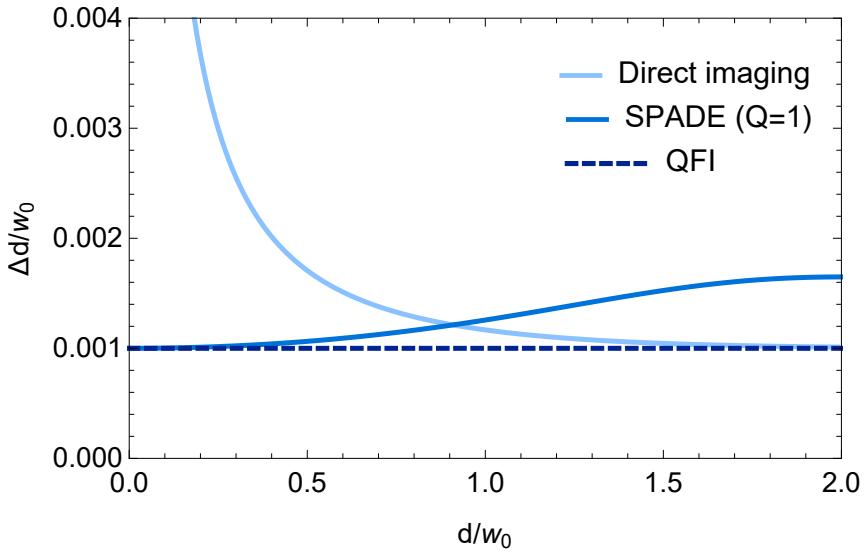

FIGURE 2.11: Standard deviation of the separation estimation associated with the QFI and the FI for SPADE and direct imaging for $\theta = \pi/6$ and $2N\kappa = 10^6$ detected photons.

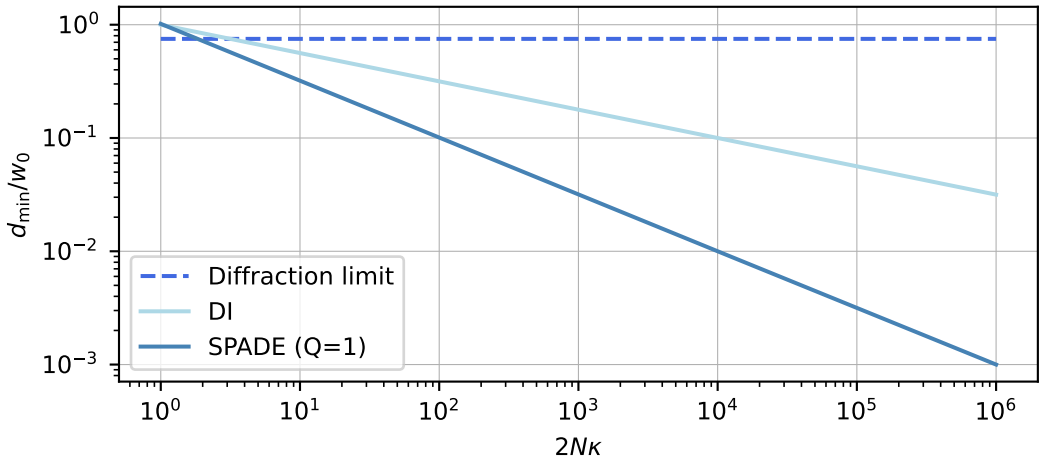

FIGURE 2.12: Theoretical minimum resolvable distance as a function of the number of detected photons for ideal direct imaging and ideal SPADE. The limit established by Rayleigh is also plotted on the graph. The minimum resolvable distance for ideal SPADE is exactly the one given by the QFI, following the scaling $(2N\kappa)^{-1/2}$ and the scaling for ideal direct imaging is $(2N\kappa)^{-1/4}$.

Minimal resolvable distance

The minimal resolvable distance $d_{\min} = \langle \tilde{d} \rangle_{\min}$ is defined as

$$\frac{\langle \tilde{d} \rangle_{\min}}{\Delta d} = 1. \tag{2.92}$$

Since, when the Cramér-Rao bound is saturated, we have

$$\Delta \tilde{d} = \frac{1}{\sqrt{2N\kappa \cdot I_F[d]}}, \tag{2.93}$$

the theoretical minimal resolvable distance can be determined by solving

$$d_{\min} \sqrt{I_F[d_{\min}]} = \frac{1}{\sqrt{2N\kappa}}, \tag{2.94}$$

where $2N\kappa$ is the mean number of detected photons and $I_F[d]$ is the Fisher information of a single photon. The minimal resolvable distance as a function of the number of incident photons is presented in fig. 2.12 for ideal SPADE and ideal direct imaging. These two measurements display different scalings, the minimal resolvable distance varies as $(2N\kappa)^{-1/4}$ for direct imaging while the behavior for SPADE reaches the one associated with the QFI as $(2N\kappa)^{-1/2}$, which enables to reach smaller separations with the same number of photons. We also represented the one corresponding to the diffraction limit, which will be established in chapter 3.

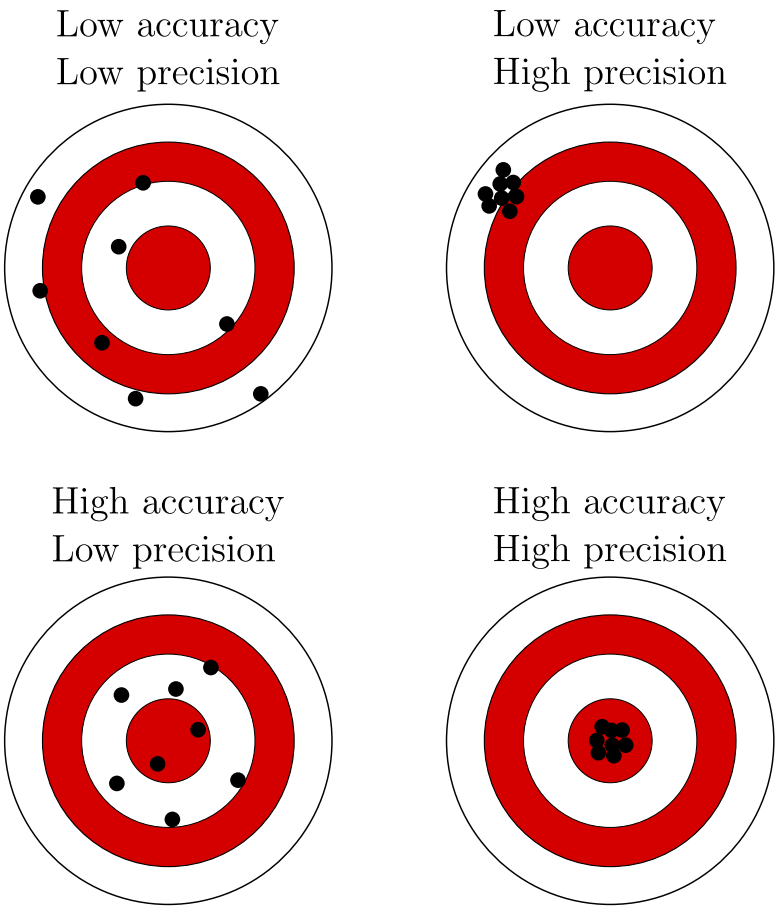

FIGURE 2.13: Accuracy vs precision.

2.6 Accuracy, precision, sensitivity and resolution

In this section, we aim to provide clarity on concepts commonly used in metrology contexts, which are occasionally used interchangeably.
Accuracy refers to the bias of the estimation, i.e. whether the mean value of the estimator is close to the true value of the parameter. A high accuracy means that the bias is narrow, and vice versa. In the case of unbiased estimators, the accuracy is perfect.
Precision describes the reproducibility of the estimation. Sensitivity corresponds to the smallest variation that is detectable, it is linked to the standard deviation of the estimation. A high sensitivity coincides with a low standard deviation, which is what we aim for. Since we are primarily concerned with unbiased estimators, sensitivity is the key figure of merit for benchmarking estimations in this thesis. Throughout this thesis, we may interchangeably use the terms 'precision' or 'sensitivity,' with a clear preference for 'sensitivity'. The distinction between accuracy and precision is illustrated in fig. 2.13.
Lastly, the term 'resolution', explored in the following chapter, quantifies the performance of imaging systems. It refers to the smallest separation between two sources at which they remain distinguishable, as defined in section 2.5.6.

Chapter 3

Surpassing Rayleigh's limit

Contents

Imaging systems are designed to increase the information available to observers beyond what can be discerned with the naked eye. In numerous contexts, this additional information refers to acquiring finer details about the observed object, which is the meaning we adopt in this work. The extent to which details can be extracted from an optical image is quantified by the resolution of the imaging systems. This chapter serves as a bridge between the historical limits imposed by diffraction on resolution and our experiment, which contributes to the field of separation estimation.

The first section revisits the famous Rayleigh criterion, while the second section presents imaging techniques employed in microscopy, astronomy, and remote sensing to surpass the diffraction limit, often referred to as "super-resolution" techniques, and demonstrates how separation estimation can be a tool to understand the fundamental limits of these imaging tasks. Section 3 provides an overview of the current state of the art concerning the experiments conducted before or during this work on the estimation of the separation between two incoherent optical point sources. This review allows us to establish the requirements for our experimental setup presented in Section 4, along with an overview of the setup. Finally, Section 5 is dedicated to the sources we employed, with a particular focus on the generation of thermal states.

3.1 Historical sensitivity limit for separation estimation

The resolving power is a common metric for benchmarking optical imaging devices, such as telescopes and microscopes. It quantifies the minimal resolvable distance between to imaged point sources, i.e. the separation below which it becomes impossible to tell whether there are one or two distinct sources. When a point source is imaged with a circular aperture, assuming there are no aberrations, it forms an Airy pattern, resulting in a blurred image due to diffraction. If two point sources are too closely situated, their images overlap, making it challenging to differentiate them. Several criteria for establishing a resolution limit were introduced between the late 19th and early 20th centuries, including Abbe's [Abbe 1873], Sparrow's [Sparrow 1916] and Rayleigh's [Rayleigh 1879] criteria. While these criteria define slightly different limits, they are essentially equivalent. Consequently, we will only elaborate on Rayleigh's criterion, which is perhaps the most renowned and continues to be widely employed for assessing the resolution of optical instruments.

Lord Rayleigh investigated the image formation of microscopes and telescopes. The resolution limit he established in his work [Rayleigh 1879] states that two point-like sources can be resolved if the first minimum of the Airy pattern formed by the image of one source coincides with the maximum of the Airy pattern of the image of the second source. This is illustrated in fig. 3.2. In other words, the resolving power of the optical device is set by the radius of the Airy disk it forms for a single point source:

$$d_{\text{min}}^{\text{Rayleigh}} \simeq 0.61 \frac{\lambda}{\text{NA}}. \tag{3.1}$$

This criterion is written in terms of the wavelength of the incident light λ and of the numerical aperture NA of the optical apparatus. The size of the image is then usually adapted to the size of the photodetector, typically a CCD camera, with a secondary linear-optical system. In the paraxial approximation, the ratio between the radius of the beam and the distance between the sources is preserved. Consequently, it can be more convenient to express Rayleigh's limit in terms of the size of the PSF. As explained in chapter 2, the Airy disk can be efficiently approximated by a Gaussian function [Zhang 2007]. Fitting an Airy pattern $I_{\text{PSF}}(r) = \left(\frac{2J_1(ar)}{ar}\right)^2$ where $a = \frac{2\pi \text{NA}}{\lambda}$ and J_1 is the first-order Bessel function of the first kind, with a Gaussian intensity

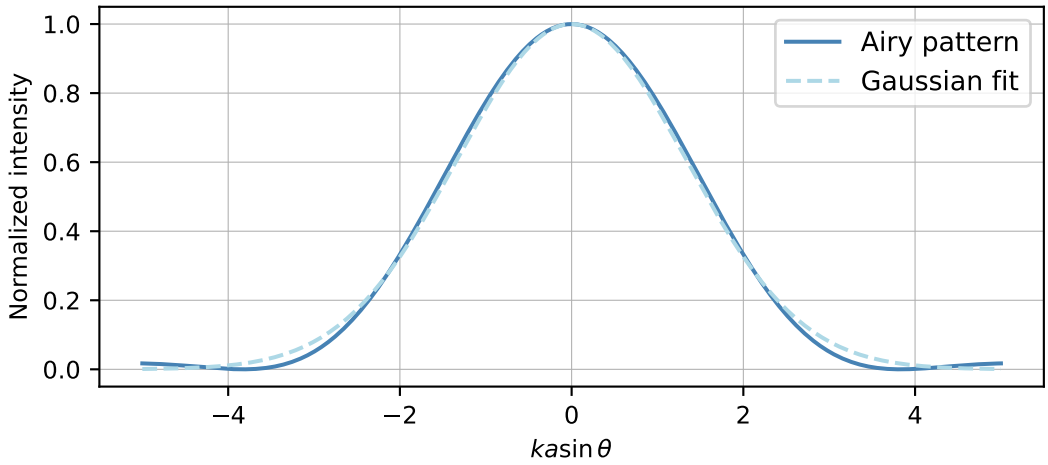

FIGURE 3.1: Airy pattern fitted with a Gaussian function.

distribution $I_G(r) = \exp\left(-\frac{2r^2}{w_0^2}\right)$ (see fig. 3.1), we find [Thomann 2002]

$$w_0 \simeq 0.42\frac{\lambda}{\mathrm{NA}}. \tag{3.2}$$

We then write Rayleigh's limit in terms of the waist of the PSF w_0:

$$d_{\min}^{\text{Rayleigh}} \simeq 1.5 w_0. \tag{3.3}$$

As mentioned earlier, other resolution criteria established at the same period are equivalent to Rayleigh's, with slightly different coefficients[1]. However, these criteria are inherently subjective, as evident from their formulation. They rely on the resolving power of the human eye, given that sensitive photodetectors using semiconductor materials only emerged in the late 20th century. It is worth mentioning that they are independent of the incident optical power because the eyes act as photodetectors that saturate relatively easily. Nevertheless, these resolution limits, which are of the

[1] Abbe's criterion [Abbe 1873]. The imaging resolution is limited to half a wavelength normalized by the numerical aperture of the system

$$d_{\min}^{\text{Abbe}} \simeq 0.5\frac{\lambda}{NA}. \tag{3.4}$$

Sparrow's criterion [Sparrow 1916], mostly used in astronomy. Two sources can be distinguished when the derivative of the total intensity around zero is negative

$$d_{\min}^{\text{Sparrow}} \simeq 0.47\frac{\lambda}{NA}. \tag{3.5}$$

In terms of the waist of the PSF, they become

$$\begin{aligned} d_{\min}^{\text{Abbe}} &\simeq 1.2 w_0, \\ d_{\min}^{\text{Sparrow}} &\simeq 1.1 w_0. \end{aligned} \tag{3.6}$$

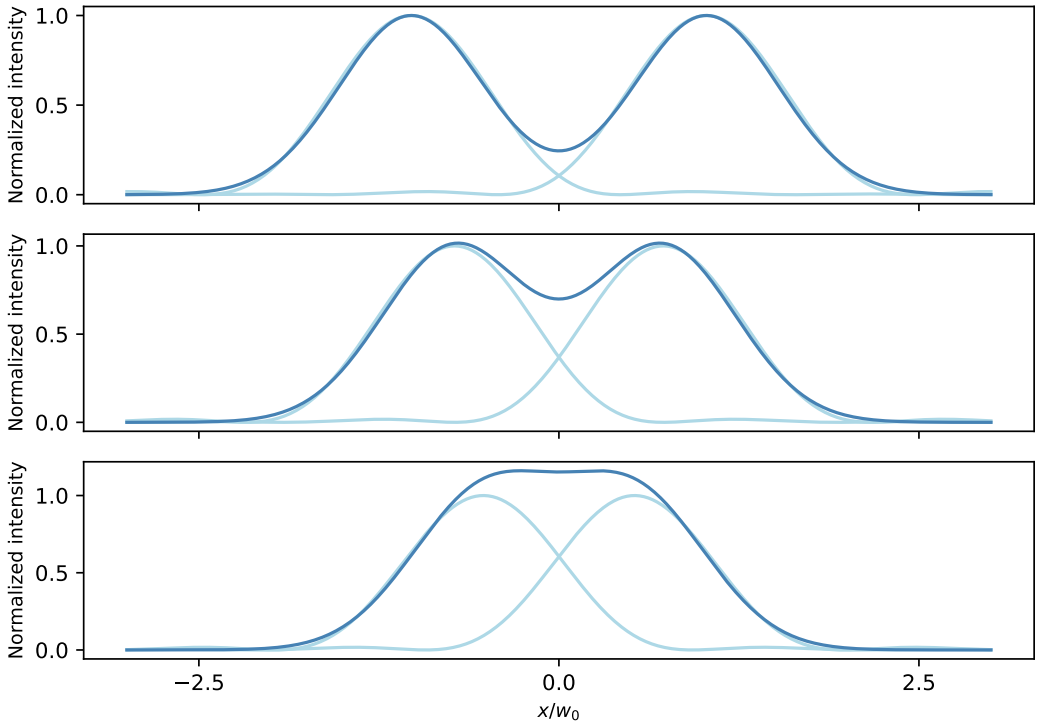

FIGURE 3.2: Resolution limit. (top) The two sources are separated by a distance larger than $d_{\text{min}}^{\text{Rayleigh}}$ and are distinguishable. (middle) The two sources are separated by exactly $d_{\text{min}}^{\text{Rayleigh}}$. (bottom) The two sources are separated by a distance shorter than $d_{\text{min}}^{\text{Rayleigh}}$ and are therefore not resolvable.

order of the size of the PSF, remain relevant to benchmark optical systems. This is because state-of-the-art instruments typically exhibit resolutions within this order of magnitude.

3.2 Super-resolution techniques in microscopy and astronomy

We use the term "super-resolution techniques" to describe imaging devices that enable resolutions surpassing Rayleigh's limit, i.e. where the minimum resolvable distance is smaller than $1.5w_0$. Over the last decade, numerous such techniques have emerged in the fields of microscopy and astronomy, and this subject remains an active area of research. This section aims at providing an overview of the current state of the art, without attempting to comprehensively cover all the techniques that exist currently.

3.2.1 Microscopy

Conventional fluorescence microscopy techniques, consisting of collecting the light emitted by fluorophores introduced in the sample after excitation, present a typical resolution around 200 nm. Super-resolution techniques in microscopy that overcome the diffraction limit can be classified into near-field and far-field techniques [Huang 2009].

Near-field microscopy

Non-optical techniques such as atomic force microscopy [Binnig 1986] and electron microscopy [Franken 2017], are able to resolve structures as fine as 1 nm in size. However, these approaches are invasive, as they require close interaction with the sample or placing it in a high vacuum [Steed 2012], and do not allow observation of objects in their native environment.
Near-field optical techniques were also developed. They are known as photon tunneling microscopy [Guerra 1990], near-field scanning optical microscopy [Hecht 2000], tip-enhanced near-field optical microscopy [Hartschuh 2008], and photon scanning tunneling microscopy [Ohtsu 1995] and use a probe to record the information of the evanescent waves that decay exponentially with the distance away from the sample [Goodman 2004].
These techniques reach resolutions of the order of 20 nm but require very low working distances and are limited to studying near-surface features. In addition, near-field microscopy techniques involve a scanning procedure to image the whole sample which is time-consuming

Far-field microscopy

Far-field microscopy requires illumination of the sample but does not rely only on fluorescence microscopy. Some of the far-field techniques are label-free - without fluorophores - taking advantage of non-linear optical processes. However, since super-resolution techniques were traditionally based on specific ways to excite the fluorophores, we focus here on far-field fluorescence super-resolution microscopy. Reviews of these approaches can be found in [Huang 2009; Leung 2011].

Confocal microscopy combines focusing the excitation laser with a pinhole for detection, effectively reducing out-of-focus fluorescence background and achieving a resolution improvement by a factor of $\sqrt{2}$ [Pawley 2006].
4Pi (referring to the 4π solid angle of a sphere) and I^5M (for image interference microscopy combined with incoherent interference illumination) microscopy are techniques that virtually increase the numerical aperture by using two opposing objectives. This results in an increase of the solid angle used for illumination and detection, leading to a resolution improvement by a factor of 2 [Gustafsson 1999; Hell 2007].
Structured illumination microscopy [Gustafsson 2000; Gustafsson 2008] illuminates the sample with a sinusoidal pattern with a high spatial frequency, which shifts the

fine details of the structures to lower frequencies, detectable by the microscope. Resolutions of the order of 100 nm are achieved by acquiring multiple images with patterns of different phases and orientations.
The previously described approaches can be applied to any fluorophores, but they are still limited in resolution enhancement. An order of magnitude on the resolution can be gained by taking advantage of the photo-physical properties of some fluorophores and non-linear effects.

The first approach to fluorescence super-resolution microscopy using non-linear effects is called the spatially patterned excitation approach. It is based on stimulated emission or saturable depletion which induces a reduction in undesirable fluorescence emission.
Stimulated emission depletion (STED) microscopy [Hell 1994; Klar 2000] reaches a resolution of around 50 nm by activating the fluorescent sample with a laser as well as a secondary torus-shaped coherent beam, which reduces the excitation effect of the primary laser. This reduces the PSF size to a narrow area around the center of the torus (where the second field is very weak, supposedly zero), leading to the resolution improvement.
RESOLFT microscopy [Hell 1995; Hofmann 2005; Bretschneider 2007] is a more general scheme where reversibly photoswitchable fluorescent probes are used to decrease the PSF size, leading to a resolution lower than 100 nm while requiring lower laser intensity than STED microscopy.
Combining saturable depletion with structured illumination microscopy sharpens the illumination patterns and enables to access higher spatial frequencies. This technique called saturated structured illumination microscopy demonstrated resolutions of the order of 50 nm.

Finally, the last way to improve the resolution of fluorescence microscopy is realized with single-molecule localization. This method requires a low density of fluorophores, otherwise, their overlapping images would prevent their localization. The probe density is thus decreased by causing individual photoswitchable fluorophores to fluoresce at different moments in time and the images are superimposed afterward. Therefore, single-point emitters can be localized with sub-diffraction precision even with a diffraction-limited PSF. This concept, independently developed in three labs at the same time and named stochastic optical reconstruction microscopy (STORM) [Rust 2006], photo-activated localization microscopy (PALM) [Betzig 2006; Lee 2012], and FPALM [Hess 2006], reaches a resolution of around 5 nm.

In conclusion, the far-field methods are dependent on specific characteristics of the fluorescent probes and require active control over the illumination of the sample.

3.2.2 Astronomy and remote sensing

In astronomy contexts, the Rayleigh criterion is formulated as

$$d_{\text{min}}^{\text{Rayleigh}} = 1.22\frac{f\lambda}{D} \tag{3.7}$$

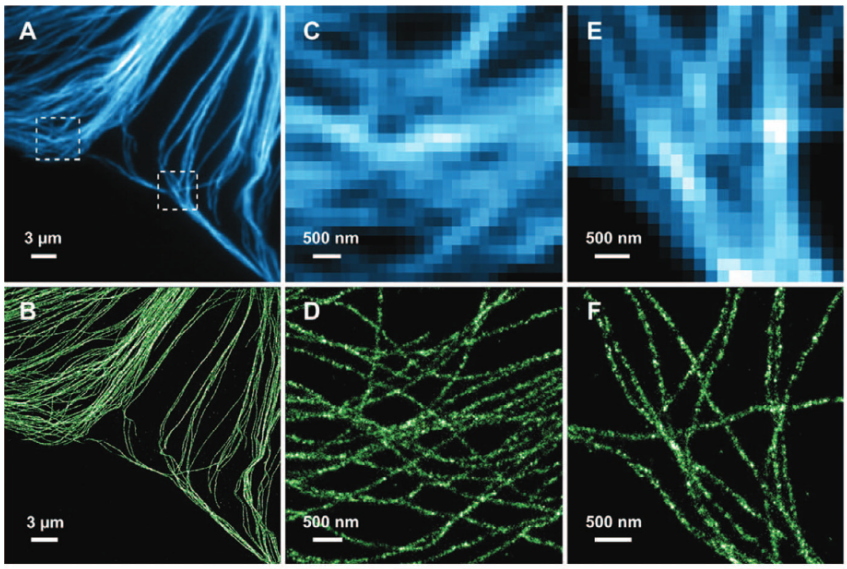

FIGURE 3.3: Comparison between images from conventional fluorescence (A, C, E) microscopy and STORM microscopy (B, D, F) [Bates 2007].

where λ is the wavelength of the observed radiation, f is the focal length of the objective of the telescope, and D its diameter. The resolution is seen as improvable only by increasing the diameter of the objective.

Thanks to aperture synthesis, it is possible to create lenses that have virtual sizes much bigger than what is technologically possible. It was initially developed and mostly used for radio astronomy since the 1950s. It is now also used for radar remote sensing and, for two decades, for optical telescopes.
Aperture synthesis is a technique where signals from different telescopes interfere, resulting in higher resolutions than when using a single telescope [Jennison 1958; Haniff 1987; Roggemann 1997; Kellermann 2001; Monnier 2003]. It requires the measurement of the phase and amplitude of the observed electromagnetic field, either by post-processing for radio-frequency signals or by having the signals physically interfere with optical frequencies. This results in having virtually larger lenses as the size of the effective lens corresponds to the size of the entire collection, hence the denomination. In radio astronomy, aperture synthesis is now combined with very long-baseline interferometry (VLBI), which enables higher separations between telescopes thanks to synchronization with atomic clocks.
For instance, the Event Horizon Telescope (EHT), an international collaboration, consists of a large array of telescopes all around the world. This array has a theoretical resolution of 25 micro-arcsecond, and this enabled the acquisition of the images of the supermassive black hole at the center of Messier 87 that were released in 2019, which display a diameter of around 40 micro-arcsecond [Collaboration 2019] (see fig. 3.4). For comparison, the Hubble Space Telescope which has a 2.4 m-objective displays a resolution of 0.1 arcsecond. Therefore, aperture synthesis has reached a

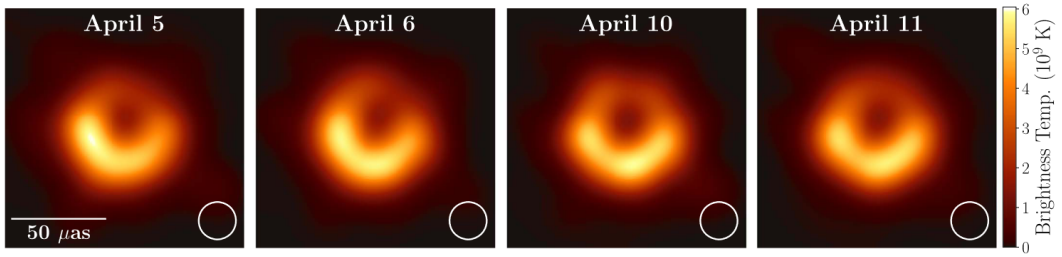

FIGURE 3.4: Images of the supermassive black hole at the center of Messier 87, obtained with aperture synthesis and very-long-baseline interferometry by the Event Horizon Telescope [Collaboration 2019].

3-order-of-magnitude gain of resolution compared to a single telescope in radio astronomy.
However, this requires the collaboration between many observatories and stable clock synchronization over large distances. This is why aperture synthesis is even more challenging for optical interferometers. For instance, with its six telescopes, the CHARA array, located in California, is one of the largest arrays of telescopes at optical frequencies and has a resolution of 200 micro-arcsecond [Hand 2010].

Astronomical observations are also time-limited as turbulence introduces noise in the measurement with time scales between 1 ms and 1 s.

3.2.3 From super-resolution imaging techniques to parameter estimation

As we saw from the previous sections, super-resolution techniques that are currently employed in microscopy and astronomy contexts are domain-specific. Near-field microscopy techniques place the samples in artificial environments, far-field microscopy approaches require the illumination of the samples, and aperture synthesis for astronomy relies on colossal apparatus.
A super-resolution technique to bridge the gap between microscopy and astronomy techniques is still missing, it has to be linear-optical, non-invasive, passive (no interaction with the sample), operational at all scales in the far-field regime, and compatible with incoherent sources.

The objective of this work is not to develop yet another technique for super-resolution imaging. Our task is more foundational, we aspire to understand the fundamental physical limits inherent in these imaging problems.
Advancements in super-resolution techniques within microscopy and astronomy have revealed that Rayleigh's limit, and more broadly the diffraction limit, is not fundamental and that the sole information of the PSF is not sufficient to determine the sensitivity and resolution of an apparatus [Goodman 2000].

Historical diffraction limits presented in section 3.1 were established at a time when the study of noise in measurements was technically infeasible. Physicists then only had access to a minimal resolvable distance between two point sources based on the saturation of the human eye.

While the detection of a substantial number of photons with a CCD camera could, in principle, provide information for surpassing the diffraction limit, even in an ideal scheme (no electronic noise, infinitely small pixels), the sensitivity of the measurement can not be infinitely large as increasing the photon count also amplifies shot noise.
From the definition given in section 2.5.6, the minimal resolvable distance is equivalent to the sensitivity of the estimation for small separations. According to fig. 2.12, the minimal resolvable distance for ideal direct imaging scales as $(2N\kappa)^{-1/4}$, where $2N\kappa$ is the total number of detected photons. This slow scaling, combined with CCD camera saturation, hinders significant improvements beyond Rayleigh's limit.

Hence, a comprehensive analysis of noise contributions to the measurement is imperative to determine the sensitivity and resolution of an apparatus. This is why we treat the task of imaging in a parameter estimation framework. We determine the sensitivity limits associated with estimating some unknown parameters, in particular the separation between sources, encoded in the incident light by processing the measurement results, as presented in chapter 2.

The exploration of this parameter estimation problem begins with the study of the simplest optical scene, the images formed by two point-like incoherent sources. The theoretical limits (QFI and Fisher information) are well-known in various configurations, when taking into account different noise sources but also in a multi-parameter estimation scenario [Tsang 2016; Nair 2016; Tsang 2017; Bonsma-Fisher 2019; Gessner 2020a; Grace 2020; Len 2020; Sorelli 2021a; Sorelli 2021b].
As explained in chapter 2, spatial-mode demultiplexing is a good candidate for improving resolution beyond the diffraction limit as it saturates the QFI for incoherent sources. It also satisfies the requirements cited at the beginning of this section - linear-optical, non-invasive, passive, operational at all scales in the far-field regime, and compatible with incoherent sources - since the demultiplexing apparatus can simply be added after any imaging system. It involves no interaction with the observed scene and is only time-limited by the bandwidths of a few photodetectors.
However, this problem is still not completely understood experimentally, and experiments on single-parameter estimation are ongoing. The figure of merit that is used to benchmark the performance is the variance of the estimation that is compared to the Fisher information of SPADE, the Fisher information of direct imaging, and the QFI of separation estimation.

3.3 Experimental separation estimation: Literature review

3.3.1 Context

As demonstrated in the previous section, the task of estimating the separation between two incoherent equally bright sources has witnessed a renewed interest on the theoretical front during the last decade, from the publication of [Tsang 2016]. This resurgence has been accompanied by the emergence of several experiments aiming at assessing the validity of the theoretical predictions as well as identifying the limitations of the existing models. In this section, we provide a comprehensive

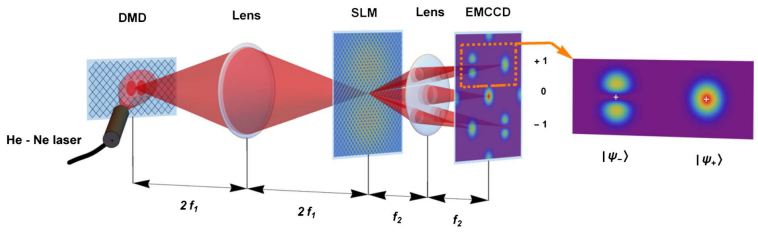

FIGURE 3.5: Schematic diagram of the experimental setup from [Paúr 2016]. Two incoherent point sources are created with a high-frequency switched digital micromirror chip (DMD) illuminated with an intensity-stabilized He–Ne laser. The sources are imaged by a low-aperture lens. In the image plane, projection onto different modes is performed with a digital hologram created with an amplitude spatial light modulator (SLM). Information about the desired projection is carried by the first-order diffraction spectrum, which is mapped by a lens onto an EMCCD camera.

review of experimental investigations for the separation estimation of two incoherent point-like sources via SPADE or a simplified version with only the HG_{10} mode. In each case, the study is conducted for an optical system with a Gaussian PSF and with the sources' centroid aligned on the measurement apparatus. Our goal is to describe the current state of the art.

3.3.2 Projection on one mode

The experimental investigations realized shortly after the proposal of [Tsang 2016] are all simplified versions of SPADE, based on the projection on only the HG_{10} mode.

Paúr *et al.* [Paúr 2016] performed separation estimation using SPADE implemented with an SLM, as explained in section 1.3.3 . Two point-like sources are generated with a digital micro-mirror device (DMD) illuminated with a He-Ne laser. The separation between the two sources is controlled by addressing the micro-mirrors individually. The sources are turned on and off alternatively to ensure spatial incoherence with the switching time being significantly shorter than the integration time of the detection. The images of the two sources are projected in the mode HG_{10} with intensity measured with an electron-multiplying CCD camera - the intensity in the HG_{00} mode is used for normalization - as illustrated in fig. 3.5. For each separation, from $0.1w_0$ to $0.8w_0$, explored with steps of $0.1w_0$, 500 measurements were carried out to characterize the performances of the estimation.
The experimental results demonstrate a negligible bias, and the standard deviation of the estimation is approximately $0.1w_0$. The small discrepancy compared to the QFI arises from the noise of the camera, from the background light reaching the detector, and from mechanical instabilities.
This measurement performs better than theoretical direct imaging, as it exhibits a variance 20 times smaller. There is, however, no mention of the number of detected photons or of the integration time, the measurement is only said to be performed in the photon counting regime.

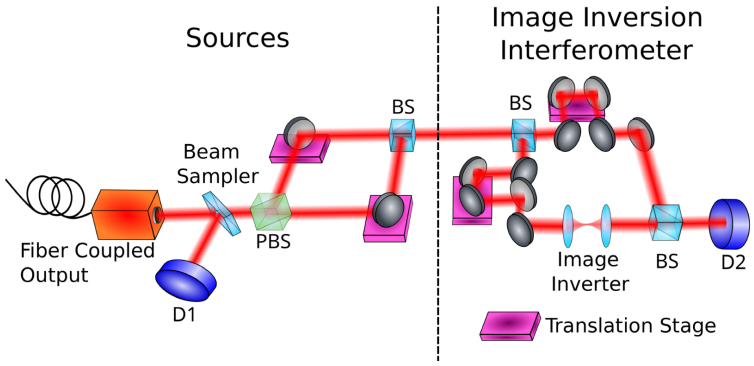

FIGURE 3.6: Schematic diagram of the experimental setup from [Tang 2016]. The two test sources, with orthogonal polarizations, are obtained from a laser-illuminated single-mode optical fiber whose output is separated by a polarizing beamsplitter (PBS). The separation of the sources is controlled by translating mirrors mounted on linear-motion stages, and can achieve complete overlap of the two light "sources". The image inversion interferometer then detects the interference value at detector D2.

Tang *et al.* [Tang 2016] realized a simplified version of SPADE with image inversion interferometry which is a self-interference technique equivalent to project on the HG_{10} mode. The experimental setup is presented in fig. 3.6. In this case, the two sources, generated from a He-Ne laser, do not interfere because they have orthogonal polarizations.
The intensity at the output of the interferometer is measured with a photodiode, and the integration time is 200 µs, for a total measurement time for each separation of 300 s allowing for statistical analysis. The total incident power is 120 µW, i.e. around 80×10^9 photons per integration time. They explore separations from $0.2w_0$ to $1.25w_0$, with steps around $0.3w_0$, using a translation stage, the reference separation value being given by its controller, which has a 1 µm-accuracy. A calibration curve is built using these measurement points from which they extract a prediction of the sensitivity of the measurement using error propagation.
According to their analysis, the minimum standard deviation would be around $0.05w_0$, but was not experimentally measured.

Yang *et al.* [Yang 2016] carried out heterodyne detection on the HG_{10} mode for preliminary results on separation estimation. They generated two sources by transmitting laser light through masks with two rectangular slits, separated by a controlled distance, as illustrated in fig. 3.7. In this situation, the diffraction pattern is not an Airy disk but a sinc function. Nevertheless, the PSF can also be approximated with a Gaussian function. The spatial incoherence between the sources is generated by moving a white card before the mask during the integration time of 1 ms.
The power transmitted through the mask is around 10 µW, corresponding to around 4×10^{10} incident photons per integration time. They also studied the situation where the two sources are mutually coherent though we will not develop on these results.
A calibration curve is built from the measurement of four separations ($0.4w_0$, $0.8w_0$,

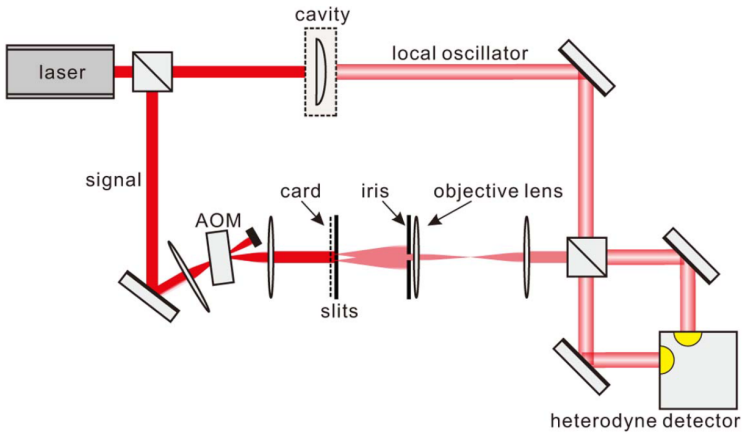

FIGURE 3.7: Schematic diagram of the experimental setup from [Yang 2016]. They carried out heterodyne detection on the HG_{10} mode for preliminary results on separation estimation. They generated two sources by transmitting laser light through masks with two rectangular slits, separated by a controlled distance. In this situation, the diffraction pattern is not an Airy disk but a sinc function. Nevertheless, the PSF can also be approximated with a Gaussian function. The spatial incoherence between the sources is generated by moving a white card before the mask during the integration time of 1 ms.

$1.25w_0$ and $1.7w_0$), and the standard deviation on the separation estimation is predicted by inverting the calibration curve to be at minimum $\Delta d = 3 \times 10^{-2} w_0$ for $d = 0.3w_0$.
The limitations of this apparatus performing heterodyne detection arise from the fluctuations of mode matching between the local oscillator and the signal of interest due to mechanical instabilities. This experiment serves as a proof-of-principle for employing heterodyne detection in higher-order Hermite-Gaussian modes in imaging contexts when combined with machine learning techniques. This concept was implemented in [Pushkina 2021] with coherent sources.

Tham *et al.* [Tham 2017] demonstrated that SPLICE (super-resolved position localization by inversion of coherence along an edge) detection improves the sensitivity of separation estimation between two sources compared to Rayleigh's limit. This technique is equivalent to projecting on the HG_{10} mode, but the projection is implemented on another spatially anti-symmetric mode $\psi_\perp(x,y) = \exp\left(-\frac{x^2+y^2}{w_0^2}\right)\mathrm{sgn}(x)$, using an edged phase plate.
Two Gaussian beams are separated using a mirror displaced by a translation stage, the separation is certified by the controller of the stage, as described in fig. 3.8. They are made incoherent with a path difference much longer than their coherence length. For each measurement, for separations from $0.02w_0$ to $1.3w_0$, approximately $N = 1200 - 1500$ photons are detected.
The separation estimation is implemented using a calibration curve, with 17 measurements for each separation. The measured standard deviation of $2.6 \times 10^{-2} w_0$ outperforms their experimental implementation of direct imaging by a factor of 4 for separations below $0.4w_0$.

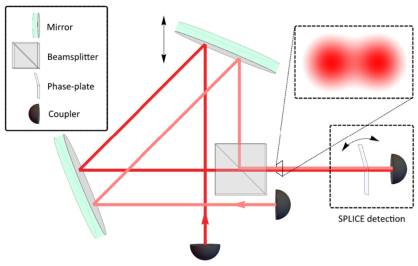

FIGURE 3.8: Schematic diagram of the experimental setup from [Tham 2017], using SPLICE (super-resolved position localization by inversion of coherence along an edge) detection. In the lower right-hand box is a representation of SPLICE, the measurement scheme tested in this experiment. In the upper right-hand box is a sketch of the spatial profile of the electromagnetic field before the measurement. The rest of the figure depicts the device used to simulate the two light sources, which can be displaced around their centroid by the displacement of the top mirror.

Parniak *et al.* [Parniak 2018] show that Hong-Ou-Mandel interference combined with spatially resolved cross-coincidences provide information on the separation between two sources theoretically and experimentally. The concept is illustrated in fig. 3.9. Because Hong-Ou-Mandel interference is sensitive to mode overlap between the photons, for small separations, a two-photon interference scheme enables to reach half of the QFI of separation estimation for perfect visibility, and this sensitivity should be improved for multi-photon interference to even saturate the QFI. The experiment was realized with visibility around 0.92 and they obtained a standard deviation Δd of approximately $0.05w_0$ for separations between $0.1w_0$ and $0.6w_0$ using maximum likelihood estimation, from 1000 coincidences, which outperforms theoretical DI by a factor of 2. They also studied the task of estimating the centroid position of the two sources.

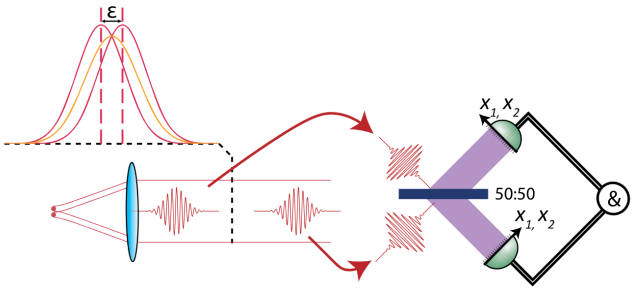

FIGURE 3.9: Concept of the experimental from [Parniak 2018]. The authors show that Hong-Ou-Mandel interference combined with spatially resolved cross-coincidences provide information on the separation between two sources theoretically and experimentally.

Zanforlin *et al.* [Zanforlin 2022] performed the separation estimation between two incoherent weak thermal sources with an interferometric setup, presented in fig. 3.10. The thermal sources are generated with the combination of a phase and

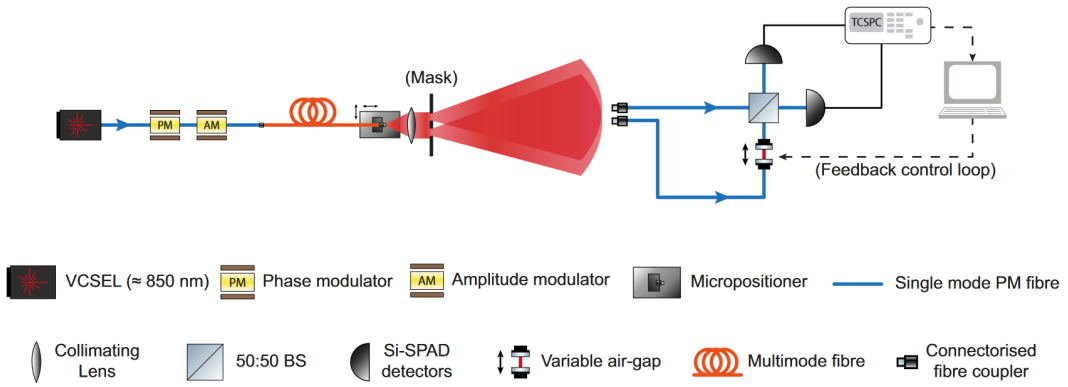

FIGURE 3.10: Schematic diagram of the experimental setup from [Zanforlin 2022]. The thermal sources are generated with the combination of a phase and an amplitude EOM, followed by a multimode fiber to reduce the spatial correlations. The separation between the sources, from 15 µm to 1 cm, is fixed with a mask, fabricated by laser-written lithography, of two pinholes with diameters from 10 µm to 50 µm. At the detection stage, two single-mode fibers are placed at 1 m from the mask, separated by 5.3 mm. The coupled light is then injected into a balanced interferometer, with an air gap in one arm to adjust the losses and single-photon avalanche photodiodes at the outputs.

an amplitude EOM, followed by a multimode fiber to reduce the spatial correlations. The separation between the sources, from 15 µm to 1 cm, is fixed with a mask, fabricated by laser-written lithography, of two pinholes with diameters from 10 µm to 50 µm. At the detection stage, two single-mode fibers are placed at 1 m from the mask, separated by 5.3 mm. The coupled light is then injected into a balanced interferometer, with an air gap in one arm to adjust the losses and single-photon avalanche photodiodes at the outputs.
They performed the estimation for 5 angular separations, $\theta = 15\ \mu$rad, 25 μrad, 40 μrad, 60 μrad and 90 μrad, where approximately $6 \cdot 10^4$ photons were detected per measurement point, using the maximum likelihood estimator.
They demonstrated a gain of a factor of 3 to 30 for the standard deviation of the estimation compared to ideal direct imaging, with a factor of 1.4 to the QCRB.
However, this setup requires phase stabilization, which is realized by controlling the sources as the thermal states are alternated with coherent states. The authors also performed hypothesis testing to distinguish between the situations where there are one or two sources, but we do not discuss the corresponding results.

Zhou *et al.* [Zhou 2019a] were interested in a slightly different problem, they were aiming at improving axial resolution which is also affected by diffraction. The experimental setup is presented in fig. 3.11. They implemented SPADE on the Laguerre-Gaussian modes using two SLMs to extract information on the axial separation between two sources. They generated a pair of incoherent sources with an SLM illuminated by a He-Ne laser, where the holograms for each source are never present at the same time. The integration time of the CCD camera is much longer than the

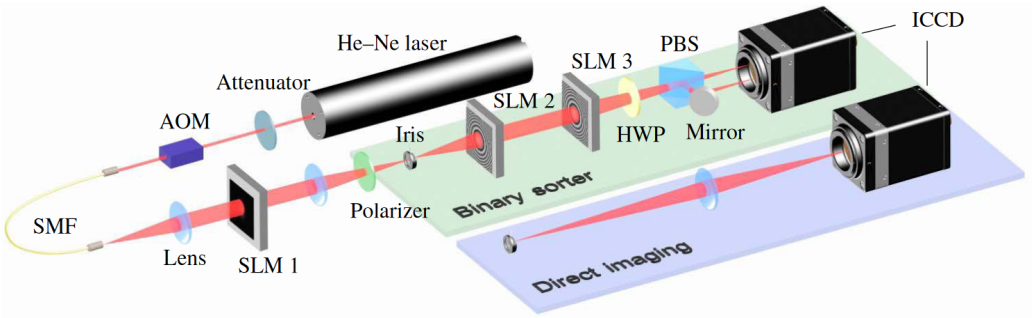

FIGURE 3.11: Schematic diagram of the experimental setup from [Zhou 2019a]. A 633 nm He–Ne laser is attenuated and modulated by an acousto-optic modulator (AOM) to generate weak pulses. A computer-generated hologram is imprinted onto a spatial light modulator (SLM 1) to generate the desired pupil function to simulate point sources. Two different methods, the binary sorter-based measurement, and the direct imaging method, are used to estimate the separation s. In the experiment, they used a flip mirror to select the measurement method.

switching time of the holograms.
The estimated separations, between $0.1z_R$ and z_R, where z_R is the Rayleigh range defined by eq. (1.21), are obtained with the maximum likelihood estimation procedure. For each separation, 2000 detected photons, and the measurement was repeated 400 times to extract the standard deviation. The measured standard deviation in this configuration is around 0.11 z_R.

3.3.3 Demultiplexing on several modes

The experimental works presented in the previous section were all based on the projection on only one spatial mode, typically the HG_{10} mode. Having access to more modes, and even better to more modes simultaneously, provides supplementary information that can enhance the sensitivity of separation estimation.

The work presented in this manuscript follows the path opened by the preliminary results of Boucher *et al.* on the use of an MPLC to improve the estimation of the separation between two incoherent sources [Boucher 2020]. The sources are generated incoherently by using a laser with low coherence length, at 1550 nm, and the incident power on the MPLC is 22 mW. The light coming from the two sources is demultiplexed by an MPLC, aligned on the centroid of the sources, from Cailabs which gives access simultaneously to 9 modes (HG_{00}, HG_{01}, HG_{10}, HG_{02}, HG_{20}, HG_{11}, HG_{21}, HG_{12} and HG_{22}).
Calibration curves, giving the intensity as a function of the separation were built and are found to be in perfect agreement with the theoretical predictions for separations ranging from 0 to $3w_0$. These calibration curves carry information on the separation between the sources, which demonstrates that SPADE with an MPLC is relevant for separation estimation, even in a practical setup where imperfections like

crosstalk arise. The predicted sensitivity is determined by inverting the calibration curve to be $2 \times 10^{-3} w_0$, mainly because of the crosstalks. This is yet to be measured experimentally.

Another experiment implementing SPADE with an MPLC from Cailabs was conducted by Santamaria *et al.* [Santamaria 2023]. Contrary to other schemes presented in this section, they studied the situation of two sources with imbalanced intensities. In order to generate incoherent sources, they used two different lasers (both at 1550 nm). The dimmer laser had a power adjustable from 0 to 11 µW, and the brighter one was at 150 µW. The beams are mode-matched to the MPLC and the intensities at the HG_{00}, HG_{01} and HG_{10} outputs were detected with InGaAs photodiodes with an integration time of 100 ms, as illustrated in fig. 3.12. They did not align the SPADE apparatus on the centroid of the two sources but on the bright beam, and tuned the separation between the sources by displacing the weaker beam.
They built calibration curves, i.e. intensity as a function of the displacement of the dim source, for the modes HG_{01} and HG_{10}, certifying the displacement, with the translation stage controller. They evaluated the resolving power of the device by inverting the calibration curves and predicted a minimum resolvable distance of $2.4 \times 10^{-2} w_0$ for a sensitivity around $10^{-3} w_0$.
They also investigated the estimation of the relative intensity between the two sources, which will not be discussed in this manuscript.

Tan *et al.* performed SPADE with an MPLC from Cailabs to study a parameter estimation task as well [Tan 2023]. They investigated how the symmetry break induced by the MPLC crosstalk enables the localization of the two incoherent sources individually. Therefore, they actually estimated the position of each source. The experimental setup is presented in fig. 3.13
The incoherence between the sources is generated by having only one source at a time per integration time. They measured the intensity at six outputs of the MPLC (HG_{00}, HG_{01}, HG_{10}, HG_{02}, HG_{20} and HG_{11}) for one source, displaced by a translation stage, for several displacements, which are certified by the translation stage controller.
The authors realized the position estimation with a calibration curve, and obtained values between $10^{-2} w_0$ and $10^{-1} w_0$.
The authors do not provide information on the incident power, it is probably around 1.5 mW according to the reference of the laser (at 1550 nm), but they also do not mention the integration time.

Table 3.1 summarize the results on the minimal separations and the minimal sensitivity, either effectively measured or predicted from preliminary measurements, from all the experiments that we discussed in this section. Note that the minimum standard deviation does not always correspond to the minimum separation that was studied, it depends on the range of separations as well as on the different sources and the number of detected photons. The notation "-" indicates that either the value is not provided or is not comparable.
We also added the results we obtained, presented in chapter 5 and in [Rouvière 2024], for the two intensity regimes we studied.

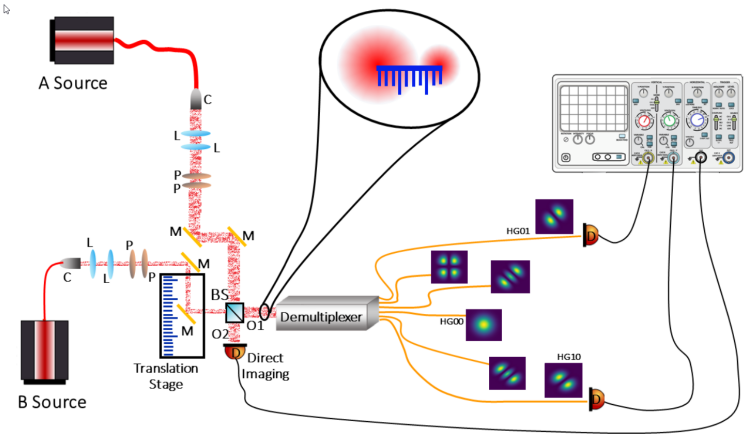

FIGURE 3.12: Schematic diagram of the experimental setup from [Santamaria 2023]. Two telecom fiber lasers (A and B sources) that exit from collimators (C) are mode-matched using simple lenses (L) systems. The intensities are tuned by changing the relative orientation of a pair of polarizers (P). The beams are combined on the input ports of a beamsplitter (BS) whose O1 output port is coupled with the demultiplexer free space input. A pair of steering (M) mirrors for each beam are used to optimize the coupling with the demultiplexer. The second mirror of beam B is mounted on a translation stage to move the beam, within the transverse plane, with micrometric resolution whereas the A beam stays centered throughout the measurement. The demultiplexer, PROTEUS-C from Cailabs, allows to perform intensity measurements on six Hermite-Gaussian modes. The HG01 and HG10 outputs of the demultiplexer are coupled with photodetectors (D) whose signals F1 and F2 are recorded using an oscilloscope. The intensity of the second output (O2) of BS is recorded using the same detector/oscilloscope used to record intensities of HG_{01} and HG_{10} modes.

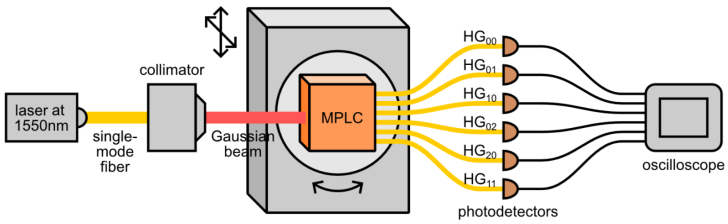

FIGURE 3.13: Schematic diagram of the experimental setup from [Tan 2023].

TABLE 3.1: Summary of experiments on separation estimation of two equally-bright incoherent sources. The (P) for "Predicted" or (M) for "Measured" indicates whether the separation estimation with the associated standard deviation was effectively implemented experimentally or if the indicated standard deviation was predicted from preliminary experimental results.

Article	Measurement method	N_{det}	d_{min}	$(\Delta d)_{\text{min}}$
[Paúr 2016]	SPADE with SLM	Low	$0.1w_0$	$\sim 0.1w_0$ (M)
[Tang 2016]	Self-interferometry	80×10^9	$0.2w_0$	$0.05w_0$ (P)
[Yang 2016]	Heterodyne detection (HG_{10})	4×10^{10}	$0.3w_0$	$0.03w_0$ (P)
[Tham 2017]	SPLICE	1500	$0.02w_0$	$0.03w_0$ (M)
[Zhou 2017]	SPADE on LG modes	2000	$0.1z_R$	$0.11z_R$ (M)
[Parniak 2018]	Two-photon interference	2000	$0.1w_0$	$\sim 0.05w_0$ (M)
[Boucher 2020]	SPADE with MPLC	High	$0.03w_0$	$2 \times 10^{-3}w_0$ (P)
[Zanforlin 2022]	Intensity interferometry	-	-	-
[Santamaria 2023]	SPADE with MPLC	10^{14}	$0.02w_0$	$0.1 \times 10^{-2}w_0$ (P)
[Tan 2023]	SPADE with MPLC	-	-	-
[Rouvière 2024]	SPADE with MPLC	3500	$0.4w_0$	$0.03w_0$ (M)
		10^{13}	$0.03w_0$	$2 \times 10^{-5}w_0$ (M)

3.4 Experimental setup

3.4.1 Designing the experiment

Our goal is to experimentally implement the estimation of the separation between two equally bright incoherent sources, populated with thermal states, with spatial-mode demultiplexing.
We aim to investigate different regimes of mean photon numbers, including bright thermal sources. The separation between the sources must be variable, from 0 to about w_0, and certified by an independent measurement. Furthermore, we want to be able to rotate the source orientation in the image plane, to modify the angle between the source axis and the demultiplexing axes.

In the long run, we would like the experiment to be versatile to explore multiparameter scenarios, as described in section 5.7.2. In this context, we want to be able to tune other parameters than the separation between the sources, in particular, their mutual coherence and their relative intensity.

3.4.2 General description

While our initial intention was to conduct the experiment using thermal states, practical constraints led us to employ phase-averaged coherent states for the incoherent sources. We studied two distinct intensity regimes, a low photon flux scenario (3500 detected photons at the outputs of the MPLC per integration time) and a high flux scenario (10^{13} detected photons at the outputs of the MPLC per integration time).

Since, for faint sources[2], thermal states exhibit Poissonian statistics, they display the same QFI for separation estimation and Fisher information for SPADE and direct imaging as for phase-averaged coherent states (with any mean photon number), which were presented in fig. 2.8. Consequently, our experimental results obtained for phase-averaged coherent states (described in chapter 5) can be extended to thermal states with low mean photon numbers.

The experimental setup is composed of three parts:

- the source generation which is completely fibered,
- the optical scene setup which controls the geometry of the sources, the alignment and mode-matching to the MPLC,
- the detection apparatus composed of the demultiplexer and the photodetectors.

Source generation The fibered laser is split into two paths, that are independently phase-modulated to generate incoherent sources, as explained in section 3.5.4. Subsequently, the light is coupled to free space with two collimating lenses.
Optical scene setup The collimators are mounted on translation stages to adjust their separation. The two laser beams are aligned and mode-matched to the MPLC free-space input.
Detection apparatus The light is injected into the MPLC, and photodetectors measure the intensity at various single-mode outputs of the MPLC. A reference photodiode detects a fraction of the total intensity for normalizing the optical powers measured at the MPLC outputs. Additionally, a quadrant detector is employed to certify the separation between the sources.

In the following subsections, we give details on these three items and their optical components. These elements constitute the PEsto (Parameter ESTimatiOn) experiment, which is displayed in figs. 3.14 and 3.15.

[2]"Faint sources" here means that the number of photons per coherence time is low.

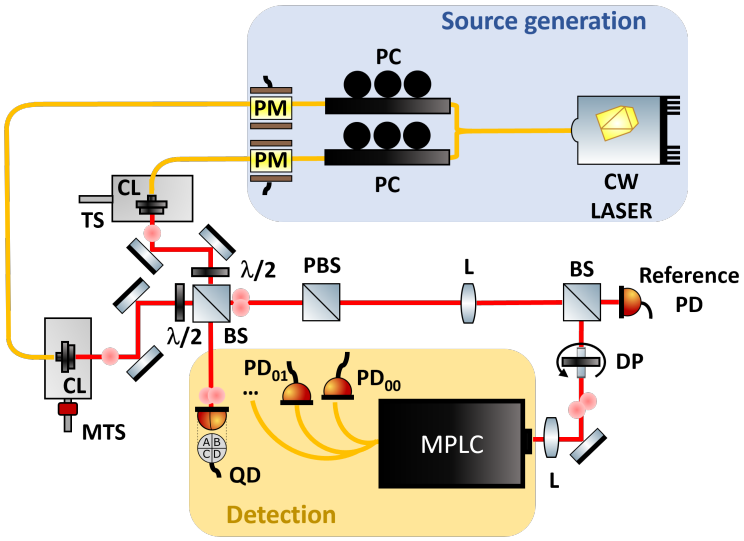

FIGURE 3.14: Setup of the PEsto experiment. The experimental setup is composed of three parts: the source generation (blue part), the detection apparatus (orange part), and the optical scene setup in between. The fibers at the outputs of the modulators are polarization-maintaining.
CW laser: Continuous-wave laser, PC: Polarization controller, PM: Phase modulator, (M)TS: (Motorized) translation stage, CL: Collimating lens, $\lambda/2$: Half-wave plate, (P)BS: (Polarizing) beamsplitter, L: Lens, QD: Quadrant detector, PD: Photodetector, DP: Dove prism, MPLC: Multi-plane light converter (spatial-mode demultiplexer).

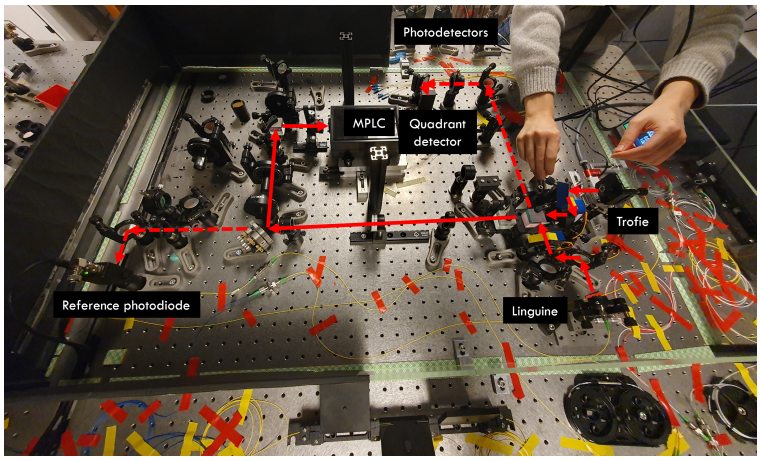

FIGURE 3.15: Picture of the PEsto experiment.

The experiment turned out to be extremely sensitive in particular to mechanical instabilities, including those induced by air flows. This is why a plexiglass cover box surrounds the experimental setup, as it can be seen in fig. 3.16.

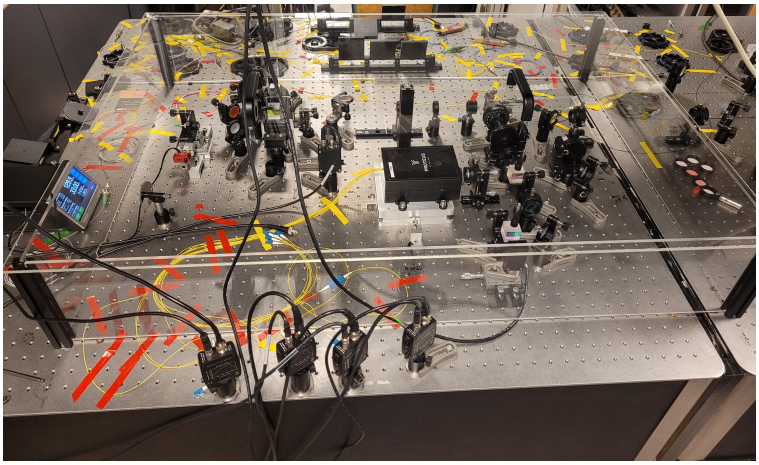

FIGURE 3.16: Picture of the PEsto experimental setup, which is surrounded by a plexiglass box to isolate it from air flows.

3.4.3 Detection apparatus

The experiment revolves around the detection apparatus, and, in particular, around the spatial-mode demultiplexing device, which is why we begin the description of the experimental setup with this section.

Spatial-mode demultiplexing

As mentioned in chapter 1, several strategies are possible to demultiplex light over a given spatial mode basis. We are using the MPLC Proteus-C from Cailabs, which is a spin-off of our group. This MPLC has 10 outputs which correspond to the modes HG_{00}, HG_{01}, HG_{10}, HG_{11}, HG_{02}, HG_{20}, HG_{12}, HG_{21}, HG_{03} and HG_{30}.
Since the commercial version of this device is designed for telecommunication purposes, its working wavelength is 1550 nm and the multimode input is a multimode fiber. However, as we use it in imaging contexts, the multimode fiber was removed from our copy, and we have a free-space input. The MPLC has an intrinsic waist, which is the waist of the mode basis on which the demultiplexing is performed, and its value is $w_0 \simeq 300\,\mu m$. Due to the multiple reflections on the spherical gold-plated mirror and to the simulation and manufacturing defects of the phase plate resulting in low couplings into the single-mode fibers, the MPLC has around 50% losses.

Photodiodes

For high photon flux regimes, the light at the outputs of the MPLC is detected by variable gain Ge photodiode (Thorlabs PDA50B2). Depending on the gain, these detectors display bandwidths from 210 Hz to 510 kHz. The maximum optical powers that can be measured by the photodiodes for each gain are presented in table 3.2. Their responsivity is $\mathcal{R} = 0.85\,A\,W^{-1}$.

Another photodiode before the MPLC collects part of the incident light for normalizing the measurement data, referred to as the reference photodiode.

TABLE 3.2: Bandwidth and maximum measurable optical power of the photodiodes (Thorlabs, PDA50B2) depending on the gain.

Gain	Bandwidth	Maximum measurable power
0 dB	DC-510 kHz	7 mW
10 dB	DC-270 kHz	2 mW
20 dB	DC-85 kHz	0.7 mW
30 dB	DC-22 kHz	0.2 mW
40 dB	DC-6.3 kHz	70 µW
50 dB	DC-2 kHz	20 µW
60 dB	DC-630 Hz	7 µW
70 dB	DC-210 Hz	2 µW

Avalanche photodiodes

To investigate the low photon flux regime, we adapted the detectors and borrowed, for two weeks, two avalanche photodiodes (APD) from Prof. Eleni Diamanti who works at LIP6 - a computer science lab of Sorbonne Université, in Paris. These single-photon detectors (IDQuantique, ID230) have a 25% quantum efficiency at 1550 nm. We also characterized their saturation by plotting the mean photon number measured by the APD, with an integration time of 100 ms, as a function of the output voltage of by the reference photodiode in fig. 3.17. This graph shows that the APD saturates quite quickly as it is not linear from around 1500 measured photons, and this is because we are illuminating it with a Poissonian light and the detector presents a deadtime of around 50 µs.

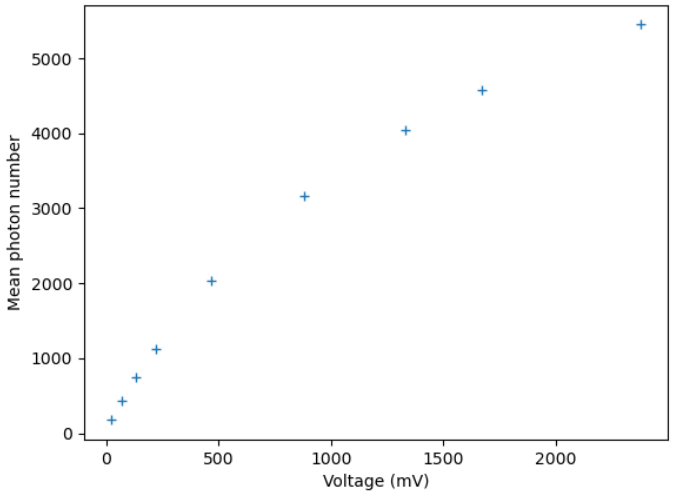

FIGURE 3.17: Mean photon number measured by the APD, with a 100 ms-integration time, as a function of the output voltage of the reference photodiode. The APD saturates quite quickly as it is not linear from around 1500 measured photons

3.4.4 Source generation

The MPLC is a telecommunication device and its working wavelength is 1550 nm, which imposes the laser wavelength. As mentioned previously, we want to be able to adapt the coherence of the sources from mutually coherent to mutually incoherent and everything in between. This is why we chose a laser (Thorlabs, SFL1550P) with a large coherence length ($\ell_c \approx 6$ km). Its output power is around 20 mW. The laser is fiber coupled and split into two paths. The light in each path is then modulated with phase and amplitude integrated modulators (iXBlue, MPX-LN-0.1 and MX-LN-0.1) appropriately to generate thermal sources or mutually incoherent sources with Poissonian statistics, as it will be explained in section 3.5. Because the modulators are based on birefringent crystals, they are sensitive to the polarization of the input field, which we adjust with polarization controllers at the input. The fibers at the output of the modulators at polarization-maintaining.

3.4.5 Optical scene setup

Collimators

After the modulation, we use triplet lens collimators (Thorlabs TC12APC-1550) to couple light into free space. The waist at the output of the collimators is $w_0 = 1.1$ mm.
The beams at the output of the collimators are then mixed on a beamsplitter to orientate them on the same optical path.

Translation stages

Both collimators are mounted on translation stages to adjust the separation between the sources. One of the translation stages is manual (Newport, M-UMR5.16) associated with a micrometer head (Newport, BM11.16), and the other one is motorized (Newport, 9066-X-P-M). The manual stage has a travel range of 16 mm, with a sensitivity of 2 µm, while the motorized stage has a travel range of 12.7 mm, for a step size of around 30 nm with an open-loop control system.

In order to distinguish them easily, we named Linguine the source corresponding to the manual stage, and Trofie the one corresponding to the motorized translation stage.

Quadrant detector for reference separation

Due to hysteresis and variability in the step size for the motorized stage and low sensitivity for the manual stage, the true value of the separation can not be extracted from the translation stage controller. This is why we wanted to have an independent measurement to certify the separation, and, for this purpose, we employed a quadrant detector. Even though, this detector can not measure separations between beams[3], as demonstrated in section 2.4, the sensitivity of quadrant detection

[3]This is due to its working principle. If two equally bright beams are symmetrically displaced by a small distance, the output signal of the quadrant detector is always zero whatever the separation.

for beam displacement estimation is close enough to the QFI to be reliable. Therefore, we measure independently the displacement of each source x_1 and x_2 with a quadrant detector to access a reference separation value $d_{\text{ref}} = |x_1 - x_2|$.

The calibration curve of the quadrant detector (Thorlabs PDQ30C) is presented in fig. 3.18. We built it by displacing the beam on the detector by a known amount - determined by the translation stage - and measuring the output signal for each displacement. The signal, normalized by the total incident power, given by the SUM output of the controller (Thorlabs KPA101), is referred to as V_{QD}.

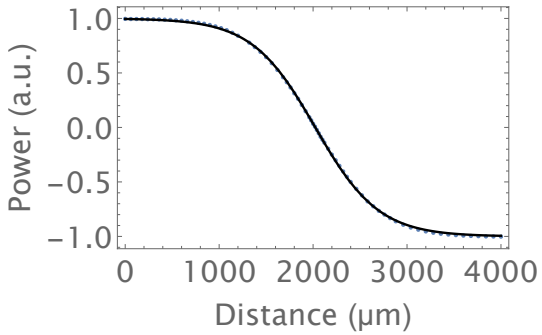

FIGURE 3.18: Calibration of the quadrant detector. The fit using eq. (3.8) gives $a = 337.2$ and $b = 2023.5$.

We fitted this calibration curve with the sigmoid function, which is a good model for the calibration of such a quadrant detector,

$$f(x) = -1 + \frac{2}{1 + \exp\left(\frac{x-b}{a}\right)}, \tag{3.8}$$

where x is the beam position, and a and b are the fitting parameters, and by inverting this function after finding a and b, it is possible to determine the position of the beam from the measured output voltage of the quadrant detector

$$x = b + a \ln\left(\frac{1 - V_{\text{QD}}}{1 + V_{\text{QD}}}\right). \tag{3.9}$$

Dove prism

We use a Dove prism (Thorlabs, PS991M) to rotate the optical scenes in the image plane. In this version of the experiment, we aligned the source axis on one of the MPLC axes, which are 45° to the horizontal and vertical axes. This is why the Dove prism is set to rotate the images by 45°.

Mode-matching

For mode matching the Gaussian beams at the output of the collimators to the intrinsic waist of the MPLC, we set up two lenses of focal lengths 300 mm and 100 mm in a telescope configuration. The mode-matching procedure, which involves the modes HG_{02} and HG_{20}, is described in section 5.2.2.

Intensity balance

Since the light generated by the laser is linearly polarized, we use a combination of half-wave plates and polarizing beamsplitter to balance the intensities of the two sources. This configuration also enables to unbalance the intensities in a controlled way.

3.5 Thermal state generation

One of our goals was to study separation estimation for light with statistics close to the one emitted by astronomical objects. Despite conducting the experiment using phase-averaged coherent states, we allocated time to produce thermal light from a laser beam. In this section, we explain how we generated thermal states with low mean photon numbers, and how we exploited a segment of this procedure to generate phase-averaged coherent states.

3.5.1 How to generate thermal states

Since thermal light emanates from black body radiation, a straightforward way to generate it would be with an incandescent bulb. However, our requirements were to produce thermal states with a non-negligible mean photon number, in a monochromatic Gaussian beam, in other words in a well-defined spatio-temporal mode. We also wanted the coherence between the two sources to be modulated. Hence the use of a laser.
We recall the P function of a thermal state, given in eq. (1.123), which corresponds to the probability distribution of the coherent states $|\alpha\rangle$ constituting the thermal state:

$$P_{th}(\alpha) = \frac{1}{\pi N_{th}} e^{-|\alpha|^2/N_{th}}, \tag{3.10}$$

where α is the complex amplitude of $|\alpha\rangle$. Thermal states can thus be seen as incoherent mixtures of coherent states weighted by a Gaussian distribution.
From this definition, there are two ways to generate what can be called pseudo-thermal light - "pseudo" because it does not originate from black body radiation - from a single laser beam: either using phase and amplitude electro-optical modulators on which we implement the probability distribution of eq. (3.10) with arbitrary signal generators, or using a rotating ground glass wheel that realizes this probability distribution in an analog manner, exploiting the speckle pattern. The former method is the one we chose and is presented in sections 3.5.2 and 3.5.3, and we also explain how we tried to implement the latter technique in section 3.5.5. We will refer to this kind of light as "thermal states of light" in this manuscript, even though it does not have the spectrum of black body radiation, since it corresponds to the formal mathematical definition.

3.5.2 Generation with electro-optical modulators

As mentioned before, using a phase and an amplitude electro-optic modulator (EOM) is a controlled way to generate thermal states from a laser beam, by modulating the amplitude A and phase θ of the coherent state $|\alpha\rangle$, with the complex amplitude $\alpha = Ae^{i\theta}$. Indeed, eq. (3.10) can be written in polar coordinates as[4]

$$P(A,\theta) = \frac{A}{\pi N_{th}} e^{-A^2/N_{th}}, \tag{3.11}$$

which is actually independent of θ. Since phase and amplitude are uncorrelated, the probability distribution eq. (3.11) is separable into a phase and an amplitude part: $P(A,\theta) = P(A)P(\theta)$. The phase is uniformly distributed over 2π, i.e.

$$P(\theta) = \frac{1}{2\pi}, \tag{3.12}$$

and the probability distribution of amplitude is thus

$$P(A) = \frac{2A}{N_{th}} e^{-A^2/N_{th}}. \tag{3.13}$$

These probability distributions can be applied to the phase and amplitude modulators in order to generate such thermal states.

Working principle of electro-optical modulators

Since the laser is fibered, we used integrated optical modulators. A phase EOM consists of a lithium niobate crystal placed in between two electrodes. When an electric field is applied to this birefringent crystal, its refractive index changes due to the Pockels effect - a second-order nonlinear effect. This is how a phase shift is implemented to the guided light. Moreover, the phase shift is proportional to the voltage applied to the crystal. The voltage corresponding to a phase shift of π is denoted V_π.

An amplitude EOM is an integrated Mach-Zehnder interferometer in which a phase modulator is inserted. A voltage is applied to induce a phase difference between both arms, which results in power variations at the output of the interferometer. The interferometer is in a push-pull configuration, which means that each arm sees an opposite phase shift, and the transmissivity of the amplitude EOM as a function of the applied voltage reads

$$T(\mathrm{U}) = \cos(k(\mathrm{U} - \mathrm{U}_0)), \tag{3.14}$$

where U_0 is the voltage corresponding to the maximum amplitude.

[4] Since we chose the convention $\hat{a}\,|\alpha\rangle = \alpha\,|\alpha\rangle$, then $|\alpha|^2$ corresponds to the laser intensity and $\alpha = \frac{1}{2}(q + ip)$ to the complex amplitude of the electric field.

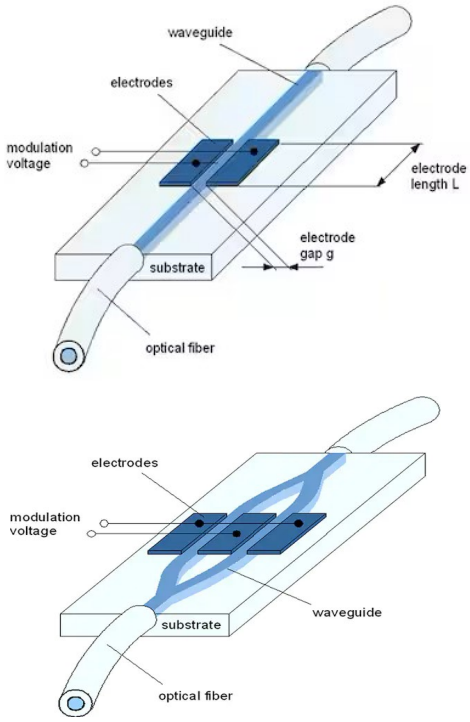

FIGURE 3.19: (top) Phase modulator, (bottom) Amplitude modulator. Source: [Jenoptik].

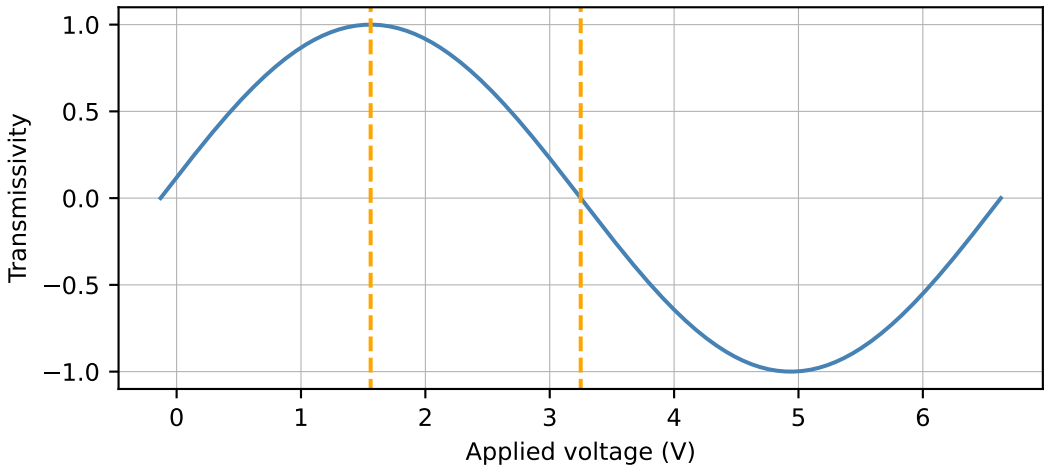

FIGURE 3.20: Transmissivity of the amplitude EOM, with $k = 1/2$ and $U_0 = 1.5\,V$. The dashed lines correspond to $U_{min} = U_0$ and $U_{max} = U_0 + \frac{\pi}{2k}$.

Phase modulation for thermal state generation

As explained previously, the phase shift induced by a phase EOM is proportional to the voltage applied to the modulator. Therefore, in order to generate the uniform phase distribution over 2π, given by eq. (3.12), the phase EOM is driven with a white voltage noise, with amplitude $2V_\pi$, produced with an arbitrary signal generator.

Amplitude modulation for thermal state generation

According to the operation of the amplitude modulator described previously, the amplitude of the field at the output of the EOM is $A = T(\mathrm{U})A_0$ where A_0 is the amplitude of the incident coherent state and $T(\mathrm{U})$ is given by eq. (3.14). Since the transmissivity function $T(\mathrm{U})$ is periodic, we limit the voltage modulation in a range where it is monotonic between $\mathrm{U_{min}} = \mathrm{U}_0$ and $\mathrm{U_{max}} = \mathrm{U}_0 + \frac{\pi}{2k}$, as presented in fig. 3.20. Using that for probability distributions, a variable change is given by

$$P(u) = P(v)\left|\frac{\mathrm{d}v}{\mathrm{d}u}\right|, \tag{3.15}$$

we obtain the probability density function of the applied voltage by applying the variable change $A = T(\mathrm{U})A_0$ to eq. (3.13):

$$P(\mathrm{U}) = C\exp\left(-\frac{\alpha_0^2}{N_{th}}T(\mathrm{U})^2\right)|T(\mathrm{U})\sin(k(\mathrm{U}-\mathrm{U}_0))|\Theta(\mathrm{U}-\mathrm{U}_{min})\Theta(\mathrm{U}_{max}-\mathrm{U}) \tag{3.16}$$

where $\Theta(x)$ is the Heaviside function which is equal to 1 for $x \geq 0$ and to 0 elsewhere, and

$$C = \frac{2kA_0^2}{N_{th}}\left[1-\exp\left(-\frac{A_0^2}{N_{th}}\right)\right]^{-1} \tag{3.17}$$

is the normalization constant.
The probability distribution of the voltage to apply to the amplitude modulator eq. (3.16) is represented in fig. 3.21 for several mean photon numbers N_{th}.

In order to generate random numbers following this probability distribution function, these voltages are applied to the amplitude EOM. For this purpose, we use inverse transform sampling which is a basic pseudo-random number sampling [Devroye 2013]. This method works as follows:

1. Generate a random number z from the random variable Z following the uniform distribution in the interval $[0, 1]$.

2. Compute $F_{\mathrm{U}}^{-1}(z)$, where F_{U} is the cumulative distribution function of $P(\mathrm{U})$, i.e. $F_{\mathrm{U}}(x) = P(\mathrm{U} \leq x)$.

For the probability distribution eq. (3.16), we find that the inverse of the cumulative distribution function is:

$$F_U^{-1}(Z) = \mathrm{U}_0 + \frac{1}{k}\arcsin\left(\frac{1}{A_0}\sqrt{N_{th}\ln\left(1+(\exp\left(\frac{A_0^2}{N_{th}}\right)-1)Z\right)}\right). \tag{3.18}$$

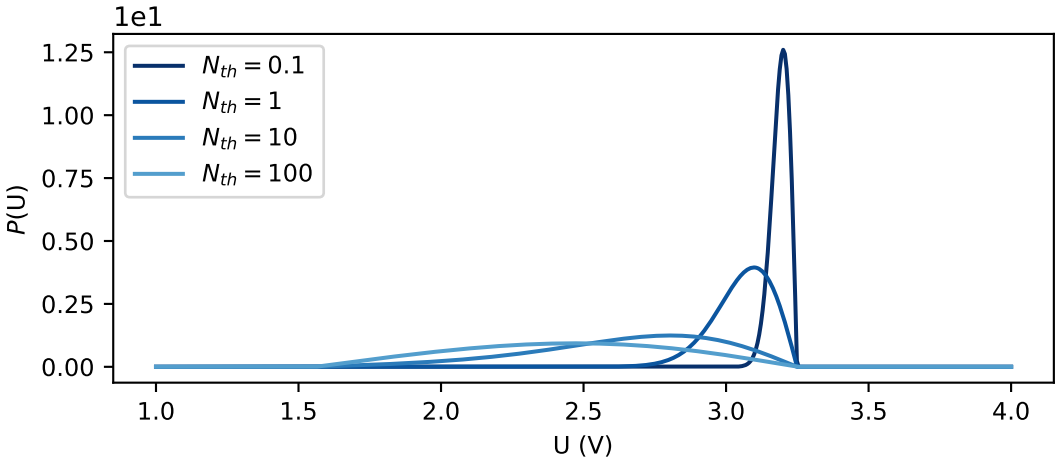

FIGURE 3.21: Probability distribution of the voltage applied to the amplitude EOM.

This function produces the voltage values for approximating the voltage probability distribution eq. (3.16) needed for thermal states generation, as illustrated in fig. 3.22.

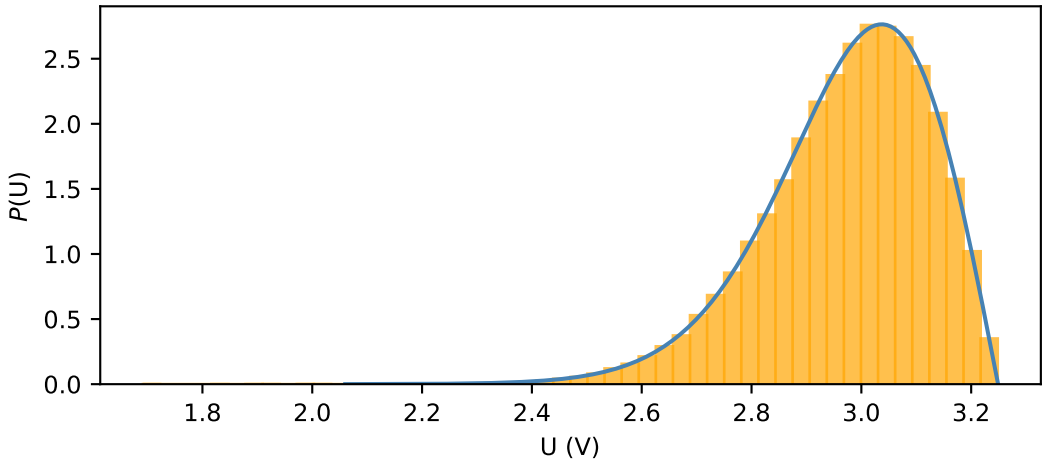

FIGURE 3.22: Probability distribution of the voltage to apply to the amplitude EOM and histogram from the inverse transform sampling method with 100000 samples.

Thermal states with EOM

Combining the two probability distribution functions, it is thus possible to generate a thermal state from a coherent state.
The P function of a state simulated using the probability distribution eq. (3.12) and the inverse transform sampling with eq. (3.18) is plotted in fig. 3.23(a), as well as the projection of the P function on the real part of α in fig. 3.23(b). These two histograms

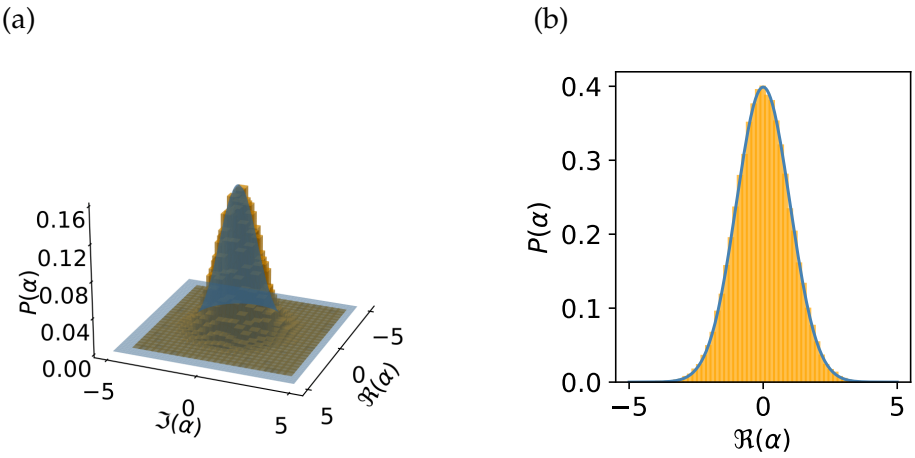

FIGURE 3.23: Simulation of a thermal state for $A_0 = 5$, $N_{\text{th}} = 2$ and $N_{\text{samples}} = 10^5$. (a) Histogram and P function. (b) Projection on the real part of α.

are plotted along with the P function of the target thermal state for comparison. Both curves are extremely similar, suggesting that high-quality thermal states can be generated with a phase and an amplitude EOM.
In order to characterize the quality of the generated states, the figure of merit that we choose is the overlap between the P function of the generated thermal state and the P function of the target state. This overlap is presented as a function of A_0 and N_{th} in fig. 3.24. This figure shows that it is not possible to generate any target thermal state with any incident coherent state, but that the amplitude of the incident coherent state must be adapted to the mean photon number of the thermal state we want to generate, or, in other words, that only a specific range of mean photon numbers is accessible with a given amplitude for the incident coherent state.

3.5.3 Experimental results

The thermal states are generated with a phase modulator and an amplitude modulator driven with an arbitrary signal generator implemented on Red Pitaya components (STEMlab, 125-14). The characterization of the EOMs can be found in Appendix. Since the Red Pitaya outputs are limited between $-1\,\text{V}$ and $1\,\text{V}$, we added homemade electronic amplifiers to match the modulators' characteristics. These amplifiers have a limited bandwidth of $1\,\text{MHz}$. We characterize the generated thermal states by performing a homodyne detection (Koheron, PD100B, bandwidth $100\,\text{MHz}$), which measures the marginals of the Wigner function, as illustrated in fig. 3.25. The bandwidths of the different devices that we use to generate and detect the thermal states are presented in table 3.3.
Since the phase is uniformly averaged over 2π, the measurement results should display rotational invariance in the phase space - this was verified experimentally, see fig. 3.27 - which is why the phase of the local oscillator does not have to be locked, as long as the phase drift of the local oscillator is slow. We therefore measure the marginals of the Wigner function of the generated states at random phases.

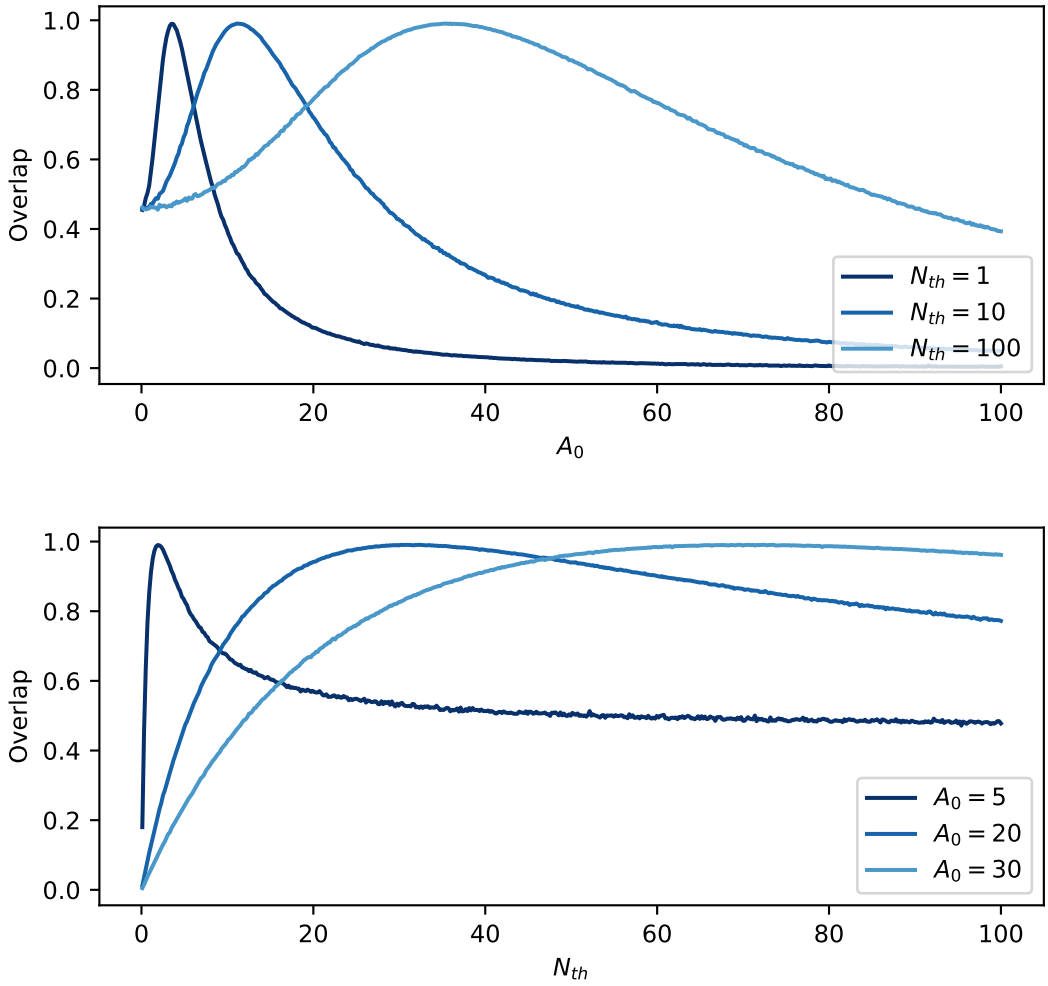

FIGURE 3.24: Overlap of the generated states compared to the target thermal state, (top) as a function of the amplitude of the input coherent state for several target mean photon numbers N_{th}, and (bottom) as a function of target mean photon numbers N_{th} for several amplitudes of the input coherent state.

TABLE 3.3: Bandwidths of the different devices used to generate and detect the thermal states.

Device	Bandwidth
EOM	DC-200 MHz
Red Pitaya	DC-60 MHz
Amplifier	DC-1 MHz
Homodyne detector	DC-100 MHz
Photodiode	DC-200 Hz
Avalanche photodiode	DC-10 Hz

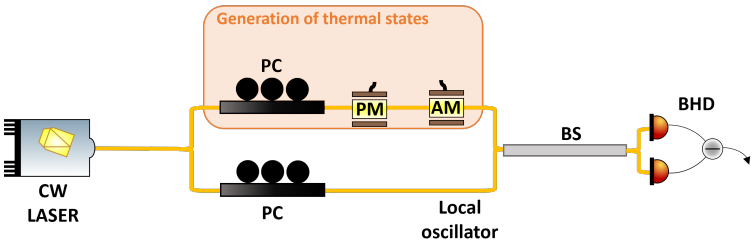

FIGURE 3.25: Experimental setup for generating thermal states with an amplitude EOM (AM) and a phase EOM (PM), and for characterizing the generated states with balanced homodyne detection (BHD). PC: Polarization controller, BS: Beamsplitter.

Figure 3.26 presents a typical measurement obtained with homodyne detection, with a measurement time of 100 ms. In this figure, we display the distributions of the phase (left plot) and amplitude (middle plot) modulation voltages measured at the outputs of the amplifiers. We observe that the modulators are properly driven by distributions of the form eqs. (3.12) and (3.16). We also display in this figure, the distribution of the voltages at the output of the homodyne detector (right plot), which measures the field modulated with the obtained phase and amplitude modulations (left and middle plots).
By fitting the obtained probability distribution with a Gaussian function, and comparing its variance to the vacuum variance, we access the temperature of the generated thermal state. Indeed, the variance of the marginal distributions of the vacuum is $\sigma_0^2 = 1$, and the variance of the marginal distributions of a thermal state with mean photon number N_{th} is $\sigma_{th}^2 = (2N_{th} + 1)^2$. This means that we have the relation:

$$N_{th} = \frac{\sigma_{th}}{2\sigma_0} - \frac{1}{2}. \tag{3.19}$$

Therefore, for the generated state of fig. 3.26, the temperature is $N_{th} = 23.3$ in this case.

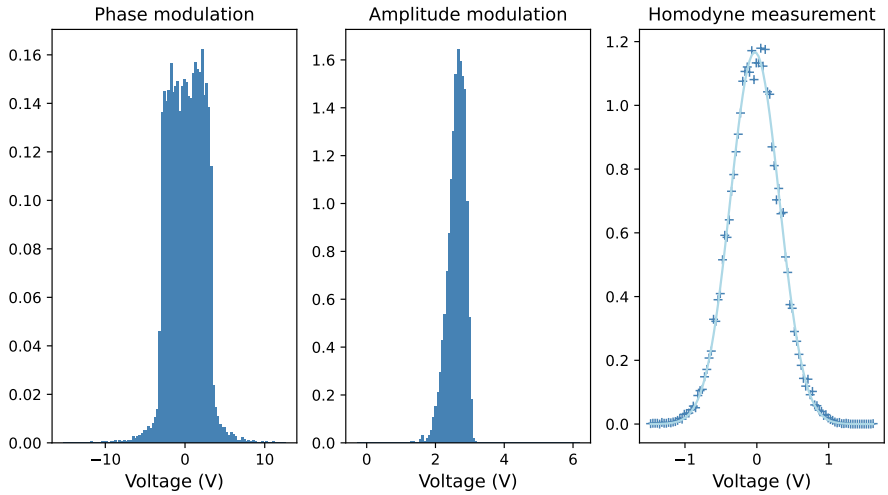

FIGURE 3.26: Thermal state measured with a measurement time of 100 ms. We display the probability distributions of the phase (left plot) and amplitude (middle plot) modulation voltages measured at the outputs of the amplifiers. We also display in this figure, the distribution of the voltages at the output of the homodyne detector (right plot), which measures the field modulated with the obtained phase and amplitude modulations (left and middle plots).

Since the modulators are sensitive to thermal fluctuations, it was important to assess how stable the generated states are. We visualize in fig. 3.27 a marginal of the Wigner function of generated thermal states, averaged over 100 ms, for a total measurement time of 1 s. For some of them, a dip appears in the center, this corresponds to a slight shift in the amplitude modulation due to thermal fluctuations, because of shifts in the amplitude modulation. Nevertheless, they remain close to a thermal state as their Gaussian fits are of good quality.

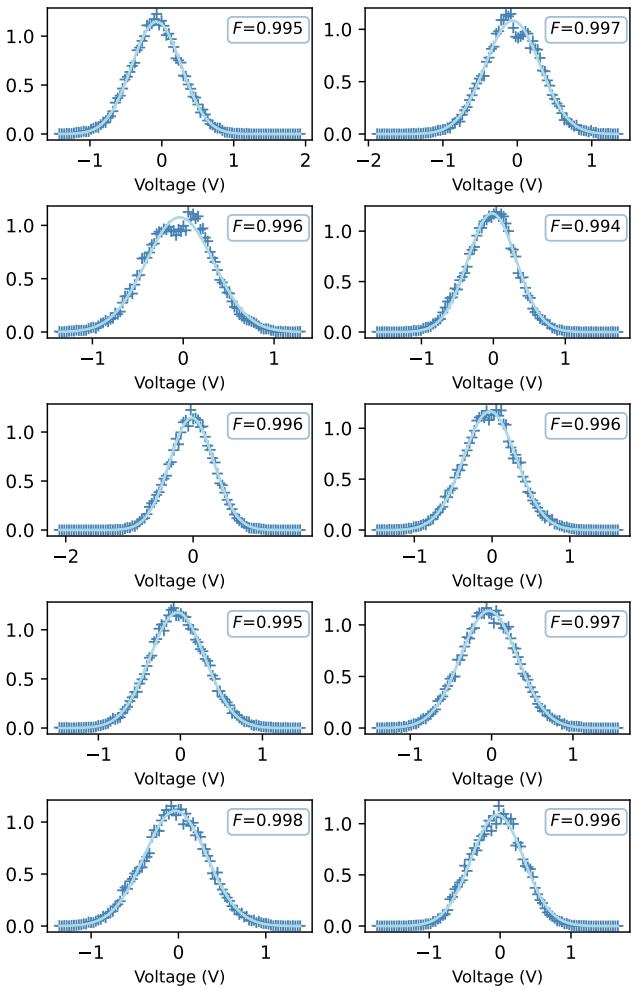

FIGURE 3.27: Evolution over time of a thermal state averaged over 100 ms, with total measurement time of 1 s. Each histogram corresponds to the probability distribution of the measured voltage and is fitted with a Gaussian function. The number F indicated in the upper right corner is the overlap between the histogram of the generated state and to the same the Gaussian function corresponding to the fit in fig. 3.26 thermal state. We observe that the overlap varies only slightly.

3.5.4 Incoherent sources

At the time when we performed the measurement, we were not able to generate thermal states with high mean photon numbers, because the laser was not powerful

enough. However, we wanted to perform the experiment in two distinct photon-flux regimes, at low flux (with 3500 detected photons in total per integration time) and at high flux (with 10^{13} detected photons in total per integration time). This is why, in order to be in the same situation for the high-flux and the low-flux regimes, we decided to have two Poissonian sources that are mutually incoherent. Note that, in the low-flux regime, thermal states are written, in each coherence time interval, as

$$\hat{\rho} = |0\rangle \langle 0| + \varepsilon |1\rangle \langle 1| , \tag{3.20}$$

with $\varepsilon \ll 1$, and, therefore, display Poissonian statistics.
For generating mutually incoherent sources, only the phase modulators are on with the same uniform phase distribution. Since this is realized with two independent phase modulators, one for each source, the two beams are mutually incoherent. We can see signatures of the incoherence spatially in fig. 3.28 and temporally in fig. 3.29.

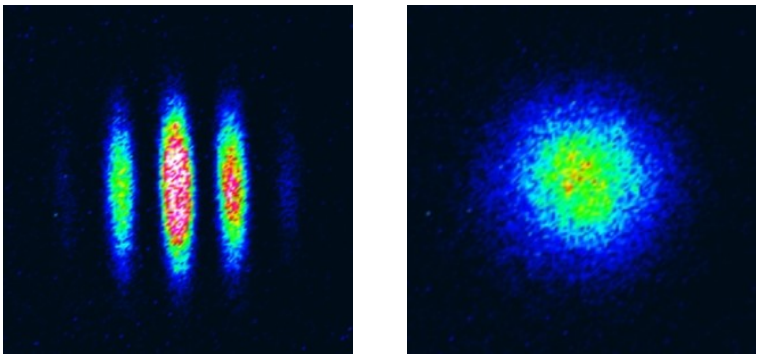

FIGURE 3.28: Spatial incoherence. Images acquired by an infrared CCD camera after the beamsplitter which mixes the two sources when the beams overlap perfectly. A small angle is introduced between the two beams for visualizing the interference fringes. The fringes appear when the phase modulators are off (left), and disappear when the modulators are turned on (right).

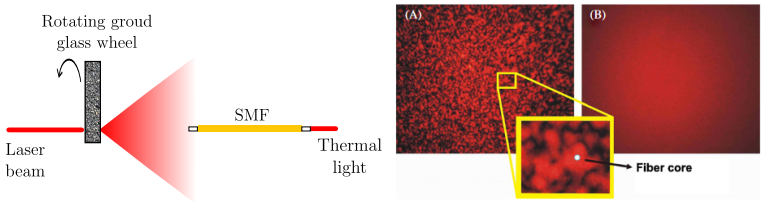

FIGURE 3.30: Generating thermal states with a rotating ground glass wheel. When the ground glass is illuminated with a laser beam, the scattered light forms speckles (A), and a single-mode fiber is placed after the disk to collect light. Rotating the round glass disk induces many speckle contributions with random amplitudes and phases to rapidly mix up (B), and light at the output of the single-mode fiber has the statistics of a thermal state. Source: [Parigi 2009].

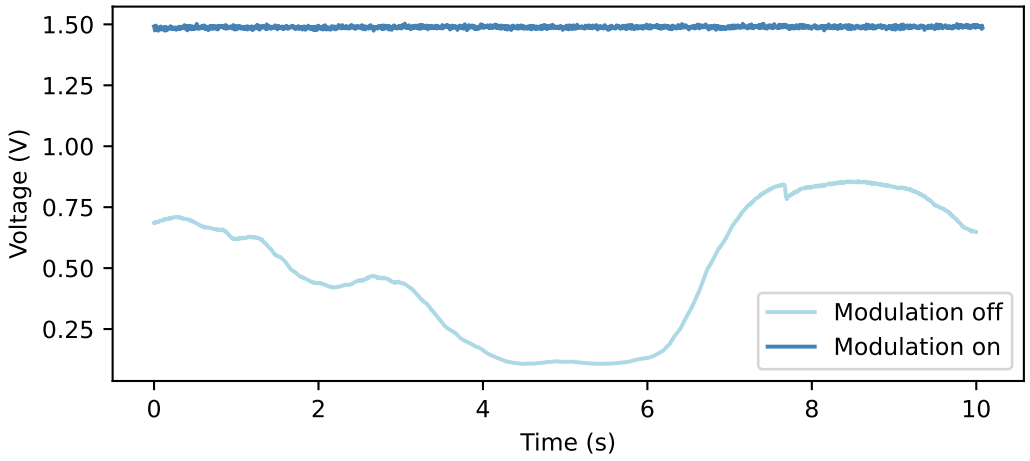

FIGURE 3.29: Temporal incoherence. Signal detected by the photodiodes after the beamsplitter which mixes the two sources, when the two beams overlap perfectly. Interference fringes appear when the phase modulators are off (light blue), and disappear when the modulators are turned on (dark blue).

The measurements were realized for two very different photon fluxes, 3500 and 10^{13} detected photons per integration time.

3.5.5 Sidenote: a first attempt to generate thermal states with speckles

A popular and cheap trick to generate thermal states that meet all the above requirements is realized using a rotating ground glass disk and a single-mode fiber. When the ground glass is illuminated with a laser beam, the scattered light forms speckles, and a single-mode fiber is placed after the disk to collect light, as illustrated in fig. 3.30.

If the core diameter of the fiber is smaller than the average size of the speckle, only a single speckle is coupled into the fiber and its output is a coherent Gaussian

beam. It has been shown experimentally that rotating the round glass disk induces many speckle contributions with random amplitudes and phases to rapidly mix up, and light at the output of the single-mode fiber has the statistics of a thermal state as defined by eq. (1.123) [Arecchi 1965; Parigi 2009]. We performed this technique with tracing paper, instead of ground glass. The intensity at the output of the fiber was too low however and did not allow to explore a large range of mean photon numbers. Moreover, it does not give access to easy control of the coherence between the two sources.

Chapter 4

Expected sensitivity of the PEsto experiment

Contents

As we saw in section 2.5.4, when performing SPADE with an infinite number of modes, the Fisher information for the estimation of the separation between two incoherent equally bright sources is constant and saturates the QFI. The sensitivity on the estimation of d is, therefore, independent of the true value and arbitrarily small separations can be resolved equally well as large ones. This is, however, only true for ideal measurements, without noises or imperfections. In realistic scenarios,

noise sources are present at different stages of the estimation scheme: quantum noise and laser noise at the source generation stage, crosstalk at the demultiplexing stage, and electronic noise at the detection stage.

Assuming the estimation is unbiased, the figure of merit to benchmark is the sensitivity, quantified with the standard deviation of the estimation $\Delta\tilde{d}$. This chapter aims to evaluate how the sensitivity of the estimation is affected by the different noise sources. The first section establishes the link between noises and sensitivity, and the following sections examine all the noise sources one after the other to determine which are the dominant ones between the electronic noise of the detection apparatus in section 4.2, the laser noise in section 4.3, and the phase noise in section 4.4. They are summarized in section 4.5 before the effects of crosstalk are studied in section 4.6.

4.1 Noise sources and expected sensitivity

The experiment aims at estimating the separation between two incoherent sources, in the short separations range, i.e. for separations shorter than the beam size w_0, and where the axis of the sources is aligned to the x-axis of the MPLC. Each source emits N photons, and, because of the losses of the detection apparatus $(1-\kappa)$, with $\kappa < 1$, the total detected photons at all the outputs of the MPLC is $2N\kappa$.
In this setting, the sensitivity for SPADE with only the mode HG_{10} saturates the QFI (see fig. 2.10). This is why we only measure the intensity at the output of the HG_{10} mode, and we denote the associated photon number $\hat{N}_{10}$. In the following, we denote $N_{10} = \langle \hat{N}_{10} \rangle$. As described in section 2.2.3, we first built a calibration curve, i.e. we determined experimentally the mean photon number N_{10} at the output of the HG_{10} mode of the MPLC as a function of the separation between the two sources. Then, by inverting the calibration curve, we have access to the estimation $\tilde{d}$ after measuring N_{10} when the two sources are separated by a distance d.
The theoretical variance of the estimation is given by eq. (2.44)

$$\Delta^2\tilde{d} = \frac{\Delta^2\hat{N}_{10}}{\mu(\partial_d N_{10})^2}, \tag{4.1}$$

where μ is the number of measurements realized to estimate the separation.
Since we study Poissonian statistics, it is equivalent to increase the integration time for one measurement and the number of measurements. We chose to have $\mu = 1$ and we determined the variance $\Delta^2\tilde{d}$ by realizing the estimation 200 times. One measurement corresponds to an integration time which is either $t_{int} = 5\,\text{ms}$, corresponding to $2N\kappa = 10^{13}$ photons detected at all the outputs of the MPLC for the high-flux regime, or $t_{int} = 100\,\text{ms}$, i.e. $2N\kappa = 3500$ detected photons, for the low-flux regime.
As eq. (4.1) emphasizes, the variance of the estimation depends on the variance of the number of measured photons N_{10}, which has several sources of fluctuations. These noise sources are the laser noise $\Delta\hat{N}_{10}^{\text{LN}}$ - composed of the quantum noise of the light (or shot noise) $\Delta\hat{N}_{10}^{\text{SN}}$ and a classical intensity noise $\Delta\hat{N}_{10}^{\text{CN}}$, the electronic noise of the detection apparatus $\Delta\hat{N}_{10}^{\text{EN}}$ or the phase noise due to the presence of two

sources $\Delta\hat{N}_{10}^{\mathrm{PhN}}$. Because all these noises are uncorrelated, we can rewrite eq. (4.1) as

$$\Delta^2\tilde{d} = \frac{\Delta^2\hat{N}_{10}^{\mathrm{LN}} + \Delta^2\hat{N}_{10}^{\mathrm{EN}} + \Delta^2\hat{N}_{10}^{\mathrm{PhN}}}{\mu(\partial_d N_{10})^2}. \tag{4.2}$$

Finally, another experimental imperfection that affects the sensitivity of the separation estimation is crosstalk [Gessner 2020a]. Crosstalk arises from the slight deviation in the decomposition of multimode light by the MPLC from the ideal Hermite-Gaussian modes (see section 4.6). Since the HG mode basis is the target basis of the decomposition performed by the MPLC, we continue to designate the diverse outputs from the single-mode fibers as HG_{nm} mode outputs, acknowledging the presence of crosstalk. The imperfect mode basis decomposition is not a noise strictly speaking, but it affects the number of photons detected at the different outputs of the MPLC, in particular N_{10}. Consequently, this imperfection has a discernible impact on the sensitivity of the separation estimation[1].

In the following sections, we study the influence of each noise on the sensitivity of the estimation from our experimental data by determining their order of magnitude. Crosstalk will be examined in the last section.

4.2 Electronic noise of the detection apparatus

In this section, we explore the noise introduced by the photodetection stage, at the output of the MPLC. The electronic noise of the detection apparatus reduces the signal-to-noise ratio. In the low-flux regime, it corresponds to the dark counts of the single-photon detectors which introduces additional photon counts that do not contain any information on the separation.
In the high-flux regime, the noise emerges from both the detectors and the oscilloscope, they also add an extra contribution to the variance in the number of detected photons. The effect of electronic noise on separation estimation using SPADE was investigated in the literature with different approaches [Lupo 2020; Len 2020; Oh 2021] in the single-photon regime. They agree that, in the presence of dark counts, the Fisher information drops to zero for short separations. Sorelli *et al.* [Sorelli 2021a] studied how to take it into account in the method of moment and how it affects the sensitivity of the estimation.
In this section, in the spirit of this chapter, we approach the electronic noise in a practical manner by determining the order of magnitude of its contribution to the estimations we conducted.

4.2.1 Bright sources: photodiodes and oscilloscope

When the MPLC is illuminated with bright sources, the intensity at its outputs is measured with photodiodes, and the experimental data are acquired with an oscilloscope. We want to determine the variance $\Delta^2\hat{N}^{\mathrm{EN}}$ introduced by these electronical

[1] In principle, the crosstalks introduce some biases too. However, since we use an experimental calibration curve for the estimation (see chapter 5), these biases are taken into account and, therefore, the estimation could be considered unbiased.

components.
We acquired the offset signals - the output voltage of the detectors, acquired with the scope, when they are not illuminated with light - for an integration time of 5 ms, which is the same as during the estimation measurements (see chapter 5). We repeated these measurements for 2000 samples, on which we extracted the variance of the measured voltage Δ^2U. Since the electronic noise depends, in practice, on the gain of the detectors and the scale of the oscilloscope, we realized this procedure for several detector gains (40 dB, 50 dB, 60 dB, 70 dB) and oscilloscope scales (10 mV, 20 mV, 50 mV, 100 mV, 200 mV, 500 mV, 1 V).
The results are plotted in fig. 4.1(top) where the standard deviation of the measured voltage ΔU is represented as a function of the scope scale. We observe that for the highest gains, especially the 70 dB-gain, the electronic noise is dominated by the noise of the detector, while, for the highest scope scales, the electronic noise is dominated by the noise of the scope.

We also expressed the electronic noise in terms of noise on the equivalent optical power. The measured offset voltages U are converted in equivalent optical powers P using

$$P = \frac{\mathrm{U}}{\mathcal{R}G}, \tag{4.3}$$

where $\mathcal{R}$ is the responsivity of the photodetectors (for our photodiodes, $\mathcal{R} = 0.85\,\mathrm{A\,W^{-1}}$) and G is the gain of the detectors.
The voltages corresponding to the scope scales $\mathrm{U_{scale}}$ are also converted into equivalent optical powers, that we denote the equivalent optical power setting P_{setting}. Indeed, while acquiring the data for separation estimation (see chapter 5), we adjusted the scale of the scope so that the measured voltage reached half of the maximal voltage of the scope, which corresponds to 5 divisions. This is why we determined the equivalent optical power for each scope scale by converting the half-maximal voltage into an optical power using eq. (4.3) using

$$P_{\mathrm{setting}} = \frac{5\,\mathrm{U_{scale}}}{\mathcal{R}G}. \tag{4.4}$$

The electronic noise in terms of the equivalent optical power ΔP as a function of the equivalent optical power setting P_{setting} is represented in fig. 4.1(bottom).

We write the variance of the electronic noise $\Delta^2 P$ as a sum of two noises $\Delta^2 P = \Delta^2 P_0 + \Delta^2 P_1$. The total electronic noise in terms of the equivalent optical power ΔP is fitted with the function

$$f(P) = \sqrt{(a \cdot P)^2 + b^2}. \tag{4.5}$$

The first term is independent of the mean measured power and is the noise offset $\Delta P_0 = b = 2.6 \times 10^{-10}\,\mathrm{W}$, and the second term is a standard deviation proportional to the measured power $\Delta P_1 = a \cdot P = 3.8 \times 10^{-4} \cdot P$. The variance $\Delta^2 P$ can also be written in terms of the number of photons as follows

$$\Delta^2 \hat{N}^{\mathrm{EN}} = 1.1 \times 10^{14} + 1.5 \times 10^{-7} \cdot N^2. \tag{4.6}$$

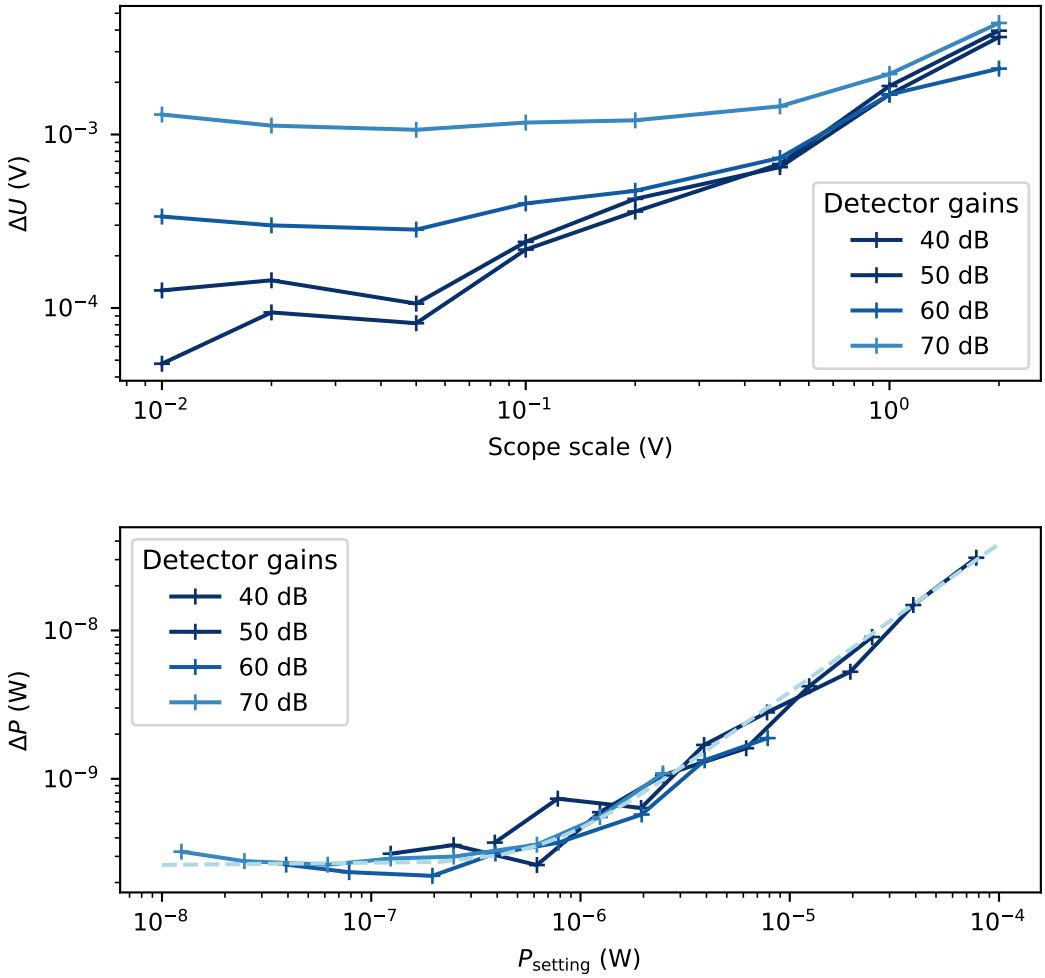

FIGURE 4.1: Electronic noise for detection in the high-flux regime, for a total measurement time of 10 s and an integration time of 5 ms. (top) Standard deviation of the voltage of the offset signal of the detectors as a function of the scope scale, for different gains of the photodiodes. (bottom) Equivalent optical power noise as a function of the equivalent optical power for the scope scale and detector gain, the experimental points are fitted with the function f in eq. (4.5) (dashed blue line).

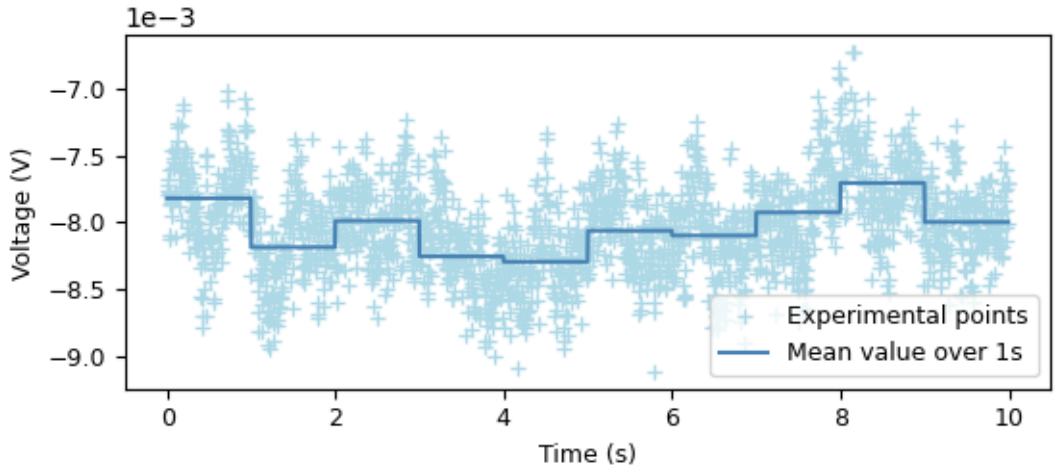

FIGURE 4.2: Offset signal of the photodiode at the HG_{10} output.

We mention that this is only an approximation of the actual electronic noise. Indeed, due to the working principle of the photodiodes, the electronic noise might vary with the incident optical power, in a different way than eq. (4.6).

We also observed that the offsets of the detectors are not stable. The offset signal of the photodiode at the HG_{10} output over 10 s is plotted in fig. 4.2. Since the estimation is obtained from the mean value over 200 samples, i.e. over 1 s for a 5 ms integration time, we evaluated the variations of the mean value of the offset signal, and these are also represented on fig. 4.2. These electronic fluctuations introduce some systematic errors in the estimation.

4.2.2 Faint sources: SPAPD

For the single-photon avalanche photodiodes (SPAPD) that we used for the low flux measurements, we assume that the dark counts are constant and independent of the incident number of photons. In order to measure the electronic noise, as explained in the previous section, we acquire the offset signal - without incident light - of the APD, and determine its variance over the same integration time of the estimation measurements 100 ms.
We found $\Delta^2\hat{N}^{\mathrm{EN}} = 30$, over 200 samples. Therefore, using eq. (4.9), the electronic-noise-limited sensitivity, for the low-flux regime is represented in fig. 4.3.

4.3 Laser noise

Lasers, in general, do not generate perfect coherent states and exhibit an intensity noise larger than the shot noise section 1.2.4, with a classical contribution. The quantum and classical contributions to the intensity noise of the laser being uncorrelated, we can artificially divide the laser noise into two noises, the shot noise

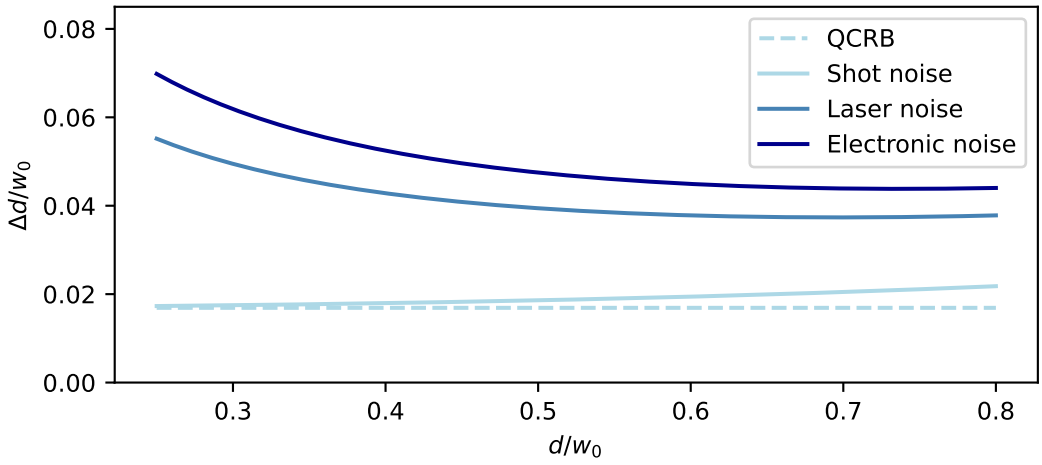

FIGURE 4.3: Standard deviation of the estimation as a function of the true value while taking into account different noise contributions in the low-flux regime. The dashed line is the quantum Cramér-Rao bound, the light blue line corresponds to the shot noise contribution, the blue line is the laser noise added to the shot noise contribution and the dark blue line is the electronic noise added to the laser and shot noises contribution. The dark blue line corresponds to our experimental configuration since it takes into account all the noise sources.

$\Delta^2\hat{N}^{\mathrm{SN}}$ and the classical noise $\Delta^2\hat{N}^{\mathrm{CN}}$, arising from electronic and thermal fluctuations: $\Delta^2\hat{N}^{\mathrm{LN}} = \Delta^2\hat{N}^{\mathrm{SN}} + \Delta^2\hat{N}^{\mathrm{CN}}$. When detecting laser light with a photodetector, the total measured noise also accounts for the electronic noise and is, therefore, $\Delta^2 N^{\mathrm{tot}} = \Delta^2\hat{N}^{\mathrm{LN}} + \Delta^2\hat{N}^{\mathrm{EN}}$.
This section examines the laser contribution to the intensity noise, compared to the electronic noise, in both the high-flux regime, where we used photodiodes for the detection, and the low-flux regime, where the detection was performed with single-photon avalanche photodiodes.

4.3.1 Shot noise

We begin to investigate the quantum noise, i.e. the only noise source that is intrinsic to the state of the electromagnetic field. Since we chose to generate phase-averaged coherent states of intensity $|\alpha|^2 = N$, the quantum noise is given by the shot noise which is $\Delta^2\hat{N}^{\mathrm{SN}} = N$. Assuming the centroid of the sources is aligned on the MPLC, the total number of photons at the output of the mode HG_{10} from two sources located in positions $x_{1,2} = \pm d/2$ reads

$$N_{10} = N\kappa \left(\beta_{10}\left(\frac{d}{2}\right)^2 + \beta_{10}\left(-\frac{d}{2}\right)^2\right) = 2N\kappa\beta_{10}\left(\frac{d}{2}\right)^2, \tag{4.7}$$

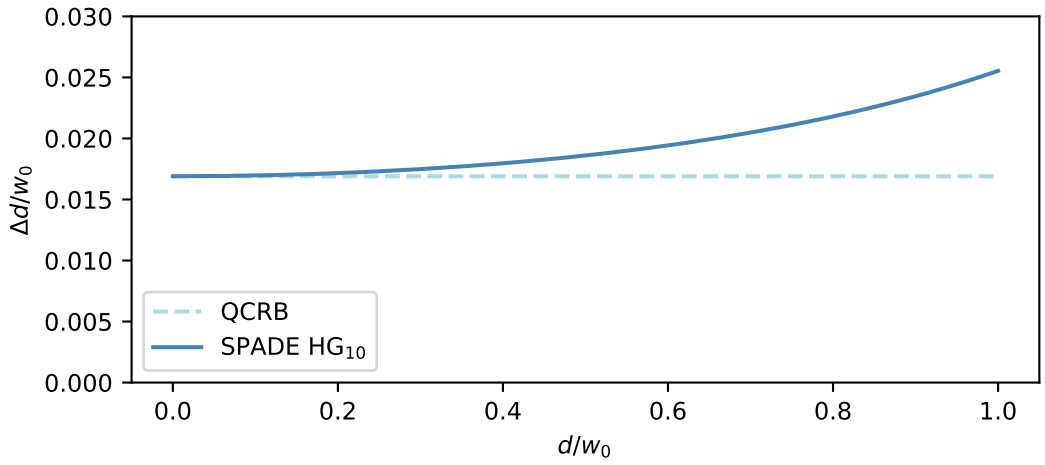

FIGURE 4.4: Shot noise-limited sensitivity for HG_{10} measurement, for $2N\kappa = 3500$ detected photons.

where each source emits N photons during the integration time t_{int} and

$$\beta_{10}(x) = \frac{x}{w_0} \exp\left[-\frac{x^2}{2w_0^2}\right] \tag{4.8}$$

is the mode overlap as defined by eq. (2.86). The derivative of eq. (4.7) with respect to d gives access to the denominator of eq. (4.2)

$$\partial_d N_{10} = 2N\kappa \frac{d}{2w_0^2}\left(1 - \frac{d^2}{4w_0^2}\right) \exp\left(-\frac{d^2}{4w_0^2}.\right) \tag{4.9}$$

Therefore, the shot-noise limited estimator has a variance given by

$$\Delta^2 d_{SN}(d) = \frac{\Delta^2 N_{10}^{\mathrm{SN}}}{(\partial_d N_{10})^2} = \frac{N_{10}}{(\partial_d N_{10})^2} = \frac{w_0^2}{2N\kappa} \frac{\exp\left(\frac{d^2}{4w_0^2}\right)}{\left(1 - \frac{d^2}{4w_0^2}\right)^2}. \tag{4.10}$$

The prefactor $\frac{w_0^2}{2N\kappa}$ corresponds to the quantum Cramér-Rao bound (for the sources with Poisson statistics), and the second part is close to 1 in the sub-Raleigh regime $d \ll w_0$, i.e. HG_{10} measurement is close to being quantum optimal for small separations, as illustrated in fig. 4.4 for $2N\kappa = 3500$.

4.3.2 Bright sources

We now examine the laser noise in the high photon flux regime.
We acquired the voltage of the output of the photodiode at the HG_{10} output of the MPLC illuminated by one source, during 5 ms, and we repeat this measurement

over 200 samples to extract the statistics, in particular, the mean value of the detected photon number which corresponds to the shot noise $\Delta^2\hat{N}_{10}^{\mathrm{SN}}$ and the variance which is the total measured noise $\Delta^2\hat{N}_{10}^{\mathrm{tot}}$.
Typically, the mean number of detected photons is $N_{10} \approx 10^{10}$, which results in an electronic noise of $\Delta^2\hat{N}_{10}^{\mathrm{EN}} \approx 10^{14}$, according to eq. (4.6). Additionally, the total measured noise is of the same order, $\Delta^2\hat{N}_{10}^{\mathrm{tot}} \approx 10^{14}$. This suggests that the laser noise is, in our case, negligible compared to the electronic noise of the photodiodes and oscilloscope.

4.3.3 Faint sources

We conducted the same analysis for the low-flux regime, only changing the integration time to 100 ms. In this regime, we used single-photon avalanche photodiodes, which are adapted to the photon flux and much less noisy than the photodiodes.
We obtained a typical laser noise of $\Delta^2\hat{N}_{10}^{\mathrm{LN}} \approx 400$ which slightly varies with the mean number of detected photons and is of the same order of magnitude as the shot noise $\Delta^2\hat{N}_{10}^{\mathrm{SN}}$. We compare this value to the electronic noise measured in section 4.2.2, $\Delta^2\hat{N}_{10}^{\mathrm{EN}} \approx 30$.
Consequently, when detecting faint sources, the laser noise has to be taken into account, along with the shot noise, and, to a lesser extent, the electronic noise of the detectors.
The laser noise is roughly constant over the range of estimated separations, accordingly, using eq. (4.9), the sensitivity limited by the laser and shot noises is represented in fig. 4.3.

4.4 Phase noise from the residual interference

We now consider the noise due to the interference between two mutually incoherent sources. Indeed, even though the mean number of photons of the two sources is the sum of the mean number of photons of each source, the variance in the photon number is increased compared to the variance of a single coherent state. This section models the interference between the two sources to extract the extra noise term, which is referred to as the phase noise, and examines if this noise is observable in the experimental results.

4.4.1 Modeling phase noise

As presented in section 3.5, we generate two incoherent sources by modulating their phase randomly. Because the two beams are a mixture of coherent states, they interfere and this effect broadens the variance of the measured intensity. This interference noise will be referred to as the phase noise and, in this section, we extract its contribution.
We consider that, within a time duration equal to the coherence time τ_c, the two beams are in two coherent states $|\alpha\rangle$ and $|\alpha e^{i\varphi}\rangle$ with a fixed phase φ. Note that the coherence time τ_c is governed by the bandwidth of the phase modulators, and is

typically of 1 µs for our measurements. Both sources have the same mean photon number $N_c = |\alpha|^2$ at the scale of the coherence time τ_c. They are mixed and detected with efficiency κ<1, resulting in the measured state being $\left|\sqrt{\kappa}(\alpha + \alpha e^{i\varphi})\right\rangle$. Therefore, the mean number of photons detected during this time interval is:

$$n(\varphi) = \kappa|\alpha + \alpha e^{i\varphi}|^2 = 2N_c\kappa(1 + \cos\varphi), \tag{4.11}$$

and the probability conditional probability to detect m photons given a phase φ, in this time interval, is

$$p(m|\varphi) = \frac{n(\varphi)^m}{m!}e^{-n(\varphi)}. \tag{4.12}$$

Using the law of total probability and eq. (4.11), we obtain the probability of detecting m photons during τ_c when φ is not known:

$$p(m) = \int_0^{2\pi} \mathrm{d}\varphi P(\varphi)p(m|\varphi) = \int_0^{2\pi} \mathrm{d}\varphi \frac{1}{2\pi}\frac{n(\varphi)^m}{m!}e^{-n(\varphi)}, \tag{4.13}$$

where $P(\varphi) = \frac{1}{2\pi}$ since the phase is a random variable with a uniform probability distribution over 2π (see section 3.5.4).
From eq. (4.12), we can find the mean value and the variance of the number of detected photons during τ_c

$$\begin{aligned}
\langle m\rangle &= \sum_{m=0}^{+\infty} p(m)m = 2N_c\kappa, \\
\langle m^2\rangle &= \sum_{m=0}^{+\infty} p(m)m^2 = 2N_c\kappa + \frac{3}{2}(2N_c\kappa)^2, \\
\Delta^2 m &= \langle m^2\rangle - \langle m\rangle^2 = 2N_c\kappa + \frac{(2N_c\kappa)^2}{2}.
\end{aligned} \tag{4.14}$$

At the scale of the integration time of the detectors t_{int} (either 5 ms or 100 ms depending on our experimental configuration), with $t_{\mathrm{int}} \gg \tau_c$, the number of detected photons N_{int} is a random variable such that

$$N_{\mathrm{int}} = \sum_{i=0}^{M} m_i \tag{4.15}$$

where $M = t_{\mathrm{int}}/\tau_c$ and $\{m_i\}$ are independent random variables with the probability distribution given by eq. (4.13). Consequently, the two first moments of the probability distribution of N_{int} are directly given by

$$\begin{aligned}
\langle N_{\mathrm{int}}\rangle &= \sum_{i=0}^{M}\langle m_i\rangle = N_{\mathrm{det}} \\
\Delta^2\hat{N}_{\mathrm{int}} &= \sum_{i=0}^{M}\Delta^2 m_i = N_{\mathrm{det}} + N_c\kappa\cdot N_{\mathrm{det}}.
\end{aligned} \tag{4.16}$$

where $N_{\mathrm{det}} = M\cdot 2N_c\kappa$ is the mean total number of photons detected during one unit of integration time.

We see that the variance of the total intensity at the scale of the integration time $\Delta^2\hat{N}_{\text{int}}$ presents two terms, the first one N_{det} corresponding to the shot noise, and the second one which is the phase noise:

$$\Delta^2\hat{N}^{\text{PhN}} = N_c\kappa \cdot N_{\text{det}}. \tag{4.17}$$

Therefore, we observe two regimes: a low-flux regime per coherence time where $N_c\kappa$<1 and the phase noise is negligible compared to the shot noise, and a high-flux regime per coherence where $N_c\kappa$>1 and the phase noise can surpass the shot noise. Our experimental configuration corresponds to the latter.

4.4.2 Experimental results

We evaluate the phase noise contribution in both photon flux regimes.
For bright sources, we acquired the signal at the output of the photodiode at the HG_{10} output, when illuminating it with either one of the beams or both beams, modulated with the uniform phase noise, as described in section 3.5.4. As for extracting the other noise contributions, the integration time was 5 ms and we determined the mean value and the variance of the number of detected photons over 2000 samples. The experimental results are presented in fig. 4.5 for typical intensity values, where we plot the detected number of photons over time. The mean photon number detected during 10 s was subtracted in order to compare the variances of the individual sources and of both sources simultaneously.
The total measured noise is the same for one and two sources, of around $\Delta^2\hat{N}_{10}^{\text{tot}} \approx 6 \cdot 10^{13}$, which corresponds to the order of magnitude of the electronic noise given by eq. (4.6) $\Delta^2\hat{N}_{10}^{\text{EN}} \approx 10^{14}$. Moreover, using eq. (4.17), we estimate the phase noise to be $\Delta^2\hat{N}_{10}^{PhN} \approx 10^{14}$. Both the electronic noise of the detection and the phase are of the same order of magnitude. The contribution of the phase can be reduced by modulating the phase faster.

We follow the same procedure for faint sources, adapting the integration time and the number of detected photons. Here, we obtain that the phase noise ($\Delta^2\hat{N}_{10}^{\text{PhN}} \approx 0.2$, using eq. (4.17)) contributes only marginally to the total measurement ($\Delta^2\hat{N}_{10}^{\text{tot}} \approx 10^3$). In this setting, the dominant noise source is the laser noise ($\Delta^2\hat{N}_{10}^{\text{LN}} \approx 4 \cdot 10^2$).

In both photon flux regimes, the measured intensities at the HG_{10} output are low enough so that the phase noise does not contribute to the sensitivity of the estimation.

4.4.3 Some remarks

We presented a simple model for the phase noise, that could be refined in several ways to reflect the experimental reality. The phase does not jump from one value to the next one and is not constant within the duration of a coherence time. Instead, the changes are continuous and the phase values present some oscillations within a coherence time. Because of these approximations, the phase noise modeling that we established does not correspond to what is observed with higher intensities, like those which are measured at the HG_{00} output. It is, however, not critical to understand the noise limitations for the estimation since only the HG_{10} output is exploited.

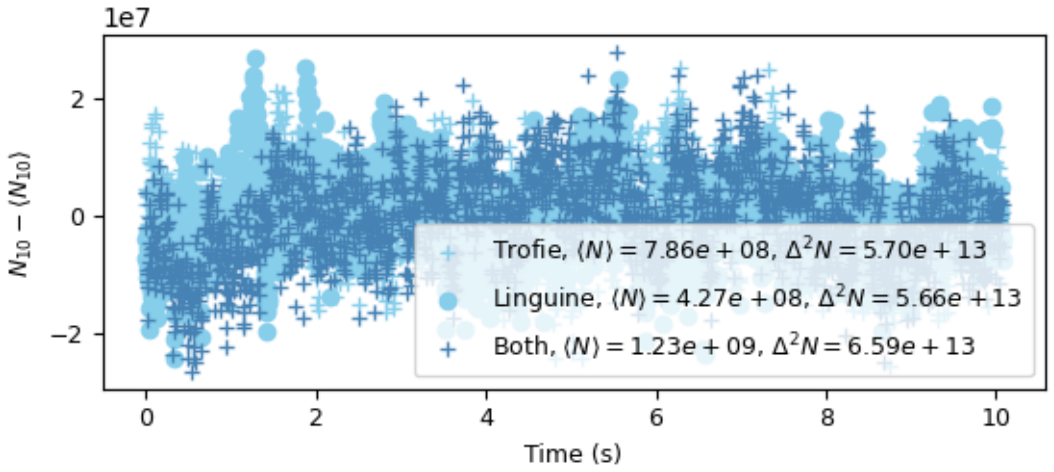

FIGURE 4.5: Number of photons detected at the HG_{10} output in the bright source regime over time, normalized by its mean value over 10 s, for each source individually and both sources simultaneously, when the sources are phase modulated with uniform noise over 2π. The integration time is 5 ms. The total measured variance of the number of detected photons is the same either with one or two sources, suggesting that the phase noise is negligible in this setting.

4.5 Summary of the noise contributions

We summarize the noise contributions in table 4.1. This table is filled with typical values corresponding to the two photon-flux regimes that were studied. It is therefore clear that the dominant contributions to the sensitivity of the estimation are very different. For bright sources, the electronic noise from the photodiode and the oscilloscope and the phase noise were very high, making them the dominant noise source. For faint sources, since the electronic noise of the single-photon avalanche photodiode is low, the sensitivity is limited by the shot noise and the intensity noise of the laser.

TABLE 4.1: Noise contributions for high flux (5 ms integration time, 10^{13} detected photons at all the MPLC outputs) and low flux (100 ms integration time, 3500 detected photons in total) regimes.

Noise	High flux	Low flux
Laser noise $\Delta^2\hat{N}_{01}^{\mathrm{LN}}$ (measured)	Negligible	400
Shot noise $\Delta^2\hat{N}_{01}^{\mathrm{SN}}$ (calculated)	10^9	200
Phase noise $\Delta^2\hat{N}_{01}^{\mathrm{PhN}}$ (measured)	10^{14}	0.2
Electronic noise $\Delta^2\hat{N}_{01}^{\mathrm{EN}}$ (measured)	10^{14}	30

4.6 Crosstalk-limited sensitivity

In chapter 2, we derived the Fisher information for SPADE in an ideal scenario. However, for a realistic apparatus, crosstalk between the modes is unavoidable, the mode basis change into the transverse Hermite-Gaussian basis is inevitably imperfect. These imperfections limit the sensitivity of the separation estimation and change the scaling of the minimal resolvable distance with the total number of detected photons. As we saw in section 2.5.6, the minimal resolvable distance is equivalent to the sensitivity for small separations. It is thus important to measure the crosstalk values to understand the sensitivity limit they set.

4.6.1 Modeling crosstalk and theoretical crosstalk-limited sensitivity

Following [Gessner 2020a] and [Sorelli 2021a], crosstalk between the detection modes are modeled with a unitary matrix $c_{k\ell}$ that maps the ideal HG modes $u_\ell(\mathbf{r})$ into the actual measurement modes $v_k(\mathbf{r}) = \sum_\ell c_{k\ell} u_\ell(\mathbf{r})$, as illustrated in fig. 4.6. Accordingly, the actual overlap functions $f_{\pm,k}$ - which correspond to the overlap between the displaced Gaussian modes $u_{00}(\mathbf{r} \pm \mathbf{r}_0)$ and the detection modes $\{v_k(\mathbf{r})\}$ - defined are linear combinations of the ideal overlap functions given by eq. (2.86)

$$f_{\pm,k}(\mathbf{r}_0) = \int \mathrm{d}^2\mathbf{r}\, v_k^*(\mathbf{r}) u_{00}(\mathbf{r} \pm \mathbf{r}_0) = \sum_\ell c_{k\ell}^* \beta_\ell(\pm\mathbf{r}_0). \tag{4.18}$$

We assume that crosstalk is weak, which means that we consider matrices $c_{k\ell}$ whose off-diagonal elements are small compared to the diagonal ones.
For an analytical study of the typical behavior at small separations, Gessner *et al.* introduce a uniform crosstalk model where the $c_{k\ell}$ matrices are $D \times D$ matrices written as follows:

$$\begin{pmatrix} t & r & \dots & r \\ r & \ddots & \ddots & \vdots \\ \vdots & \ddots & \ddots & r \\ r & \dots & r & t \end{pmatrix} \tag{4.19}$$

The diagonal elements t and off-diagonal elements r are such that $|t|^2 + (D-1)|r|^2 = 1$, and D is the number of modes. The quantity $|r|^2$ is referred to as the crosstalk probability.

For weak crosstalk probabilities ($|r|^2 \ll 1$) and small separations ($d \ll w_0$), Gessner *et al.* established that, for any $Q \geq 1$ (where Q is the largest index of the measured modes in both spatial dimensions, defined like in section 2.5.4), the Fisher information of SPADE with crosstalk is [Gessner 2020a]

$$\frac{w_0^2}{2N\kappa} I_F(d,\theta) \simeq \left(\frac{d}{2w_0}\right)^2 \left(\frac{3+\cos(4\theta)}{4}\right) \frac{1}{|r|^2}, \tag{4.20}$$

where θ is the angle between the source axis and the x-axis of the MPLC.
We can also express eq. (4.20) in terms of the standard deviation of the separation

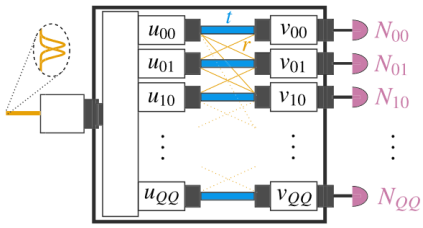

FIGURE 4.6: Crosstalk is an unavoidable imperfection of demultiplexing devices. The actual measurement basis $v_k(\mathbf{r})$ is slightly different from the ideal basis $u_k(\mathrm{r})$, which is the Hermite-Gaussian mode basis in this work. It is schematically represented by each mode being either transmitted into the correct output or reflected into another mode due to crosstalk before the photodetection. Source: [Gessner 2020a].

estimation as follows

$$\frac{\Delta\tilde{d}}{w_0} \approx \frac{|r|}{\sqrt{2N\kappa}} \frac{2w_0}{d} \sqrt{\frac{4}{3+\cos(4\theta)}}. \tag{4.21}$$

This results in a change of scaling in the minimal resolvable distance, using the definition given in section 2.5.6, which becomes

$$d_{\min} = \frac{w_0}{(2N\kappa)^{1/4}} \sqrt{2|r|} \left(\frac{4}{3+\cos(4\theta)}\right)^{1/4}, \tag{4.22}$$

in the presence of crosstalk. We observe that, for low intensities, the minimal resolvable distance keeps the $N^{-1/2}$ scaling of ideal demultiplexing, but when the number of detected photons increases, the presence of crosstalk induces a deviation from this scaling, which becomes a $N^{-1/4}$ scaling, like ideal direct imaging, as illustrated in fig. 4.7.

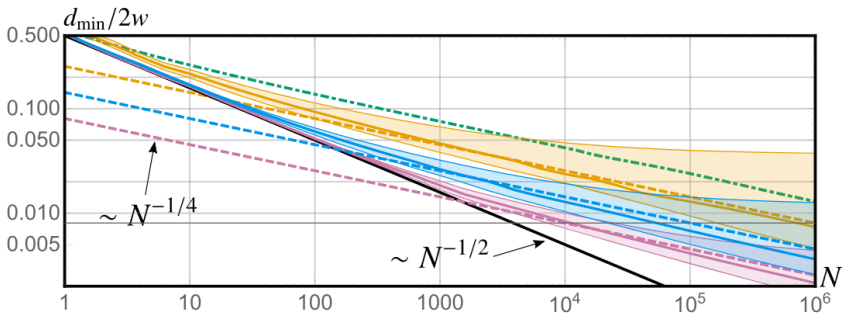

FIGURE 4.7: Minimal resolvable distance as a function of the number of detected photons (N on the graph corresponds to $2N\kappa$ with our notations) in the presence of crosstalk, with low (violet), medium (blue), and high (orange) crosstalk probability for measurements up to $Q = 2$. The ideal $N^{-1/2}$ scaling (black) and the $N^{-1/4}$ scaling of an ideal direct imaging measurement (green) are also represented. Source: [Gessner 2020a].

Even though the scaling of the minimal resolvable distance changes significantly for SPADE when considering crosstalk and meets the $N^{-1/4}$ scaling of ideal direct imaging, the prefactor depends on the crosstalk probability and still might provide an advantage over direct imaging. This is why it is critical to determine this value and, more generally, to determine the transmission matrix of the demultiplexing device.

4.6.2 How to measure the crosstalks

To analyze the behavior of the MPLC we used, we measure its crosstalk matrix, with the input modes being HG_{00}, HG_{10}, HG_{01}, HG_{11}, HG_{20}, HG_{02}, HG_{21}, HG_{12}, HG_{30} and HG_{03} and the output modes are the ten outputs of the single-mode fibers, thus here $D = 10$.
In order to determine the amplitude and the phase of the crosstalks, we generate the ten Hermite-Gaussian modes with high intensities, using another MPLC in the multiplexing direction. Then, injecting each mode in the multimode input of the MPLC of interest and measuring the outputs of the single-mode fibers, we should be able to access the crosstalk values. However, crosstalks are induced in both directions of the basis change (demultiplexing and multiplexing), therefore, the HG modes at the output of the MPLC are imperfect and if we inject them into the MPLC we want to characterize, we would measure the crosstalk of both MPLCs without being able to uncouple them. Consequently, the modes at the output of the multiplexing MPLC have to be cleaned before being coupled into the MPLC of interest, and, for this purpose, we use a cavity of which the HG modes are eigenmodes (see section 4.6.3).

We measured the crosstalk matrix in two steps, first their amplitude and then their phase because they did not involve the same experimental procedure. The amplitude measurement relies on coupling one HG mode to the cavity and measuring the output intensity at each single-mode fiber output. However, to measure their phase, we need to mix two modes. These requirements result in two protocols that will be described in the following sections and that exhibit different degrees of difficulties. Indeed, measuring the amplitude crosstalk was simpler, and experimental results are displayed in fig. 4.14, while we did not established yet the phase crosstalks due to experimental challenges that will be described.

4.6.3 Cleaning the modes with a cavity

Design of the cavity

The simplest design for the mode cleaner cavity would be a linear cavity, as presented in section 1.1.3. However, as displayed in fig. 4.8, in a linear cavity, modes with the same $n + m$ are degenerate. In order to lift the degeneracy for most of the modes, since they are the ones that are critical for estimating short separations, while keeping a simple design and a simple setup for the lock, we chose a triangular cavity. Even though the triangular cavity does not allow to separate all the modes of the MPLC (see fig. 4.8), since the HG_{10} and HG_{01} are the most critical modes to estimate short separations, having them not degenerate with this geometry is sufficient for our study.

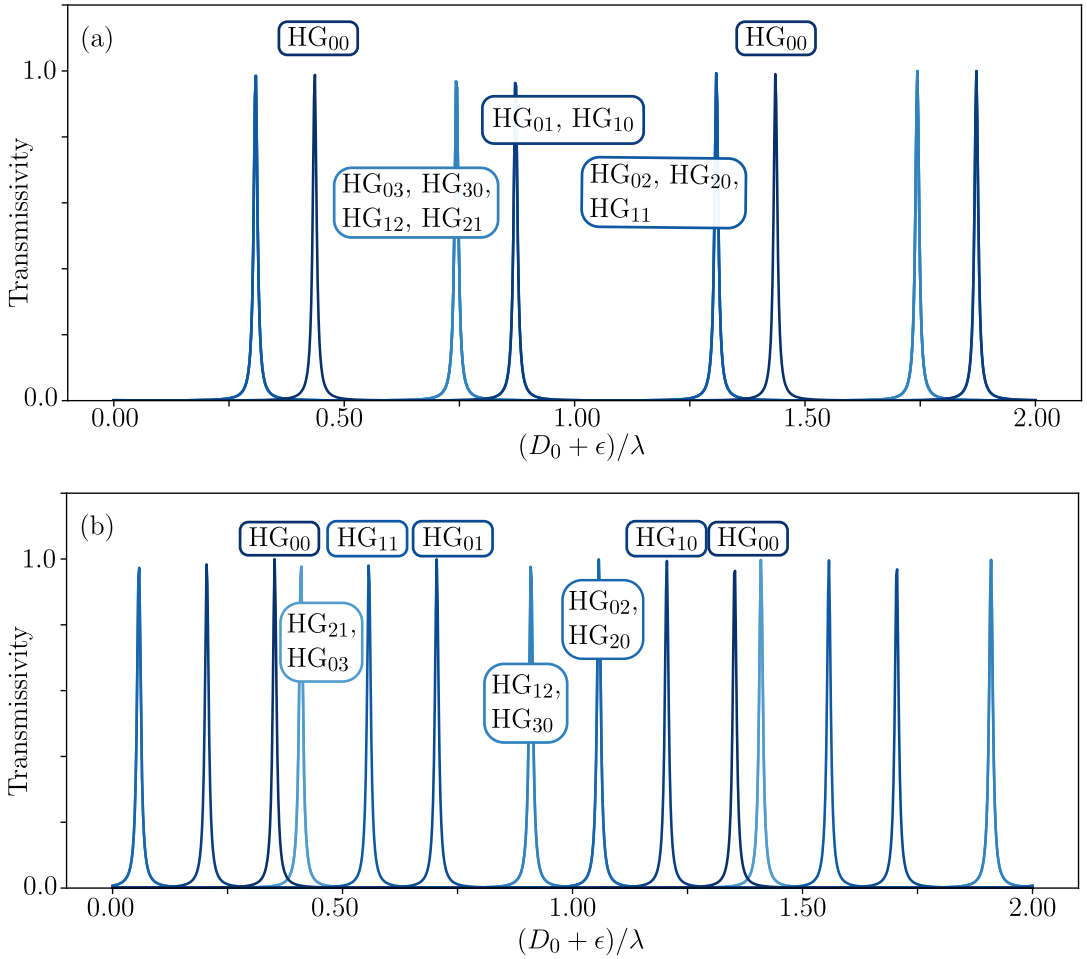

FIGURE 4.8: Transmissivity of (a) a linear and (b) a triangular cavity, with $T = 0.03$ for the modes of the MPLC.

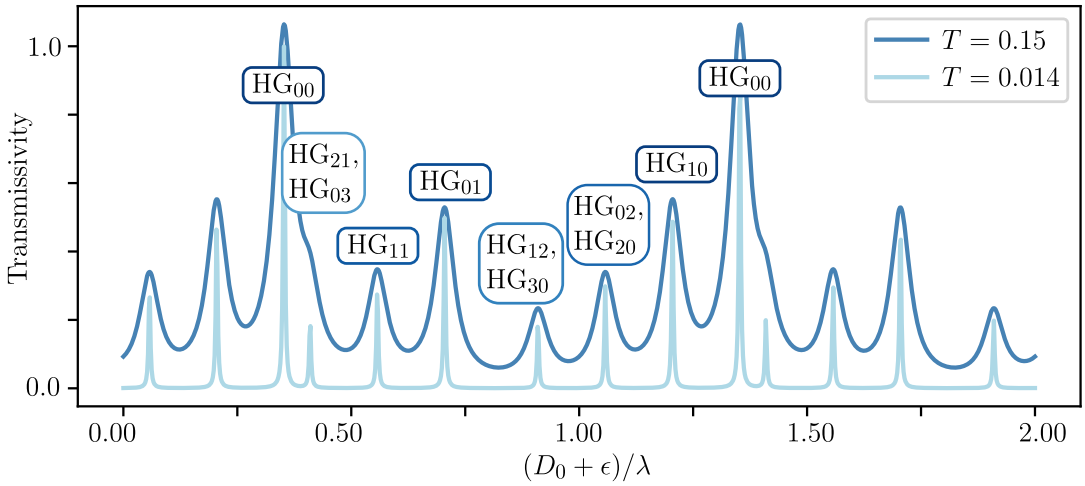

FIGURE 4.9: Comparison of the transmissivity of the triangular cavity with a low and a high finesse.

Following the design presented in section 1.1.3, we chose two plane mirrors (Thorlabs BSX12) as the input and output mirror and a spherical mirror (Thorlabs, CM254-1000-M01, $R_c = 2000\,\text{mm}$), which is on a piezo transducer for adjusting the length of the cavity. The transmissivity T of the plane mirrors depends on the polarization, either $T = 0.15$ when the light is polarized vertically or $T = 0.014$ for the horizontal polarization. The theoretical transmissivity of the cavity is plotted in fig. 4.9, and the actual transmissivities are presented in fig. 4.10. Even though some peaks overlap for the low finesse, the lock of the cavity does not work when using the high finesse peaks because the laser is too noisy, which is why we worked with the high transmissivity.

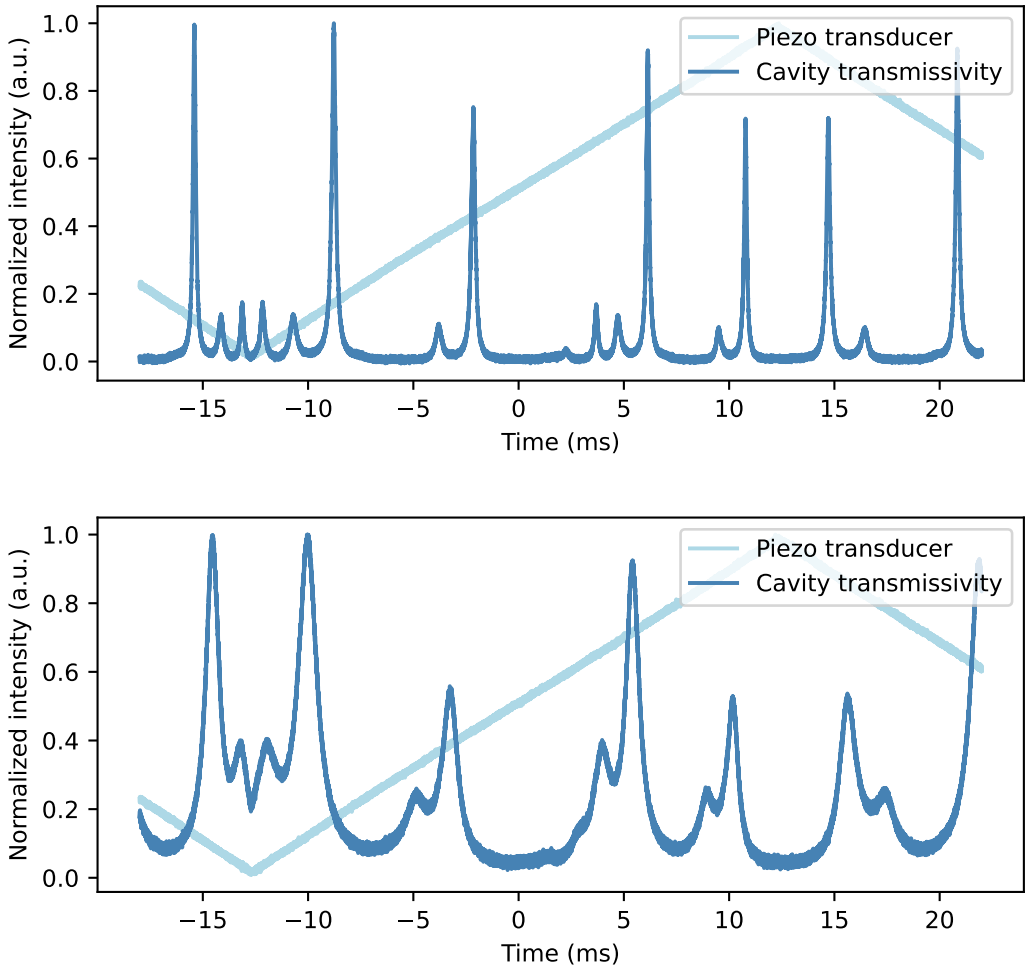

FIGURE 4.10: Experimental transmissivity of the cavity for high (top) and low (bottom) finesse. The piezo transducer is driven by the ramp signal, allowing the scanning of the cavity length.

Locking the cavity

As displayed in fig. 4.8, each HG mode is resonant for a given length of the cavity and, therefore, we need the chosen length of the cavity to be stable, while we do the measurement. The lock of the cavity is realized following the Pound-Drever-Hall technique [Drever 1983; Black 2001], which is commonly used for metrology purposes. We are summarizing here the working principle and how we adapted it to our setup.

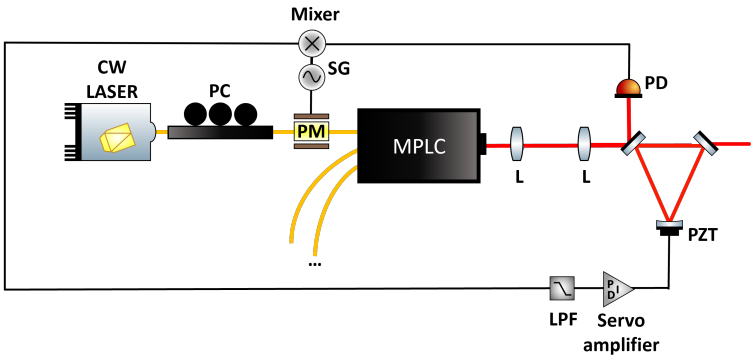

FIGURE 4.11: Experimental setup for locking the cavity. The light at the output of the laser is modulated with a phase EOM (PM), driven with a signal generator (SG) and placed after a polarization controller (PC). The beam is mode-matched to the cavity with lenses (L) and the reflected light at the input of the cavity is detected by a photodiode (PD). The output of the photodiode is mixed with the signal sent to the phase modulator. The output of the mixer is then filtered with a low-pass filter (LPF) and the filtered signal is fed to a servo amplifier, which output controls the piezo transducer (PZT) of the cavity.

The Pound-Drever-Hall technique is based on the fact that the derivative of the intensity of reflected light at the input of the cavity is antisymmetric, and, therefore, can be used as an error signal (see fig. 4.12).
In our setup, the lock only worked for the low finesse, i.e. with transmissivity of the input and output mirrors being $T = 0.15$, leading to a finesse $\mathcal{F} = 19.3$ and a cavity bandwidth $f_{\text{cavity}} = \frac{f_{FSR}}{\mathcal{F}} = \frac{c}{D_0 \mathcal{F}} = 48.6\,\text{MHz}$ (see section 1.1.3).
The light at the output of the laser (at the frequency $\omega = 2\pi \cdot c/\lambda$) is modulated sinusoïdally (amplitude around 0.8 V, frequency $\Omega = 7\,\text{MHz}$) with a fibered electro-optic phase modulator (iXBlue, MPX-LN-0.1), introducing two sidebands to the reflected signal at $\omega \pm \Omega$ around the carrier at ω. The reflected light at the input of the cavity is detected with a fast photodiode (Thorlabs PDA20CS-EC, bandwidth 10 MHz) and the output signal of the photodiode is [Black 2001]

$$\begin{aligned} V_r = B \\ &+ A\,\text{Re}\left[R(\omega)R^*(\omega+\Omega) - R^*(\omega)R(\omega-\Omega)\right]\cos(\Omega t) \\ &+ A\,\text{Im}\left[R(\omega)R^*(\omega+\Omega) - R^*(\omega)R(\omega-\Omega)\right]\sin(\Omega t) \\ &+ (2\Omega \text{ terms}) \end{aligned} \tag{4.23}$$

where $R(\omega)$ is the reflection coefficient of the cavity, plotted in fig. 4.12, and A and B are constants. Since $\Omega \ll f_{\text{cavity}}$, we have

$$R(\omega)R^*(\omega+\Omega) - R^*(\omega)R(\omega-\Omega) \approx 2\Omega\,\text{Re}\left\{R(\omega)\frac{\mathrm{d}}{\mathrm{d}\omega}R^*(\omega)\right\} = \Omega\frac{\mathrm{d}|R|^2}{\mathrm{d}\omega}. \tag{4.24}$$

Therefore, the quantity $R(\omega)R^*(\omega+\Omega) - R^*(\omega)R(\omega-\Omega)$ is real and the sine term in eq. (4.23) does not survive for small Ω.

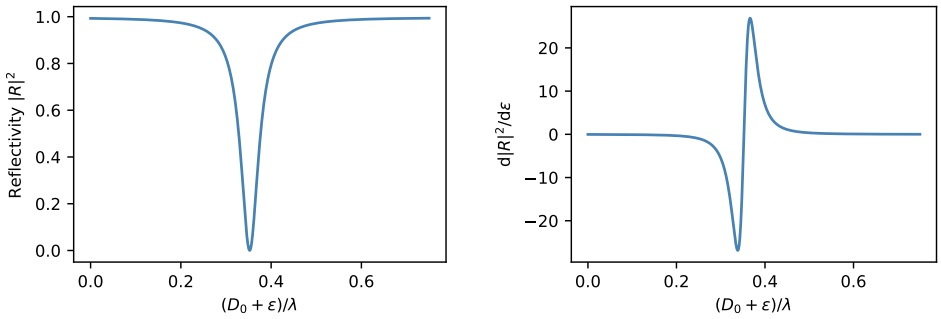

FIGURE 4.12: (a) Reflected signal. (b) Error signal of the Pound-Drever-Hall technique.

Moreover, according to fig. 4.12(a), the sign of the derivative of the reflected signal carries information on how to act on the cavity. Using that resonant frequencies ω_0 are such that

$$D_0 = p\lambda = p\frac{2\pi c}{\omega_0}, \tag{4.25}$$

where D_0 is the length of the cavity and $p \in \mathbb{N}$, then small variations in the cavity length δD, near the resonance, are proportional to small variations in the frequency δf:

$$\delta D = -p\frac{2\pi c}{\omega_0^2}\delta\omega. \tag{4.26}$$

Thus, the sign of the derivative of the reflected signal carries information about whether the length of the cavity D_0 should be increased or decreased with the piezo transducer.

Therefore, we want to isolate eq. (4.24) with the following procedure. The output of the photodetector is mixed with the sine signal sent to the electro-optic modulator at Ω. Since the mixer forms the products of its inputs and

$$\sin(\Omega t)\cos\big(\Omega' t\big) = \frac{1}{2}(\sin\big((\Omega - \Omega')t\big) - \sin\big((\Omega + \Omega')t\big)), \tag{4.27}$$

when $\Omega = \Omega'$, as it is the case in our setup, the $\sin((\Omega - \Omega')t)$ term is a DC signal. We isolate this DC signal with a low-pass filter ($f_c = 15\,\text{kHz}$), after which we obtain the Pound-Drever-Hall error signal:

$$\epsilon_{\text{PDH}} \propto \Omega\frac{\mathrm{d}|R|^2}{\mathrm{d}\omega}. \tag{4.28}$$

This DC signal, plotted in fig. 4.12(b), is finally fed to a servo amplifier (Newport LB10005) whose output is sent to the piezo transducer of the cavity, resulting in stabilizing the length of the cavity.
The parameters of the servo amplifier can be adapted to choose the mode on which the cavity is locked.

4.6.4 Measuring the amplitude crosstalks

Experimental procedure

Our experimental procedure for measuring amplitude crosstalk followed the steps presented below, with the experimental setup presented in fig. 4.13.

1. First, we generated a beam in a specific mode of the MPLC (HG_{00}, HG_{10}, HG_{01}, HG_{11}, HG_{20}, HG_{02}, HG_{21}, HG_{12}, HG_{30} or HG_{03}) by injecting laser light in the corresponding single-mode fiber. This MPLC is referred to as the MUX MPLC (MUX for multiplexing).

2. Subsequently, this mode was cleaned using the triangular cavity, which was locked to the corresponding mode, in order to eliminate the crosstalk introduced by the MUX MPLC.

3. Finally, we conducted measurements of optical powers at each output of the second MPLC, which was the MPLC to be characterized. This MPLC is referred to as the DEMUX MPLC (DEMUX for demultiplexing).

This entire procedure was repeated for each input mode. Using the measurement results, we constructed the amplitude crosstalk matrix C_A for the DEMUX MPLC so that the term $(C_A)_{ij}$ is given in dB as

$$(C_A)_{ij} = 10 \times \log\left(\frac{P_{\text{out},j}}{P_{\text{in},i}}\right) \tag{4.29}$$

where $P_{\text{in},i}$ is the input power for the mode i and $P_{\text{out},j}$ is the optical power measured at the output corresponding to mode j with $i, j \in \{HG_{30}, HG_{20}, HG_{10}, HG_{21}, HG_{00}, HG_{11}, HG_{12}, HG_{01}, HG_{02}, HG_{03}\}$.

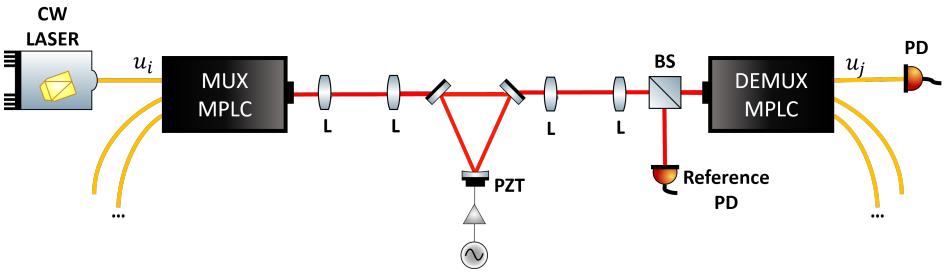

FIGURE 4.13: Experimental setup for the measurement of the amplitude crosstalk matrix. Light is injected in the single-mode fiber input of the MPLC corresponding to mode u_i, and mode matched to the cavity with lenses (L). The length of the cavity is locked with the piezo transducer (PZT) to the length corresponding to u_i, to clean it from the crosstalk introduced by the MUX MPLC. At the output of the cavity, the beam is mode-matched to the DEMUX MPLC, and detected at the output corresponding to the mode u_j with a photodiode (PD). Before the DEMUX MPLC, the light is separated into two paths with a beamsplitter (BS), in order to measure a reference intensity with another photodiode.

TABLE 4.2: Efficiencies of the MPLC, values in dB and linear scale.

HG_{30}	HG_{20}	HG_{10}	HG_{21}	HG_{00}	HG_{11}	HG_{12}	HG_{01}	HG_{02}	HG_{03}
-2.8 dB	-3.0 dB	-2.8 dB	-3.7 dB	-2.7 dB	-3.3 dB	-4.0 dB	-2.6 dB	-3.4 dB	-4.2 dB
0.52	0.51	0.53	0.42	0.54	0.46	0.40	0.54	0.46	0.38

Experimental results

The measured amplitude crosstalk matrix, determined using eq. (4.29), is presented in fig. 4.14. The order of the modes does not correspond to the normal ordering of the HG modes due to geometry reasons for the construction of the MPLC, the modes are ordered as follows: HG_{30}, HG_{20}, HG_{10}, HG_{21}, HG_{00}, HG_{11}, HG_{12}, HG_{01}, HG_{02} and HG_{03}. This matrix is almost diagonal, and the highest crosstalk values are located on the upper and lower sub-diagonals, i.e. light leaks mostly from the closest neighbors. The losses of the MPLC are presented in table 4.2.

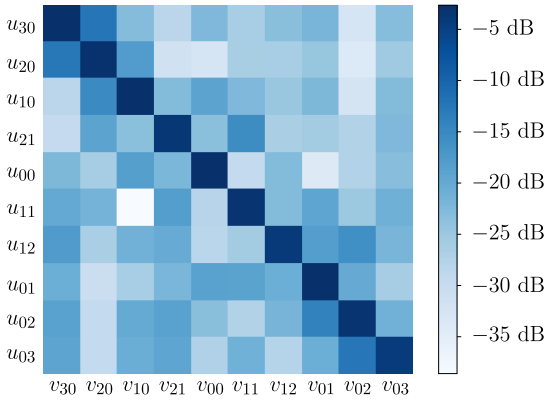

FIGURE 4.14: Amplitude crosstalk matrix.

For the experiment, as it will be presented in chapter 5, we only use the modes HG_{00}, HG_{10}, HG_{01}, HG_{20} and HG_{02}. As it will be explained in section 5.2, these modes are the most efficient to exploit for centering and mode matching the input beams to the MPLC, which is critical for the reproducibility of the experiment.
Moreover, when the crosstalk is too high, Gessner *et al.* demonstrated that it limits the separation estimation sensitivity [Gessner 2020a]. Since we extract the estimation on the separation from measurements in the mode HG_{10}, we therefore have to minimize the crosstalk in this mode.
Because the HG_{00} mode is the most populated one (see fig. 2.7), since we are studying small separations, the more critical crosstalk would be the ones from this mode to the modes HG_{10}, HG_{01}, HG_{20} and HG_{02}, which is why we choose to give their value in table 4.3 along with the typical values measured by Cailabs. They obtained these values by implementing the same procedure as we did, except they did not use the cavity to clean the modes. They, therefore extracted the crosstalk values by assuming the two MPLCs are identical and dividing the measured values by 2. Comparing these two sets of values indicates that we measured values within a consistent order of magnitude.

TABLE 4.3: Crosstalk from the mode HG_{00} measured experimentally and comparison with the typical measured values from Cailabs, using the back-to-back measurement, values in dB.

Modes	HG_{20}	HG_{10}	HG_{01}	HG_{02}
Exp	-26.0	-18.3	-33.9	-27.4
Cailabs	-20.1	-28.4	-30.0	-18.6

4.6.5 Measuring the phase crosstalks

Crosstalks are also characterized by their phase, i.e. the field that leaks into other modes encounters a phase shift. We will explain the experimental procedure we implemented to measure the phase crosstalk and why we could not extract them from our measurement results.
We used only one MPLC and the cavity. This time, since we wanted to determine phase shifts between modes, we generated beams in superpositions of two modes by injecting laser light into two single-mode fibers of the MPLC. To overcome the problem of phase shifts induced by phase drifts in the fibers, we modulated the phase of one of the modes, sinusoidally. The cavity was locked on the other mode.

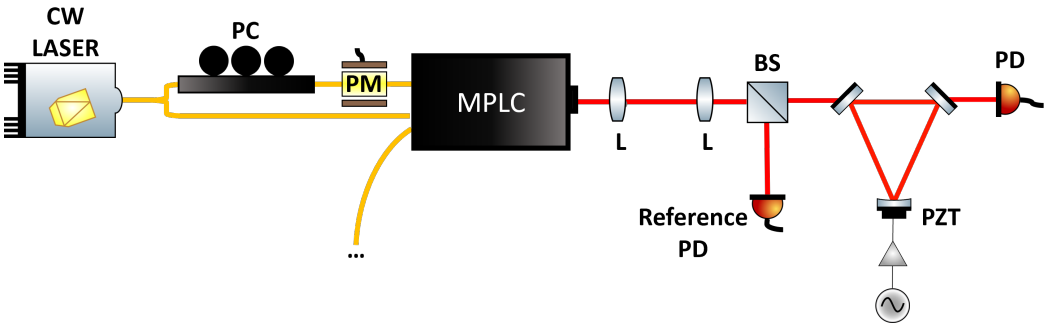

FIGURE 4.15: Experimental setup for the measurement of the phase crosstalk. Light is injected into two single-mode fiber inputs of the MPLC. One of the inputs is phase-modulated with a phase EOM (PM), placed after a polarization controller (PC). The beam is mode matched, with lenses (L), to the cavity, which is locked on one of the modes that is not phase modulated. The intensities at the input and output of the cavity are measured with photodiodes (PD).

Ideal scenario

For clarity, we consider that we want to evaluate the phase crosstalk from mode HG_{10} onto mode HG_{00}, referred to as φ_{00}^{10}. The following demonstration is obviously applicable to any other pair of modes.
The phase $\varphi(t)$ at the HG_{10} input is modulated and the cavity is locked on the HG_{00} mode. The field at the output of the MPLC (and the input of the cavity) is

$$\mathbf{E}_{\text{in}} = \left(\alpha_{00} + c_{00}^{10} e^{i(\varphi_{00}^{10}+\varphi(t))}\alpha_{10}\right)\mathbf{u}_{00} + \left(e^{i\varphi(t)}\alpha_{10} + c_{10}^{00} e^{i\varphi_{10}^{00}}\alpha_{00}\right)\mathbf{u}_{10} \tag{4.30}$$

where c_{00}^{10} (resp. c_{10}^{00}) is the amplitude of crosstalk from HG_{10} to HG_{00} (resp. from HG_{00} to HG_{10}), and φ_{00}^{10} (resp. φ_{10}^{00}) its associated phase. α_{00} (resp. α_{10}) is the complex amplitude of the field in mode HG_{00} (resp. HG_{10}). We measure the reference signal before the cavity with a photodiode measuring half of the image (otherwise the intensity would be constant and equal to $|\alpha_{00}|^2 + |\alpha_{10}|^2$). The measured reference intensity oscillates with $\varphi(t)$ since we have

$$I_{\text{ref}} \propto |\alpha_{00}|^2 + |\alpha_{10}|^2 + 2\,\text{Re}[\alpha_{00}^* \alpha_{10} e^{i\varphi(t)}] + \mathcal{O}\left(c_{00}^{10}, c_{10}^{00}\right). \tag{4.31}$$

The cavity being locked on the mode HG_{00}, has output intensity

$$I_{\text{out}}^{00} \propto |\alpha_{00}|^2 + 2c_{00}^{10}\,\text{Re}[\alpha_{00}^* \alpha_{10} e^{i(\varphi(t)+\varphi_{00}^{10})}] + \mathcal{O}\left((c_{00}^{10})^2\right). \tag{4.32}$$

Therefore, the dephasing between I_{ref} and I_{out}^{00} is directly the phase crosstalk φ_{00}^{10}. We present in fig. 4.16 some typical results that we obtained. When we repeated the same procedure, in the same configuration, we obtained different values, for example here $\varphi_{00}^{10} \approx 0$ and for the second one, we obtain $\varphi_{00}^{10} \approx \pi/2$. The results were therefore not reproducible.

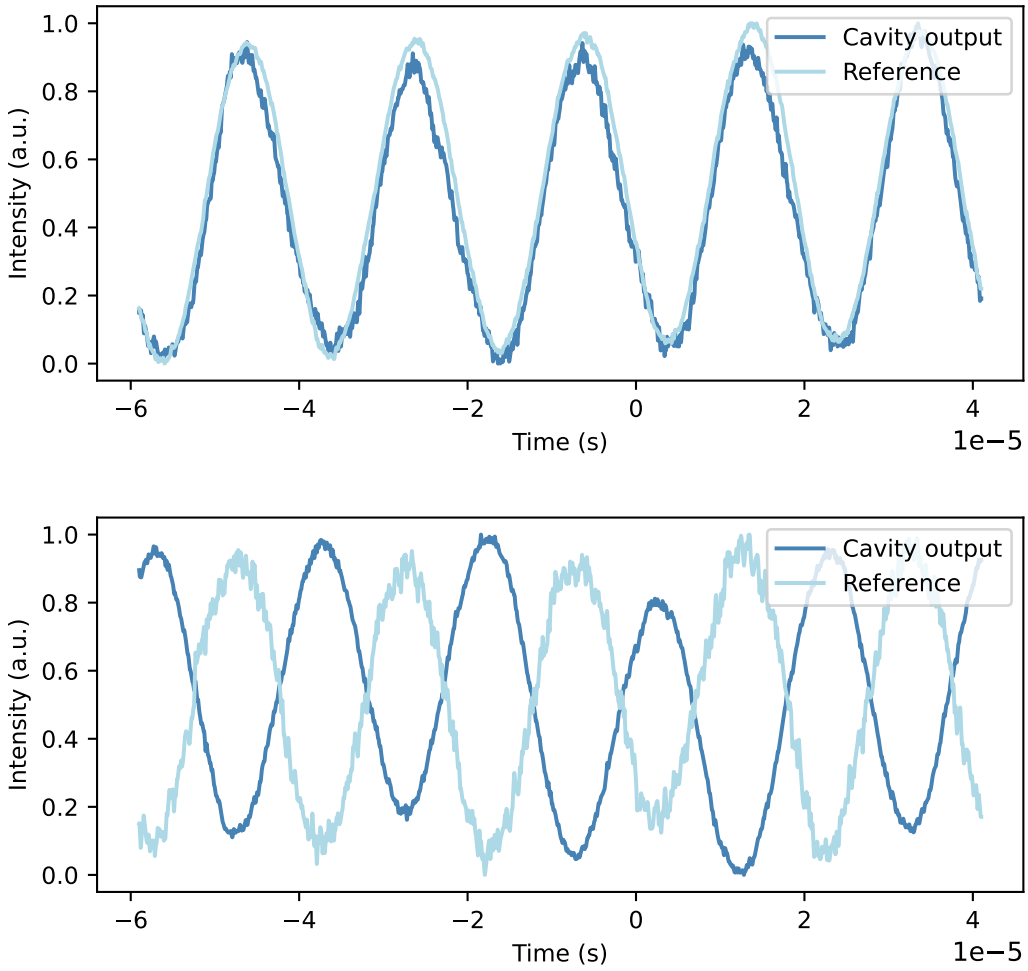

FIGURE 4.16: Interferences between modes HG_{00} and HG_{10}. We plotted the reference signal (light blue) and the output of the cavity locked on the HG_{00} mode ((blue). The two plots correspond to two measurements in the same configuration, for the first (top), we obtain $\varphi_{00}^{10} \approx 0$ and for the second one, we obtain $\varphi_{00}^{10} \approx \pi/2$.

Phase crosstalks of the cavity

We realized that the non-reproducibility comes from the imperfect alignment of the cavity. Indeed, the cavity, just like the MPLC, presents some unavoidable crosstalks, which are more or less strong depending on the alignment. Note that this is also true for the amplitude crosstalk but we assume that those of the cavity are negligible compared to the ones of the MPLC. We denote δ_{00}^{10} the crosstalk from HG_{10} to HG_{00} of the cavity and ϕ_{00}^{10} its associated phase. Taking this crosstalk into consideration, eq. (4.32) becomes

$$I_{\text{out}}^{00,\text{misaligned}} \propto |\alpha_{00}|^2 + 2c_{00}^{10}\,\text{Re}[\alpha_{00}^{*}\alpha_{10}e^{i(\varphi(t)+\varphi_{00}^{10})}] + 2\delta_{00}^{10}\,\text{Re}[\alpha_{00}^{*}\alpha_{10}e^{i(\varphi(t)+\phi_{00}^{10})}] + \mathcal{O}\left((c_{00}^{10})^2, (\delta_{00}^{10})^2\right). \tag{4.33}$$

There is therefore a beating between the crosstalk of the MPLC and the crosstalk of the cavity, preventing us from determining the phase crosstalk of the MPLC. This limitation might be due to the fact that we had to use a low finesse because the laser was too noisy in phase to be locked with a higher finesse. This low finesse leads to the modes to overlap (see fig. 4.10) and might increase the phase crosstalk of the cavity. Therefore, we should be able to access the phase crosstalk of the MPLC with a less noisy laser.

Phase crosstalk in the displacement calibration curve

During this work, we did not have time to investigate other methods to determine the phase crosstalk values. A possible path to explore would be to extract these values from the displacement calibration curve, i.e. the mean number of photons measured in the HG_{10} mode as a function of the displacement of one beam with respect to the center of the MPLC, as displayed in fig. 4.17.
Indeed, the presence of crosstalk, and their phase in particular, has an influence on the mean number of photons N_{01} measured at the output of the HG_{10} mode. The relation between N_{01} and the beam displacement x_0 along the x-axis of the MPLC is given by

$$N_{01}(x_0) = N\kappa \ \left|\beta_{10}(x_0) + c_{10}^{00}\beta_{00}(x_0)\right|^2, \tag{4.34}$$

where $c_{10}^{00} = |c_{10}^{00}|e^{i\varphi_{10}^{00}}$ is the crosstalk from mode HG_{00} to mode HG_{10} with amplitude $|c_{10}^{00}|$ and phase φ_{10}^{00}, and β_{10} and β_{00} are the mode overlap defined by eq. (2.86) so that

$$\beta_{n0}(x) = \frac{1}{\sqrt{n!}}\left(\frac{x}{w_0}\right)^n \exp\left(-\frac{x^2}{2w_0^2}\right). \tag{4.35}$$

In fig. 4.17, following eq. (4.34), we represented the displacement calibration curve with a given crosstalk amplitude $|c_{10}^{00}| = 0.015$ (corresponding to the -18.3 dB measured experimentally) and different phases φ_{10}^{00}, from 0 to π. We observe that the position of the minimum intensity in the HG_{10} mode depends on the value of the phase crosstalk, and this property could in principle be used to determine the phase crosstalk values φ_{10}^{00}, and φ_{01}^{00} if the beam is displaced along the y-axis of the MPLC.
The dependence of the minimum position in the calibration curve can, however, be hardly exploited to determine the value of the phase crosstalk. Indeed, it would require good precision on the position x_0, given by the maximum intensity at the HG_{00} output, i.e. the maximum of

$$N_{00}(x_0) = N\kappa \ |\beta_{00}(x_0)|^2 = \exp\left(-\frac{x_0^2}{w_0^2}\right). \tag{4.36}$$

Since $N_{00}(x_0)$ is almost flat around $x_0 = 0$, it results in a low sensitivity in the determination of the position $x_0 = 0$.

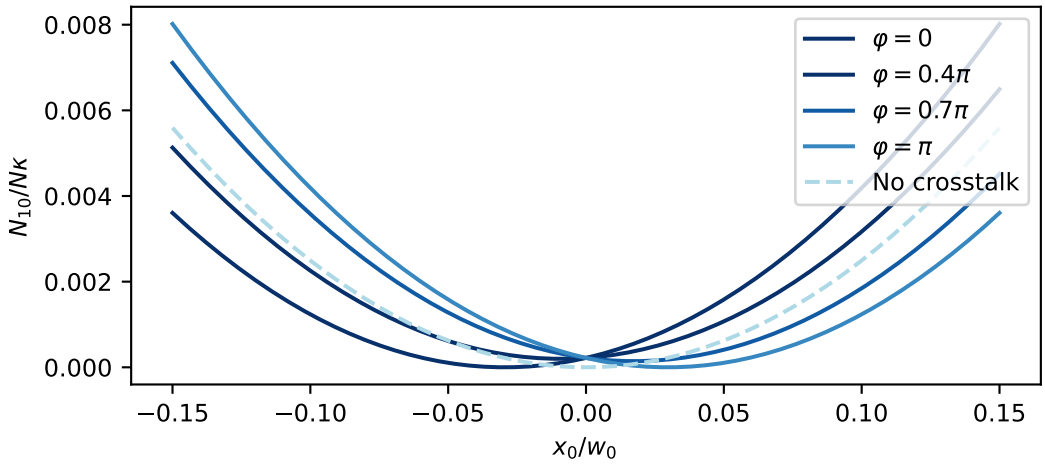

FIGURE 4.17: Displacement calibration curve without crosstalk (dashed light blue line) and with crosstalk for a given crosstalk amplitude $|c_{10}^{00}| = 0.015$ (or -18.3 dB) and different phases φ_{10}^{00}, from 0 to π.

4.6.6 Experimental sensitivity of separation estimation and crosstalk

In the presence of crosstalk, when the two sources are separated by a distance d, with symmetric source positions $x_{1,2} = \pm d/2$, the mean number of photons in the HG_{10} mode, assuming the main crosstalk contribution is from the HG_{00} mode, reads

$$\begin{aligned} N_{10}(d) &= N\kappa \left| \beta_{10}\left(\frac{d}{2}\right) + c_{01}^{00}\beta_{00}\left(\frac{d}{2}\right)\right|^2 \\ &+ N\kappa \left| \beta_{10}\left(-\frac{d}{2}\right) + c_{01}^{00}\beta_{00}\left(-\frac{d}{2}\right)\right|^2 \\ &= 2N\kappa \left(\beta_{10}\left(\frac{d}{2}\right)^2 + |c_{01}^{00}|^2 \beta_{00}\left(\frac{d}{2}\right)^2 \right) \\ &+ 2N\kappa |c_{01}^{00}| \cos(\varphi_{10}^{00}) \left(\beta_{10}\left(\frac{d}{2}\right)\beta_{00}\left(\frac{d}{2}\right) + \beta_{10}\left(-\frac{d}{2}\right)\beta_{00}\left(-\frac{d}{2}\right)\right) \end{aligned} \tag{4.37}$$

$c_{10}^{00} = |c_{10}^{00}| e^{i\varphi_{10}^{00}}$ is the crosstalk from mode HG_{00} to mode HG_{10} with amplitude $|c_{10}^{00}|$ and phase φ_{10}^{00}, and β_{10} and β_{00} are the mode overlap. Using eq. (4.35), we see that

$$\beta_{10}\left(\frac{d}{2}\right)\beta_{00}\left(\frac{d}{2}\right) = -\beta_{10}\left(-\frac{d}{2}\right)\beta_{00}\left(-\frac{d}{2}\right), \tag{4.38}$$

consequently, eq. (4.37) becomes

$$N_{10}(d) = 2N\kappa \left(\beta_{10}\left(\frac{d}{2}\right)^2 + |c_{01}^{00}|^2 \beta_{00}\left(\frac{d}{2}\right)^2 \right). \tag{4.39}$$

Therefore, the phase of the crosstalk has no impact on the sensitivity of short separation estimation, only the amplitude $|c_{01}^{00}|$ has to be taken into account.

We injected eq. (4.39), instead of eq. (4.7), into the noise contributions taken into account in the previous sections, i.e. the electronic noise of the photodiodes (eq. (4.6)) and the shot noise (eq. (4.10)), in order to determine the sensitivity of the separation estimation in the presence of crosstalk. We recall that we considered the laser noise in both regimes and the dark counts of the APD to be independent of N_{10}. We plot the expected sensitivity with and without crosstalk for both intensity regimes in fig. 4.18.
We observe that, for bright sources, the presence of crosstalk has no impact on the sensitivity of the estimation. This is due to the fact that electronic noise is dominant and constant in this regime.
Similarly, for faint sources, crosstalk has little impact on the sensitivity, because dark counts and laser noise are assumed to be constant, and therefore crosstalk would only affect the shot noise contribution. This is why crosstalk appears to improve the sensitivity. However, in more realistic modeling, laser noise should increase with the separation (in the considered separation range) which would alter the sensitivity in the presence of crosstalk.

4.7 Conclusion

In this chapter, we studied the different noise contributions of the PEsto setup introduced in section 3.4, in the two intensity regimes we chose for the separation estimation experiment described in chapter 5. We observe that in both cases we are limited by technical noises, but with different dominant contributions. In the low-flux regime, the sensitivity is mainly limited by the laser noise, while for bright sources, the noise mostly comes from the electronic noise of the scope and detectors and from the phase noise from the residual interference between the two incoherent sources. These fluctuations are not fundamental and can be reduced such that the sensitivity of the separation estimation gets closer to the QFI.
Additionally, we investigate the imperfections of the MPLC by determining experimentally the crosstalk matrix, i.e. the actual mode decomposition of the MPLC that is slightly different from the HG mode basis. These imperfections limit in theory the sensitivity of the estimation. Even if the current setup is not limited by crosstalk yet, it is still interesting to know their value to predict when they would be the limiting factor.

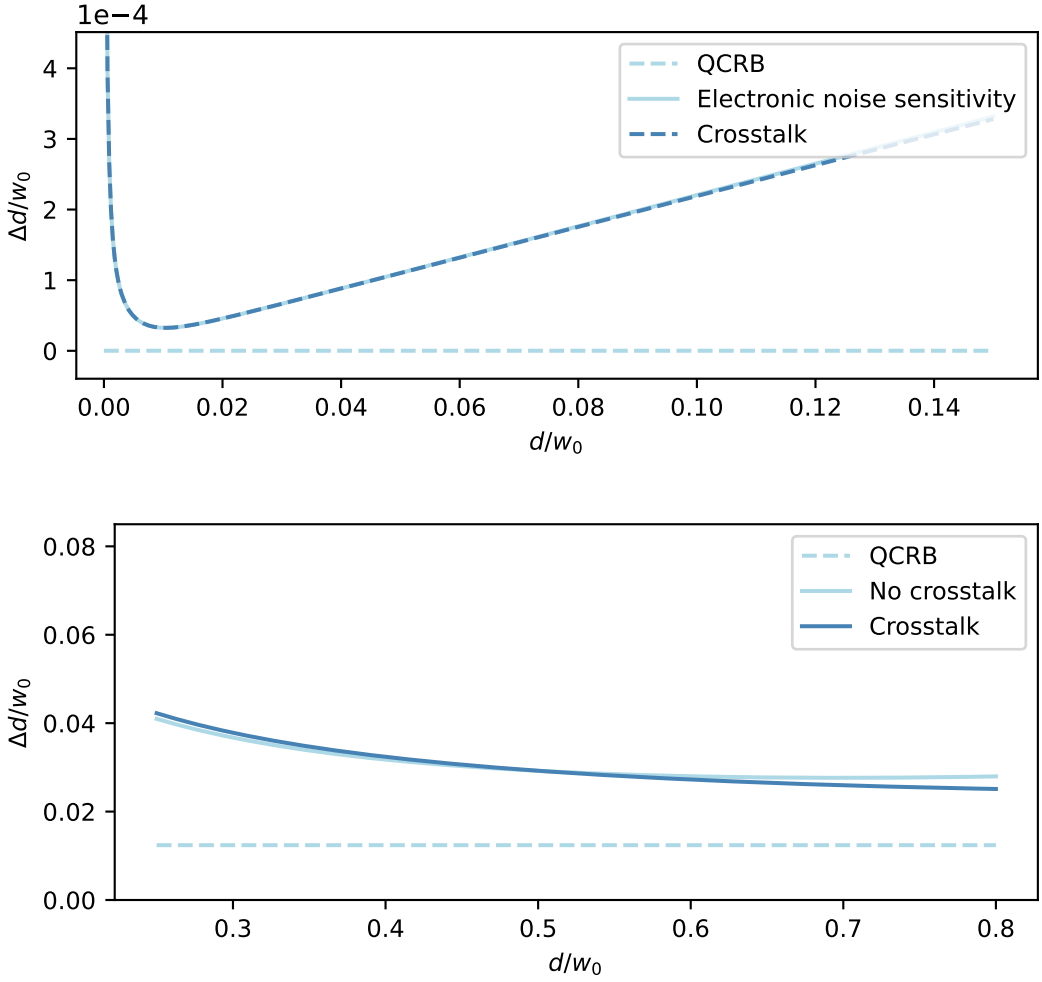

FIGURE 4.18: Comparison of the expected sensitivity of the separation estimation with and without taking crosstalk into account for the high-flux regime (top) and the low-flux regime(bottom). For both plots, we represented the quantum Cramér-Rao bound (dashed light blue line), the sensitivity with all noise sources without crosstalk (light blue line) and with crosstalk (blue line). For the high-flux regime (top), the curves with and without crosstalk are perfectly superimposed, suggesting that crosstalk is negligible in this regime.

Chapter 5

Reaching high sensitivities with the PEsto experiment

Contents

As discussed in chapter 3, several quantum-metrology-inspired experiments were performed to estimate the separation between two point-like sources. This was, however, not realized yet with a multi-plane light converter, which enables a multimodal approach. This final chapter presents the experimental results we obtained

on the separation estimation for incoherent equally bright sources, via spatial-mode demultiplexing with an MPLC, with the setup introduced in section 3.4.

Section 5.1 recalls the context in which we implemented the experiment and the assumptions we used to process the experimental data. Sections 5.2 and 5.3 explain the experimental procedure we performed. Sections 5.4 and 5.5 contain the results we obtained which are interpreted in relation to the noise analysis depicted in chapter 4, each section being dedicated to a different intensity regime, and section 5.6 describes how the experimental setup can be improved regarding the observed limitations. Finally, section 5.7 suggest some prospects that can be explored in the future.

5.1 Context and assumptions

The goal of the experiment is to perform a single parameter estimation task. This means that we assume every parameter is known, except for the one of interest, being here the separation d between the two sources in the image plane.
We assume that the optical scene is composed of two equally bright incoherent sources and that the centroid is known and aligned on the MPLC. We also assume that the two sources are identical, i.e. they are two Gaussian beams with the same waist w_0, same polarization and the same spectrum. We place ourselves in the range of short separations i.e. $d < w_0$.
The estimation is realized using the method of moments, presented in section 2.2.3, using one observable, the number of photons $\hat{N}_{10}$ measured at the output HG_{10} of the MPLC, assuming this estimation is unbiased.
To perform this experiment, called PEsto (for Parameter Estimation), we use the experimental setup presented in chapter 3, which noise sources were analyzed in chapter 4.

The concept of the experiment is illustrated in fig. 5.1. The light from two incoherent equally bright Gaussian beams with the same waist w_0, separated by a distance d, is injected into the MPLC. Measuring the light at 5 outputs of the MPLC (corresponding to the modes HG_{00}, HG_{10}, HG_{01}, HG_{20} and HG_{02}) gives access to an estimation of the separation with high sensitivity, as it will be presented in sections 5.4 and 5.5.

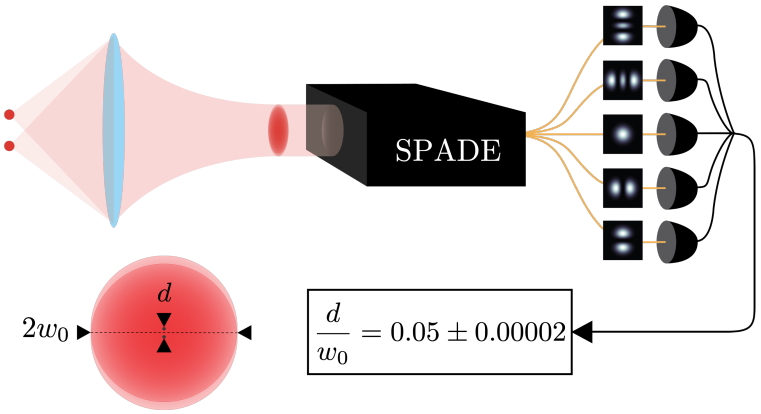

FIGURE 5.1: Concept of the PEsto experiment, an experiment of separation estimation. The light from two incoherent equally bright Gaussian beams with a waist w_0, separated by a distance d, is injected into the MPLC. Measuring the light from 5 modes (HG_{00}, HG_{10}, HG_{01}, HG_{20}, HG_{02}) gives access to an estimation of the separation with high sensitivity. We provide a result obtained with 10^{13} detected photons: we estimated a separation $\frac{d}{w_0} = 5 \cdot 10^{-2}$ with a standard deviation $\frac{\Delta d}{w_0} = 2 \cdot 10^{-5}$.

5.2 The MPLC as an alignment and mode-matching tool

As for any experiment in optics, the alignment and mode matching are critical. In the present case, misalignment and imperfect mode matching can be seen as a decomposition in a basis slightly different from the Hermite-Gaussian mode basis [Sorelli 2021a]. They introduce extra crosstalk to the intrinsic crosstalk of the MPLC, which limits the sensitivity as explained in section 4.6. In this section, we consider the MPLC to be without intrinsic crosstalk, and we explain how to align and mode match to the MPLC with a multimode approach.

5.2.1 Tilt and displacement

The MPLC is sensitive to the displacement and the tilt of an input beam $u(x, y, z) = u_{00}(\mathbf{r})$ as defined by eq. (1.23). We assume the input beam is mode matched to the MPLC, it is a Gaussian beam with the same waist as the waist of the decomposition of the MPLC, denoted w_0. Then, a small displacement x_0 or a small tilt angle θ_x along the x-axis will result in a non-zero signal in the mode HG_{10}. This can be seen with the Taylor development analysis, developed in the following paragraphs.
We define $\tilde{u}(x_0, p_x; x, y, z)$, which will be simplified as $\tilde{u}(x_0, p)$, as

$$\tilde{u}(x_0, p_x) = u(x - x_0, y, z)e^{ip_x x} \tag{5.1}$$

with $p_x = 2\pi\theta_x/\lambda$. At the first order in x_0 and p_x, the Taylor development gives

$$\tilde{u}(x_0, p_x) \simeq \tilde{u}(0,0) + x_0 \frac{\partial \tilde{u}}{\partial x_0}(0,0) + p_x \frac{\partial \tilde{u}}{\partial p_x}(0,0). \tag{5.2}$$

Since we have

$$\begin{aligned}\frac{\partial \tilde{u}}{\partial x_0}(x_0, p_x; x, y, z) &= \frac{1}{w_0} u_{10}(x, y, z),\\ \frac{\partial \tilde{u}}{\partial p_x}(x_0, p_x; x, y, z) &= \frac{i w_0}{2} u_{10}(x, y, z),\end{aligned} \tag{5.3}$$

where $u_{10}(x, y, z)$ is the HG_{10} mode as defined by eq. (1.25), we can write eq. (5.2) as

$$\tilde{u}(x_0, p_x; x, y, z) \simeq u_{00}(x, y, z) + \left[\frac{x_0}{w_0} + \frac{i p_x w_0}{2}\right] u_{10}(x, y, z). \tag{5.4}$$

As expected, this equation shows that, for a centered mode-matched Gaussian beam, the intensity is maximum at the HG_{00} output and zero at the HG_{10} output. Therefore, small displacements and tilts along the x-axis can be detected as they result in non-zero intensities at the HG_{10} output. Similarly, small displacements and tilts along the y-axis can be detected in the HG_{01} mode.
Consequently, minimizing the intensity at the outputs of the modes HG_{10} and HG_{01} results in centering the beam at the input of the MPLC.

5.2.2 Waist-size changes

Similarly to the previous subsection, we can show that the MPLC is sensitive to waist-size changes which allows us to mode match the input beam to the demultiplexing basis, with waist w_0. Indeed, assuming the input beam is not displaced or tilted with respect to the MPLC, we denote $\tilde{u}(\delta w_0; x, y, z)$ the beam with the waist $w_0 + \delta w_0$. For a small waist-size change, the Taylor development at the first order in δw_0 gives

$$\tilde{u}(\delta w_0, x, y, z) \simeq u_{00}(x, y, z) + \delta w_0 \frac{\partial u}{\partial w_0}(x, y, z), \tag{5.5}$$

and we have

$$\tilde{u}(\delta w_0, x, y, z) \simeq u_{00}(x, y, z) + \frac{\delta w_0}{\sqrt{2} w_0}(u_{02}(x, y, z) + u_{20}(x, y, z)). \tag{5.6}$$

where $u_{20}(x, y, z)$ and $u_{20}(x, y, z)$ are the HG_{02} and HG_{20} modes as defined by eq. (1.25). this expansion confirms that, for centered and mode-matched Gaussian beams, the intensity is maximum at the HG_{00} output and zero at the HG_{20} and HG_{02} outputs. Therefore, small waist changes can be detected when measuring non-zero intensities at the HG_{02} and HG_{20} outputs.
This is why we mode matched the input beam by minimizing the intensity at these outputs of the MPLC.

5.3 Experimental procedure

This section presents the experimental procedure we performed. It is composed of three steps which will be detailed in the following subsections:

- Alignment

- Calibration
- Measurement.

We realized the separation estimation in two intensity regimes: a low photon flux regime (3500 photons at all the MPLC outputs per integration time) and a high photon flux regime (10^{13} detected photons in total per integration time). The photodetectors at the outputs of the MPLC were adapted to each regime, i.e. they were APDs with a 100 ms-integration time for the faint sources, and photodiodes with an integration time of 5 ms for the bright sources.

5.3.1 Alignment

The aim of the alignment procedure is for the beams from both sources to be individually mode matched and centered on the MPLC input - the two sources will be separated with a given distance for the measurement step. Since the crosstalk induced by misalignment and imperfect mode matching is by nature variable, it is important, for the reproducibility of the estimation, to have a reliable and reproducible alignment procedure. This stage is realized with bright sources.
In the beginning, the alignment of one source is done roughly by maximizing the intensity at the output of the HG_{00} mode. However, as shown by eq. (4.36), the mean photon number at the HG_{00} output has very poor sensitivity to displacement. This means that only maximizing the intensity at the output of the HG_{00} mode is not sufficient to meet the reproducibility requirement. Then, we minimize the intensities at the HG_{01}, HG_{10}, HG_{02} and HG_{20} outputs, which ensures low variations in waist size, tilts, and displacements in x and y directions. Using these five modes is critical for the robustness and repeatability of the procedure.
As explained in section 3.4, a reference separation d_{ref} is determined using a quadrant detector, by measuring separately the position of each beam, x_1 and x_2, and having $d_{\text{ref}} = |x_1 - x_2|$. The quadrant detector is aligned with the MPLC center.

5.3.2 Calibration

In order to implement the method of moments, we build a calibration curve, i.e. we determine the mean number of photons N_{10} measured at the HG_{10} output as a function of the separation between the two sources: $N_{10} = g(d)$.
For building this curve, only one of the two beams is turned on (for practicability, the one of Trofie, which corresponds to the motorized translation stage) and translated in discrete steps, from -100 µm to 100 µm, with steps of 6 µm, where the origin is the center of the MPLC. For each position, which is certified with the quadrant detector, the intensity at the output of the HG_{10} mode is acquired for 10 s. Its mean value is normalized with the mean value of the optical power measured by the reference photodiode.
The experimental points are then fitted with a 6th-order polynomial function. This is the calibration curve for one source $f(x)$, where x is the position of the beam. This calibration curve is presented in fig. 5.2. Thanks to the precise and reproducible alignment procedure, this calibration can be done once and for all.

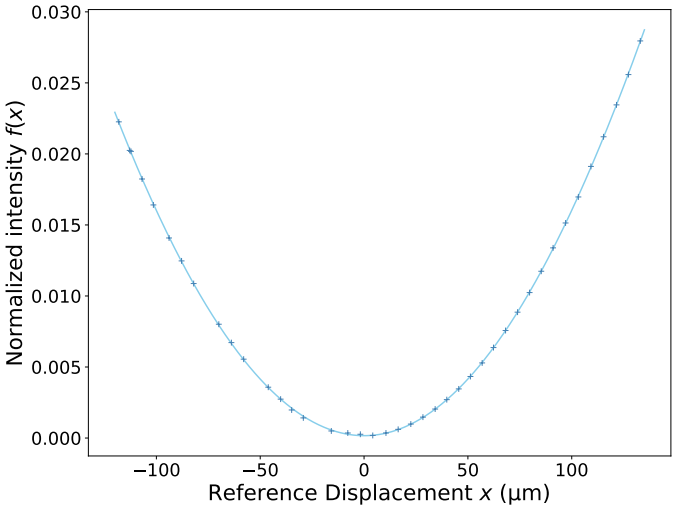

FIGURE 5.2: Calibration curve for the source displacement. It gives the normalized intensity measured at the HG_{10} output of the MPLC as a function of the displacement of one source with respect to the MPLC. The experimental points are fitted with a 6th-order polynomial function.

Using the assumption that the scene is composed of two identical incoherent sources and that the centroid is known, we construct the two-source calibration curve $g(d)$. This calibration curve has to be built for each estimated separation, where the normalizing optical power p_1 and p_2 is measured for each source with the reference photodiode. This curve is constructed as follows: we assume that both sources have the same calibration curve - since they are identical - but are displaced symmetrically with respect to the MPLC center, each by a distance x, resulting in a separation $d = 2x$. Therefore, in order to build $g(d)$, we sum the contributions $f(x)$ and $f(-x)$ corresponding to each source. The two sources are close to being equally bright but due to polarization fluctuations in the independent fiber paths, they have a slight power imbalance. This relative intensity ratio is assumed to be known, since measured with the reference photodiode, and taken into account by the weights in front of the corresponding calibration curve $f(x)$ and $f(-x)$. Consequently, the two-source calibration curve $g(d)$ is

$$g(d = 2x) = \frac{p_1}{p_1 + p_2} f(x) + \frac{p_2}{p_1 + p_2} f(-x), \tag{5.7}$$

and is displayed in fig. 5.3.

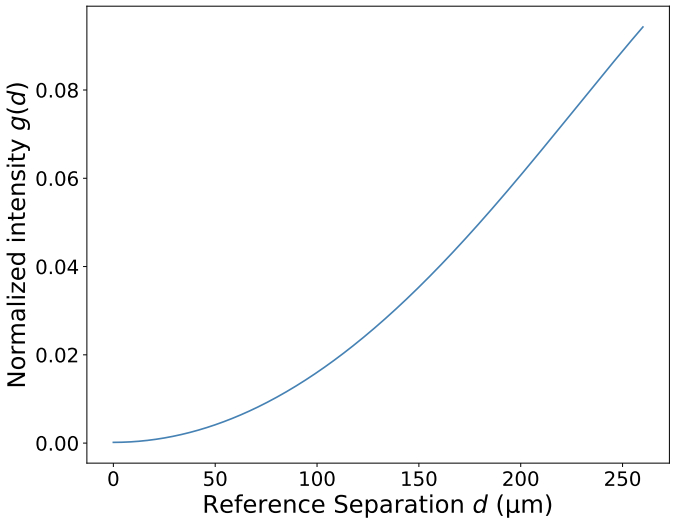

FIGURE 5.3: Calibration curve for the source separation, this curve gives the normalized intensity that should be measured at the HG_{10} output of the MPLC as a function of the separation between the two sources. This graph was obtained by symmetrizing the polynomial fit of the experimental points presented in fig. 5.2, assuming the two sources are identical, i.e. they are two Gaussian beams with the same waist w_0, same polarization and the same spectrum, and the centroid is aligned on the MPLC input.

5.3.3 Measurement

Finally, for the separation estimation itself, the sources are displaced symmetrically with respect to the center of the MPLC by a given distance. The symmetry is guaranteed by the quadrant detector by measuring the position of each beam x_1 and x_2 while turning off the other one with a shutter. This detector delivers a zero signal with two sources when the positions are symmetric and is therefore unable to give any information on the separation between the sources directly, but the reference separation value is given by $d_{\text{ref}} = |x_1 - x_2|$.
With both sources turned on, the optical power at the HG_{10} output is then measured over a specific integration time. The separation is estimated at last by inverting the two-source calibration curve $g(d)$ of fig. 5.3.
For each optical setting, this measurement is repeated 200 times to evaluate the statistical moments of the estimation. The estimated separation d is then the average of the 200 estimations, and the sensitivity is given by the standard deviation Δd.

5.4 Experimental results: Low-flux regime

This section presents the results of the separation estimation we performed with faint sources. The total incident power, i.e. of both sources combined, was around 50 fW during an integration time of 100 ms. Due to the quantum efficiency of the

APDs and the losses of the MPLC, this results in around $2N\kappa = 3500$ detected photons (for all the outputs) per integration time. We studied separations ranging from $0.35w_0$ to $0.76w_0$. We will examine the accuracy and the sensitivity of the estimation, implemented as introduced in the previous section.

5.4.1 Accuracy

In order to check the assumption of the unbiased estimation, we plotted the estimated separation as a function of the reference separation, measured with the quadrant detector, presented in fig. 5.4.

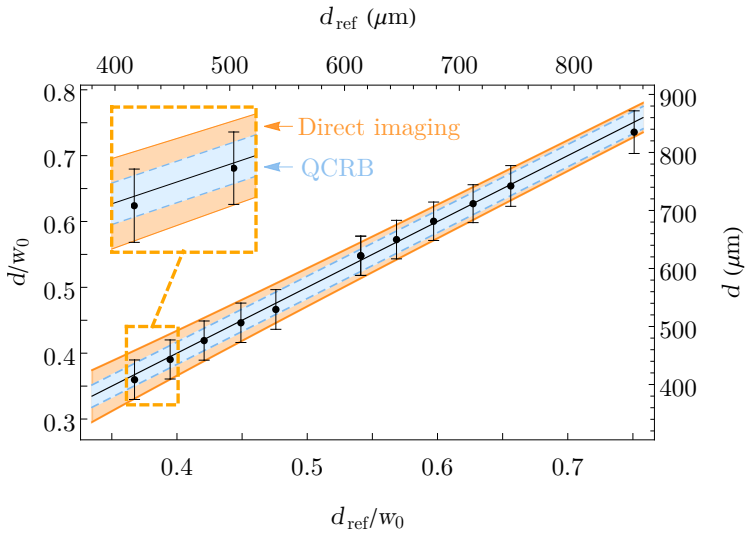

FIGURE 5.4: Estimated separation as a function of the reference separation in the low-flux regime ($2N\kappa = 3500$ detected photons in total during 100 ms). Both axes are presented with absolute values and values relative to the size of the beam $w_0 = 1.135$ mm. Error bars due to statistical uncertainty on the reference separation and the estimation, determined with 200 measurements (each during one integration time of 100 ms), are displayed as well as the line $d_{\mathrm{ref}}/w_0 = d/w_0$ corresponding to the unbiased estimation line (black line). The QCRB (light blue) and the Cramér-Rao bound for ideal direct imaging (orange) for the same number of detected photons are also plotted as shaded areas for comparison.

The experimental points, in black, are obtained with the mean values of the 200 estimations, and the error bars around them correspond to one standard deviation determined over the 200 estimations for each separation. The black line corresponds to the unbiased estimation and is compatible with the statistical uncertainties. The experimental estimations follow, therefore, a perfect linear trend with a negligible bias to the true value.

5.4.2 Sensitivity

As stated in chapter 2, the figure of merit we use to benchmark unbiased estimators is the standard deviation of the estimation, which characterizes the sensitivity of the estimation. Along with the standard deviation of the estimations, we plotted the ones corresponding to the Cramér-Rao bound of ideal direct imaging in orange and to the QCRB in blue. They are presented as error bars and shaded areas in fig. 5.4, and their values are also plotted as a function of the reference separation in fig. 5.5.

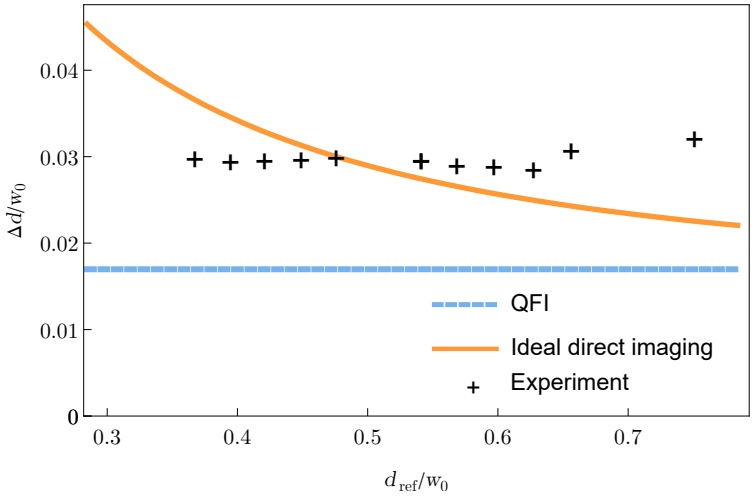

FIGURE 5.5: Sensitivity on the source separation estimation as a function of the reference separation in the low-flux regime ($2N\kappa = 3500$ detected photons in total during 100 ms). The experimental points (black) are presented along with the QCRB (dashed blue line) and the Cramér-Rao bound for perfect direct imaging (orange line), calculated for the same number of detected photons.

The standard deviation of the estimation is constant around $\Delta d = 0.03 w_0$ over the studied range of separations and is very close to the quantum Cramér-Rao bound, which, in this setting, is $\frac{1}{\sqrt{2N\kappa}} = 1.7 \times 10^{-2} w_0$, according to eq. (2.75). The discrepancy arises from the laser noise, and marginally from the dark counts of the APDs (see chapter 4).

In order to compare to standard imaging techniques, we determine the sensitivity for direct imaging. This could be done experimentally, however, the performances of the estimation depend a lot on the performances of the camera, which are not optimal at telecom wavelength. This is why we chose to compare the sensitivity of SPADE to the one of ideal direct imaging, corresponding to a camera without noise, with infinitely small pixels and with the same losses as our detection apparatus for SPADE. The SPADE scheme outperforms this idealized setting since we achieved lower standard deviation δd for separations below $0.5 w_0$.
In practice, as discussed in chapter 3, the sensitivity of passive imaging is currently of the order of the Rayleigh limit. This means that we gain two orders of magnitude on the sensitivity compared to practical superresolution techniques.
Note that, in this setting, we reached this sensitivity by measuring only 200 photons

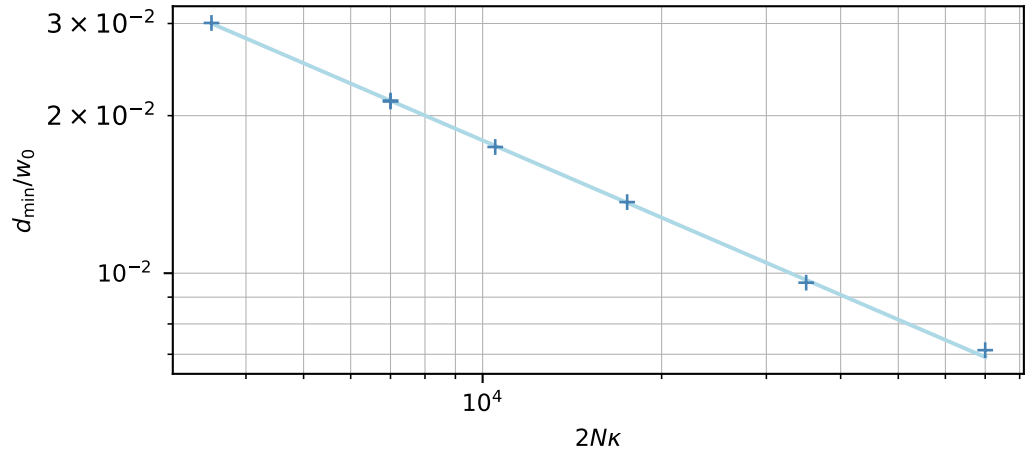

FIGURE 5.6: Minimum resolvable distance as a function of the detected number of photons. The experimental points (blue points) are fitted with the function $y = b \times (2N\kappa)^a$, we obtain the scaling $a = -0.49$.

per integration time at the output of the HG_{10} mode. The sensitivity enhancement obtained with SPADE can be traced back to the fact that, contrary to direct imaging, the demultiplexing enables the detection of mostly the photons containing the relevant information by routing them to the HG_{10} output.

5.4.3 Scaling with the number of photons

To study the scaling of the minimum resolvable distance with the number of detected photons, we acquired experimental data in the same regime of intensity but over a total measurement time of 1 s, resulting in 2000 measurement points each for an integration time of 100 ms. Therefore, we can access different mean numbers of detected photons by changing the integration time in post-processing.
The theoretical predictions were presented in section 2.5.6. We recall that, for the QFI and ideal SPADE, the scaling is $(2N\kappa)^{-1/2}$, and it is $(2N\kappa)^{-1/4}$ for ideal direct imaging, as illustrated in fig. 2.12. Moreover as discussed in section 4.6, the scaling of SPADE is degraded in the presence of imperfections. In particular, in the presence of crosstalk, the scaling meets the one of ideal direct imaging fig. 4.7).
We chose different integration times (resp. 100 ms, 200 ms, 250 ms, 333 ms, 500 ms, 1 s, 2 s), and repeated the previous analysis. For each separation, we estimated the separation over the corresponding number of points (1000, 500, 400, 300, 200, 100, 50) and determined the statistical moments of these estimations. In particular, we extracted the standard deviation Δd and we assume that, in this regime, Δd is a good approximation of the minimal resolvable distance as defined by eq. (2.92). In fig. 5.6, we plot the obtained minimum resolvable distances as a function of the detected photons $2N\kappa$, along with a fit with the function $y = b \cdot (2N\kappa)^a$, with $a = -0.49$.

Thus, our experimental points display the same scaling as the ideal SPADE, and therefore, in this regime, we are not limited by crosstalk, but, as discussed in chapter 4, by the laser noise and the shot noise, and marginally by the electronic noise of the APD. This plot is another visualization of how our setup outperforms ideal direct imaging.

5.5 Experimental results: High-flux regime

We now analyze the experimental results with bright sources. The incident power was around 650 µW for an integration time of 5 ms, and this results in around 10^{13} detected photons at all the outputs of the MPLC. Similarly to the low-flux regime, we study the accuracy and the sensitivity of the estimation.

5.5.1 Accuracy

We plot the estimated separation as a function of the reference separation in fig. 5.7, for separations ranging from 1.7×10^{-2} w_0 to 0.14 w_0. The black line corresponds to an unbiased estimation. We note a linear agreement between the estimated values and the reference.

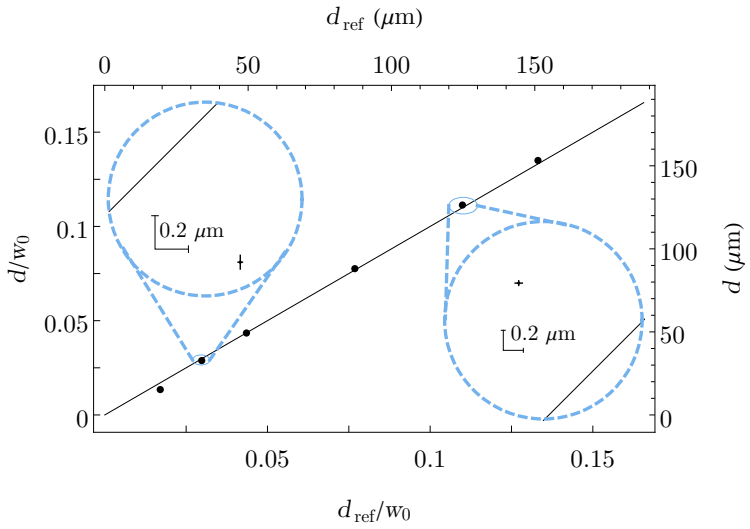

FIGURE 5.7: Estimated separation as a function of the reference separation in the high-flux regime (10^{13} detected photons in total during 5 ms. Both axes are presented with absolute values and values relative to the size of the beam $w_0 = 1.135$ mm. Error bars due to statistical uncertainty on the reference separation and the estimation, determined with 200 measurements (each during one integration time of 5 ms), are displayed as well as the unbiased estimation line (black line).

However, when looking closer to the experimental points, we see a deviation of the estimations of 1 µm on average compared to the true value. This bias arises from small differences between the two sources because the symmetrized calibration

curve is built on the assumption that they are identical, except for their position, i.e. they are Gaussian beams with the same waist, same wavelength, and same tilt angle at the input of the MPLC. However, as noticeable in the experimental setup (see fig. 3.14), the sources are generated from two independent collimators and may display slightly different spatial shapes, they are not true point sources. Moreover, their optical paths are different which might result in different spatial shapes and tilt angles. These spatial differences influence the mode decomposition corresponding to each source and are, therefore, visible in the calibration curves of each source in fig. 5.8. The two curves are similar but slightly shifted horizontally and vertically from each other.

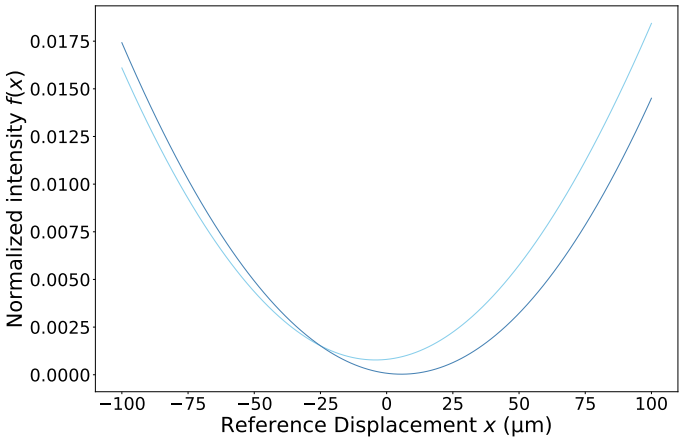

FIGURE 5.8: Comparison between the calibration curves, i.e. mean photon number in the HG_{10} mode as a function of the displacement of the source, for Trofie (dark blue) and Linguine (light blue).

These differences give rise to the systematic errors that we observe in the experimental results. Consequently, the assumption of having identical sources should be tempered in settings where the error bars are small enough so that slight differences in sources are revealed. Note that the inaccuracy does not originate from the detection apparatus itself. In realistic scenarios, like microscopy or astronomy setups, this bias will depend on the optical imaging device and the type of sources, and can eventually be largely improved.

5.5.2 Sensitivity

The most critical figure of merit being the standard deviation of the estimation, we plot the statistical errors on the estimated separations as a function of the reference separation in fig. 5.9. We demonstrate sensitivities ranging from 97 nm for our shortest separation of 20 µm to as low as 20 nm for larger separations. This corresponds to five orders of magnitude beyond the beam size. This is ensured by the single-source independent calibration, as well as by the precise alignment and mode matching, made possible by the information from multimode MPLC outputs.
We also compare the experimentally measured sensitivities to theoretical values. The

dashed blue line at $3.5 \times 10^{-7}\ w_0$ is the quantum Cramér-Rao bound, calculated for the same number of detected photons, and the black line is the sensitivity of the SPADE measurement taking the electronic noise of the detection into account since all the other noise sources are negligible as presented in chapter 4.

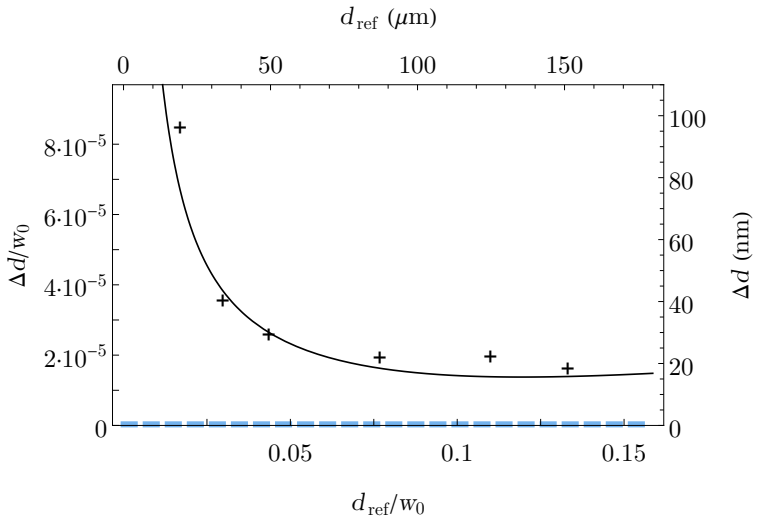

FIGURE 5.9: Experimental sensitivity in the high-flux regime (10^{13} detected photons in total during 5 ms). Both axes are presented with absolute values and values relative to the size of the beam $w_0 = 1.135$ mm. The QCRB (dashed blue line), calculated for the same number of detected photons, and the sensitivity for the SPADE measurement taking into account the detection noise (black line) are also plotted for comparison.

The discrepancy between the experimental values and the QCRB is therefore quantitatively reproduced by our theoretical model, presented in chapter 4. This demonstrates that the limiting noise source of our setup is the detection noise. Note that the absolute values of the measured sensitivities are given at the plane of the collimators where $w_0 = 1.135$ mm, and, at the input plane of the MPLC, the beam underwent a magnification factor of around $1/4$. Therefore, the measured sensitivity corresponds to a standard deviation on the separation of approximately 5 nm in the input plane of the MPLC, which is a regime where the setup is extremely sensitive to mechanical fluctuations.

5.5.3 Differential measurements

To elucidate the full potential of our apparatus and the extremely low statistical errors, we performed differential measurements. From a scene with a given separation between the two sources, for instance 50 µm, only one source is displaced by a series of very small steps, of approximately 200 nm each - to be sure that the error bars of consecutive points do not overlap. At each step, we determined the reference separation and we performed the separation estimation. The results are displayed in fig. 5.10, where we plotted the experimental points along with a linear fit as a guide for the eye.

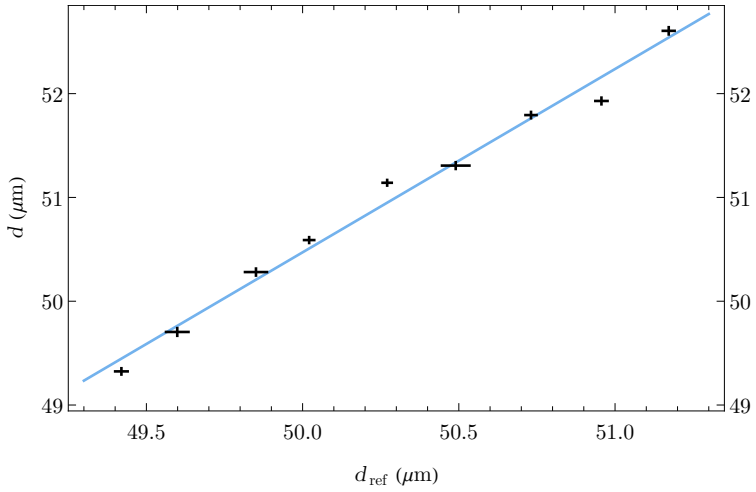

FIGURE 5.10: Estimated separation as a function of the reference separation for differential measurements in the high-flux regime (10^{13} detected photons in total during 5 ms). A separation of around 50 µm is fixed, and one source was displaced by several steps, each of approximately 200 nm. For each point, 200 measurements (each during one integration time of 5 ms) were realized to determine the statistical errors. The experimental points follow a linear tendency (orange line). The horizontal error bars are determined from the quadrant detector measurements, exactly in the same manner as for the estimation error bars.

We observe in this case statistical errors over the estimation of about 20 nm, and a linear trend consistent with the error bars. The slope of the linear fit is not equal to one, due to the limited accuracy, however, this demonstrates that our apparatus displays the unprecedented ability to distinguish between two scenes with a difference in separation of the order of 20 nm. Note that some small deviations from the estimated separation and the linear fit can be observed, this is to be expected in such an ultra-sensitive measurement where the actual scene is dependent on any mechanical or electronic fluctuations. These fluctuations also account for the differences in the measured error bars. Indeed, the horizontal error bars are determined from the quadrant detector measurements, exactly in the same manner as for the estimation error bars. Therefore, different fluctuations between the electronic noise of the quadrant detector and the photodiode at the HG_{10} output and between the mechanical fluctuations between the two optical paths leading either to the MPLC or the quadrant detector result in different error bars.

5.5.4 Stability

We also studied how stable the experimental setup is by acquiring the intensity at the HG_{10} output over 200 s, a time much longer than the integration time of 5 ms. The recorded voltage over time at the output of the photodiode is displayed in fig. 5.11(top). We observe a slow drift of the voltage, of around $0.15\,\mathrm{V\,s^{-1}}$, which is due to some mechanical instabilities in the mounts of the optical elements.

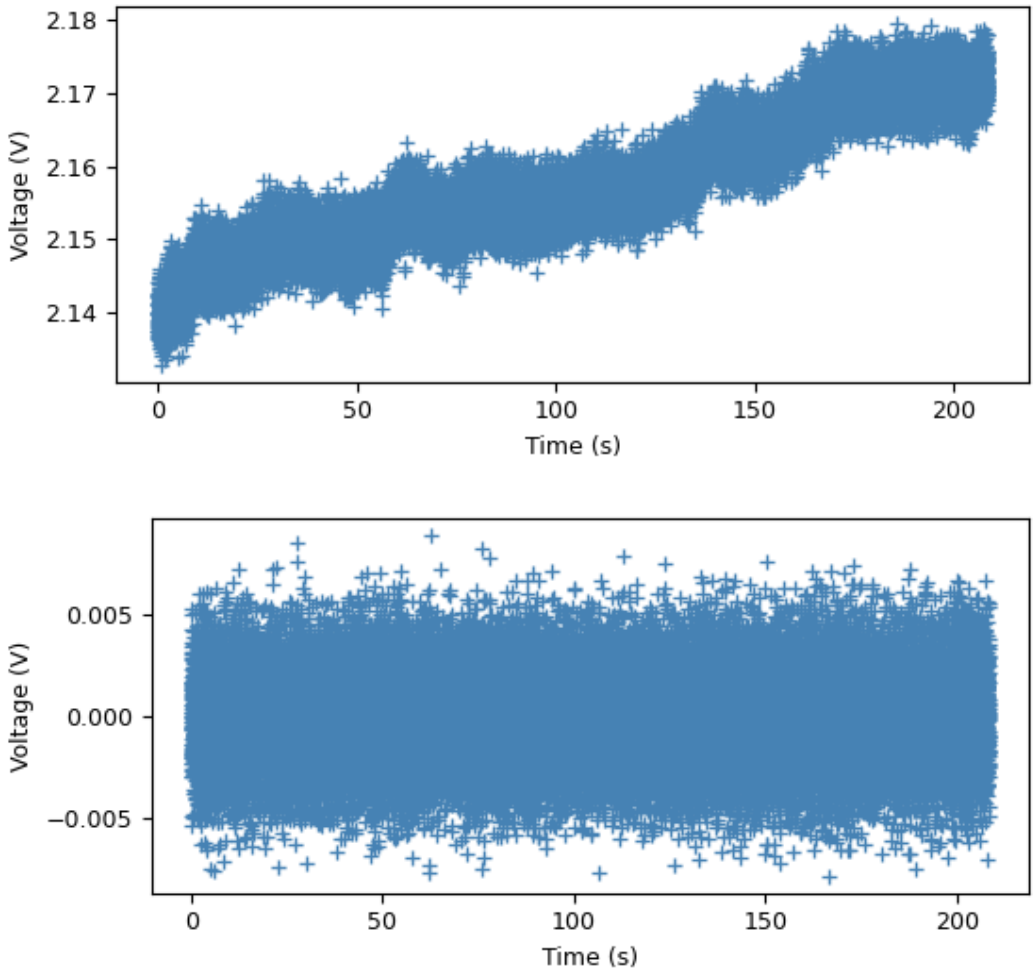

FIGURE 5.11: Temporal signal of the photodiode at the HG_{10} output over a measurement time of 200 s, for an integration time of 5 ms, (top) without and (bottom) with applying a high-pass filter.

When this drift is removed, using a numerical high-pass filter, the remaining noise is the dominant noise, extracted in chapter 4, i.e. the electronic noise of the detectors, which is constant, as shown in fig. 5.11(bottom).

5.6 Improvements of the setup

The results presented in this chapter, and, in particular, in figs. 5.4, 5.7 and 5.9 and in [Rouvière 2024] demonstrate a high level of sensitivity and are very promising for the future of the experiment. Indeed, the PEsto experiment does not end with these results and will be continued and improved in the next years.
The first type of improvement concerns the measured sensitivity that does not saturate the QCRB, even if we are very close to it in the low-flux regime. This is due to the presence of technical noise, as studied in chapter 4: mostly the laser noise for faint sources and the electronic noise of the detection apparatus for bright sources. Both these limiting noise sources will be reduced by using a less noisy laser and less noisy photodiodes associated with an acquisition card. We are also replacing the amplifiers that limit the bandwidth of the phase modulation Once these technical noises are reduced, it is reasonable to suppose that crosstalk will limit the sensitivity for bright sources [Gessner 2020a], and we should compensate them for example with a spatial light modulator before the MPLC.
The second type of improvement aims at enhancing the stability of the experimental setup. The mounts of the optical elements are being replaced with more stable ones. Moreover, most of the mechanical instabilities arise from the fact the optical table is unfortunately situated right under the AC output, resulting in a disruptive airflow. Even though a plexiglass box was placed around the setup during the measurement, the alignment was painful due to the presence of airflow. The plexiglass box will be replaced by a protective cage around the optical table to facilitate this stage.
Moreover, we did not study the contribution of mechanical instabilities to the sensitivity of the estimation. Actually, in our analysis in chapter 4, we only examined the noise sources arising from the sources - the laser noise and phase noise - and those from the detection apparatus - the electronic noise of the detectors and the scope. We implicitly included the fast mechanical fluctuations of the setup to the laser noise. We plan to conduct a more thorough analysis of this noise contribution, and this would allow the investigation of more realistic settings where turbulence limits the sensitivity.
Finally, the last type of improvement involves the calibration stage. Thanks to the precise alignment procedure, it is not necessary to measure the calibration curve every time an estimation measurement is performed, as long as the experimental setup stays identical. However, the calibration needs to be performed every time the setup is modified. It would be therefore more comfortable to automatize this stage, which is not yet the case. For this, we will add an acquisition card and a second motorized translation stage for Linguine.

5.7 Some prospects

As mentioned earlier, we obtained great results with a simple setup of spatial-mode demultiplexing, which is very encouraging for exploring more complex optical scenes. Indeed, the single-parameter study we performed can be extended to a multi-parameter scenario to release some assumptions that were presented in section 5.1 and get closer to more realistic scenes that can be found in microscopy contexts for example. This requires getting more information, by measuring more observables, and extracting it optimally, adapted to this multi-parameter estimation task.

5.7.1 Prospect 1: Larger separation estimation

First, we aim at estimating larger separations. As shown in fig. 2.9, this requires measuring the intensity at the output of more modes, and thus, knowing how to optimally extract the information from the measurement of several observables. The method of moments was extended to a multi-observable estimation [Gessner 2019], as presented in section 2.2.3 and was also adapted to noisy setups in [Sorelli 2021b]. We plan on exploring separations larger than w_0 which requires measuring the intensity at the output of the HG_{00}, HG_{20} and HG_{30} modes - depending on the separation.

Toward this goal, we performed some preliminary experimental measurements with bright sources that, unfortunately, were not conclusive and need to be improved. We measured the calibration curves for the HG_{00}, HG_{20} and HG_{30} modes, presented in fig. 5.12. In order to have a reliable fit of the experimental points with a 6th-order polynomial for short separations, we took more measurement points in the central range, which is why we see an almost continuous line. We observe that, because of the electronic noise of the detection apparatus, the intensities in the modes HG_{20} and HG_{30} are relatively flat as a function of the separation, which will limit the sensitivity of the estimation.
We implemented the method of moments and performed the separation estimation for each mode separately. The results for a reference separation of 520 µm are presented in fig. 5.13. We observe that the accuracy is different for each mode, mostly due to the electronic noise of the detection, when we performed the measurement in the high-flux regime, and, therefore, we could not implement the method of moments on our current measurements.

5.7.2 Prospect 2: Multiparameter estimation

In a more practical scenario, we might have less prior knowledge on the optical scene than what was assumed in this chapter, and more specifically presented in section 5.1. It is therefore interesting to understand how to perform, in a controlled experiment, the estimation of multiple parameters. Various parameters that can be studied and how they can be varied with the experimental setup presented in section 3.4, are displayed in table 5.1. In addition to the cited parameters, it would be also useful to study the situation where more than two sources are close to each other. Questions arise for the data processing and the estimation stage, in particular,

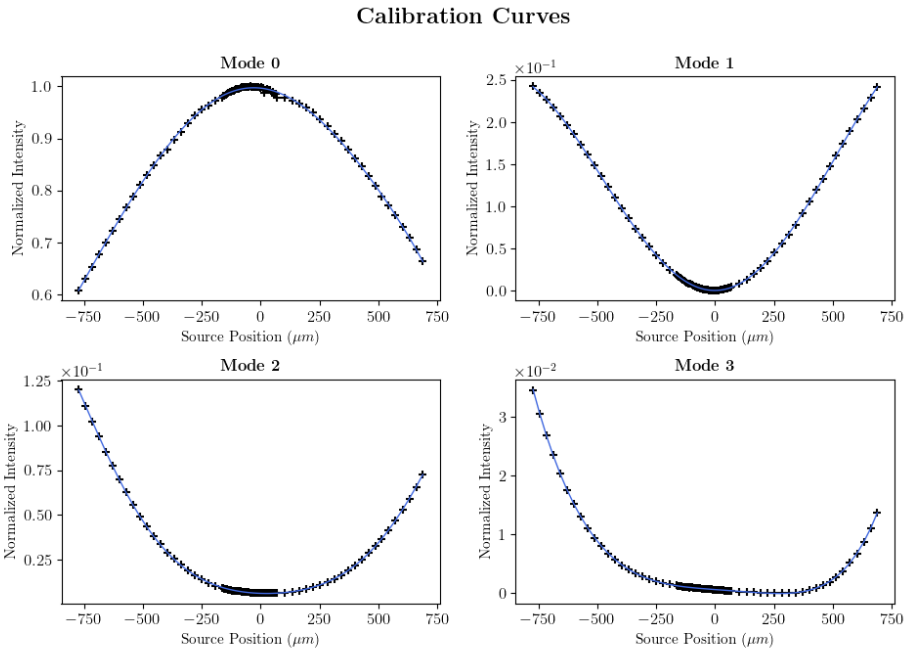

FIGURE 5.12: Calibration curves for the displacement of Trofie, for the modes HG_{00} (mode 0), HG_{10} (mode 1), HG_{20} (mode 2) and HG_{30} (mode 3). The experimental points (black) are fitted with a 6th-order polynomial (blue line).

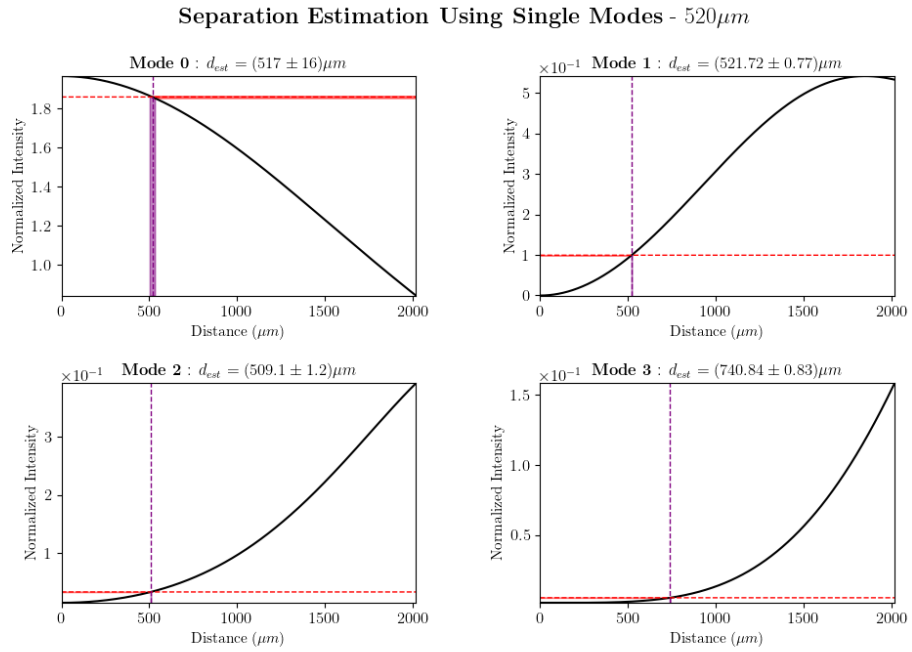

FIGURE 5.13: Separation estimation for the modes HG_{00}, HG_{10}, HG_{20} and HG_{30}.

TABLE 5.1: Various parameters that can be investigated with the PEsto setup.

Parameter	Experimental control
Separation between the sources	Translation stages
Relative intensity between the sources	Half-wave plates
Partial coherence between the source	Phase modulators
Relative size of the waist of the beams	Collimators
Orientation of the source axis	Dove prism
Position of the centroid of the sources	Mirror before the MPLC

not all the parameters can be estimated with an optimized sensitivity at the same time, and trade-offs will have to be met.

The formalism of quantum parameter estimation and the method of moments can also be adapted to a multiparameter estimation task. This section aims at giving an overview of the multiparameter framework, detailed works and reviews on multiparameter estimation can be found in [Tsang 2016; Řehaček 2017; Nichols 2018; Gessner 2020b; Barbieri 2022].

We show how the formalism of single-parameter estimation presented in section 2.1 is generalized to a multiparameter scheme. We aim at estimating a set of parameters $\boldsymbol{\theta} = (\theta_1, \theta_2, ...)^T$, with the best possible sensitivity, which are inferred from a set of estimators $\tilde{\boldsymbol{\theta}} = (\tilde{\theta}_1, \tilde{\theta}_2, ...)^T$. The estimators $\tilde{\boldsymbol{\theta}}$ are functions of the outcomes $\mathbf{x}$ of the measurement of the set of observables $\hat{\mathbf{X}}$. We introduce the covariance matrix Σ as

$$\Sigma_{\ell,k} = \langle (\tilde{\theta}_\ell - \langle \tilde{\theta}_\ell \rangle)(\tilde{\theta}_k - \langle \tilde{\theta}_k \rangle) \rangle, \tag{5.8}$$

where the diagonal elements $\Sigma_\ell = \Delta^2 \tilde{\theta}_\ell$ are the variance on the estimators, and the off-diagonal terms quantify the statistical correlations between estimators. We also express the Fisher information as a symmetric matrix [Helstrom 1969]:

$$(F[\boldsymbol{\theta}])_{\ell,k} = \int \mathrm{d}x \frac{1}{p(\mathbf{x}|\boldsymbol{\theta})} \frac{\partial p(\mathbf{x}|\boldsymbol{\theta})}{\partial \theta_\ell} \frac{\partial p(\mathbf{x}|\boldsymbol{\theta})}{\partial \theta_k}. \tag{5.9}$$

When $\hat{X}$ is measured $\mu \gg 1$ times, the central limit theorem provides the multiparameter CRB as:

$$\Sigma \geq \frac{1}{\mu} (F[\boldsymbol{\theta}])^{-1}, \tag{5.10}$$

which means that for any ℓ, k, we have

$$\left(\Sigma - \frac{1}{\mu} (F[\boldsymbol{\theta}])^{-1} \right)_{\ell,k} \geq 0. \tag{5.11}$$

Finally, we can also define a QFI matrix for the probe state $\hat{\rho}_{\boldsymbol{\theta}}$ as [Helstrom 1969; Holevo 2011]

$$(Q[\boldsymbol{\theta}, \hat{\rho}_{\boldsymbol{\theta}}])_{\ell,k} = \frac{1}{2} \mathrm{Tr}\left[\hat{\rho}_{\boldsymbol{\theta}} \{\hat{L}_\ell, \hat{L}_k\}\right], \tag{5.12}$$

where $\hat{L}_\ell$ is the symmetric logarithmic derivative operator associated with the parameter θ_ℓ, as defined in eq. (2.19), and the curly brackets denote the anti-commutator. It can be shown that a matrix QCRB is:

$$\Sigma \geq \frac{1}{\mu} \left(F[\boldsymbol{\theta}]\right)^{-1} \geq \frac{1}{\mu} \left(Q[\boldsymbol{\theta}, \hat{\rho}_{\boldsymbol{\theta}}]\right)^{-1}. \tag{5.13}$$

This inequality shows some limitations regarding the simultaneous estimations of several parameters. Indeed, an estimation protocol optimized for one parameter might not be optimized for the others, leading to a trade-off in attainable sensitivities [Crowley 2014; Ragy 2016].

The QFI matrix was derived in the context of the simultaneous estimation of the separation, centroid, and relative intensity between the sources, assuming no prior knowledge about these parameters, for two mutually incoherent sources, in [Řehaček 2017]. They demonstrated that $Q[\boldsymbol{\theta}, \hat{\rho}_{\boldsymbol{\theta}}]$ is independent of the centroid, as expected, but not of the relative intensity. When the sources are equally bright, the separation estimation is uncorrelated with the other parameters, and the corresponding QFI is the same as in the single-parameter estimation task derived in section 2.5. However, for unbalanced intensities, the separation estimation is correlated with the centroid, and the centroid estimation is correlated with the intensity ratio, since unequal brightness results in asymmetrical images.

Similarly, a multiparameter version of the method of moments, presented in section 2.2.3, was derived in [Gessner 2020b], which is a generalization of the estimation strategy introduced in [Gessner 2019]. Therefore, this procedure could, in principle, be implemented in the context of multiparameter estimation tasks with various parameters presented in table 5.1, to determine the sensitivity of the estimations and determine whether the QCRB can be saturated experimentally.

5.7.3 Prospect 3: MPLC after a microscope - Collaboration with Geneva

This last section introduces an unfinished business which consists of associating the MPLC with an actual diffraction-limited imaging system, namely a microscope, and real point sources. We are collaborating with Jean-Pierre Wolf's group, at the University of Geneva, which specializes in biophotonics and non-linear microscopy.
Our goal is to implement a proof-of-principle experiment to demonstrate that SPADE at the output of a microscope can enhance the sensitivity of the measurement.
Several samples that mimic pairs of point sources separated by various distances were fabricated by lithography at EPFL in Lausanne. The samples were constituted of gold nanostructures engraved on indium-tin oxide, which are pairs of disks with a diameter of 300 nm and separated by distances of 100 nm, 300 nm and 500 nm. The samples are highly reflective and, therefore, the SPADE measurements were realized on the light reflected on the samples. The experimental setup is presented in fig. 5.14.
At the moment when this manuscript is being written, the data are still under processing.

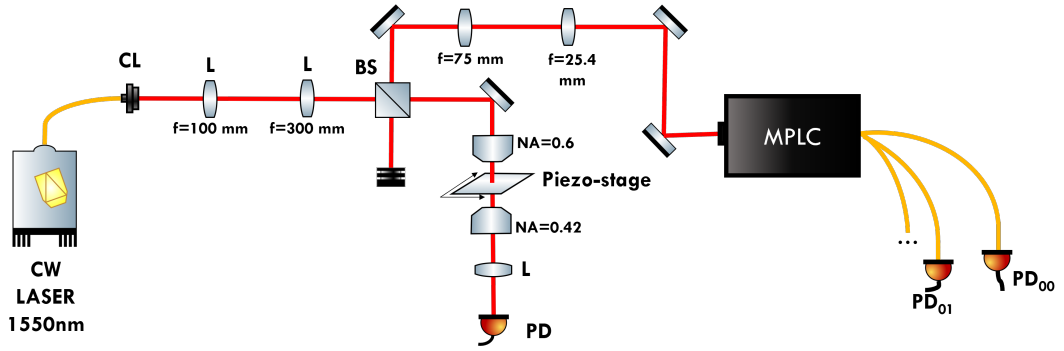

FIGURE 5.14: Experimental setup in Geneva.

5.8 Conclusion

In this chapter, we presented the main experimental results that were obtained in the course of this thesis [Rouvière 2024].
We implemented an experiment for source separation estimation using a spatial-mode demultiplexer, the MPLC from Cailabs, which allows to access several modes, in particular the modes HG_{00}, HG_{10}, HG_{01}, HG_{20} and HG_{02}. We show how the information from these modes can be exploited to align and mode match the sources to the MPLC which then ensures a high sensitivity to the separation estimation.
The experiment was realized in two very different intensity regimes, one with a total of 3500 detected photons during the integration time of the SPAPD and one with a total of 10^{13} detected photons during the integration time of the photodiodes. Consequently, these two distinct experimental situations display specific limitations.
The low-flux regime is dominated by the noise of the laser and presents a lower sensitivity due to the low number of detected photons. However, this relatively lower sensitivity allows for good accuracy and, nonetheless, (almost) saturates the QCRB while outperforming the sensitivity obtained for direct imaging with any current or future camera.
On the other hand, for bright sources, the sensitivity of the estimation, even if limited by the electronic noise of the detection apparatus which prevents it from saturating the QCRB, reaches a five-order of magnitude gain on Rayleigh's limit. This high sensitivity results in a degradation in the accuracy, because the estimation holds on the assumption that the two sources are identical, which is only true to a certain extent.
In general, the separation estimation experiment we presented in this thesis relies on many assumptions that would need to be released to account for more realistic scenarios. This is why we introduce some prospects either in a multiparameter scheme or in associating spatial-mode demultiplexing to actual imaging systems that will be implemented in the future. The experimental scheme we set up is versatile and allows us to explore more complex optical scenes, with many variations that were not discussed here: dynamical scenes, turbulence, finite-size, sources, and various states for the sources.

Conclusion and prospects

In this thesis, we presented the results of an experiment of separation estimation of optical incoherent sources. This experiment was performed using a commercial spatial-mode demultiplexer, the MPLC from Cailabs, which allowed for reaching high sensitivities for faint and bright sources, respectively outperforming ideal direct imaging and beating the diffraction limit by five orders of magnitude.

We presented the theoretical concepts behind this measurement, introducing the multimode description of the electromagnetic field and the quantum parameter estimation theory. In particular, we derived the quantum Fisher information for incoherent sources and we showed that it is saturated by the Fisher information for SPADE. This demonstrates that SPADE is a quantum-optimal measurement for separation estimation of incoherent sources, i.e. that it reaches the ultimate sensitivity limit. This can have applications in many contexts where imaging is needed but still limited by diffraction, such as microscopy, astronomy or remote sensing.

Experimentally, the sensitivity enhancement we obtained was possible thanks to a multimode approach for SPADE, even in the short separation range. Indeed, in principle, it is sufficient to perform a single-mode measurement in the HG_{10} mode. However, extracting information from higher-order modes enables us to limit the impact of experimental imperfections, such as misalignment and imperfect mode matching, on the sensitivity and to ensure reproducibility of the measurements.

By conducting a thorough analysis of the noise sources of the experimental setup, we understand the technical constraints at the source generation and the detection stages, in the two intensity regimes. In particular, the laser and the detectors will be replaced in the near future to enhance the separation-estimation sensitivity even further, eventually reaching the QCRB.
We also performed an experimental characterization of the MPLC, by determining its amplitude crosstalk matrix. We also made a preliminary evaluation of the phase crosstalk. Indeed, even if the sensitivity of the estimation is not limited by its crosstalk for now, it is important to know their order of magnitude to understand their influence once other noise contributions are reduced. The determination of the crosstalk matrix would also give information on how to compensate it to counteract its impact.

We performed experimental single-parameter estimation in one of the simplest optical scenes: two equally bright incoherent sources, with the same spatial shape, assuming that we know everything except for the separation that we want to estimate.
Therefore, many exciting prospects can be envisioned, in particular for exploring

more realistic optical scenes. Indeed, it is useful to study the performances of the estimation when some assumptions are released. Notably, the versatility of the setup enables the investigation of the simultaneous estimation of the separation, the centroid position, the relative intensity and the partial coherence between the sources. As a complement to the analysis of multiparameter estimation for controlled optical scenes, as produced by the PEsto setup, it is also interesting to examine how to extract the relevant information at the output of an actual imaging system like a microscope.
Finally, we conducted experimental separation estimation with phase-averaged coherent states. However, it is worth exploring other states of the field, with different statistics. In particular, we initiated work in this direction by investigating the generation of thermal states with high mean photon numbers from a laser using a combination of phase and amplitude electro-optic modulators. An experimental separation estimation with this type of state is yet to be implemented. We can also imagine variations of the PEsto experiment with non-classical states to examine whether they can provide a quantum advantage in some situations.

Appendix A

Quantum Electromagnetic field and thermal states

This appendix presents the development for the quantization of the electromagnetic field, in particular of the expressions of the quadrature operators eqs. (1.71) and (1.72) and the electric field eq. (1.62). The content given here is from a lecture by Nicolas and [Mandel 1995; Grynberg 2010].
The last section provides details on the statistics of thermal states and gives the derivation of the photon-number probability from [Mandel 1995] for eq. (1.113).

A.1 Canonical quantization

We want to use the Hamiltonian equations to identify pairs of conjugated variables and a Hamiltonian, as it is done to quantize a system of material particles. Therefore, the procedure for quantizing the electromagnetic field goes as follows:

- Write the dynamical equations, i.e. Maxwell's equations, as Hamilton equations to identify conjugated variables,
- Introduce the corresponding quantum operators and the commutation relation.

A.2 Quantization of the electromagnetic field

A.2.1 Potential vector

Maxwell's equations in the vacuum are:

$$\mathbf{E}(\mathbf{r},t) = -\frac{\partial \mathbf{A}(\mathbf{r},t)}{\partial t} \qquad \mathbf{B}(\mathbf{r},t) = \nabla \times \mathbf{A}(\mathbf{r},t) \tag{A.1}$$

where $\mathbf{A}$ is the potential vector and satisfies the wave equation.
We write the potential vector as the sum of its positive frequency component and its negative frequency component:

$$\mathbf{A}(\mathbf{r},t) = \mathbf{A}^{(+)}(\mathbf{r},t) + \mathbf{A}^{(-)}(\mathbf{r},t) \tag{A.2}$$

where $\mathbf{A}^{(-)}(\mathbf{r},t) = [\mathbf{A}^{(+)}(\mathbf{r},t)]^*$.

A.2.2 Field energy

We assume the system is in a box of size L and periodic boundary conditions. Thus, we can decompose $\mathbf{A}^{(+)}(\mathbf{r},t)$ over an orthonormal mode basis $\{\mathbf{u}_\ell(\mathbf{r},t)\}$ and write $\mathbf{A}^{(+)}(\mathbf{r},t) = \sum_\ell \mathcal{A}_\ell(t)\mathbf{u}_\ell(\mathbf{r},t)$, where $\mathcal{A}_\ell(t) = \mathcal{A}_\ell(0)e^{-i\omega_\ell t}$.
We obtain the field energy:

$$H_R = \frac{1}{2}\int_V d^3\mathbf{r}\,(\mathbf{E}(\mathbf{r},t)^2 + c^2\mathbf{B}(\mathbf{r},t)^2) = 2\varepsilon_0 V\sum_\ell \omega_\ell^2|\mathcal{A}_\ell|^2. \tag{A.3}$$

We write $\mathcal{A}_\ell(t) = Q_\ell(t) + iP_\ell(t)$, where $Q_\ell(t)$ and $P_\ell(t)$ are real quantities. Hence

$$H_R = 2\varepsilon_0 V\sum_\ell \omega_\ell^2(Q_\ell(t)^2 + P_\ell(t)^2). \tag{A.4}$$

A.2.3 Conjugated variables

From Eq A.1, we have

$$\frac{\mathrm{d}\mathcal{A}_\ell(t)}{\mathrm{d}t} = -i\omega_\ell\mathcal{A}_\ell(t) \tag{A.5}$$

Hence, the real and imaginary parts of the potential vector satisfy the relations:

$$\begin{aligned}\frac{\partial Q_\ell(t)}{\partial t} &= \omega_\ell P_\ell(t) = \frac{1}{4\varepsilon_0 V\omega_\ell}\frac{\partial H_R}{\partial P_\ell(t)}\\ \frac{\partial P_\ell(t)}{\partial t} &= -\omega_\ell Q_\ell(t) = -\frac{1}{4\varepsilon_0 V\omega_\ell}\frac{\partial H_R}{\partial Q_\ell(t)}\end{aligned} \tag{A.6}$$

Renormalizing the variables $P_\ell(t)$ and $Q_\ell(t)$ as follows:

$$q_\ell(t) = 2\sqrt{\varepsilon_0 V\omega_\ell}Q_\ell(t) \tag{A.7}$$

$$p_\ell(t) = 2\sqrt{\varepsilon_0 V\omega_\ell}P_\ell(t), \tag{A.8}$$

we obtain the Hamiltonian equations

$$\begin{aligned}\frac{\partial q_\ell(t)}{\partial t} &= \frac{\partial H_R}{\partial p_\ell(t)}\\ \frac{\partial p_\ell(t)}{\partial t} &= -\frac{\partial H_R}{\partial q_\ell(t)}.\end{aligned} \tag{A.9}$$

We introduce the corresponding time-independent quantum operators $\hat{q}_\ell$ and $\hat{p}_\ell$ and we impose the commutation relation[1]

$$[\hat{q}_\ell, \hat{p}_{\ell'}] = i\hbar\delta_{\ell\ell'}. \tag{A.10}$$

[1] According to the postulates of quantum mechanics, each pair of canonically conjugate operators has the commutator $i\hbar$.

A.2.4 Creation and annihilation operators

We want to define creation and annihilation operators that satisfy the commutation relations

$$\begin{aligned}[\hat{a}_\ell, \hat{a}^\dagger_{\ell'}] &= \delta_{\ell\ell'}, \\ [\hat{a}_\ell, \hat{a}_{\ell'}] &= 0\end{aligned} \tag{A.11}$$

and that give an energy of the form $\hat{H} \approx \sum_\ell \hbar\omega_\ell \hat{a}^\dagger_\ell \hat{a}_\ell$, which correspond to quantum harmonic oscillators.

From Eq A.7 and A.8, we obtain the operator

$$\hat{\mathcal{A}}_\ell = \frac{1}{2\sqrt{\varepsilon_0 V \omega_\ell}}(\hat{q}_\ell + i\hat{p}_\ell) \tag{A.12}$$

and the commutator is

$$\begin{aligned}[\hat{\mathcal{A}}_\ell, \hat{\mathcal{A}}^\dagger_{\ell'}] &= \frac{1}{4\varepsilon_0 V\sqrt{\omega_\ell \omega_{\ell'}}}[\hat{q}_\ell + i\hat{p}_\ell, \hat{q}_{\ell'} - i\hat{p}_{\ell'}] \\ &= \frac{\hbar}{2\varepsilon_0 V \omega_\ell}\delta_{\ell\ell'}\end{aligned} \tag{A.13}$$

Hence, we define $\hat{a}_\ell$ the creation operator of mode ℓ as

$$\hat{a}_\ell = \sqrt{\frac{2\varepsilon_0 V\omega_\ell}{\hbar}}\hat{\mathcal{A}}_\ell = \frac{1}{\sqrt{2\hbar}}(\hat{q}_\ell + i\hat{p}_\ell) \tag{A.14}$$

so that $\hat{a}_\ell$ satisfies the commutation relations Eq A.11. We can then express $\hat{q}_\ell$ and $\hat{p}_\ell$ in terms of the creation and annihilation operators[2]

$$\hat{q}_\ell = \sqrt{\frac{\hbar}{2}}(\hat{a}^\dagger_\ell + \hat{a}_\ell) \tag{A.18}$$

$$\hat{p}_\ell = i\sqrt{\frac{\hbar}{2}}(\hat{a}^\dagger_\ell - \hat{a}_\ell). \tag{A.19}$$

[2]It is possible to choose another normalization (change of units) for the field operators such as

$$\begin{aligned}\hat{q}_\ell &= (\hat{a}^\dagger_\ell + \hat{a}_\ell) \\ \hat{p}_\ell &= i(\hat{a}^\dagger_\ell - \hat{a}_\ell),\end{aligned} \tag{A.15}$$

so that

$$[\hat{q}_\ell, \hat{p}_{\ell'}] = 2i\delta_{\ell\ell'} \tag{A.16}$$

while keeping

$$[\hat{a}_\ell, \hat{a}^\dagger_{\ell'}] = \delta_{\ell\ell'}. \tag{A.17}$$

This is the normalization that is chosen throughout the manuscript.

A.2.5 Energy of the quantum field

From Eq A.4, the quantum Hamiltonian associated to the field is

$$\begin{aligned}\hat{H}_R &= 2\varepsilon_0 V \sum_\ell \omega_\ell^2 (\hat{Q}_\ell^2 + i\hat{P}_\ell^2) \\ &= 2\varepsilon_0 V \sum_\ell \omega_\ell^2 \frac{1}{4\varepsilon_0 V \omega_\ell} (\hat{q}_\ell^2 + i\hat{p}_\ell^2).\end{aligned} \tag{A.20}$$

Hence, using Eq A.18, A.19 and A.11, we obtain

$$\hat{H}_R = \sum_\ell \hbar\omega_\ell \Big(\hat{a}_\ell^\dagger \hat{a}_\ell + \frac{1}{2}\Big). \tag{A.21}$$

This expression is formally identical to the Hamiltonian of an assembly of decoupled quantum harmonic oscillators.

A.2.6 Electric field operator

Using Eq A.14, the potential vector operator is written

$$\hat{\mathbf{A}}^{(+)}(\mathbf{r}) = \sum_\ell \hat{\mathcal{A}}_\ell \mathbf{u}_\ell(\mathbf{r}) = \sum_\ell \sqrt{\frac{\hbar}{2\varepsilon_0 V \omega_\ell}} \hat{a}_\ell \mathbf{u}_\ell(\mathbf{r}), \tag{A.22}$$

and since $\mathbf{E}(\mathbf{r},t) = -\frac{\partial \mathbf{A}(\mathbf{r},t)}{\partial t}$, we have $\mathbf{E}^{(+)}(\mathbf{r},t) = i\sum_\ell \omega_\ell \mathcal{A}_\ell(t)\mathbf{u}_\ell(\mathbf{r},t)$. From which we obtain

$$\hat{\mathbf{E}}^{(+)}(\mathbf{r}) = i\sum_\ell \mathcal{E}_\ell^{(1)} \hat{a}_\ell \mathbf{u}_\ell(\mathbf{r}) \qquad \text{with} \quad \mathcal{E}_\ell^{(1)} = \sqrt{\frac{\hbar\omega_\ell}{2\varepsilon_0 V}}. \tag{A.23}$$

A.3 Details on thermal states

A.3.1 Density operator

A system with total energy $\hat{H}$ in thermal equilibrium at temperature T can be described by the density operator ρ_{th} given by the Maxwell-Boltzmann (or Bose-Einstein, it does not matter here) statistics [Mandel 1995]:

$$\hat{\rho}_{th} = \frac{\exp\big(-\hat{H}/k_B T\big)}{\mathrm{Tr}\big[\exp\big(-\hat{H}/k_B T\big)\big]}, \tag{A.24}$$

where k_B is the Boltzmann constant. For a single-mode black-body, we have $\hat{H} = \hbar\omega\left(\hat{n} + \frac{1}{2}\right)$, and therefore

$$\hat{\rho}_{th} = \frac{\exp(-\hat{n}\hbar\omega/k_B T)}{\mathrm{Tr}[\exp(-\hat{n}\hbar\omega/k_B T)]}. \tag{A.25}$$

Note that the zero point energy has conveniently dropped out from the normalization. Since in the Fock basis, we can write

$$\mathrm{Tr}[f(\hat{n})] = \sum_n \langle n| f(\hat{n}) |n\rangle = \sum_n f(n), \tag{A.26}$$

we have

$$\hat{\rho}_{th} = \frac{\exp(-\hat{n}\hbar\omega/k_\mathrm{B}T)}{\sum_n \exp(-n\hbar\omega/k_\mathrm{B}T)]} = (1-\exp(-n\hbar\omega/k_\mathrm{B}T))\exp(-\hat{n}\hbar\omega/k_\mathrm{B}T). \tag{A.27}$$

Using that $1 = \sum_n |n\rangle \langle n|$, we obtain

$$\begin{aligned}\hat{\rho}_{th} &= \sum_n (1-\exp(-n\hbar\omega/k_\mathrm{B}T))\exp(-n\hbar\omega/k_\mathrm{B}T)\,|n\rangle\langle n| \\ &= \sum_n P(n)\,|n\rangle\langle n|\,.\end{aligned} \tag{A.28}$$

A.3.2 Moments of the number of photons operator

Let us define the function

$$F(\xi) = \langle (1+\xi)^{\hat{n}} \rangle. \tag{A.29}$$

Using the binomial series, we have

$$F(\xi) = \sum_{r=0}^{\infty} \frac{\xi^r}{r!} \langle \hat{n}^{(r)} \rangle \tag{A.30}$$

where

$$\langle \hat{n}^{(r)} \rangle = \langle \hat{n}(\hat{n}-1)...(\hat{n}-r+1) \rangle = \frac{\langle \hat{n} \rangle !}{\langle \hat{n}-r \rangle !}. \tag{A.31}$$

Moreover, with the expectation value definition, we also have

$$\begin{aligned}F(\xi) &= \sum_n P(n)(1+\xi)^n \\ &= \frac{1-\exp(-\hbar\omega/k_\mathrm{B}T)}{1-(1+\xi)\exp(-\hbar\omega/k_\mathrm{B}T)},\end{aligned} \tag{A.32}$$

using that

$$\frac{1}{1-x} = \sum_n x^n. \tag{A.33}$$

Therefore, we obtain

$$\sum_{r=0}^{\infty} \frac{\xi^r}{r!} \langle \hat{n}^{(r)} \rangle = \sum_{r=0}^{\infty} \left(\frac{\xi}{\exp(\hbar\omega/k_\mathrm{B}T) - 1} \right)^r. \tag{A.34}$$

It follows that

$$\langle \hat{n}^{(r)} \rangle = \frac{r!}{(\exp(\hbar\omega/k_\mathrm{B}T) - 1)^r}. \tag{A.35}$$

A.3.3 Photon number statistics

From eq. (A.35), we obtain

$$\exp(\hbar\omega/k_B T) = 1 + \frac{1}{\langle\hat{n}\rangle}, \tag{A.36}$$

and finally, we get

$$P(n) = \frac{\langle\hat{n}\rangle^n}{(\langle\hat{n}\rangle + 1)^{n+1}}. \tag{A.37}$$

Appendix B

Method of Moments

This appendix presents the derivation of eqs. (2.46) and (2.47).

We consider a multi-observable and single-parameter method of moments where K observables $\hat{\mathbf{X}} = (\hat{X}_1, ..., \hat{X}_K)^T$ are accessible to estimate a parameter θ. Their linear combination is given by $\hat{X}_\mathbf{m} = \mathbf{m}^T\ \hat{\mathbf{X}}$, where $\mathbf{m} = (m_1, ..., m_K)^T$ is the coefficient vector. The error propagation formula (eq. (2.44)) gives the sensitivity as

$$\chi^{-2}[\theta, \hat{X}_\mathbf{m}] = \frac{(\partial_\theta \langle \hat{X}_\mathbf{m} \rangle)^2}{\Delta^2 \hat{X}_\mathbf{m}}, \tag{B.1}$$

with

$$\begin{aligned} \partial_\theta \langle \hat{X}_\mathbf{m} \rangle &= \mathbf{m}^T\ \partial_\theta \langle \hat{\mathbf{X}} \rangle \\ \Delta^2 \hat{X}_\mathbf{m} &= \langle \mathbf{m}^T\ \hat{\mathbf{X}} \hat{\mathbf{X}}^T\ \mathbf{m} \rangle - \langle \mathbf{m}^T\ \hat{\mathbf{X}} \rangle \langle \hat{\mathbf{X}}^T\ \mathbf{m} \rangle = \mathbf{m}^T \Gamma[\theta, \hat{\mathbf{X}}] \mathbf{m} \end{aligned} \tag{B.2}$$

where $\Gamma[\theta, \hat{\mathbf{X}}]$ is the covariance matrix defined in eq. (1.137) as

$$\Gamma[\theta, \hat{\mathbf{X}}]_{ij} = \langle \hat{X}_i \hat{X}_j \rangle - \langle \hat{X}_i \rangle \langle \hat{X}_j \rangle. \tag{B.3}$$

We use the Cauchy-Schwarz inequality, which states

$$|\mathbf{u}^T \mathbf{v}|^2 \leq (\mathbf{u}^T \mathbf{u})(\mathbf{v}^T \mathbf{v}), \tag{B.4}$$

with

$$\begin{aligned} \mathbf{u} &= \Gamma[\theta, \hat{\mathbf{X}}]^{1/2} \mathbf{m}, \\ \mathbf{v} &= \Gamma[\theta, \hat{\mathbf{X}}]^{-1/2} \partial_\theta \langle \hat{\mathbf{X}} \rangle. \end{aligned} \tag{B.5}$$

Therefore, the sensitivity eq. (B.1) can be written

$$\chi^{-2}[\theta, \hat{X}_\mathbf{m}] = \frac{|\mathbf{u}^T \mathbf{v}|^2}{\mathbf{u}^T \mathbf{u}}, \tag{B.6}$$

hence the Cauchy-Schwarz inequality eq. (B.4) gives

$$\chi^{-2}[\theta, \hat{X}_\mathbf{m}] \leq M[\theta, \hat{X}], \tag{B.7}$$

with the optimal sensitivity

$$M[\theta, \hat{X}] = \partial_\theta \langle \hat{\mathbf{X}}^T \rangle \Gamma[\theta, \hat{\mathbf{X}}]^{-1} \partial_\theta \langle \hat{\mathbf{X}} \rangle. \tag{B.8}$$

The Cauchy-Schwarz inequality is saturated for $\mathbf{u} \propto \mathbf{v}$, i.e. $\mathbf{m} \propto \Gamma[\theta, \hat{\mathbf{X}}]^{-1} \partial_\theta \langle \hat{\mathbf{X}} \rangle$. We therefore choose the optimal coefficients as

$$\mathbf{m} = \Gamma[\theta, \hat{\mathbf{X}}]^{-1} \partial_\theta \langle \hat{\mathbf{X}} \rangle. \tag{B.9}$$

Appendix C

Details on calculations for separation estimation

C.1 Quantum Fisher information for separation estimation

In this section, we provide some expressions that are useful to derive Eq 2.75, there are extracted from [Sorelli 2023].

The initially populated modes are

$$\begin{aligned} u_0[d](\mathbf{r}) &= \frac{u_{00}(\mathbf{r}+\mathbf{r}_0)+u_{00}(\mathbf{r}-\mathbf{r}_0)}{\sqrt{2(1+\delta)}} \\ v_0[d](\mathbf{r}) &= \frac{u_{00}(\mathbf{r}+\mathbf{r}_0)-u_{00}(\mathbf{r}-\mathbf{r}_0)}{\sqrt{2(1-\delta)}}, \end{aligned} \tag{C.1}$$

where δ is the overlap between the source images with

$$\delta = \int d^2\mathbf{r}\; u_0[d](\mathbf{r}) v_0[d](\mathbf{r}) = e^{-\frac{d^2}{2w_0^2}}. \tag{C.2}$$

The normalized derivative modes are

$$\begin{aligned} u_0'[d](\mathbf{r}) &= \partial_d u_0[d](\mathbf{r})/\eta_u \\ v_0'[d](\mathbf{r}) &= \partial_d v_0[d](\mathbf{r})/\eta_v, \end{aligned} \tag{C.3}$$

where

$$\begin{aligned} \eta_u^2 = ||\partial_d u_0[d](x)||^2 &= \int \mathrm{d}^2\mathbf{r}\; (\partial_d u_0[d](x))^2 = \frac{(\Delta k)^2-\beta}{4(1+\delta)} - \frac{(\partial_d\delta)^2}{4(1+\delta)^2} \\ \eta_v^2 = ||\partial_d v_0[d](x)||^2 &= \int \mathrm{d}^2\mathbf{r}\; (\partial_d v_0[d](x))^2 = \frac{(\Delta k)^2+\beta}{4(1-\delta)} - \frac{(\partial_d\delta)^2}{4(1-\delta)^2} \end{aligned} \tag{C.4}$$

with

$$\begin{aligned} (\Delta k)^2 &= \int \mathrm{d}^2\mathbf{r}\; (\partial_d u_{00}(x))^2 \\ \beta &= \int \mathrm{d}^2\mathbf{r}\; \partial_d u_{00}(\mathbf{r}+\mathbf{r}_0)\partial_d u_{00}(\mathbf{r}-\mathbf{r}_0). \end{aligned} \tag{C.5}$$

For Gaussian beams, i.e. beams in mode

$$u_{00}(\mathbf{r}) = \sqrt{\frac{2}{\pi w_0^2}} e^{-\frac{x^2+y^2}{w_0^2}}, \tag{C.6}$$

the overlap δ is

$$\delta = e^{-\frac{d^2}{2w_0^2}} \tag{C.7}$$

and its derivative is given by

$$\partial_d \delta = -\frac{d e^{\frac{d^2}{2w_0^2}}}{w_0^2}. \tag{C.8}$$

Moreover, inserting eq. (C.6) in eq. (C.5), we obtain:

$$\begin{aligned} (\Delta k)^2 &= \frac{1}{w_0^2} \\ \beta &= \frac{-d^2 + w^2}{w^4} e^{-\frac{d^2}{2w_0^2}}. \end{aligned} \tag{C.9}$$

For small separations, we note that we have the following behaviours:

$$\delta = 1 - (\Delta k)^2 \frac{d^2}{2} + \mathcal{O}(d^4) \tag{C.10}$$

$$\beta = (\Delta k)^2 + \mathcal{O}(d^2) \tag{C.11}$$

C.2 Expectation values of the field operators for separation estimation

This section derives eq. (2.78) and is based on [Sorelli 2021a].

C.2.1 P function of the sources

As depicted in section 2.5.1, the sources are described by the quantum state

$$\hat{\rho}_0 = \hat{\rho}_{s_1}(N) \otimes \hat{\rho}_{s_2}(N) = \int \mathrm{d}^2\alpha_1 \mathrm{d}^2\alpha_2 P_{s_1,s_2}(\alpha_1, \alpha_2) \left|\alpha_1, \alpha_2\right\rangle \left\langle\alpha_1, \alpha_2\right| \tag{C.12}$$

where $\hat{\rho}_a(N)$ are density operators associated with a thermal state with mean photon number N in the mode associated with the operator $\hat{a}$, $|\alpha_a\rangle$ are coherent states of the field $\hat{a}$, and $P_{s_1,s_2}(\alpha_1, \alpha_2) = P_{s_1}(\alpha_1) P_{s_2}(\alpha_2)$ is the Glauber-Sudarshan function such that

$$P_a(\alpha_a) = \frac{1}{\pi N} \exp\left(-\frac{|\alpha_a|^2}{N}\right). \tag{C.13}$$

We define the modes $\hat{s}_\pm$ as

$$\begin{pmatrix} \hat{s}_+ \\ \hat{s}_- \end{pmatrix} = \frac{1}{\sqrt{2}} \begin{pmatrix} 1 & 1 \\ 1 & -1 \end{pmatrix} \begin{pmatrix} \hat{s}_1 \\ \hat{s}_2 \end{pmatrix} \tag{C.14}$$

and the associated coherent states $|\alpha_\pm\rangle$ as

$$|\alpha_\pm\rangle = \left|\frac{\alpha_1 \pm \alpha_2}{\sqrt{2}}\right\rangle. \tag{C.15}$$

We can therefore write the quantum state of the sources in terms of the coherent states $|\alpha_\pm\rangle$:

$$\hat{\rho}_0 = \int \mathrm{d}^2\alpha_+ \mathrm{d}^2\alpha_- P_{s_+,s_-}(\alpha_+,\alpha_-)\,|\alpha_+,\alpha_-\rangle\,\langle\alpha_+,\alpha_-|\,, \tag{C.16}$$

where $P_{s_+,s_-}(\alpha_+,\alpha_-) = P_{s_1,s_2}\left(\frac{\alpha_1\alpha_2}{\sqrt{2}}, \frac{\alpha_1-\alpha_2}{\sqrt{2}}\right)$.

C.2.2 P function in the image plane

We propagate the quantum state of the source to the image plane. Using eq. (2.66) for the propagation through the imaging system:

$$\hat{b}_\pm = \sqrt{\kappa_\pm}\hat{s}_\pm + \sqrt{1-\kappa_\pm}\hat{v}_\pm, \tag{C.17}$$

we have $|\alpha_+,\alpha_-\rangle \to |\beta_+,\beta_-\rangle = \left|\sqrt{\kappa_+}\alpha_+, \sqrt{\kappa_-}\alpha_-\right\rangle$, with $|\beta_\pm\rangle$ the coherent states of the field operators $\hat{b}_\pm$. The quantum state in the image plane can thus be written

$$\hat{\rho} = \int \mathrm{d}^2\beta_+ \mathrm{d}^2\beta_- P_{b_+,b_-}(\beta_+,\beta_-)\,|\beta_+,\beta_-\rangle\,\langle\beta_+,\beta_-|\,, \tag{C.18}$$

with

$$P_{b_+,b_-}(\beta_+,\beta_-) = \frac{1}{\kappa_+\kappa_-} P_{s_+,s_-}\left(\frac{\beta_+}{\sqrt{\kappa_+}}, \frac{\beta_-}{\sqrt{\kappa_-}}\right). \tag{C.19}$$

Combining eqs. (C.13) and (C.19), we obtain

$$P_{b_+,b_-}(\beta_+,\beta_-) = \frac{1}{\pi^2 N_+ N_-} \exp\left(-\frac{|\beta_+|^2}{N_+} - \frac{|\beta_-|^2}{N_-}\right), \tag{C.20}$$

with $N_\pm = N\kappa_\pm = N\kappa(1\pm\delta)$.

C.2.3 Expectation values of the field operators

In sections 2.5.3 and 2.5.4, we need to calculate expressions of the form $\sum_{i,j=\pm} c_{ij}\langle\hat{b}_i^\dagger\hat{b}_j\rangle$. The expectation values of the field operators $\hat{b}_i$ can be calculated with the P function, and we have

$$\langle\hat{b}_i^\dagger\hat{b}_j\rangle = \int \beta_i^*\beta_j P_{b_+,b_-}(\beta_+,\beta_-)\mathrm{d}^2\beta_+\mathrm{d}^2\beta_-. \tag{C.21}$$

Since the P function eq. (C.20) is Gaussian, we use the Gaussian integrals:

$$\begin{aligned}\int_{-\infty}^{\infty} \exp\left(-x^2/\alpha\right)\mathrm{d}x &= \sqrt{\alpha\pi},\\ \int_{-\infty}^{\infty} x\exp\left(-x^2/\alpha\right)\mathrm{d}x &= 0,\\ \int_{-\infty}^{\infty} x^2\exp\left(-x^2/\alpha\right)\mathrm{d}x &= \frac{\alpha\sqrt{\alpha\pi}}{2},\end{aligned} \tag{C.22}$$

where α is real, to determine eq. (C.21). Consequently, we have

$$\langle \hat{b}_+^\dagger \hat{b}_- \rangle = \langle \hat{b}_-^\dagger \hat{b}_+ \rangle = 0, \tag{C.23}$$

and

$$\langle \hat{b}_\pm^\dagger \hat{b}_\pm \rangle = \frac{1}{\pi N_\pm} \times 2\sqrt{\pi N_\pm} \int_{-\infty}^{\infty} \exp\left(-\frac{x^2}{N_\pm}\right)\mathrm{d}x = N_\pm. \tag{C.24}$$

Appendix D

Experimental characterizations

In this appendix, I grouped some characterization measurements that I did for different devices. In particular, I provide details on the characterization of the electro-optical modulators.

D.1 Electro-optical modulators

D.1.1 Experimental setup

The phase (iXBlue, MPX-LN-0.1) and amplitude (iXBlue, MX-LN-0.1) modulators are integrated devices with bandwidths from DC to 200 MHz. They are driven with are arbitrary signal generator implemented on Red Pitaya components (STEMlab 125-14). Since the outputs of the Red Pitayas are limited to -1 V to 1 V, which is too low to drive the modulators, amplifiers built by the electronic workshop are added before the EOMs. These amplifiers are closed-loop operational amplifiers with a bandwidth of 1 MHz, and a variable gain of up to 10. The Red Pitayas are also used to generate the modulating signals for producing the thermal states. In order to implement accurate inverse transverse sampling, we need to characterize the modulators to extract the V_pi of the phase modulators, the transmissivity of the amplitude modulators as well as their bandwidths. Measurements are realized either with a homodyne detector (Koheron, PD100B) with a DC to 100 MHz bandwidth for the characterization of the phase modulators, or with a photodiode (Thorlabs, PDA50B2) for the characterization of the amplitude modulators.

D.1.2 V_π of the phase EOM

The V_π of the phase EOM is the voltage amplitude corresponding to a π phase shift. We measured it for both phase modulators by modulating the EOM with a ramp signal with variable amplitude and performing a homodyne detection between the signal at the output of the modulator and a local oscillator.
As illustrated by Figure D.1, when the amplitude of the modulating signal is small, only a fraction of a period of the interference pattern appears during one period of the modulation, while for larger amplitudes, several periods of the interference pattern are formed during one period of the modulation. We chose to use a ramp signal for the modulation, instead of a sine, to have sharp transitions when the monotony of the modulation changes for an easier determination.

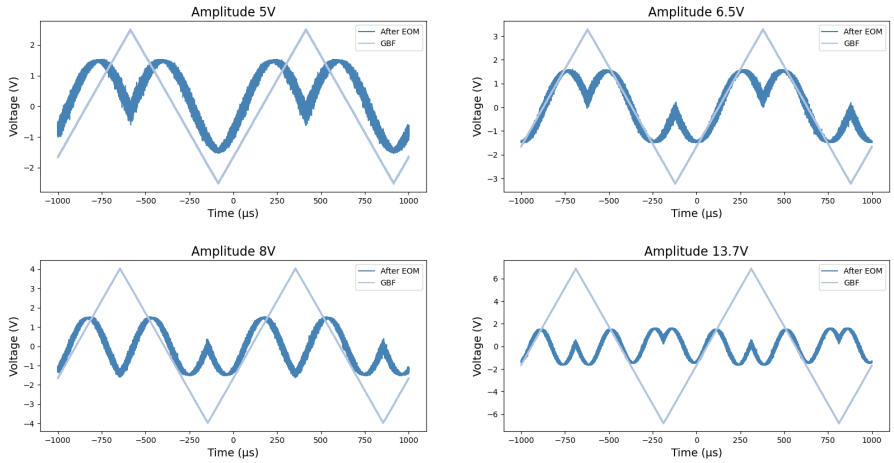

FIGURE D.1: V_π characterization of a PM EOM.

For simplicity, we actually determined the $2V_\pi$, or $V_{2\pi}$ by the linearity of the modulator, which is given by the voltage for which we obtain exactly one period of the interference pattern. We measured $V_{2\pi} \simeq 6.5\,\mathrm{V}$ for the modulator corresponding to Figure D.1 and $V_{2\pi} \simeq 8.5\,\mathrm{V}$ for the second one. These values can not be determined precisely due to noises, they also change from day to day because of thermal fluctuations, which is why we need to adapt the gain of the amplifiers by doing this procedure daily.

D.1.3 Transmissivity of the amplitude EOM

The transmissivity of the amplitude EOMs is obtained by modulating with a DC signal and measuring the output power of the modulator with a photodiode as a function of the modulation voltage. The obtained calibration curve for one of the amplitude modulators is displayed in Figure D.2. Fitting with $f(\mathrm{U}) = A\cos(k(\mathrm{U}-\mathrm{U}_0)) + B$, we obtain the parameters $k = 1.29$ and $\mathrm{U}_0 = -0.05$ for the displayed modulator, and $k = 0.93$ and $\mathrm{U}_0 = 1.56$ for the second one. These parameters are not constant, particularly the voltage U_0, and change with thermal fluctuations, which is why they are not determined with high precision. The gains of the amplifiers corresponding to the amplitude modulators need therefore to be adapted daily to match the statistics of thermal states.

D.1.4 Bandwidth

We also add a look at the behavior of the EOMs depending on the frequency of the modulating signal. As displayed on Figures D.3 and D.4, the modulators display expected behaviors up to 1 MHz. The bandwidth was expected to be limited by the electronic amplifiers.

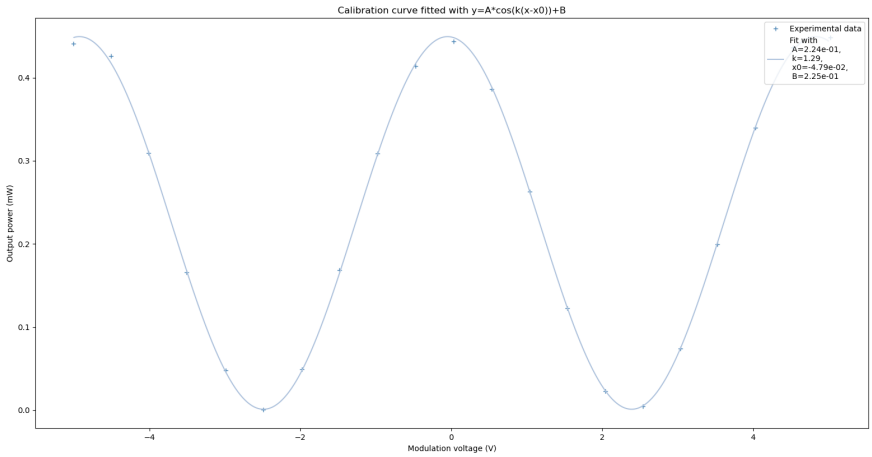

FIGURE D.2: Calibration of one amplitude modulator EOM.

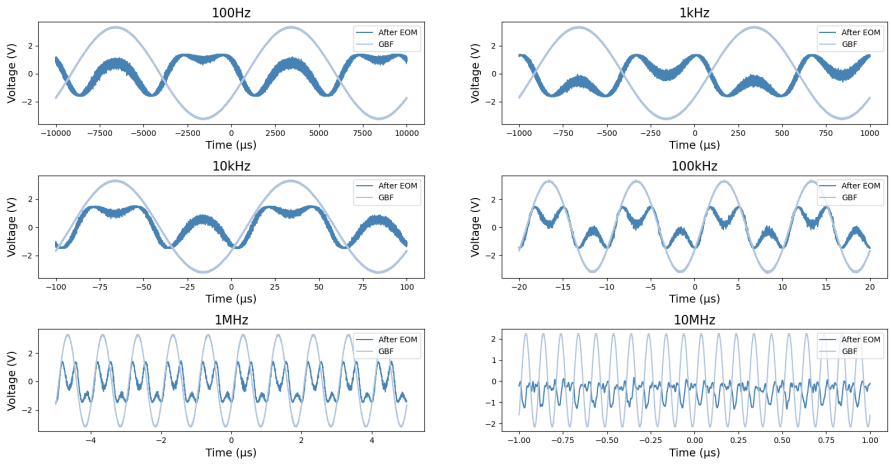

FIGURE D.3: Bandwidth of a phase EOM.

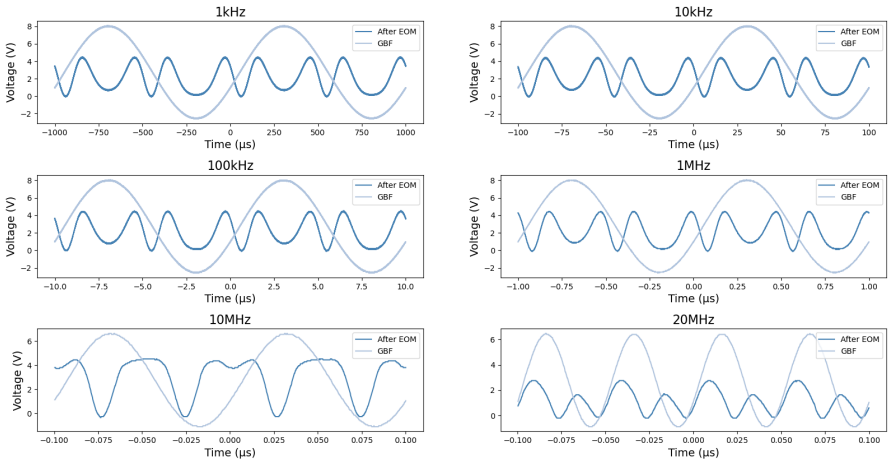

FIGURE D.4: Bandwidth of an amplitude EOM.

D.2 Laser diode

I measured the power spectral density $\Gamma(f)$ of the laser diode (Thorlabs, SFL1550P) with a photodiode and the spectrum analyzer (see fig. D.5) and, from this measurement, I extracted the relative intensity noise (RIN) of the laser (see fig. D.6), with

$$\mathrm{RIN} = 10 \log_{10} \left(\frac{\Gamma(f)}{V_{\mathrm{mean}}} \right), \tag{D.1}$$

where V_{mean} is the mean voltage value measured by the photodiode.

D.3 Red Pitaya

We measured, with the oscilloscope, the voltage distribution generated by the Red Pitaya (STEMlab, 125-14) for the amplitude noise using the inverse transform sampling (see eq. (3.18)), to check that it corresponds to eq. (3.16). We also measured this distribution at the output of the homemade 1MHz amplifier that amplifies the Red Pitaya's output, so that we were sure that the amplifier does not distort the distribution. The results are presented in fig. D.7.

D.4 Homodyne detector

The homodyne detector (Koheron, PDB100B), which was used to characterize the thermal states, was characterized beforehand. We measured its spectrum for different local oscillator powers and a vacuum input. The results are presented in fig. D.8. In order to have an idea of the clearance of the homodyne detector, we plotted its clearance i.e. its signal-to-noise ratio, where the signal is the power of the detector

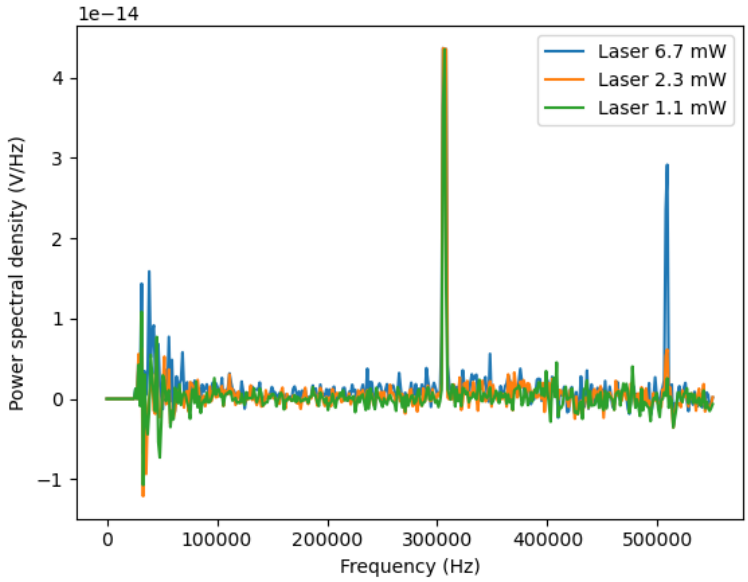

FIGURE D.5: Power spectral density of the laser diode.

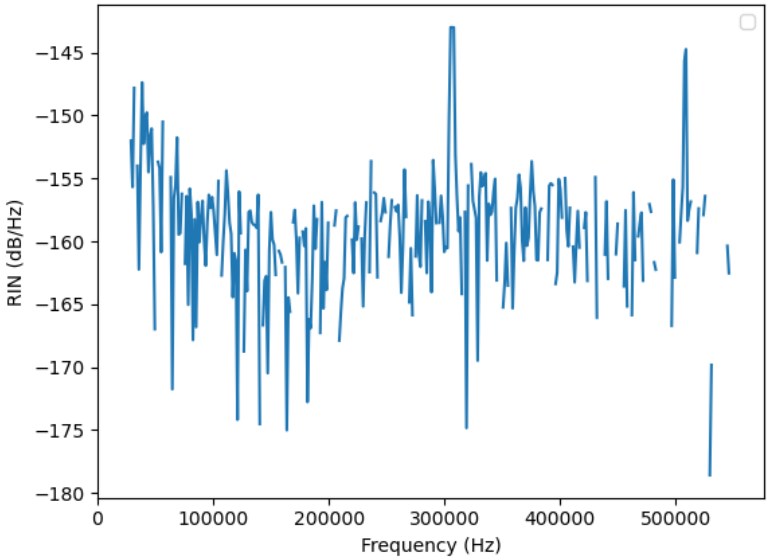

FIGURE D.6: Measured relative intensity noise of the laser diode.

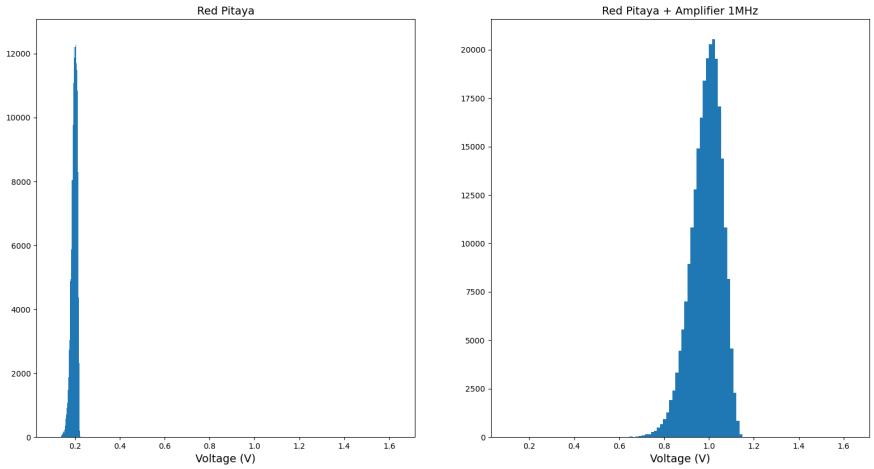

FIGURE D.7: Histograms of the output voltages of the Red Pitaya generating the amplitude noise (left) and of the homemade 1MHz amplifier (right).

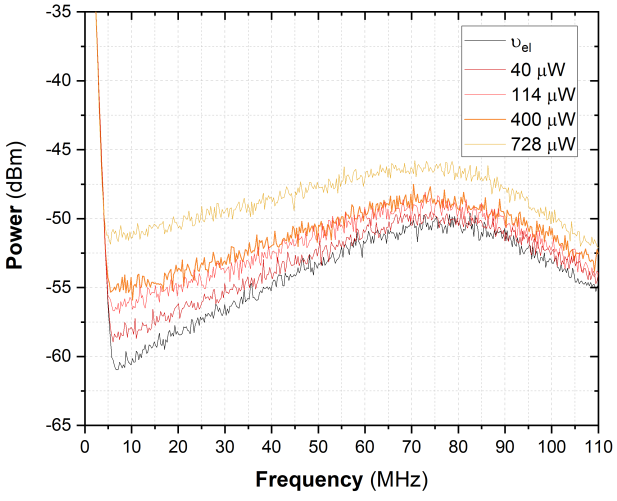

FIGURE D.8: Noise spectrum of the Koheron homodyne detector for different local oscillator powers. The electronic noise of the spectrum analyzer is plotted in black.

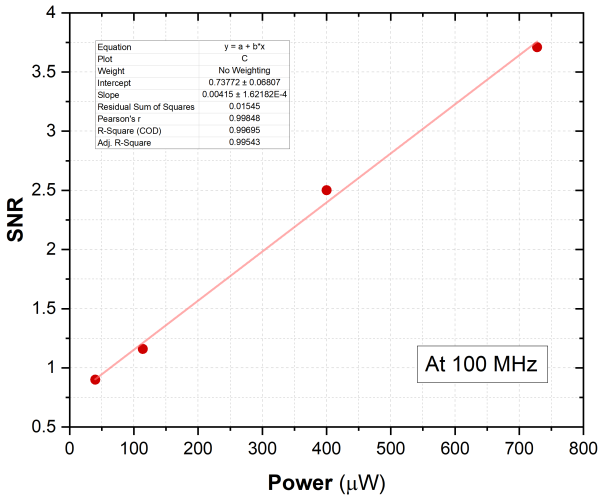

FIGURE D.9: Clearance of the Koheron homodyne detector.

and the noise is the power of the electronic noise, at 100 MHz. The clearance is presented in fig. D.9.

Bibliography

[Abbe 1873] E. Abbe. “Beiträge zur Theorie des Mikroskops und der mikroskopischen Wahrnehmung”. *Archiv für Mikroskopische Anatomie* 9.1 (Dec. 1873), pp. 413–468. DOI: 10.1007/BF02956173 (cit. on pp. 2, 68, 69).

[Aniano 2011] G. Aniano et al. “Common-Resolution Convolution Kernels for Space- and Ground-Based Telescopes”. *Publications of the Astronomical Society of the Pacific* 123.908 (Sept. 2011). Publisher: University of Chicago Press, p. 1218. DOI: 10.1086/662219 (cit. on p. 52).

[Ansquer 2022] Matthieu Ansquer. “Modal approach to the dynamics of optical frequency combs and applications”. PhD thesis. Sorbonne Université, Feb. 2022 (cit. on p. 19).

[Arecchi 1965] F T Arecchi. “Measurement of the Statistical Distribution of Gaussian and Laser Sources”. 15.24 (1965), p. 5 (cit. on p. 103).

[Arvind 1995] Arvind et al. “The Real Symplectic Groups in Quantum Mechanics and Optics”. *Pramana* 45.6 (Dec. 1995). arXiv:quant-ph/9509002, pp. 471–497. DOI: 10.1007/BF02848172 (cit. on p. 31).

[Ashby 2020] James Ashby et al. “Temporal mode transformations by sequential time and frequency phase modulation for applications in quantum information science”. *Optics Express* 28.25 (Dec. 2020), p. 38376. DOI: 10.1364/OE.410371 (cit. on p. 37).

[Bachor 2019] Hans-A. Bachor and Timothy C. Ralph. *A Guide to Experiments in Quantum Optics*. 3e édition. Weinheim: Blackwell Verlag GmbH, Sept. 2019 (cit. on pp. 26, 34).

[Barbieri 2022] Marco Barbieri. “Optical Quantum Metrology”. *PRX Quantum* 3.1 (Jan. 2022), p. 010202. DOI: 10.1103/PRXQuantum.3.010202 (cit. on pp. 1, 40, 49, 153).

[Bates 2007] W. Mark Bates et al. "Multicolor Super-resolution Imaging with Photo-switchable Fluorescent Probes". *Science (New York, N.Y.)* 317.5845 (Sept. 2007), pp. 1749–1753. DOI: 10.1126/science.1146598 (cit. on p. 73).

[Beijersbergen 1993] M W Beijersbergen and L Allen. "Astigmatic laser mode converters and transfer of orbital angular momentum". *OPTICS COMMUNICATIONS* 96.1 (1993) (cit. on p. 36).

[Betzig 2006] Eric Betzig et al. "Imaging Intracellular Fluorescent Proteins at Nanometer Resolution". *Science* 313.5793 (Sept. 2006). Publisher: American Association for the Advancement of Science, pp. 1642–1645. DOI: 10.1126/science.1127344 (cit. on pp. 2, 72).

[Binnig 1986] G. Binnig, C. F. Quate, and Ch. Gerber. "Atomic Force Microscope". *Physical Review Letters* 56.9 (Mar. 1986). Publisher: American Physical Society, pp. 930–933. DOI: 10.1103/PhysRevLett.56.930 (cit. on p. 71).

[BIPM 2019] BIPM. *Le Système international d'unités (SI)*. 2019 (cit. on p. 1).

[Birks 2015] T. A. Birks et al. "The photonic lantern". *Advances in Optics and Photonics* 7.2 (June 2015). Publisher: Optica Publishing Group, pp. 107–167. DOI: 10.1364/AOP.7.000107 (cit. on p. 34).

[Black 2001] Eric D. Black. "An introduction to Pound–Drever–Hall laser frequency stabilization". *American Journal of Physics* 69.1 (Jan. 2001), pp. 79–87. DOI: 10.1119/1.1286663 (cit. on pp. 122, 123).

[Bonsma-Fisher 2019] Kent A G Bonsma-Fisher et al. "Realistic sub-Rayleigh imaging with phase-sensitive measurements". *New Journal of Physics* 21.9 (Sept. 2019), p. 093010. DOI: 10.1088/1367-2630/ab3d97 (cit. on p. 75).

[Boucher 2018] Pauline Boucher. "Spatial mode multiplexing : from fundamental concepts to applications". These de doctorat. Sorbonne université, Nov. 2018 (cit. on p. 3).

[Boucher 2020] Pauline Boucher et al. "Spatial optical mode demultiplexing as a practical tool for optimal transverse distance estimation". *Optica* 7 (Oct. 2020), pp. 1621–1626. DOI: 10.1364/OPTICA.404746 (cit. on pp. 3, 81, 84).

[Box 2015] George E. P. Box et al. *Time Series Analysis: Forecasting and Control*. 5th edition. Hoboken, New Jersey: Wiley, June 2015 (cit. on p. 40).

[Braat 2008] Joseph J. M. Braat et al. "Chapter 6 Assessment of optical systems by means of point-spread functions". *Progress in Optics*. Ed. by E. Wolf. Vol. 51. Elsevier, Jan. 2008, pp. 349–468. DOI: 10.1016/S0079-6638(07)51006-1 (cit. on p. 52).

[Braunstein 1994] Samuel L. Braunstein and Carlton M. Caves. "Statistical distance and the geometry of quantum states". *Physical Review Letters* 72.22 (May 1994), pp. 3439–3443. DOI: 10.1103/PhysRevLett.72.3439 (cit. on pp. 1, 44).

[Brecht 2015] B. Brecht et al. "Photon Temporal Modes: A Complete Framework for Quantum Information Science". *Physical Review X* 5.4 (Oct. 2015), p. 041017. DOI: 10.1103/PhysRevX.5.041017 (cit. on pp. 19, 37).

[Bretschneider 2007] Stefan Bretschneider, Christian Eggeling, and Stefan W. Hell. "Breaking the Diffraction Barrier in Fluorescence Microscopy by Optical Shelving". *Physical Review Letters* 98.21 (May 2007). Publisher: American Physical Society, p. 218103. DOI: 10.1103/PhysRevLett.98.218103 (cit. on p. 72).

[Caves 1981] Carlton M. Caves. "Quantum-mechanical noise in an interferometer". *Physical Review D* 23.8 (Apr. 1981), pp. 1693–1708. DOI: 10.1103/PhysRevD.23.1693 (cit. on p. 1).

[Chalopin 2009] Benoît Chalopin. "Optique quantique multimode : des images aux impulsions". These de doctorat. Paris 6, Jan. 2009 (cit. on p. 3).

[Chao 2016] Jerry Chao, E. Sally Ward, and Raimund J. Ober. "Fisher information theory for parameter estimation in single molecule microscopy: tutorial". *Journal of the Optical Society of America A* 33.7 (July 2016), B36. DOI: 10.1364/JOSAA.33.000B36 (cit. on pp. 52, 53, 56, 58).

[Cheezum 2001] Michael K. Cheezum, William F. Walker, and William H. Guilford. "Quantitative Comparison of Algorithms for Tracking Single Fluorescent Particles". *Biophysical Journal* 81.4 (Oct. 2001), pp. 2378–2388. DOI: 10.1016/S0006-3495(01)75884-5 (cit. on p. 52).

[Cohen-Tannoudji 1997] Claude Cohen-Tannoudji, Jacques Dupont-Roc, and Gilbert Grynberg. *Photons and Atoms*. Weinheim: John Wiley & Sons, Feb. 1997 (cit. on p. 20).

[Collaboration 2019] The Event Horizon Telescope Collaboration et al. "First M87 Event Horizon Telescope Results. IV. Imaging the Central Supermassive Black Hole". *The Astrophysical Journal Letters* 875.1 (Apr. 2019). Publisher: The American Astronomical Society, p. L4. DOI: 10.3847/2041-8213/ab0e85 (cit. on pp. 73, 74).

[collectif 2012] VIM collectif. *International vocabulary of metrology – Basic and general concepts and associated terms*. 2012 (cit. on p. 1).

[Cramér 1999] Harald Cramér. *Mathematical Methods of Statistics*. Google-Books-ID: jV2YDwAAQBAJ. Princeton University Press, Apr. 1999 (cit. on p. 43).

[Crowley 2014] Philip J. D. Crowley et al. "Tradeoff in simultaneous quantum-limited phase and loss estimation in interferometry". *Physical Review A* 89.2 (Feb. 2014), p. 023845. DOI: 10.1103/PhysRevA.89.023845 (cit. on p. 154).

[Delaubert 2006] V. Delaubert et al. "TEM 10 homodyne detection as an optimal small-displacement and tilt-measurement scheme". *Physical Review A* 74.5 (Nov. 2006), p. 053823. DOI: 10.1103/PhysRevA.74.053823 (cit. on p. 56).

[Delaubert 2007] Vincent Delaubert. "Imagerie quantique à petit nombre de modes transverses". These de doctorat. Paris 6, Jan. 2007 (cit. on p. 3).

[Demkowicz-Dobrzański 2015] Rafal Demkowicz-Dobrzański, Marcin Jarzyna, and Jan Kołodyński. "Chapter Four - Quantum Limits in Optical Interferometry". *Progress in Optics*. Ed. by E. Wolf. Vol. 60. Elsevier, Jan. 2015, pp. 345–435. DOI: 10.1016/bs.po.2015.02.003 (cit. on p. 49).

[Devroye 2013] Luc Devroye. *Non-uniform Random Variate Generation*. 1986e édition. New York Heidelberg: Springer-Verlag New York Inc., Nov. 2013 (cit. on p. 94).

[Dickson 1997] Robert M. Dickson et al. "On/off blinking and switching behaviour of single molecules of green fluorescent protein". *Nature* 388.6640 (July 1997). Number: 6640 Publisher: Nature Publishing Group, pp. 355–358. DOI: 10.1038/41048 (cit. on p. 2).

[Drever 1983] R. W. P. Drever et al. "Laser phase and frequency stabilization using an optical resonator". *Applied Physics B* 31.2 (June 1983), pp. 97–105. DOI: 10.1007/BF00702605 (cit. on p. 122).

[Fabre 2020] Claude Fabre and Nicolas Treps. "Modes and states in Quantum Optics". *Reviews of Modern Physics* 92.3 (Sept. 2020). arXiv:1912.09321 [quant-ph], p. 035005. DOI: 10.1103/RevModPhys.92.035005 (cit. on p. 5).

[Fisher 1925] R. A. Fisher. "Theory of Statistical Estimation". *Mathematical Proceedings of the Cambridge Philosophical Society* 22.5 (July 1925), pp. 700–725. DOI: 10.1017/S0305004100009580 (cit. on p. 43).

[Fontaine 2021] Nicolas K. Fontaine et al. "Hermite-Gaussian mode multiplexer supporting 1035 modes". *Optical Fiber Communication Conference (OFC) 2021 (2021), paper M3D.4*. Optica Publishing Group, June 2021, p. M3D.4. DOI: 10.1364/OFC.2021.M3D.4 (cit. on p. 36).

[Franken 2017] Linda E. Franken, Egbert J. Boekema, and Marc C. A. Stuart. "Transmission Electron Microscopy as a Tool for the Characterization of Soft Materials: Application and Interpretation". *Advanced Science (Weinheim, Baden-Wurttemberg, Germany)* 4.5 (May 2017), p. 1600476. DOI: 10.1002/advs.201600476 (cit. on p. 71).

[Gessner 2019] Manuel Gessner, Augusto Smerzi, and Luca Pezzè. "Metrological Nonlinear Squeezing Parameter". *Physical Review Letters* 122.9 (Mar. 2019). arXiv: 1811.12443, p. 090503. DOI: 10.1103/PhysRevLett.122.090503 (cit. on pp. 51, 151, 154).

[Gessner 2020a] Manuel Gessner, Claude Fabre, and Nicolas Treps. "Superresolution Limits from Measurement Crosstalk". *Physical Review Letters* 125.10 (Aug. 2020), p. 100501. DOI: 10.1103/PhysRevLett.125.100501 (cit. on pp. 2, 60, 75, 107, 117, 118, 126, 150).

[Gessner 2020b] Manuel Gessner, Augusto Smerzi, and Luca Pezzè. "Multiparameter squeezing for optimal quantum enhancements in sensor networks". *Nature Communications* 11.1 (July 2020). Number: 1 Publisher: Nature Publishing Group, p. 3817. DOI: 10.1038/s41467-020-17471-3 (cit. on pp. 153, 154).

[Gigan 2004] Sylvain Gigan. "Amplification paramétrique d'images en cavité : Effets classiques et quantiques". PhD thesis. Université Pierre et Marie Curie - Paris VI, Oct. 2004 (cit. on p. 3).

[Giovannetti 2011] Vittorio Giovannetti, Seth Lloyd, and Lorenzo Maccone. "Advances in quantum metrology". *Nature Photonics* 5.4 (Apr. 2011), pp. 222–229. DOI: 10.1038/nphoton.2011.35 (cit. on pp. 1, 40, 49).

[Glauber 1963] Roy J. Glauber. "Coherent and Incoherent States of the Radiation Field". *Physical Review* 131.6 (Sept. 1963), pp. 2766–2788. DOI: 10.1103/PhysRev.131.2766 (cit. on p. 28).

[Goodman 2000] Joseph W. Goodman. *Statistical Optics*. 1st edition. New York: Wiley-Interscience, Aug. 2000 (cit. on pp. 52, 74).

[Goodman 2004] Joseph Goodman. *Introduction to Fourier Optics*. 3rd edition. Englewood, Colorado: Roberts and Company Publishers, Dec. 2004 (cit. on p. 71).

[Grace 2020] Michael R. Grace et al. "Approaching quantum-limited imaging resolution without prior knowledge of the object location". *JOSA A* 37.8 (Aug. 2020). Publisher: Optica Publishing Group, pp. 1288–1299. DOI: 10.1364/JOSAA.392116 (cit. on p. 75).

[Grace 2022] Michael R. Grace and Saikat Guha. "Identifying Objects at the Quantum Limit for Superresolution Imaging". *Physical Review Letters* 129.18 (Oct. 2022), p. 180502. DOI: 10.1103/PhysRevLett.129.180502 (cit. on p. 2).

[Grynberg 2010] Gilbert Grynberg, Alain Aspect, and Claude Fabre. *Introduction to Quantum Optics: From the Semi-classical Approach to Quantized Light*. Cambridge University Press. 2010 (cit. on pp. 5, 20, 23, 159).

[Guerra 1990] John M. Guerra. "Photon tunneling microscopy". *Applied Optics* 29.26 (Sept. 1990), p. 3741. DOI: 10.1364/AO.29.003741 (cit. on p. 71).

[Gustafsson 1999] Gustafsson, Agard, and Sedat. "I^5 M: 3D widefield light microscopy with better than 100 nm axial resolution". *Journal of Microscopy* 195.1 (July 1999), pp. 10–16. DOI: 10.1046/j.1365-2818.1999.00576.x (cit. on p. 71).

[Gustafsson 2000] M. G. Gustafsson. "Surpassing the lateral resolution limit by a factor of two using structured illumination microscopy". *Journal of Microscopy* 198.Pt 2 (May 2000), pp. 82–87. DOI: 10.1046/j.1365-2818.2000.00710.x (cit. on p. 71).

[Gustafsson 2008] Mats G. L. Gustafsson et al. "Three-Dimensional Resolution Doubling in Wide-Field Fluorescence Microscopy by Structured Illumination". *Biophysical Journal* 94.12 (June 2008), pp. 4957–4970. DOI: 10.1529/biophysj.107.120345 (cit. on p. 71).

[Hand 2010] Eric Hand. "Telescope arrays give fine view of stars". *Nature* 464.7290 (Apr. 2010). Number: 7290 Publisher: Nature Publishing Group, pp. 820–821. DOI: 10.1038/464820a (cit. on p. 74).

[Haniff 1987] C. A. Haniff et al. "The first images from optical aperture synthesis". *Nature* 328.6132 (Aug. 1987), pp. 694–696. DOI: 10.1038/328694a0 (cit. on p. 73).

[Hartschuh 2008] Achim Hartschuh. "Tip-enhanced near-field optical microscopy". *Angewandte Chemie (International Ed. in English)* 47.43 (2008), pp. 8178–8191. DOI: 10.1002/anie.200801605 (cit. on p. 71).

[Hecht 2000] Bert Hecht et al. "Scanning near-field optical microscopy with aperture probes: Fundamentals and applications". *The Journal of Chemical Physics* 112.18 (May 2000), pp. 7761–7774. DOI: 10.1063/1.481382 (cit. on p. 71).

[Hell 1994] Stefan W. Hell and Jan Wichmann. "Breaking the diffraction resolution limit by stimulated emission: stimulated-emission-depletion fluorescence microscopy". *Optics Letters* 19.11 (June 1994). Publisher: Optica Publishing Group, pp. 780–782. DOI: 10.1364/OL.19.000780 (cit. on pp. 2, 72).

[Hell 1995] S. W. Hell and M. Kroug. "Ground-state-depletion fluorscence microscopy: A concept for breaking the diffraction resolution limit". *Applied Physics B* 60.5 (May 1995), pp. 495–497. DOI: 10.1007/BF01081333 (cit. on p. 72).

[Hell 2007] Stefan W. Hell. "Far-Field Optical Nanoscopy". *Science* 316.5828 (May 2007). Publisher: American Association for the Advancement of Science, pp. 1153–1158. DOI: 10.1126/science.1137395 (cit. on pp. 2, 71).

[Helstrom 1967] C. W. Helstrom. "Minimum mean-squared error of estimates in quantum statistics". *Physics Letters A* 25.2 (July 1967), pp. 101–102. DOI: 10.1016/0375-9601(67)90366-0 (cit. on pp. 1, 44, 45).

[Helstrom 1969] Carl W. Helstrom. "Quantum detection and estimation theory". *Journal of Statistical Physics* 1.2 (June 1969). tex.ids= helstrom1969a, pp. 231–252. DOI: 10.1007/BF01007479 (cit. on pp. 1, 153).

[Hess 2006] Samuel T. Hess, Thanu P. K. Girirajan, and Michael D. Mason. "Ultra-High Resolution Imaging by Fluorescence Photoactivation Localization Microscopy". *Biophysical Journal* 91.11 (Dec. 2006). Publisher: Elsevier, pp. 4258–4272. DOI: 10.1529/biophysj.106.091116 (cit. on p. 72).

[Hofmann 2005] Michael Hofmann et al. "Breaking the diffraction barrier in fluorescence microscopy at low light intensities by using reversibly photoswitchable proteins". *Proceedings of the National Academy of Sciences* 102.49 (Dec. 2005). Publisher: Proceedings of the National Academy of Sciences, pp. 17565–17569. DOI: 10.1073/pnas.0506010102 (cit. on p. 72).

[Holevo 2011] Alexander S. Holevo. *Probabilistic and Statistical Aspects of Quantum Theory*. Pisa, 2011 (cit. on p. 153).

[Huang 2009] Bo Huang, Mark Bates, and Xiaowei Zhuang. "Super-Resolution Fluorescence Microscopy". *Annual Review of Biochemistry* 78.1 (June 2009), pp. 993–1016. DOI: 10.1146/annurev.biochem.77.061906.092014 (cit. on p. 71).

[Jarvis 2020] M Jarvis et al. "Dark Energy Survey year 3 results: point spread function modelling". *Monthly Notices of the Royal Astronomical Society* 501.1 (Dec. 2020), pp. 1282–1299. DOI: 10.1093/mnras/staa3679 (cit. on p. 52).

[Jedrzejewski 2002] Franck Jedrzejewski. *Histoire universelle de la mesure*. Paris: ELLIPSES, May 2002 (cit. on p. 1).

[Jennison 1958] R. C. Jennison. "A Phase Sensitive Interferometer Technique for the Measurement of the Fourier Transforms of Spatial Brightness Distributions of Small Angular Extent". *Monthly Notices of the Royal Astronomical Society* 118.3 (June 1958), pp. 276–284. DOI: 10.1093/mnras/118.3.276 (cit. on p. 73).

[Joshi 2022] Chaitali Joshi et al. "Picosecond-resolution single-photon time lens for temporal mode quantum processing". *Optica* 9.4 (Apr. 2022), p. 364. DOI: 10.1364/OPTICA.439827 (cit. on p. 37).

[Justice 1985] J. H. Justice, D. J. Hawkins, and G. Wong. "Multidimensional attribute analysis and pattern recognition for seismic interpretation". *Pattern Recognition*. Artificial Intelligence and Signal Processing in Underwater Acoustics and Geophysics Problems 18.6 (Jan. 1985), pp. 391–399. DOI: 10.1016/0031-3203(85)90010-X (cit. on p. 40).

[Kay 1993] Steven Kay. *Fundamentals of Statistical Signal Processing, Volume I: Estimation Theory*. 1st edition. Upper Saddle River, NJ: Pearson, Apr. 1993 (cit. on pp. 1, 40, 43, 49, 50).

[Kellermann 2001] K. I. Kellermann and J. M. Moran. "The Development of High-Resolution Imaging in Radio Astronomy". *Annual Review of Astronomy and Astrophysics* 39.1 (2001). _eprint: https://doi.org/10.1146/annurev.astro.39.1.457, pp. 457–509. DOI: 10.1146/annurev.astro.39.1.457 (cit. on p. 73).

[Klar 2000] Thomas A. Klar et al. "Fluorescence microscopy with diffraction resolution barrier broken by stimulated emission". *Proceedings of the National Academy of Sciences* 97.15 (July 2000). Publisher: Proceedings of the National Academy of Sciences, pp. 8206–8210. DOI: 10.1073/pnas.97.15.8206 (cit. on p. 72).

[Labroille 2014] Guillaume Labroille et al. "Efficient and mode selective spatial mode multiplexer based on multi-plane light conversion". *Optics Express* 22.13 (June 2014), p. 15599. DOI: 10.1364/OE.22.015599 (cit. on pp. 36, 37).

[Leach 2002] Jonathan Leach et al. "Measuring the Orbital Angular Momentum of a Single Photon". *Physical Review Letters* 88.25 (June 2002), p. 257901. DOI: 10.1103/PhysRevLett.88.257901 (cit. on p. 35).

[Lee 2012] Sang-Hyuk Lee et al. "Counting single photoactivatable fluorescent molecules by photoactivated localization microscopy (PALM)". *Proceedings of the National Academy of Sciences* 109.43 (Oct. 2012). Publisher: Proceedings of the National Academy of Sciences, pp. 17436–17441. DOI: 10.1073/pnas.1215175109 (cit. on p. 72).

[Len 2020] Yink Loong Len et al. "Resolution limits of spatial mode demultiplexing with noisy detection". *International Journal of Quantum Information* 18.01 (Feb. 2020), p. 1941015. DOI: 10.1142/S0219749919410156 (cit. on pp. 2, 75, 107).

[Leon-Saval 2015] Sergio G Leon-Saval. "Photonic Lantern". *Advanced Photonics 2015*. Boston, Massachusetts: OSA, 2015, NeS2D.2. DOI: 10.1364/NETWORKS.2015.NeS2D.2 (cit. on pp. 34, 35).

[Leonhardt 2005] Ulf Leonhardt. *Measuring the Quantum State of Light*. Cambridge New York Melbourne: Cambridge University Press, Nov. 2005 (cit. on pp. 23, 27).

[Leung 2011] Bonnie O. Leung and Keng C. Chou. "Review of Super-Resolution Fluorescence Microscopy for Biology". *Applied Spectroscopy* 65.9 (Sept. 2011), pp. 967–980. DOI: 10.1366/11-06398 (cit. on p. 71).

[Lu 2018] Xiao-Ming Lu et al. "Quantum-optimal detection of one-versus-two incoherent optical sources with arbitrary separation". *npj Quantum Information* 4.1 (Dec. 2018), pp. 1–8. DOI: 10.1038/s41534-018-0114-y (cit. on p. 2).

[Lupo 2016] Cosmo Lupo and Stefano Pirandola. "Ultimate Precision Bound of Quantum and Subwavelength Imaging". *Physical Review Letters* 117.19 (Nov. 2016), p. 190802. DOI: 10.1103/PhysRevLett.117.190802 (cit. on pp. 2, 52, 56, 57).

[Lupo 2020] Cosmo Lupo. "Subwavelength quantum imaging with noisy detectors". *Physical Review A* 101.2 (Feb. 2020), p. 022323. DOI: 10.1103/PhysRevA.101.022323 (cit. on pp. 2, 107).

[Mandel 1995] Leonard Mandel and Emil Wolf. *Optical Coherence and Quantum Optics*. Cambridge: Cambridge University Press, 1995. DOI: 10.1017/CBO9781139644105 (cit. on pp. 20, 26, 28, 159, 162).

[Monnier 2003] John D Monnier. "Optical interferometry in astronomy". *Reports on Progress in Physics* 66.5 (May 2003), pp. 789–857. DOI: 10.1088/0034-4885/66/5/203 (cit. on p. 73).

[Morizur 2010] Jean-François Morizur et al. "Programmable unitary spatial mode manipulation". *Journal of the Optical Society of America A* 27.11 (Nov. 2010), p. 2524. DOI: 10.1364/JOSAA.27.002524 (cit. on pp. 2, 36).

[Morizur 2011] Jean-François Morizur. "Quantum protocols with transverse spatial modes". These de doctorat. Paris 6, Jan. 2011 (cit. on pp. 3, 36).

[Murphy 2008] T. W. Murphy et al. "The Apache Point Observatory Lunar Laser-ranging Operation: Instrument Description and First Detections". *Publications of the Astronomical Society of the Pacific* 120.863 (Jan. 2008). Publisher: University of Chicago Press, p. 20. DOI: 10.1086/526428 (cit. on p. 2).

[Nair 2016] Ranjith Nair and Mankei Tsang. "Far-Field Superresolution of Thermal Electromagnetic Sources at the Quantum Limit". *Physical Review Letters* 117.19 (Nov. 2016), p. 190801. DOI: 10.1103/PhysRevLett.117.190801 (cit. on pp. 2, 57, 75).

[Napoli 2019] Carmine Napoli et al. "Towards Superresolution Surface Metrology: Quantum Estimation of Angular and Axial Separations". *Physical Review Letters* 122.14 (Apr. 2019), p. 140505. DOI: 10.1103/PhysRevLett.122.140505 (cit. on p. 2).

[Nichols 2018] Rosanna Nichols et al. "Multiparameter Gaussian quantum metrology". *Physical Review A* 98.1 (July 2018), p. 012114. DOI: 10.1103/PhysRevA.98.012114 (cit. on p. 153).

[Oh 2021] Changhun Oh et al. "Quantum Limits of Superresolution in a Noisy Environment". *Physical Review Letters* 126.12 (Mar. 2021), p. 120502. DOI: 10.1103/PhysRevLett.126.120502 (cit. on p. 107).

[Ohtsu 1995] M. Ohtsu. "Progress of high-resolution photon scanning tunneling microscopy due to a nanometric fiber probe". *Journal of Lightwave Technology* 13.7

(July 1995). Conference Name: Journal of Lightwave Technology, pp. 1200–1221. DOI: 10.1109/50.400696 (cit. on p. 71).

[Parigi 2009] V Parigi, A Zavatta, and M Bellini. "Implementation of single-photon creation and annihilation operators: experimental issues in their application to thermal states of light". *Journal of Physics B: Atomic, Molecular and Optical Physics* 42.11 (June 2009), p. 114005. DOI: 10.1088/0953-4075/42/11/114005 (cit. on pp. 102, 103).

[Parniak 2018] Michał Parniak et al. "Beating the Rayleigh Limit Using Two-Photon Interference". *Physical Review Letters* 121.25 (Dec. 2018), p. 250503. DOI: 10.1103/PhysRevLett.121.250503 (cit. on pp. 3, 79, 84).

[Paúr 2016] Martin Paúr et al. "Achieving the ultimate optical resolution". *Optica* 3.10 (Oct. 2016), pp. 1144–1147. DOI: 10.1364/OPTICA.3.001144 (cit. on pp. 2, 37, 76, 84).

[Pawley 2006] James Pawley, ed. *Handbook of Biological Confocal Microscopy*. 3rd edition. New York, NY: Springer, June 2006 (cit. on p. 71).

[Pezzè 2014] Luca Pezzè and Augusto Smerzi. *Quantum theory of phase estimation*. arXiv:1411.5164 [cond-mat, physics:quant-ph]. Nov. 2014 (cit. on pp. 40, 45, 46).

[Pinel 2012] Olivier Pinel et al. "Ultimate sensitivity of precision measurements with intense Gaussian quantum light: A multimodal approach". *Physical Review A* 85.1 (Jan. 2012), p. 010101. DOI: 10.1103/PhysRevA.85.010101 (cit. on p. 46).

[Proakis 2007] John Proakis and Massoud Salehi. *Digital Communications*. 5e édition. Boston: McGraw-Hill Higher Education, Nov. 2007 (cit. on p. 40).

[Pushkina 2021] A. A. Pushkina et al. "Superresolution Linear Optical Imaging in the Far Field". *Physical Review Letters* 127.25 (Dec. 2021), p. 253602. DOI: 10.1103/PhysRevLett.127.253602 (cit. on p. 78).

[Racine 1996] Rene Racine. "The telescope point spread function". *Publications of the Astronomical Society of the Pacific* 108.726 (Aug. 1996). Publisher: The Astronomical Society of the Pacific, p. 699. DOI: 10.1086/133788 (cit. on p. 52).

[Ragy 2016] Sammy Ragy, Marcin Jarzyna, and Rafał Demkowicz-Dobrzański. "Compatibility in multiparameter quantum metrology". *Physical Review A* 94.5 (Nov. 2016). tex.ids= ragy2016a, p. 052108. DOI: 10.1103/PhysRevA.94.052108 (cit. on p. 154).

[Rao 1994] Calyampudi Radhakrishna Rao and S. Das Gupta. *Selected Papers of C. R. Rao*. Google-Books-ID: NKTgAAAAMAAJ. Wiley, 1994 (cit. on p. 43).

[Rayleigh 1879] Rayleigh. "XXXI. Investigations in optics, with special reference to the spectroscope". *The London, Edinburgh, and Dublin Philosophical Magazine and Journal of Science* 8.49 (Oct. 1879), pp. 261–274. DOI: 10.1080/14786447908639684 (cit. on pp. 2, 68).

[Řehaček 2017] J. Řehaček et al. "Multiparameter quantum metrology of incoherent point sources: Towards realistic superresolution". *Physical Review A* 96.6 (Dec. 2017), p. 062107. DOI: 10.1103/PhysRevA.96.062107 (cit. on pp. 2, 153, 154).

[Renault 2022] Paul Renault. "Non Markovian behavior and spectral density measurement in optical quantum networks". PhD thesis. Sorbonne Université, Apr. 2022 (cit. on pp. 19, 26).

[Roggemann 1997] Michael C. Roggemann, Byron M. Welsh, and Robert Q. Fugate. "Improving the resolution of ground-based telescopes". *Reviews of Modern Physics* 69.2 (Apr. 1997). Publisher: American Physical Society, pp. 437–506. DOI: 10.1103/RevModPhys.69.437 (cit. on pp. 58, 73).

[Rouvière 2024] Clémentine Rouvière et al. "Ultra-sensitive separation estimation of optical sources". *Optica* 11.2 (Feb. 2024). Publisher: Optica Publishing Group, pp. 166–170. DOI: 10.1364/OPTICA.500039 (cit. on pp. 82, 84, 150, 155).

[Rust 2006] Michael J. Rust, Mark Bates, and Xiaowei Zhuang. "Sub-diffraction-limit imaging by stochastic optical reconstruction microscopy (STORM)". *Nature Methods* 3.10 (Oct. 2006). Number: 10 Publisher: Nature Publishing Group, pp. 793–796. DOI: 10.1038/nmeth929 (cit. on p. 72).

[Santamaria 2023] Luigi Santamaria et al. "Spatial-mode demultiplexing for enhanced intensity and distance measurement". *Optics Express* 31.21 (Oct. 2023),

p. 33930. DOI: 10.1364/OE.486617 (cit. on pp. 3, 82–84).

[Santos 2021] G. H. dos Santos et al. "Decomposing spatial mode superpositions with a triangular optical cavity". *Physical Review Applied* 16.3 (Sept. 2021). arXiv: 2104.04635, p. 034008. DOI: 10.1103/PhysRevApplied.16.034008 (cit. on p. 36).

[Schuster 1898] Arthur Schuster. "On the investigation of hidden periodicities with application to a supposed 26 day period of meteorological phenomena". *Terrestrial Magnetism* 3.1 (1898), pp. 13–41. DOI: 10.1029/TM003i001p00013 (cit. on p. 40).

[Schwob 1997] Catherine Schwob. "Utilisation des faisceaux correles au niveau quantique produits par un oscillateur parametrique optique en spectroscopie de grande sensibilite". These de doctorat. Paris 6, Jan. 1997 (cit. on p. 3).

[Serafini 2017] Alessio Serafini. *Quantum Continuous Variables: A Primer of Theoretical Methods*. 1er édition. CRC Press, July 2017 (cit. on p. 46).

[Siegman 1986] Anthony E. Siegman. *Lasers*. Mill Valley, Calif: University Science Books,U.S., Nov. 1986 (cit. on p. 12).

[Sit 2017] Alicia Sit et al. "High-dimensional intracity quantum cryptography with structured photons". *Optica* 4.9 (Sept. 2017). Publisher: Optica Publishing Group, pp. 1006–1010. DOI: 10.1364/OPTICA.4.001006 (cit. on p. 18).

[Slussarenko 2017] Sergei Slussarenko et al. "Unconditional violation of the shot-noise limit in photonic quantum metrology". *Nature Photonics* 11.11 (Nov. 2017). Number: 11 Publisher: Nature Publishing Group, pp. 700–703. DOI: 10.1038/s41566-017-0011-5 (cit. on pp. 2, 49).

[Sorelli 2021a] Giacomo Sorelli et al. "Moment-based superresolution: Formalism and applications". *Physical Review A* 104.3 (Sept. 2021), p. 033515. DOI: 10.1103/PhysRevA.104.033515 (cit. on pp. 51, 52, 59, 75, 107, 117, 137, 168).

[Sorelli 2021b] Giacomo Sorelli et al. "Optimal Observables and Estimators for Practical Superresolution Imaging". *Physical Review Letters* 127.12 (Sept. 2021), p. 123604. DOI: 10.1103/PhysRevLett.127.123604 (cit. on pp. 2, 51, 75, 151).

[Sorelli 2022] Giacomo Sorelli et al. *Quantum limits for resolving Gaussian sources*. May 2022 (cit. on p. 57).

[Sorelli 2023] Giacomo Sorelli et al. *Gaussian quantum metrology for mode-encoded parameters*. arXiv:2202.10355 [quant-ph]. Feb. 2023 (cit. on pp. 46, 47, 53, 54, 57, 167).

[Sparrow 1916] C. M. Sparrow. "On spectroscopic resolving power". *Astrophys. J.* 44 (1916), p. 76 (cit. on pp. 68, 69).

[Stallinga 2010] Sjoerd Stallinga and Bernd Rieger. "Accuracy of the Gaussian Point Spread Function model in 2D localization microscopy". *Optics Express* 18.24 (Nov. 2010). Publisher: Optica Publishing Group, pp. 24461–24476. DOI: 10.1364/OE.18.024461 (cit. on p. 52).

[Steed 2012] Jonathan W. Steed and Philip A. Gale, eds. *Supramolecular Chemistry: From Molecules to Nanomaterials*. 1st edition. Chichester: Wiley, Mar. 2012 (cit. on p. 71).

[Sudarshan 1963] E. C. G. Sudarshan. "Equivalence of Semiclassical and Quantum Mechanical Descriptions of Statistical Light Beams". *Physical Review Letters* 10.7 (Apr. 1963), pp. 277–279. DOI: 10.1103/PhysRevLett.10.277 (cit. on p. 28).

[Tan 2023] Xiao-Jie Tan et al. "Quantum-inspired superresolution for incoherent imaging". *Optica* 10.9 (Sept. 2023), p. 1189. DOI: 10.1364/OPTICA.493227 (cit. on pp. 82–84).

[Tang 2016] Zong Sheng Tang, Kadir Durak, and Alexander Ling. "Fault-tolerant and finite-error localization for point emitters within the diffraction limit". *Optics Express* 24.19 (Sept. 2016), pp. 22004–22012. DOI: 10.1364/OE.24.022004 (cit. on pp. 3, 77, 84).

[Taylor 2007] Stephen J. Taylor. *Modelling Financial Time Series*. 2nd edition. New Jersey: World Scientific Publishing Company, Dec. 2007 (cit. on p. 40).

[Tham 2017] Weng-Kian Tham, Hugo Ferretti, and Aephraim M. Steinberg. "Beating Rayleigh's Curse by Imaging Using Phase Information". *Physical Review Letters* 118.7 (Feb. 2017), p. 070801. DOI: 10.1103/PhysRevLett.118.070801 (cit. on pp. 3, 78, 79, 84).

[Thomann 2002] D. Thomann et al. "Automatic fluorescent tag detection in 3D with super-resolution: application to the analysis of chromosome movement". *Journal of Microscopy* 208.1 (2002), pp. 49–64. DOI: 10.1046/j.1365-2818.2002.01066.x (cit. on p. 69).

[Thompson 2002] Russell E. Thompson, Daniel R. Larson, and Watt W. Webb. "Precise Nanometer Localization Analysis for Individual Fluorescent Probes". *Biophysical Journal* 82.5 (May 2002), pp. 2775–2783. DOI: 10.1016/S0006-3495(02)75618-X (cit. on p. 52).

[Treps 2001] Nicolas Treps. "Effets quantiques dans les images optiques". These de doctorat. Paris 6, Jan. 2001 (cit. on p. 3).

[Treps 2003] Nicolas Treps et al. "A Quantum Laser Pointer". *Science* 301.5635 (Aug. 2003). Publisher: American Association for the Advancement of Science, pp. 940–943. DOI: 10.1126/science.1086489 (cit. on p. 2).

[Tsang 2016] Mankei Tsang, Ranjith Nair, and Xiao-Ming Lu. "Quantum Theory of Superresolution for Two Incoherent Optical Point Sources". *Physical Review X* 6.3 (Aug. 2016), p. 031033. DOI: 10.1103/PhysRevX.6.031033 (cit. on pp. 2, 50, 56–60, 75, 76, 153).

[Tsang 2017] Mankei Tsang. "Subdiffraction incoherent optical imaging via spatial-mode demultiplexing". *New Journal of Physics* 19.2 (Feb. 2017), p. 023054. DOI: 10.1088/1367-2630/aa60ee (cit. on pp. 2, 75).

[Virgo Collaboration 2019] Virgo Collaboration et al. "Increasing the Astrophysical Reach of the Advanced Virgo Detector via the Application of Squeezed Vacuum States of Light". *Physical Review Letters* 123.23 (Dec. 2019). tex.ids= acernese2019, acernese2019a publisher: American Physical Society, p. 231108. DOI: 10.1103/PhysRevLett.123.231108 (cit. on pp. 1, 2, 49).

[Wadood 2021] S. A. Wadood et al. "Experimental demonstration of superresolution of partially coherent light sources using parity sorting". *Optics Express* 29.14 (July 2021), pp. 22034–22043. DOI: 10.1364/OE.427734 (cit. on p. 3).

[Walschaers 2021] Mattia Walschaers. "Non-Gaussian Quantum States and Where to Find Them". *PRX Quantum* 2.3 (Sept. 2021), p. 030204. DOI: 10.1103/PRXQuantum.2.030204 (cit. on p. 29).

[Widrow 1985] Bernard Widrow and Peter Stearns. *Adaptive Signal Processing*. Prentice Hall, 1985 (cit. on p. 40).

[Williamson 1936] John Williamson. "On the Algebraic Problem Concerning the Normal Forms of Linear Dynamical Systems". *American Journal of Mathematics* 58.1 (1936). Publisher: Johns Hopkins University Press, pp. 141–163. DOI: 10.2307/2371062 (cit. on p. 31).

[Wizinowich 2000] P. Wizinowich et al. "First Light Adaptive Optics Images from the Keck II Telescope: A New Era of High Angular Resolution Imagery". *Publications of the Astronomical Society of the Pacific* 112.769 (Mar. 2000). Publisher: The University of Chicago Press, p. 315. DOI: 10.1086/316543 (cit. on p. 58).

[Yang 2016] Fan Yang et al. "Far-field linear optical superresolution via heterodyne detection in a higher-order local oscillator mode". *Optica* 3.10 (Oct. 2016), p. 1148. DOI: 10.1364/OPTICA.3.001148 (cit. on pp. 2, 77, 78, 84).

[Yariv 1977] Amnon Yariv. *Introduction to optical electronics*. 2nd edition. New York: Holt McDougal, Jan. 1977 (cit. on pp. 8, 10, 12).

[Zanforlin 2022] Ugo Zanforlin et al. "Optical quantum superresolution imaging and hypothesis testing". *Nature Communications* 13.1 (Sept. 2022), p. 5373. DOI: 10.1038/s41467-022-32977-8 (cit. on pp. 3, 79, 80, 84).

[Zhang 2007] Bo Zhang, Josiane Zerubia, and Jean-Christophe Olivo-Marin. "Gaussian approximations of fluorescence microscope point-spread function models". *Applied Optics* 46.10 (Apr. 2007). Publisher: Optica Publishing Group, pp. 1819–1829. DOI: 10.1364/AO.46.001819 (cit. on pp. 52, 68).

[Zhang 2023] Yuanhang Zhang and Nicolas K. Fontaine. *Multi-Plane Light Conversion: A Practical Tutorial*. arXiv:2304.11323 [physics]. May 2023 (cit. on p. 36).

[Zhou 2017] Yiyu Zhou et al. "Sorting Photons by Radial Quantum Number". *Physical Review Letters* 119.26 (Dec. 2017), p. 263602. DOI: 10.1103/PhysRevLett.119.263602 (cit. on pp. 35, 36, 84).

[Zhou 2018] Yiyu Zhou et al. "Hermite-Gaussian mode sorter". *Optics Letters* 43.21 (Nov. 2018). arXiv:1810.00229 [physics, physics:quant-ph], p. 5263. DOI: 10.1364/OL.43.005263 (cit. on p. 36).

[Zhou 2019a] Yiyu Zhou et al. "Quantum-limited estimation of the axial separation of two incoherent point sources". *Optica* 6.5 (May 2019). tex.ids= zhou2019a, p. 534. DOI: 10.1364/OPTICA.6.000534 (cit. on pp. 3, 80, 81).

[Zhou 2019b] Yiyu Zhou et al. "Using all transverse degrees of freedom in quantum communications based on a generic mode sorter". *Optics Express* 27.7 (Apr. 2019). Publisher: Optica Publishing Group, pp. 10383–10394. DOI: 10.1364/OE.27.010383 (cit. on p. 18).

[Zmuidzinas 2003] Jonas Zmuidzinas. "Cramér–Rao sensitivity limits for astronomical instruments: implications for interferometer design". *JOSA A* 20.2 (Feb. 2003). Publisher: Optica Publishing Group, pp. 218–233. DOI: 10.1364/JOSAA.20.000218 (cit. on p. 53).